Development of an intense pulsed THz source to trigger structural and electronic response of materials

Lucas Gournay

UNIVERSITÉ DE RENNES 1

THESE DE DOCTORAT DE

L'UNIVERSITE DE RENNES 1

ECOLE DOCTORALE N° 596
Matière, Molécules, Matériaux
Spécialité : « Physique »

Par
Lucas Gournay

Development of an intense pulsed THz source to trigger structural and electronic response of materials.

Thèse présentée et soutenue à Rennes, le 16 février 2022
Unité de recherche : Institut de Physique de Rennes UMR 6251

Rapporteurs avant soutenance :

Davide Boschetto	Professeur, ENSTA Paris-Tech
Elsa Abreu	Chef d'équipe, ETH Zurich

Composition du Jury :

Président :	Maciej Lorenc	Directeur de Recherches, Université de Rennes 1
Examinateurs :	Davide Boschetto	Professeur, ENSTA Paris-Tech
	Elsa Abreu	Chef d'équipe, ETH Zurich
	Maciej Lorenc	Directeur de Recherches, Université de Rennes 1
Dir. de thèse :	Laurent Guérin	Maître de conférences Université de Rennes 1

Invité(s)

	Marco Cammarata	Responsable de ligne, ESRF Grenoble

Development of an intense pulsed THz source to trigger structural and electronic response of materials

Lucas Gournay

May 16, 2022

Contents

Resumé en français

Déclencher des réponses structurelles et électroniques des matériaux s'inscrit dans l'étude des transitions de phases. Un matériau peut présenter deux états ayant des propriétés macroscopiques différentes. Ces propriétés peuvent-être structurelles, électriques, mécaniques, magnétiques etc. On peut passer d'un état à l'autre via un paramètre de contrôle le plus souvent la température. Par exemple, l'eau peut passer de glace à liquide à vapeur. Cependant, il existe d'autres paramètres de contrôle comme la pression, le champ électrique ou même la lumière.

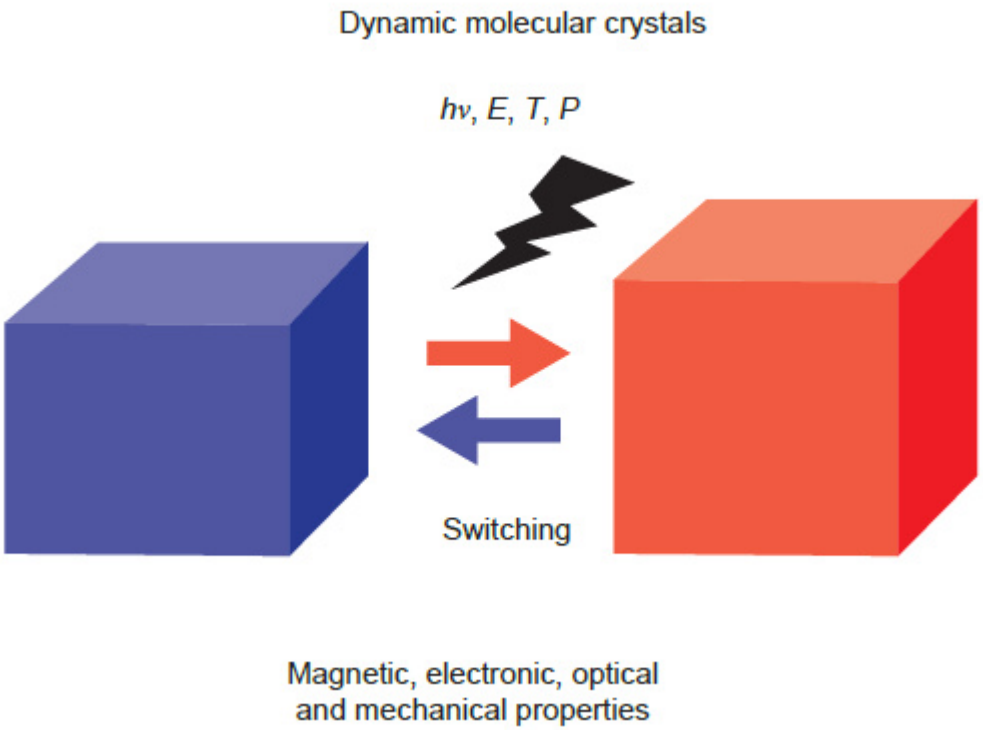

Figure 1: Schéma représentatif des transitions de phases, figure adaptée de [1]

En particulier, l'étude des transitions de phases où le paramètre de contrôle est la lumière est appelée transition de phases photo-induite. La lumière est utilisée pour exciter la matière depuis son état fondamental vers un état excité. Si le matériau présente de la coopérativité, il va relaxer à travers une myriade d'états. Le chemmin suivi pourra le conduire vers un nouvel état métastable dont les propriétés macroscopiques peuvent-être différentes de celles de l'état fondamental. Le concept de transition de phase photo-induite a été défini par Nasu et al.[2] (voir figure 2)

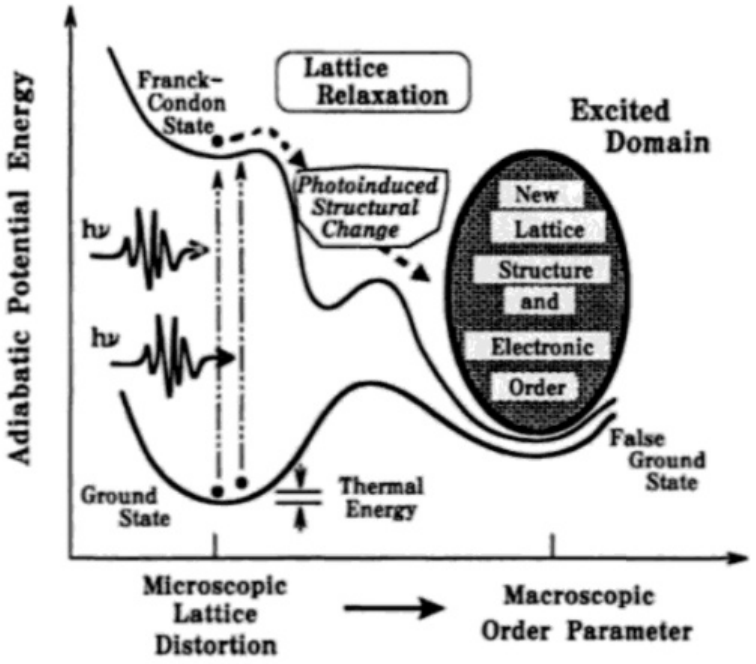

Figure 2: Représentation schématique d'une transition de phase photoinduite. Le système traverse différents avant d'atteindre le faux état fondamentale qui change le paramètre d'ordre désiré. Figure adaptée de [2]

L'une des techniques permettant la mesure de cet état métastable est la technique dite pompe sonde. Cette technique utilise deux faisceaux lumineux. Le premier est appelé pompe et sert à exciter la matière, le second est retardé et mesure les nouvelles propriétés de la matière. Ainsi, comme les faisceaux lasers peuvent atteindre la durée de la fs il est possible de mesurer des états métastables dont la durée de vie est très courte.

Généralement, la lumière visible est utilisée comme pompe. L'énergie apportée par la pompe est ainsi beaucoup plus importante que l'écart entre l'état d'énergie fondamentale et le nouvel état cible métastable. Ainsi, la coopérativité est cruciale dans les matériaux présentant des transitions de phases photo-induite afin d'éviter que la matériel ne relaxe directement dans l'état fondamental.

Le rayonnement THz présente une énergie beaucoup plus faible que celle de la lumière visible et comparable à l'écart d'énergie entre le niveau fondamental et le nouvel état métastable. La question à laquelle ce manuscrit de thèse se propose de répondre est la suivante : Peut-on utiliser le rayonnement THz pour induire des transitions de phases photo-induites ?

Les charactéristiques du rayonnement THz sont présentés en Table 1

Fréquence	Energie	Longueur d'onde	Nombre d'onde	Durée de pulse
1 THz	4meV	300 mum	33 cm-1	1ps

Table 1: Unités usuelles pour 1 THz

Le rayonnement THz intense présente le plus souvent des champs électriques dits simple cycle. Un champ électrique simple cycle présente une forte intensité dans une

seule direction dont la durée est de l'ordre de la picoseconde. De tels champs électriques peuvent atteindre des champs électriques de l'ordre du MV/cm. Un tel exemple de champ électrique THz simple cycle intense peut être trouvé en figure 3 :

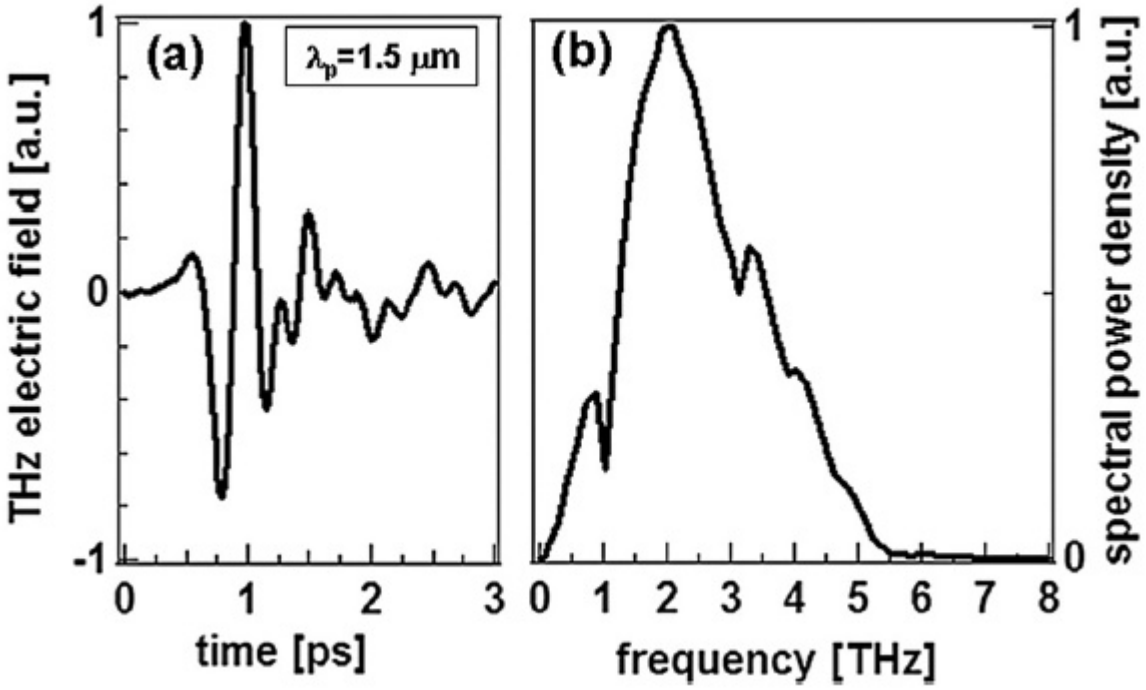

Figure 3: Exemple de champ électrique THz simple cycle obtenu à partir de redressement optique dans un crystal de DAST. Figure adaptée de la référence [3]

La forme temporelle du champ électrique simple cycle permet d'utiliser le rayonnement THz soit pour déclencher des réponses électroniques dans les matériaux soit pour modifier directement la structure des matériaux ce qui justifie le titre de cette thèse. Le rayonnement THz a déjà été utilisé sur le cristal moléculaire appelé TTF-CA de ces deux manières afin de déclencher des effets différents en particulier la génération ou la modulation de Seconde Harmonique dans le matériel[4]. Ainsi le développement de source THz intense est fondamental pour la poursuite de ces études.

Une source basée sur la technique du redressement optique a ainsi été développée pendant ce travail de thèse. Le redressement optique est un phénomène non linéaire d'ordre 2 qui transforme un rayonnement dont la durée est proche de la 100fs en rayonnement simple cycle de durée 1 ps. Le spectre associé au rayonnement ainsi généré s'étend sur une échelle de fréquence allant de 0.1 à 5 THz. En particulier, pour un rayonnement source dont la durée est de 100fs, le rayonnement THz attendu est présenté en Fig.4.

Nous avons choisi le crystal de LiNbO3 comme crystal de génération. Ce crystal présente les caractéristiques optimales de génération THz par rapport à nos caractéristiques laser. En revanche, une technique doit être employée pour accomplir l'accord de phase dans ce crystal. En effet, le rayonnement THz n'est pas généré colinéairement à l'impulsion source dans le crystal entraînant des interférences destructives. En inclinant le front d'onde suivant le même angle que la génération THz on peut ainsi générer un

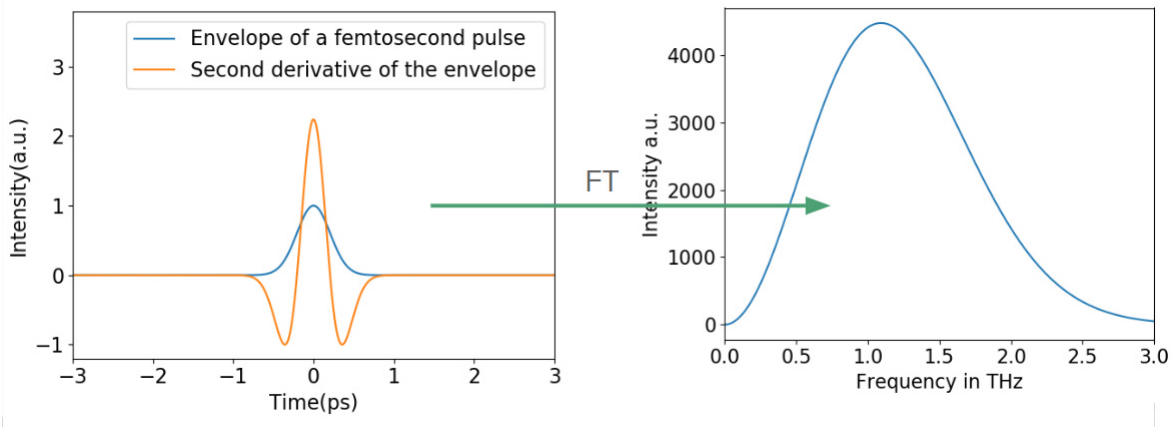

Figure 4: La figure de gauche est la forme temporelle de deux impulsions. Bleu : Enveloppe d'un rayonnement fs dont la durée est de 100fs. Orange : Impulsion obtenue par redressement optique de l'impulsion bleu. La figure de droite représente la transformée de Fourrier de l'impulsion orange qui s'étend de 0 à 2 THz.

rayonnement THz optimal.

Pour obtenir la source THz la plus intense possible une excellent focalisation doit être réalisée. Un système de trois mirroirs paraboliques en or est utilisée pour aggrandir puis focaliser le faisceau. Le choix des miroirs parabolique est expliqué pasr le très faible taux de perte qu'elles présentent dans le régime THz. Une plaque métallique développée cojointement avec l'atelier mécanique de Rennes fut créée pour faciliter l'allignement des mirroirs paraboliques.

L'utilisation du rayonnement THz étant relativement récent, les outils usuels de visualisation n'existent pas encore. Pour imager le faisceau, une caméra pyroélectrique Pyrocam III a été utilisé. Une image du faisceau THz prise avec la Pyrocam III est présentée en figure 5. Le système de focalisation a permis d'obtenir une tâche focale d'environ 800 μm.

La caractérisation du champ électrique THz obtenue a été réalisée en utilisant la technique de l'échantillonnage électro optique ou EOS. Cette technique se repose sur l'effet Pockels, certains matériaux deviennent biréfringeants sous l'effet d'un champ électrique. Cette biréfringence est responsable d'un changement de polarisation de la lumière incidente dont la polarisation passe de linéaire à elliptique. En mesurant le degré d'ellipticité à l'aide par exemple d'un prisme de Wollaston, on peut déduire la valeur du champ électrique appliquée sur le crystal. Un champ électrique d'une valeur de 800kV/cm a ainsi été obtenu et est présenté en figure 6.

Les caractéristiques de cette source la hisse parmi les meilleurs sources mondiales utilisant le redressement optique allié à la technique du front d'onde tilté dans le crystal de $LiNbO_3$.

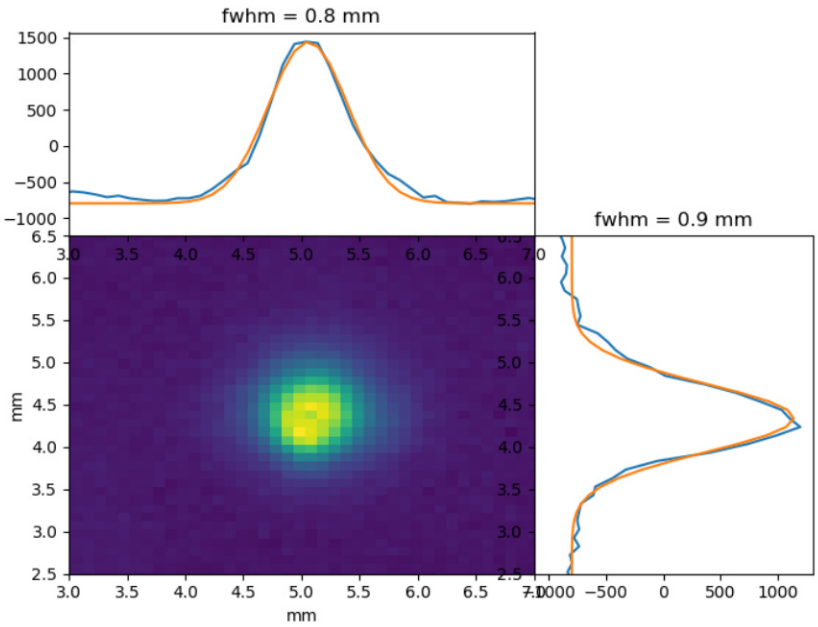

Figure 5: Image du faisceau THz focalisé après le système de miroirs paraboliques obtenu avec la PyrocamIII. Les tailles horizontales et verticales du faisceau sont extraites par des coupes horizontales et verticales présentés au dessus et à côté de l'image.

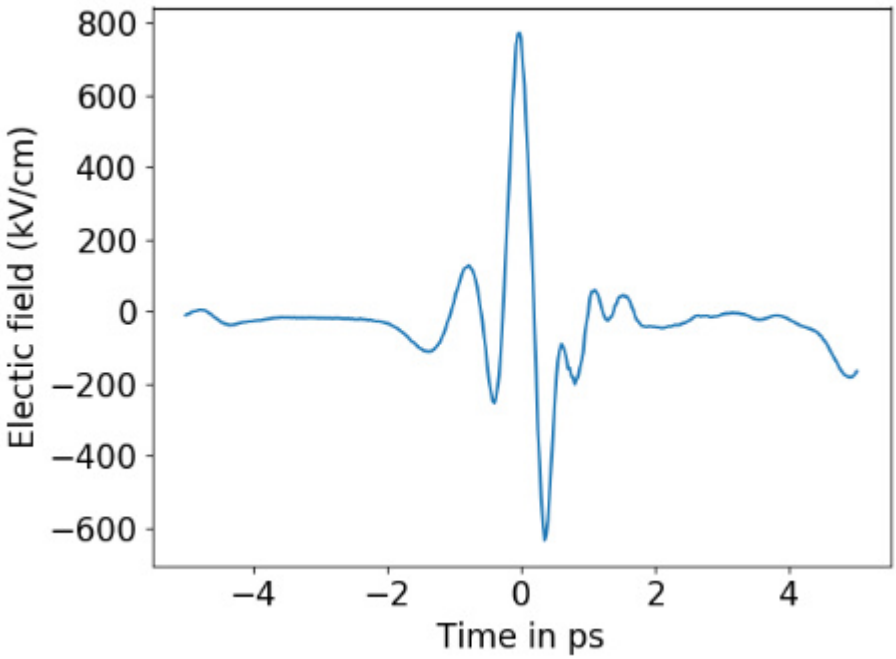

Figure 6: Profil temporel du champ électrique THz. Une valeur maximale de 800kV/cm est obtenue

Cette source a été développée dans le but de réaliser des expériences pompe THz sonde optique. La dernière étape pour que cette source soit complêtement fonctionnelle est la validation sur une expérience test. Nous avons choisi de reproduire l'expérience de Chen et al.[5] sur le $\beta - BBO$. Dans cette expérience, le rayonnement THz est util-

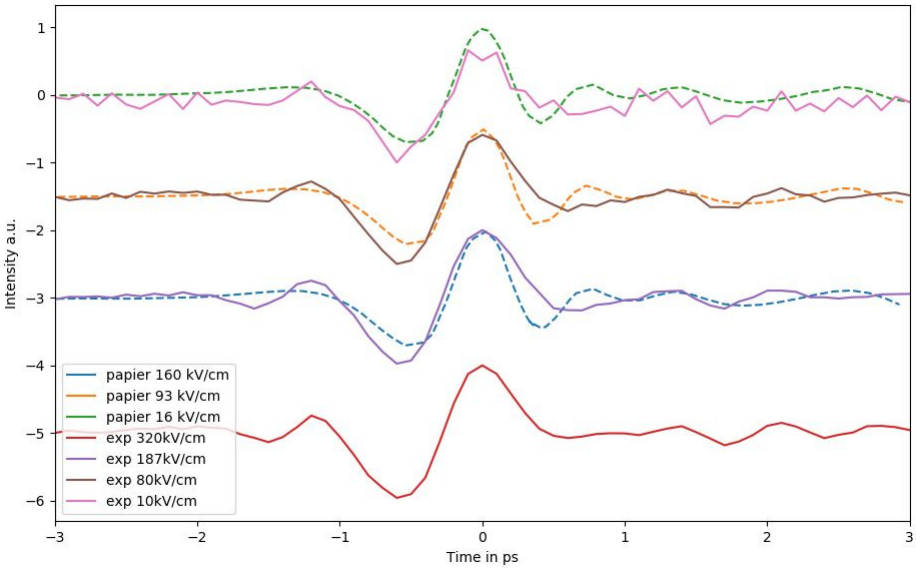

Figure 7: Modulation de génération de second harmonique en fonction du temps pour valeurs du champ électrique THz. Les résultats de Chen et al. sont en pointillés tandis que les résultats de ce travail de thèse sont en traits pleins.

isé pour moduler la génération de seconde harmonique dans le cristal de $\beta - BBO$. L'expérience de Chen et al. a été réalisée avec un champ électrique maximale de 160kV/cm tandis que l'expérience réalisée dans ce travail de thèse l'a été avec un champ électrique maximale de 300kV/cm. Les résultats comparatifs entre ceux de Chen et al. (pointillés) et ceux de ce travail (traits pleins) sont présentés en Fig. 7. On observe une modulation de la seconde harmonique similaire dans les deux travaux en dessous de 160kV/cm. A 300kV/cm, les résultats obtenues restent semblables à ceux obtenues à plus basse valeur du champ électrique. On peut conclure par cette similarité que non seulement la source est utilisable mais permet également de valider les résultats de Chen et al. pour de plus grandes valeurs du champ électrique.

Pour finaliser ce travail de thèse, le choix a été fait d'appliquer le rayonnement THz à une nouvelle famille de composée, les composés dits à transitions de spins. Cette famille de composée présente une transition de phase entre une phase dite Bas Spin (LS) à basse température vers une phase dîte Haut Spin (HS) à haute température. Ces composés sont généralement constitués de molécules ayant un coeur de Fe entouré d'un ligand organique. Le ligand organique exerce un champ cristallin sur les orbitales 3d du Fe causant une levée de dégénerescence. L'écart d'énergie entre les deux nouveaux états est directement lié à la distance entre le Fe et son ligand. Ce phénomène est résumé en Fig.8

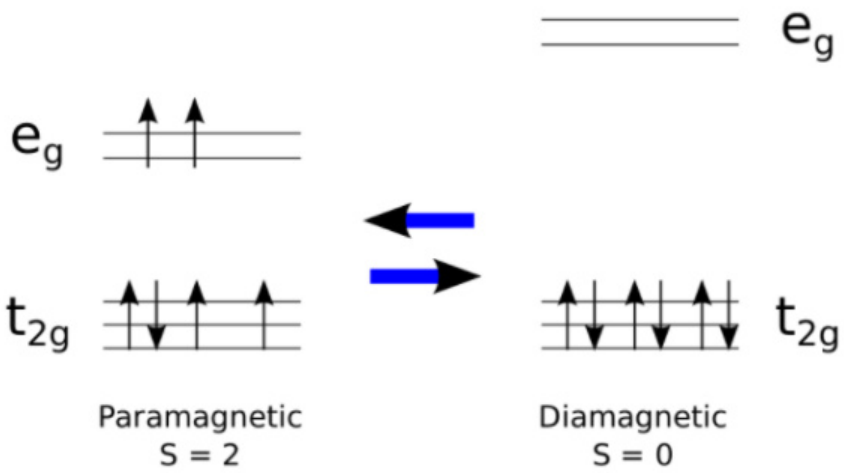

Figure 8: Orbitales 3d du fer après lever de la dégénerescence. A gauche et à droite sont représentés respectivement les cas Bas Spin et les cas Haut Spin.

Un composé en particulier a été plus étudié dans le cadre du travail de thèse, il s'agit du $Fe(phen)_2(NCS)_2$. Ce composé présente l'intérêt de posséder un moment dipolaire, centré sur l'atome de Fe. L'amplitude de ce moment dipolaire dépend de la distance entre le Fe et son ligand. Ainsi, il serait possible de moduler la distance entre le Fe et son ligand et donc sur l'écart d'énergie des niveaux dégénérés responsable de la transition de spin. Le rayonnement THz simple cycle est un moyen de contrôler ce dipôle et donc d'induire la transition de spin.

Les deux états de spins présentent des absorptions optiques différentes l'une de l'autre. Par conséquent, il est possible d'utiliser une sonde optique afin d'observer la changement de spin [6, 7, 8]. Ainsi, on peut réaliser une expérience THz pompe sonde optique afin de mesurer le changement d'état de spin potentiellement induit par le rayonnement THz. Cet expérience a été réalisée avec une lumière sonde à 720nm et le rayonement THz de la source comme pompe, les résultats sont présentés en figure 9. On peut observer une diminution de la transmission qui précéde une brusque augmentation de la transmission. Il s'en suit une nouvelle diminution de la transmission avant un retour à la normale. Cette modulation est similaire à l'aspect simple cycle du rayonnement THz. On peut donc conclure que le rayonnement THz a modulé la structure électronique du cristal uniquement pendant le passage du champ, de plus cette modulation est proportionnelle au rayonnement THz.

La structure cristalline du cristal est Pbcn impliquant un centre d'inversion dans la symmétrie du crystal. Par conséquent, le résultat présenté est difficile à interprêter.

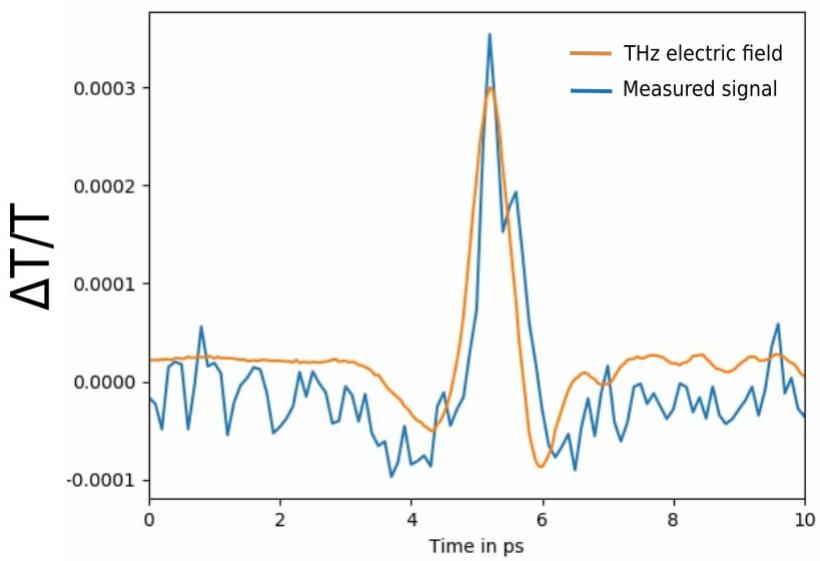

Figure 9: Bleu : Modulation de la transmission optique à 720nm en fonction du délai entre la pompe et la sonde. Orange : Champ Electrique THz mesuré via EOS renormalisé pour comparaison.

Néanmoins, ce résultat représente la première modulation de transmission optique par le rayonnement THz dans un composé type Spin Crossover.

En conclusion, ce travail de thèse a permis le développement d'une source de rayonnement THz dont le niveau égale les meilleurs sources de l'état de l'art. Cette source a pu être validée en reproduisant et prolongeant des résultats de l'art. Pour finir, cette source a pu donner des résultats inédits sur une nouvelle famille de composé : les composés à transition de spins.

Introduction to Photoinduced phase transition and THz pump probe experiment

The control and understanding of matter is an important part of physics. All along its history man has tried to find new materials and new ways to use them to help him out in its life. One recent way of controlling matter is by the use of an external stimuli. This external stimuli can be temperature, pressure, electric field or even light. This external stimuli can trigger structural reordering, appearance of a magnetic momentum, insulator to metal transition...

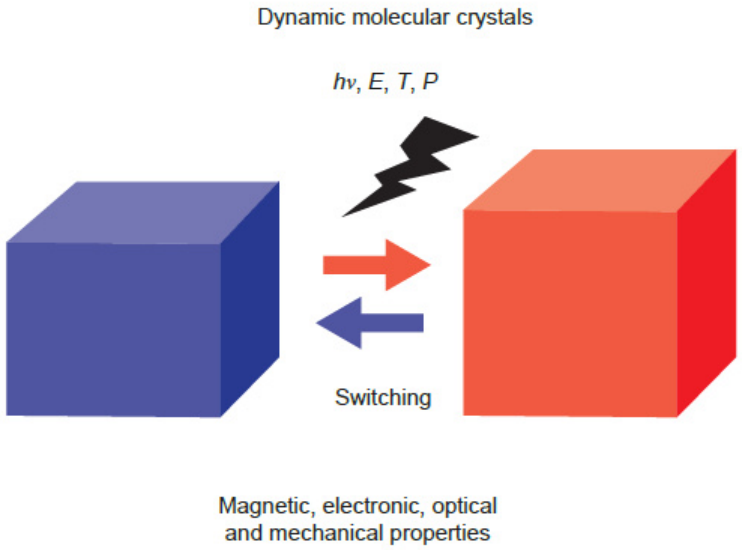

Figure 10: Under an external stimuli, the properties of matter can be changed. Figure adapted from [1].

The study of control of matter using light is the domain of Photo Induced Phase Transition (PIPT). PIPT is a concept that was pioneered by Nasu et al.[2]. Static external stimuli such as pressure or temperature are macroscopic quantities which change the thermodynamic potential of the matter to induce a phase transition. Light on the other hand will force matter in a non stable excited state, matter will relax into a more stable state which properties can be different from the real ground state. As such PIPT are involving multi-step processes that must be understood to control matter. The concept of PIPT is resumed in Fig.11

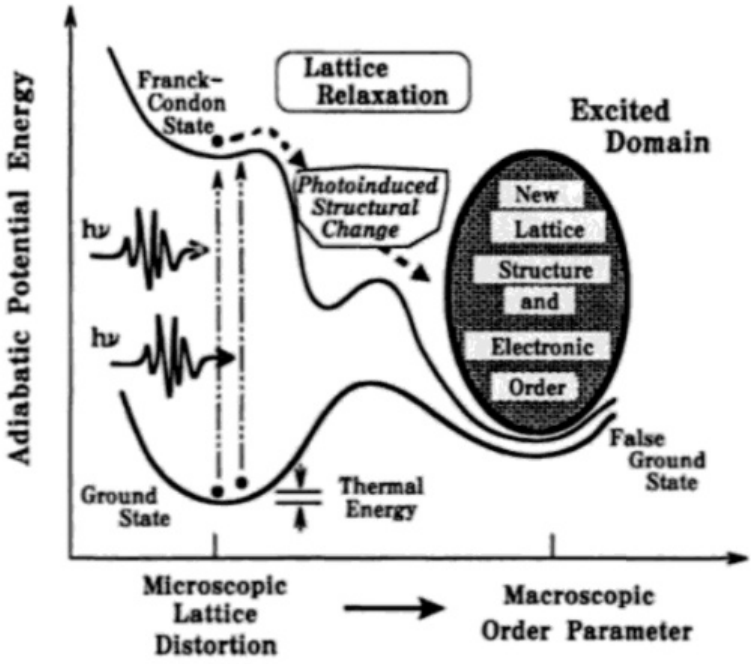

Figure 11: Schematic representation of a photo-induced phase transition. The system goes through different states before reaching the false ground state that changes the desired order parameter. Figure adapted from [2]

To have a proper understanding of photo-induced phase transition, it is important to have a good knowledge of the structural and electronic structure of materials as well as the coupling between them. Moreover, the timescales involved are very broad in PIPT, electron movements timescale is 100 fs, atomic motions timescale is ps and elastic movements within the crystal is ns. This implies that techniques that can probe a very broad scale of time need to be developed.

In that sense one of the most promising tool for study PIPT is pump probe experiment. Depending of the wavelength of the light used, the excitation can be very different. Optical light is used to excite electrons from the Ground state [9], Ultraviolet pulses can break molecular bonding [10], infrared light can directly excite the collective vibrational modes in solids or phonons [11]. We called the light used to generate the excitation "pump".

Light can be also used as a way to measure physical properties of the system. Indeed, the absorption and therefore the electronic transition available in the material can be measured with optical light, the phonon spectra of a solid with infrared light. X-Rays by measuring the diffraction pattern gives access to the structure of solids. Because of the wide range of properties light can measure, it has been extensively used in recent experiments. Light used that way is called a probe.

Allying both techniques is a so called Pump Probe experiment. First, a pump beam is used to excite the sample, then after a small delay the probe arrives on the sample. Then, measuring the probe allows to see the changes in the material properties induced by the pump. The process is resumed in Fig.12.

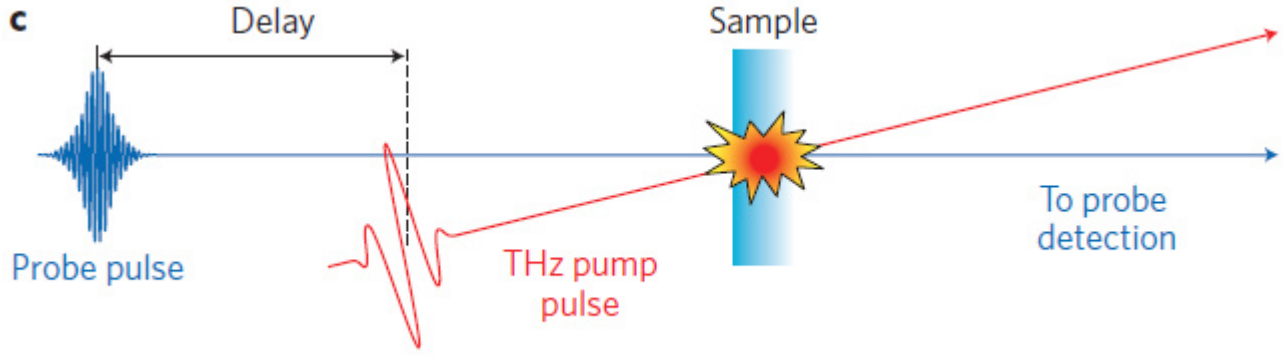

Figure 12: Schematic of a pump probe experiment. The pump is send onto the sample then after a chosen time Δt the probe is sent onto the sample. In this example, the pump light is a THz wave. Figure adapted from [12]

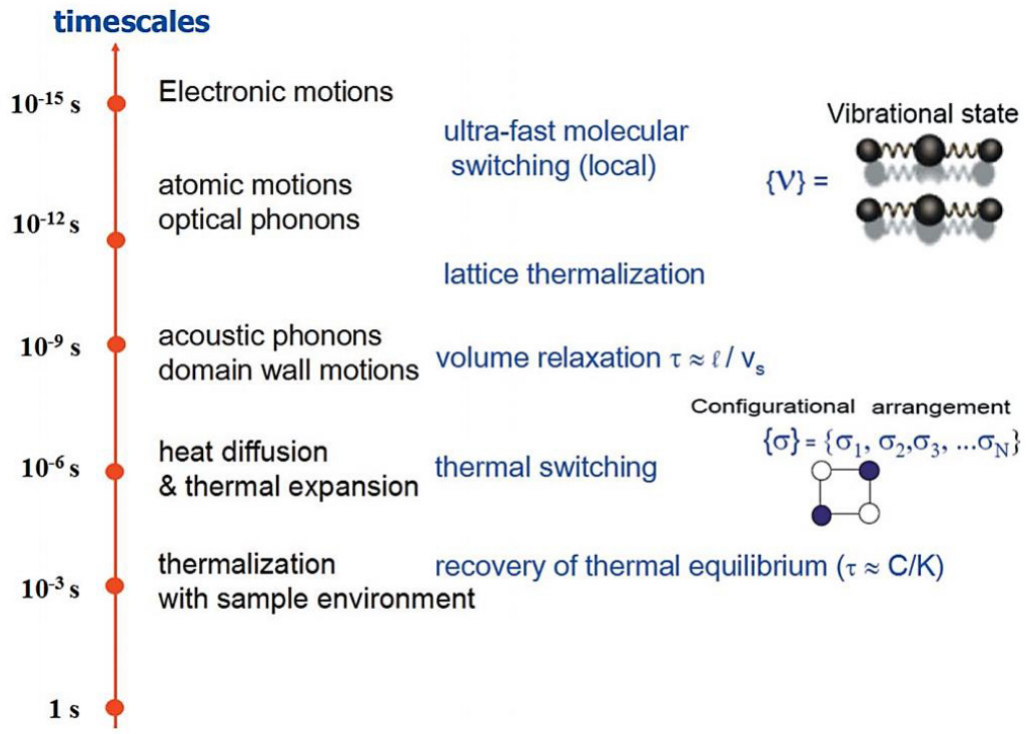

Figure 13: Chronological order of time scales adapted from [13]

One of the most interesting part of using light for pump probe experiment is time resolution. Indeed, electronic is limited to the ns response time. However, shorter time scales are also interesting as presented in Fig. 13. As delay stage motor are very precise nowadays, the main limitation in time resolution for pump probe experiment is the pulse duration. The shorter the probe duration the more important time resolution is. However, even though attosecond pulse are more and more generate in laboratories the standard time resolution remains to be in the 10-100fs order of magnitude mainly because of the commercial availability of such lasers.

One striking example of ultrafast photoinduced phenomena is the case of the bismuth

crystal. The bismuth crystal structure is rhombohedral with two atoms in the unit cell. Under an important laser fluence the system is excited into a new state. The equilibrium distance between the two atoms is modified in this new state (see Fig. 14a). The intensity of the (111) Bragg peak will be decreased by the change of equilibrium distance, this implies that the transition can be probed using time resolved X-rays. Fritz et al.[14, 15] used fs X-rays from the Linear Coherent Light Source (LCLS) X-FEL, their results is presented in Fig. 14b). Similarly to what was demonstrated by Sokolowski et al.[16], they observed a decrease in the intensity of the (111) Bragg peak. The difference in signal to noise ratio between those two experiments is explained by the extreme brilliance that can only be obtained in X-FEL. The oscillations correspond to an A_g coherent phonon mode, the frequency of this mode is 2.7 THz. A femtosecond laser pulse can initiate collective, in-phase atomic motions in solids called coherent phonons. When the pump laser changes the potential, the distance between the two atoms is disturbed, this corresponds to the the large decreasing at time 0, then the two atoms are oscillating to the new equilibrium positions, this movement corresponds to the coherent phonon.

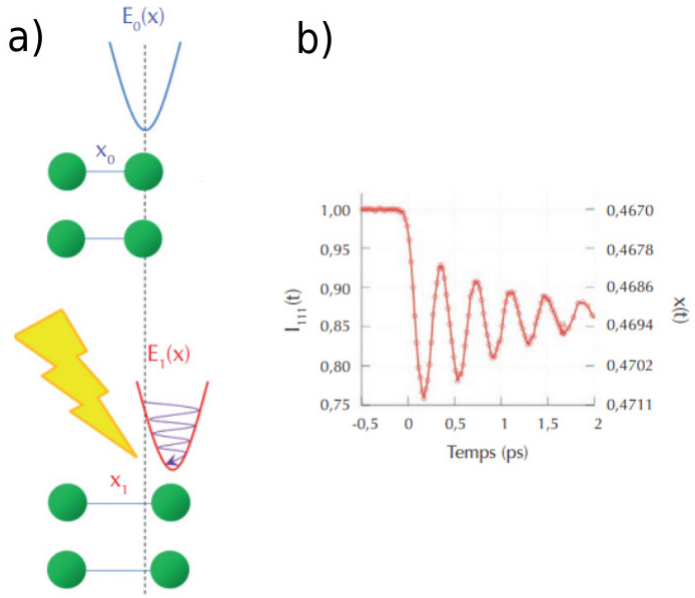

Figure 14: a) Up : Bismuth structure in the stable state, the equilibrium distance is x_0 between the two atoms and is given by the potential energy $E_0(x)$. Down : Bismuth structure in the photo-excited state, the new potential $E_1(x)$ gives a new equilibrium distance x_1. b) I of the (111) Bragg peak as a function of time. Figure adapted from [17]

This coherent phonon is generated through electron-phonon correlation as explained by Boschetto et al.[18]. In their experiment, they did an optical pump probe experiment at 800nm and measured the change in reflectivity in Bismuth (111) crystal, their results are shown in Fig.15. They observed the same behaviour, a large change in reflectivity followed by oscillations to the new equilibrium positions. They showed that the frequency of the coherent phonon was dependent of the pump fluency, the frequency of the mode is 2.9 THz at 2.7 mJ/cm^2 and 2.86 THz at 6.7mJ/cm^2. This example

demonstrates that the correlation between electrons and phonon is important to understand photoinduced phenomena. While phonon can be observed indirectly using optical spectroscopy, direct observations of phonon requires to use either infrared light or lower energy light.

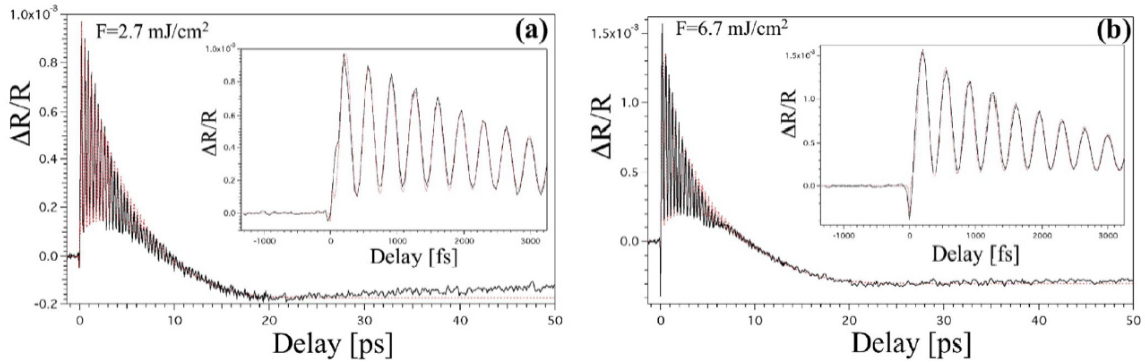

Figure 15: Change in reflectivity on bismuth (111) crystal with a light wavelength of 800nm for different excitation flux. a) The excitation flux is 2.7 mJ/cm^2 b) The excitation flux is 6.7 mJ/cm^2. Figure adapted from [18]

A large number of phonon modes are within the infrared range and so accessible with commercial lasers, but most of them (as in Bismuth) are in the THz range. Efforts THz were made to have accessible THz light, still most of those THz-Set-Up are homemade. THz offers a wide range of applications in PIPT which are presented in Fig.16. THz can be used to drive ionic motion in ionic crystal, use the associated magnetic field to act directly on spins, or finally to accelerate electrons.

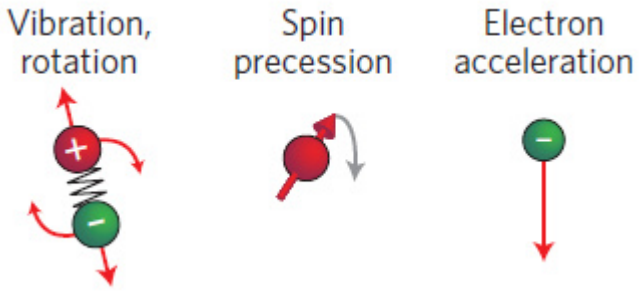

Figure 16: THz can be used to drive ionic movement, spin precession are electron acceleration. Figure adapted from [12]

THz can be found in a lot of different domain where other units are used. To help the reader, all the usual units are presented in table 2.

Frequency	Energy	Wavelength	Wavenumber	Pulse duration
1 THz	4meV	300 mum	33 cm-1	1ps

Table 2: Usual units for 1 THz

THz Time Domain spectroscopy (THz-TDS) allows the study of phonon modes. This technique has the huge advantage to be a coherent technique. As such, both real and imaginary components of the optical refractive index of the material can be extracted from a single measurement. A full explanation of THz-TDS will be given in the chapter 3 of this manuscript. There exists now commercially available THz-TDS set-up that allows to measure the properties of materials. An example of such measure is given in Fig.17. In this example, Agulto et al.[19] are interested in the electronic properties of the monoclinic $\beta - Ga_2O_3$ compound. THz-TDS is a non invasive and non destructive technique and as such is a technique of choice for such measurements. They used a commercially available THz-TDS set-up based on Photo Conductive Antenna.

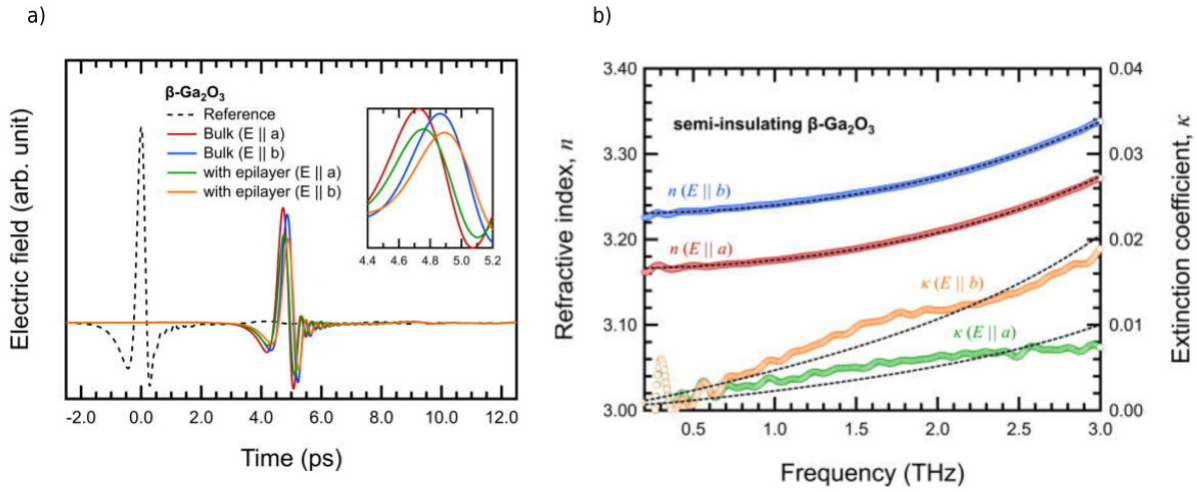

Figure 17: a) THz waveform in the time domain. The dashed line is the reference without sample, the solid line are the THz electric field observed for different experimental conditions. b) Extracted refractive index for this measurements. Both figures are adapted from [19].

Thanks to the coherent measurement allowed by the THz-TDS set-up the THz electric field is directly measured. This is shown in Fig. 17a. Because of the non zero value of the real refractive index in the $\beta - Ga_2O_3$ compound, the electric field is delayed in time with respect to the reference. The waveform in the frequency domain can be exploited both in phase and in magnitude. The study of the phase allows the measure of the real refractive index n, while the study of the magnitude allows extraction of the imaginary part (or extinction coefficient) κ. Their results are presented in Fig.17b. As THz light is linearly polarized, Agulto et al. shown that the dielectric responds of $\beta - Ga_2O_3$ is anisotropic and were able to gives quantitative measure of the refractive index in both direction.

Photoconductive antennas are one of the easiest THz set-up to implement but have the disadvantage of generating low intensity THz waves. This is not an issue with linear TDS but with more intense THz, new effects can be probed. Katayama et al.[20] performed THz-TDS on $SrTiO_3$ thin films deposited on MgO. $SrTiO_3$ is a perovskite crystal which structure is shown in Fig. 18a). This crystal exhibits a soft mode (mode which frequency goes to zero close to the transition temperature), this mode is characterized by a movement of the O atoms towards the upper state of the cube

while the Ti moves downward (see Fig.18a). The experiment was realized using THz generated from Optical rectification in $LiNbO_3$ with the tilted pulse front technique.

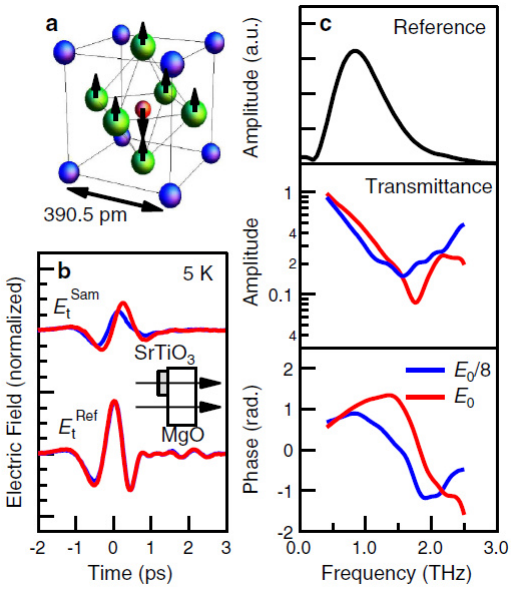

Figure 18: a) $SrTiO_3$ unit cell, the movements induced by the soft mode are represented by the black arrows. b) Normalized THz waveform in the time domain, each waveform is normalized by its reference. The red line corresponds to an electric field value of $E_0 = 80$kV/cm, the blue line corresponds to an electric field value of 10 kV/cm. c) Associated phase and amplitude, the Fourier transform of the reference is plotted in black. Figure adapted from [20]

By applying different electric field intensities, they observe a modification of the absorption of the soft mode (see Fig. 18c). The soft mode absorption maximum is shifted toward higher frequencies, and a spectral narrowing can be observed. Katayama et al. explained this shift and narrowing by the quartic aspect of the potential. As such non linearity plays an important role in THz-TDS.

Another example of non linearity probed by THz-TDS is given by Jewariya et al. [21]. They performed non linear THz-TDS on the L-arginine compound. L-arginine is an organic powder compound that presents an absorption mode at 1 THz. THz were generated the same way than for Katayama et al.[20]. Their results is presented in Fig.19. They measured the absorption spectra for different values of the electric field. They observe a spectral redistribution from the high frequency to the low frequency region. They explained this shift again by the non linearity of the potential. If the potential is fully harmonic, then the quantified energies in the potential should be equi distant, i.e. to increase the mode population all quantum of energies should be the same. However, if the potential is not perfectly quadratic, then the energy required to populate the mode from 1 to 2 is greater than the one from 19 to 20. Therefore, with an high enough electric field, the ladder can be climbed more easily to population 20 than if the potential was fully harmonic.

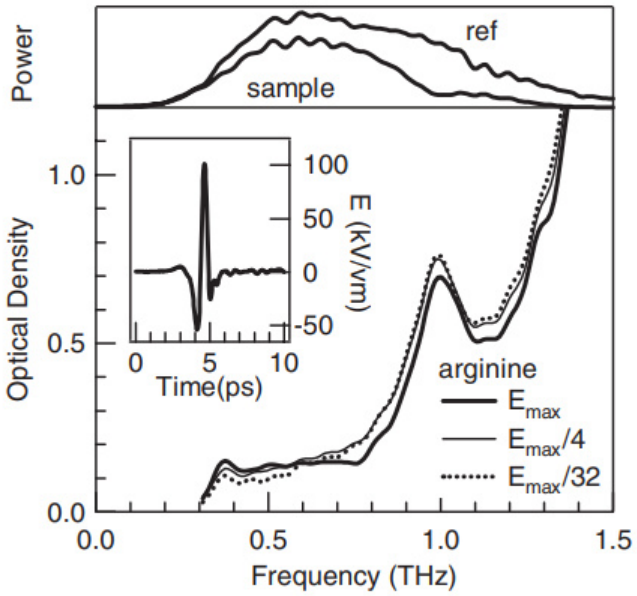

Figure 19: Optical density of an L-arginine pellet at different incident amplitudes of THz pulses. The inset shows the incident THz pulse. The upper part shows the power spectra of the THz pulse passing through the sample and without the sample. Figure adapted from [21]

Those two examples showed that THz-TDS is a good tool to probe non linearity. However, for both case the same pulse acts as the pump and the probe of the system. Therefore, no dynamics can be probed using only one pulse. THz-TDS is a probe of the phonon spectra. We have seen that if the probe THz is strong enough it can change the properties of the material. If one wants to disentangle the effects of pump and probe, a pump has to be added. Such kind of experiment has been conducted by Houver et al.[22]. In their experiment, they used THz generated through Optical Rectification in a DSTMS (organic crystal) and THz generated from an air plasma source as the probe.

THz pump can also induce effects that are probed using other techniques. Morimoto et al. [4] realized a THz pump optical probe experiment on the tetrathiafulvalene-p-chloranil (TTF-CA) organic compound. TTF-CA is composed of two molecules the donor (D) TTF and acceptor (A) CA. The molecules form a quasi 1 dimensional chain along the a axis of the crystal. The molecule undergoes a phase transition from a neutral phase transition at high temperature to a ionic phase transition at low temperature. The temperature of transition is 92K for this compound. A macroscopic polarization along the a axis appears in the ionic phase. The polarization does not originate from ions but from the electronic cloud of the molecules, and is opposed in direction from the dipolar momentum of the ions.[23]. The THz were generated from Optical Rectification in $LiNbO_3$ but with an electric field more important than in references [20] and [21] with a value of 400kV/cm, a waveform is presented in Fig. 20b. There were two probes in their experiment, first a second harmonic probe at 2.6 eV and a reflectivity optical probe at 1.3eV. The experimental set-up they used is presented in Fig.20a.

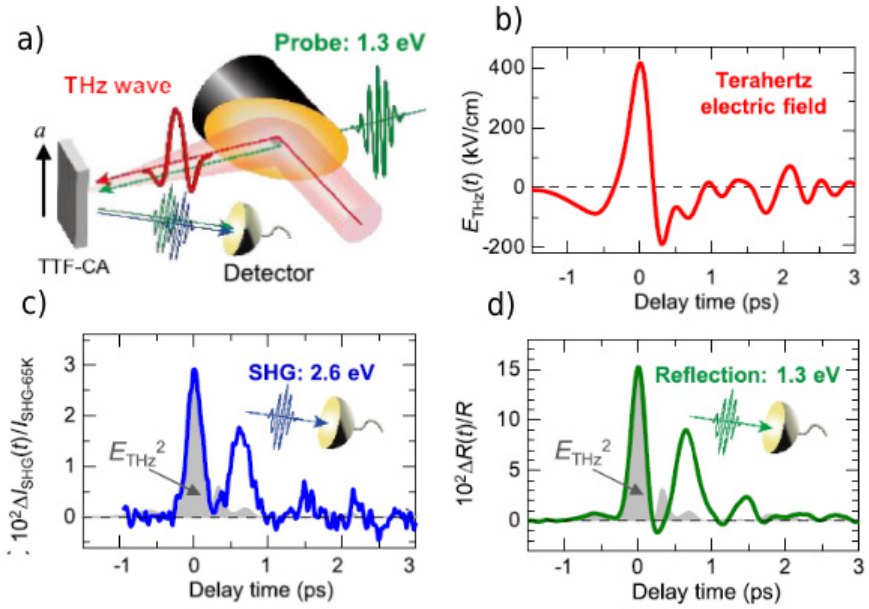

Figure 20: a)Schematic setups of terahertz pump Second Harmonic Generation(SHG) probe and optical reflectivity probe measurements. b) A waveform of the terahertz electric field $E_{THz}(t)$. c) A time evolution of the SH intensity at 90 K normalized by the Second Harmonic intensity at 65 K ($\Delta I_{SHG}(t)/I_{SHG65K}$). d) A time evolution of $\Delta R(t)/R$ at 90 K. Shaded areas in (f) and (g) show $|E_{THz}|^2$. Figure adapted from [4]

Second Harmonic Generation can be used as a tool to probe the appearance of macroscopic polarization in a compound. Morimoto et al. used the Second Harmonic generated in the ionic phase where there exists a spontaneous polarization as a reference. The THz electric field will activate the dimerisation on the TTF and CA and creates the polarization. As such, Second Harmonic Generation should be activated by the THz electric field. The results they obtained are presented in Fig. 20c. The signal obtained with Second Harmonic as a probe follows the squared of the electric field. The change in reflection at 1.3 eV is presented in Fig. 20d. Here again, the reflectivity signal is following the square of the THz electric field. The origin of the signal is linked to charge transfer between the donor and acceptor. Both signals present oscillations but the interpretation explained by Morimoto et al. is beyond the scope of this introduction. However, a photo-induced polarization has been generated which proves that THz used as a pump can also induce PIPT.

In the last example, the THz electric field was used to trigger a neutral to ionic phase transition. Another interesting aspect of the THz electric field is its associated magnetic field. The magnetic field associated to 1MV/cm is 0.33 T. As such single cycle intense magnetic field can be used to act directly on a spin level. In materials presenting a magnetic order, spins are aligned along a particular direction B_{int}. The external magnetic field will give an external direction for the spins to align on. To relax back to their original direction B_{int}, the spins will oscillate at a frequency which depends on the material. It is under 100 GHz for ferromagnet and can exceed 1 THz for anti-ferromagnet. Anti-ferromagnet are the most common materials with a magnetic order. Therefore, THz light is the good tool to control spins.

One striking example of spin control using THz was realized by Kampfrath et al.[24]. Kampfrath et al. shined a 400kV/cm THz electric field, 0.13 T magnetic field, with a frequency range 0.1 to 3 THz on the NiO anti-ferromagnet. The NiO anti-ferromagnet presents a magnetic resonance at 1 THz and so the THz electric field they apply is adequate to trigger a magnetic response. They measure the change in magnetic order using the Faraday effect. The induced magnetization will change the polarization direction of the probe pulse with an angle called the Faraday angle. Their results are presented in Fig.21. We observed a strong oscillatory component that is 1 ps periodic which corresponds to a 1 THz frequency which showed that magnetic resonance can be observed using THz as a pump. Magnetic resonance can also be probed using THz-TDS as demonstrated by Grishunin et al. [25]. They used THz-TDS to measure the magnetic resonance of the anti-ferromagnet $TmFeO_3$.

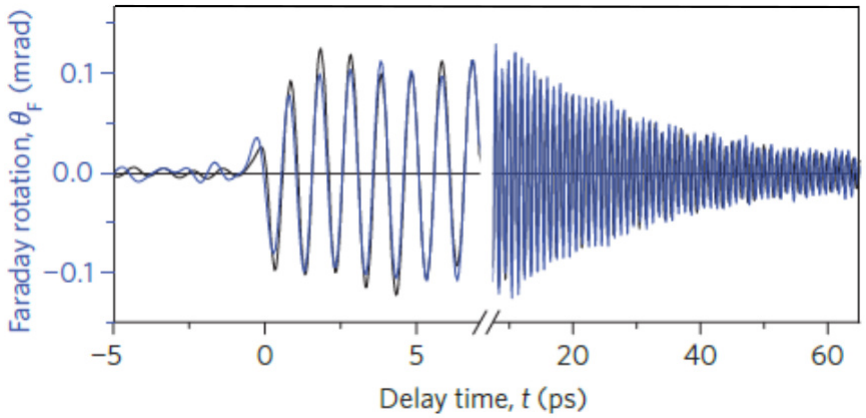

Figure 21: Utrafast Faraday rotation as a function of time. The Faraday rotation is proportional to the magnetization.

THz light is a promising tool to study PIPT as presented in this chapter. The development of more intense THz light source is still a challenge, but these sources are more and more accessible in the laboratories around the world. This is the motivation of this PhD Thesis: to build an intense THz source. This intense THz source will be used to trigger structural changes by resonantly excited phonon modes, but also to use the electric field of the THz to work on an electronic level.

Outlook of the manuscript

In the **first chapter** of this manuscript, I will introduce some crucial element of non linear optic that will be necessary for the understanding of this manuscript. Then, some THz generation techniques as well as THz detection techniques will be presented.

In the **second chapter** of this manuscript, I will detail the full characterization of our THz experimental set-up. The alignment procedure developed during this PhD thesis will be presented as well. The full beam characterization will be presented including THz beamsize and waveform. The study of THz generation efficiency in function of the THz pulse duration will be detailed. Finally, the validation of the set-up will be presented by reproducing and continuing results of the literature with two samples : the $\beta - BaryumBorate$ and thin film of V_2O_3.

The **third chapter** will be dedicated to the explanation of THz-TDS. Both theory and data treatment will be presented. The characterization of the THz-TDS set-up built in this work will be presented using the Bi-Chlorophenyle sulphone (or BCPS) as a reference sample which has been studied in the far-infrared region.

In the **fourth chapter** of this manuscript, I will present the study performed on a Spin Crossover compound the $Fe(phen)_2(NCS)_2$. First, I will introduce the physic of Spin Crossover compound, then I will explained the link between phonon modes and symmetry. The study of photo-induced effect in the $Fe(phen)_2(NCS)_2$ using Raman Spectroscopy will be presented. Results using THz-TDs on the $Fe(phen)_2(NCS)_2$ compound will be shown as well. Finally, THz photo-induced effect on the $Fe(phen)_2(NCS)_2$ Spin Crossover compound will be detailed in a numerical and experimental way.

Chapter 1

THz electromagnetic wave from generation to detection

1.1 Introduction

The spectra of light available in laboratory has been gradually expanding over the years. Laser technology was first based on Ti:Sapphire or YaG providing two wavelength usable in the laboratories. Then, with the advent of highly non linear crystal such as Baryum Borate more known as BBO, the whole visible spectra and a part of the near infrared spectra became available. X-ray tubes was the base source diffractometers. At the end of 80s, almost all the spectra of light was covered using different techniques expect for THz light. This hole in the electromagnetic spectra was called the THz gap and is pictured in Fig.1.1.

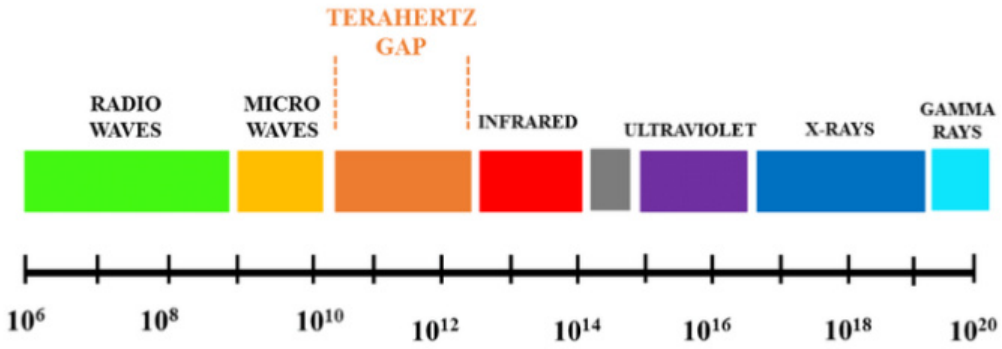

Figure 1.1: Electromagnetic spectra of light. The THz gap is the hole in the electromagnetic spectra.

Despite this THz gap, far infrared light was used to observe the low energy light absorption and allows for measure up to 2 THz but rarely below. Such light was obtained using interferometry but was not easily accessible. One of the difficulty of such generation using continuous light is that the energy of THz light is of the same order that room temperature.

The development of ps laser duration in the laboratory and the development of third and fourth laser generation (Synchrotron and Free Electron laser) allowed new discoveries but THz light was still not well developed. We have to wait the end of the

90s to obtain first THz light generated. Then, it began to be developed in laboratories till the beginning of the 2010s to observe μJ pulses. The development of light in Free Electron Laser also helped to generate intense TeraHertz sources.

Because of the nature of THz generation, non linear optic is at the core of most THz generation techniques. Therefore, a good understanding of non linear optic is mandatory before any THz generation explanation and will be detailed first in the first section of this chapter. Then, the principal generation sources will be presented in the second section. Finally, in the last section, I will present the most common detection techniques.

1.2 Basics of Second Order Optical Non Linear Effect

The aim of this section is to introduce to the reader who doesn't know anything about Non Linear optics the basics that will be used in this chapter. If the reader knows about Non Linear optics, he is invited to go directly to the next section. All the results presented in this section were taken from the book of Boyd Non Linear Optical [26].

Optic is the study of light transport through different media. One equation is ruling the transport of light in media. This is the Maxwell Equation. In the vacuum, this is written as :

$$\Box \overrightarrow{E} = 0 \tag{1.1}$$

Where $\Box$ is the d'Alembertien of the field : $\Box = \Delta - \frac{1}{c^2}\frac{\partial^2}{\partial t^2}$. A solution of this equation is the usual plane wave and was the explanation for the wave aspect of the light before the work of De Brogli on duality. Within a material, this equation transforms to become :

$$\Box \overrightarrow{E} = \mu_0 \frac{\partial^2 \overrightarrow{P}}{\partial t^2} \tag{1.2}$$

Where $\overrightarrow{P}$ is the polarization. This equation is valid if $\nabla div \overrightarrow{P} = \nabla div \overrightarrow{E} = 0$, this means the space is free of charges. This is true for most of the material as they mostly doesn't carry charge in the bulk (metals by example). The polarization is therefore a source term in the Maxwell Equation. Indeed, in vacuum light is only transported which corresponds to the polarization term equal to zero. When traveling through a media, light interacts with matter. Light will induce polarization (dipole) within the media which will emits new light. In linear optics, the polarization is proportional to the Electric field, solving the equation leads then to the classical optical refractive index of the material. However, with the advent of intense electric field namely the invention of laser this approximation was no more valid. The polarization must therefore be expanded in a power series of the electric field :

$$\overrightarrow{P} = \chi^{(1)}\overrightarrow{E} + \chi^{(2)}\overrightarrow{E^2} + \chi^{(3)}\overrightarrow{E^3} + ... \tag{1.3}$$

This expansion will lead to various different elements. The χ_i are the dielectric susceptibilities of the material. They are often very small but as the electric field becomes more intense, their non zero value raise new phenomena. Before, digging into

the Lorenz Model to give a better explanation of those susceptibilities, let's take a look at the impact of the first non linear term on Maxwell Equation.

1.2.1 Second order non linear effects

Let E_1 and E_2 be two complex oscillatory electric fields of frequency ω_1 and ω_2. Let E be the sum of those two waves. Note that we take ω_1 and ω_2 to be different so that we are in the most general case. By example it can be multiple frequency in a non monochromatic laser or just two different laser.

$$E = E_1 + E_2 = E_1 e^{i\omega_1 t} + E_2 e^{i\omega_2 t} + c.c. \tag{1.4}$$

Note that c.c. means complex conjugate. The second order polarization is written :

$$P^{(2)} = \chi^{(2)} E^2 \tag{1.5}$$

Replace E in 1.5 to get :

$$P^{(2)} = \chi^{(2)}(E_1 e^{i\omega_1 t} + E_2 e^{i\omega_2 t} + c.c.)^2 \tag{1.6}$$

Developing the square, we find :

$$P^{(2)} = \chi^{(2)}(E_1^2 e^{2i\omega_1 t} + E_2^2 e^{2i\omega_2 t} + 2E_1 E_2(e^{i(\omega_1+\omega_2)t} + 2E_1 E_2^*(e^{-i(\omega_1-\omega_2)t} + c.c) + 2\chi^{(2)}(E_1 E_1^* + E_2 E_2^*) \tag{1.7}$$

Separating the different terms, one can find all the different second order non linear effects :

$$\begin{aligned} E_i^2 e^{2i\omega_i t}\ (SHG), \\ 2E_1 E_2(e^{i(\omega_1+\omega_2)t})\ (SFG), \\ 2E_1 E_2^*(e^{-i(\omega_1-\omega_2)t})\ (DFG), \\ E_1 E_1^* + E_2 E_2^*\ (OR) \end{aligned} \tag{1.8}$$

Note that it is convenient to write the polarization as the following:

$$P^{(2)}(t) = \sum_n P(\omega_n) e^{-i\omega_n t} \tag{1.9}$$

The summation over n is for both positive and negative frequencies.

The first term is describing the double of frequency of the wave and is more known as Second Harmonic Generation (SHG). SHG happens when two photons of same energy combined themselves to give another photon doubled in energy (see Fig 1.2).

The second and third terms correspond at different combinations of the two incoming photons. Either the photons add their energy, the Sum Frequency Generation (SFG) see Fig 1.3 a, or one remove its energy to the other, the Difference Frequency Generation (DFG) see Fig 1.3 b. In both those cases (also in SHG), virtual energy levels are at work. For SFG, materials absorb the ω_1 photon and arrives in a virtual level of excitation. Then, it absorbs the second photon and achieves the $\omega_1 + \omega_2$. Finally, it relaxes giving birth to a photons which combines the two energy. This is the exact same pattern for SHG and reverse for DFG.

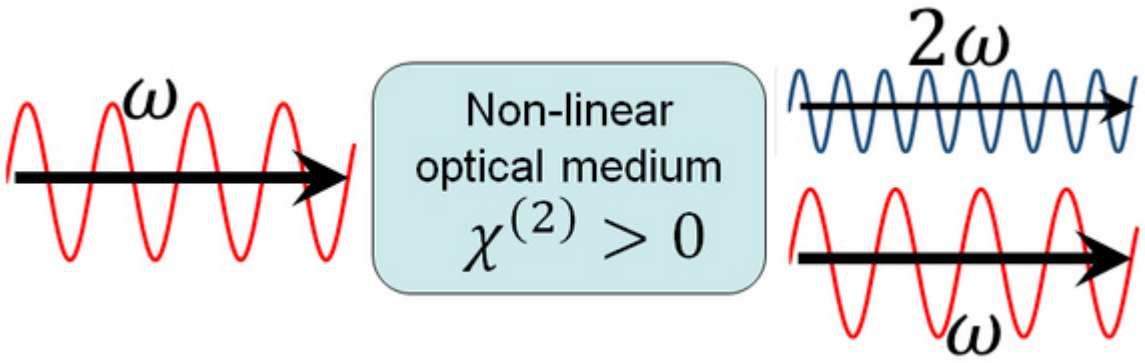

Figure 1.2: In non linear optical media, photons can recombine themselves to produce photons twice the frequency, this is Second Harmonic Generation

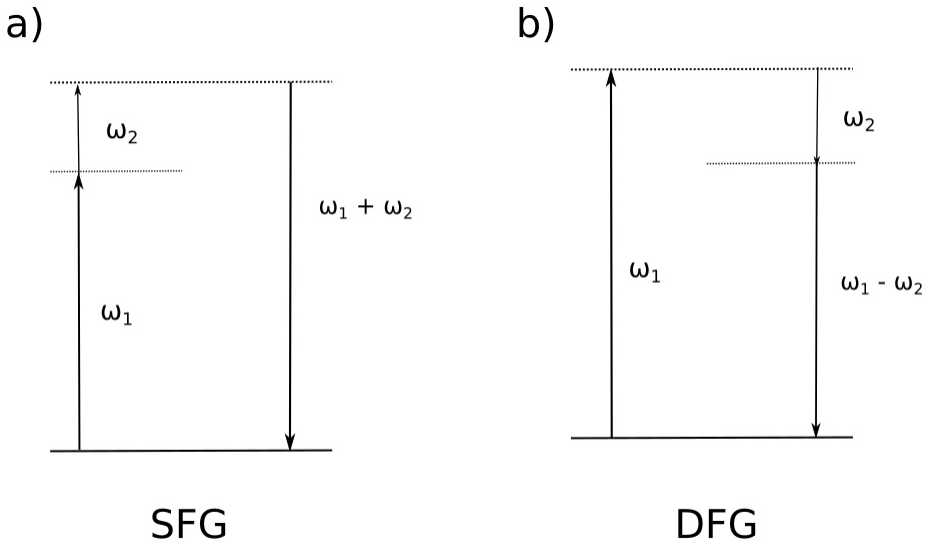

Figure 1.3: a) Representation of the energy levels for Sum Frequency Generation (SFG) b) Representation of the energy levels for Difference Frequency Generation (DFG)

Finally, the last term corresponds to the optical rectification (OR) . For continuous light, this term is just a static electric field within the medium. For most pulsed laser, this term can still be considered as static if pulse duration is long with respect to the frequency of the light. This term is therefore often discarded and this approximation is called the slowly variable envelope approximation. However, this is not true for femtosecond pulses where the pulse duration is comparable to the frequency of the light. This term will be more precisely explained in section 1.3.2 as this will be used to generate THz pulses.

Second order non linear effects are possible only in non centrosymmetric materials, namely they don't have inversion symmetry. Let us assume that a medium possess inversion symmetry. Then, this medium presents :

$$P(t) = -P(t) \tag{1.10}$$

This implies the following :

$$\chi^{(2)}E^2 = -\chi^{(2)}E^2 \tag{1.11}$$

The second order susceptibility vanishes and so the second order non linear effects.

Assuming that the polarization can be extended into a power series of the electric field, demonstration has been made that second order non linear optic can be assessed from those phenomena.

1.3 THz generation techniques

While the interest of THz light as both pump and probe as increased in the past decades, intense and broadband THz cannot be purchased easily nowadays. Therefore the necessity to develop new inhouse sources have become a field of study in itself. Three main axis are nowadays studied, Photoconductive Antenna (PCA)[27], Laser plasma generated in air [28] and Optical Rectification in non centrosymmetric media [29, 30]. I will present the two latter techniques that are of interest in our work. Both of them have been used during my PhD thesis.

Moreover, coherent THz sources are generated at large scale facilities such as Free Electron Lasers. They will be briefly described at the end of this section.

1.3.1 Two color Air plasma generation

Laser plasma techniques are multiples, their common points is that they generate a plasma in a gas. The plasma generated in the gas is the source of the THz wave[28, 31, 32]. The air plasma is based on two colors air induced plasma [33],[34]. In this section, I will present the two color air plasma generation scheme. This method mixes a femtosecond optical pulse and its second harmonic to generate THz wave. The figure 1.4 illustrates the concept :

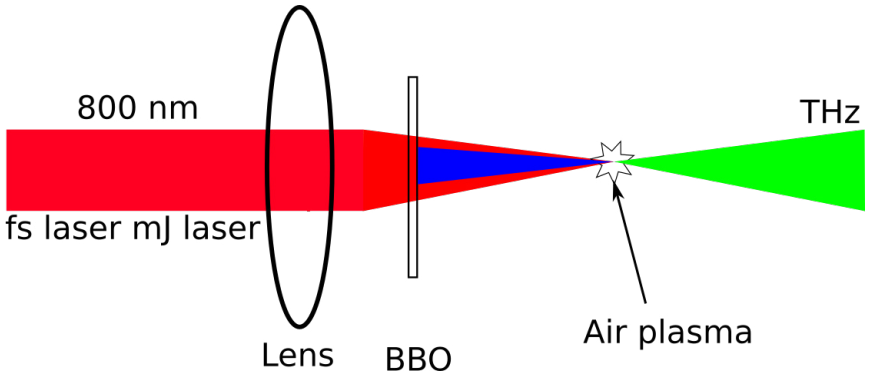

Figure 1.4: Air plasma generation setup

On this example, a 800nm laser (red on the figure) is focalized through a BBO crystal to generate both air plasma and second harmonic (blue on the figure). Both are mixed in the air plasma and THz is generated (green). The mechanism behind this generation are still debated in the community a theory that fits the data as been proposed by Kim et al.[35, 36]. They claim that THz is generated from a surge of photo current happening

during the ionization of the gas. As gas is a centrosymmetric media, a directional photocurrent cannot occur spontaneously within the media, a photocurrent recquires a perturbation that breaks the symmetry to exist. The asymmetry is generated by the sum of the two optical components in the scheme of two colors generation. Following the theory of Kim and al, the THz electric field is proportional to the derivative of the photo current J :

$$J = -en_e v_e \tag{1.12}$$

where e is the electron charge, n_e is the electron density and v_e is the electron velocity within the plasma, the THz electric field can be then written as :

$$E_{THz} \propto \frac{dJ}{dt} = en_e a = \frac{n_e e^2}{m_e} E_{laser} \tag{1.13}$$

m_e is the electron mass, a is the electron acceleration which is defined according to Fundamental Principal of Dynamics $a = \frac{e}{m_e} E_{laser}$. Finally, E_{laser} is the sum of both the laser and its second harmonic. E_{laser} can be defined as follows :

$$E_{laser} = [E_\omega(t)cos(\omega t) + E_{2\omega}(t)cos(2\omega t + \phi)]e^{-\frac{4ln(2)t^2}{d^2}} \tag{1.14}$$

$$E_{\omega,2\omega} = \sqrt{\frac{2I_\omega, 2\omega}{c\epsilon 0}} \tag{1.15}$$

d is the pulse duration. ϕ is representing the phase difference between the first harmonic and second harmonic. In order to generate a photocurrent, this phase must be set equal to $\pi/2$. This is usually done by controlling the distance between the BBO crystal used for generating second harmonic and the generated plasma. I_ω and $I_{2\omega}$ are the laser intensities at fundamental frequency ω and its second harmonic 2ω.

In order to simulate the THz electric field, the electron density must be computed. The electronic density n_e can be obtained by summing over the variation of each ionization degree :

$$\frac{dn_e}{dt} = \sum_{i=0}^{N} i\frac{dn_i}{dt} \tag{1.16}$$

N is the number of ionization states and n_i is the population of the i-th ionization state.

$$\frac{dn_i}{dt} = n_{i-1}W_{i-1} - n_i W_i \tag{1.17}$$

W_i is representing the ionization rate. As ionization is only due do the photoionization from the laser, W_i depends only on the laser characteristics. With right laser parameters, THz are generated and can be computed taking into account other effects such as tunnel ionization and laser-induced electron motion [28, 37].

Using such techniques, 4.4 MV/cm pulses with spectra going up to 15 THz where obtained [38] using 1800 nm light. More recently, 8 MV/cm were obtained using 800 nm light, 15 mJ, 30 fs laser.[?]

1.3.2 THz generation using Optical Rectification

Optical rectification (OR) is a second order non linear effect and as such is present in non-centrosymmetric media. This technique is used in a lot of different set-ups [39], [40], [20]. This technique is widely used in the THz community as it allows the use of of large single cycle electric field to trigger non-resonant effects such as dipole displacement. This is also a good technique to perform low THz spectroscopy.

When using femtosecond time scale pulses, the slowly varying envelope is not a good approximation anymore as the timescale of the envelope is matching the period of the oscillations of the electromagnetic field. Therefore, we cannot discard the OR term in the second order non linear effects. If we take a monochromatic field of pulsation ω, then the second order polarization will raise two components:

$$P^{(2)} = \chi^{(2)}(EE^* + E^2 e^{2\omega}) \tag{1.18}$$

In the Maxwell equation, the two components will be the source for two different waves, the second harmonic and the wave originating from the Optical rectification. For a femtosecond timescale, the wave has the frequency of THz. A simulation used a pulse with duration is 100 fs centered at 800 nm is presented in Fig 1.5. Fig. 1.5a) represents the variation of the electric field over time for respectively in blue the square of the electric field, in orange its envelope and in green the second derivative of the envelope. In Fig b) is represented the Fourier transform of the second derivative of the electric Field. Theory is predicting a THz pulse which spectra is centered around 1 THz going from 0 - 2 THz for this chosen pulse duration.

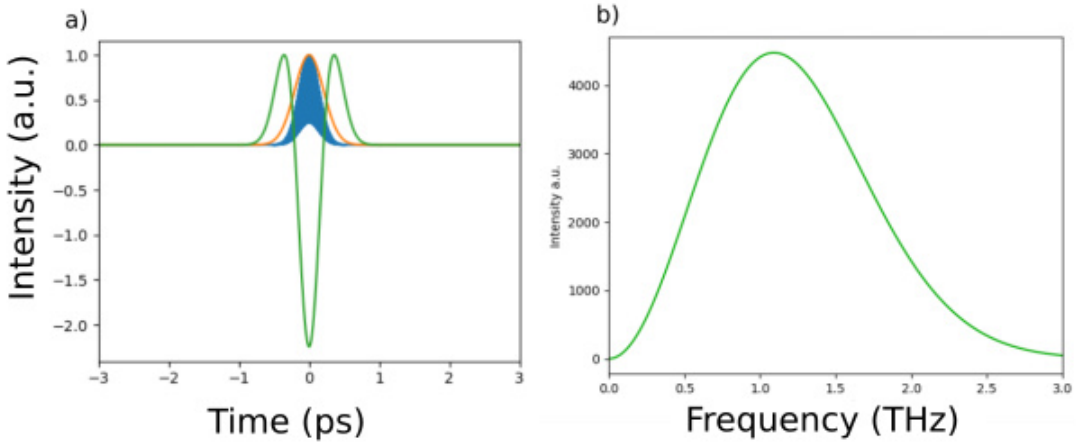

Figure 1.5: a)Variation of electric over time for the square of an electric field (pulse duration 100fs centered at 800nm) in blue, its envelope in orange and the second derivative of the envelope in green. The THz field expected is supposed to follow the green curve. b) Fourier Transform of the second derivative of the envelope.

In order to enhance and select optical rectification within all the nonlinear effects of order 2, the phase matching conditions are to be studied. As optical rectification is

a similar process as DFG (just takes two arbitrary close frequencies) we can apply it to OR.

We need to have match between the energy (conservation of the energy), and between the phase :

$$\begin{aligned} \omega_1 - \omega_2 &= \Omega_{THZ} \\ k_1 - k_2 &= k_{THZ} \end{aligned} \tag{1.19}$$

Dividing by one another the two terms, we have :

$$\frac{\omega_1 - \omega_2}{k_1 - k_2} = \frac{\Omega_{THZ}}{k_{THZ}} \tag{1.20}$$

By setting ω_1 and k_1 arbitrary close to ω_2 and k_2, it follows :

$$\frac{\partial \omega}{\partial k} = \frac{\Omega_{THZ}}{k_{THZ}} \tag{1.21}$$

This implies the equality between phase velocity of the THz light and group velocity of the pump within the medium :

$$v_g^{pump} = v_\phi^{THz} \tag{1.22}$$

THz are generated by the envelope of the pump, the phase velocity needs to match the group velocity of the pump. Indeed, the phase of THz light generated at the first edge of the crystal would mismatch the one at the out edge and creates destructive interference ending with fewer THz in the end. In order to fulfilled the phase matching conditions, the refractive index of the material must be equal at the pump frequency and the THz frequency. This is accidentally true for crystal such as ZnTe ($n_{800} = 3.13$, n_{THz} but it is not in the case of $LiNbO_3$ (LN). Indeed, the refractive index of 800 nm is 2.25 while it is 4.96 at 1 THz meaning that velocity of pump light is twice the velocity of the generated THz light (see Table 1.3.2).

The factor of merit FOM is a quantity described by Hebling et al [41] which allows to choose the good crystals for OR. This quantity is described as follows :

$$FOM_{NA} = \frac{d_{eff}^2 L^2}{n_{NIR}^2 n_{THz}} \tag{1.23}$$

$$FOM_A = \frac{4 d_{eff}^2}{n_{NIR}^2 n_{THz} \alpha_{THz}} \tag{1.24}$$

Equation 1.23 represents the case where crystal doesn't absorb THz, while equation 1.24 represents the case of absorbing crystal. d_{eff} represents the non linear coefficient of the crystal, L is the length of the crystal, n_{NIR} and n_{THz} represents the refractive index for the pump and the THz wave in the crystal. d_{eff} is computed from the electro optic component r of the materials as follows :

$$d_{eff} = -n_{NIR}^4 \frac{r}{4} \tag{1.25}$$

Finally, α_{THz} is the absorption coefficient of the crystal for the THz. This factor has been put in table 1.3.2 [42].

Materials	$d_{eff}(pm/V)$	n_{NIR} for 800nm	n_THz	α_{THz}	$FOM(pm^2cm^2/V^2)$
ZnTe	68.5	3.13	3.17	1.3	7.27
DAST	615	3.39	2.58	50	41.5
$LiNbO_3$	168	2.25	4.96	17	18.2

Table 1.1: Table showing the factor of merit for different materials. All those crystals are absorbing THz, so the FOM used is the one from equation 1.24. The absorption coefficient is measured at 1 THz expect for DAST which is 0.8THz as there is a strong absorption peak at 1.1THz.

In table 1.3.2 is referenced a list of used OR crystal FOM and attributes considering an 800nm pump. ZnTe was the first crystal used for Optical rectification [43, 44]. ZnTe is the perfect candidate for first THz generation using Optical Rectification. Indeed, the FOM is not bad and as there is matching between the refractive indexes the THz can be generated colinearly with the 800nm pump for simple experiment.

The second in performance is the $LiNbO_3$ (LN). The large band gap (3.8eV) of the LN allows more fluency of the pump laser as it prevents two photon absorption which is the main limitation of THz generation using ZnTe [45]. More energy in the pump allows more energy in the THz field which permits very high electric field. However, due to the difference of refractive index (which implies a difference of light speed in the crystal), the phase matching condition is not fulfilled. There is a need for a trick to be able to achieve intense electric field with this crystal. This is the tilted pulse front technique that will be described later. Using this technique, electric fields up to 1.2MV/cm have been obtained [46].

Nowadays, the ionic organic crystal 4-N-methylstilbazolium tosylate (DAST) are more and more used. This crystal exhibits a very strong electro optic component and has attracted the attention for second order nonlinear effects. For this crystal, phase matching is achieved using 1500 nm light. As most laboratory are using Ti:Sapphire based laser, central wavelength is mostly 800 nm and there Optical Parametric Amplifier (OPA) must be used. In Fig. 1.6 adapted from Hauri and al. [3] an example of the field obtained using Optical rectification in DAST.

Hauri and al used light centered at 1500 nm light, 60 fs pulse duration and around 1 mJ pulses to generate the THz Electric field. The THz pulse energy was measured at 20 μJ using a Golay cell. The focal spot of their pulse was of 0.7 mm. Using the time duration extract from the EOS trace (see Fig.1.6a),the peak value of the electric field was estimated to be 1.35 MV/cm. The frequency spectra generated exhibits a strong absorption at 1.1 THz (Fig.1.6b). This absorption line is due to a known Transerve Optic (TO) Phonon mode of the crystal [47]. This absorption line led to the use of another crystal 4-N, N-dimenthylamino-4'-N'-methyl-stilbazolium2, 4, 6-trimethylbenzenesulfonate (DSTMS). The DSTMS crystal is very similar to the DAST for the property of phase matching and non linear coefficient. However, crystal growth in this crystal is easier to achieve and the TO phonon is not present in this crystal. Electric field exceeding the MV/cm are commonly achieved using such crystal [48]

While organic crystals DAST and DSTMS are presenting very large single cycle electric fields, the pump used to generate such electric fields is centered at 1500 μm. As already said, the pump wavelength is typically obtained using OPA to convert an 800

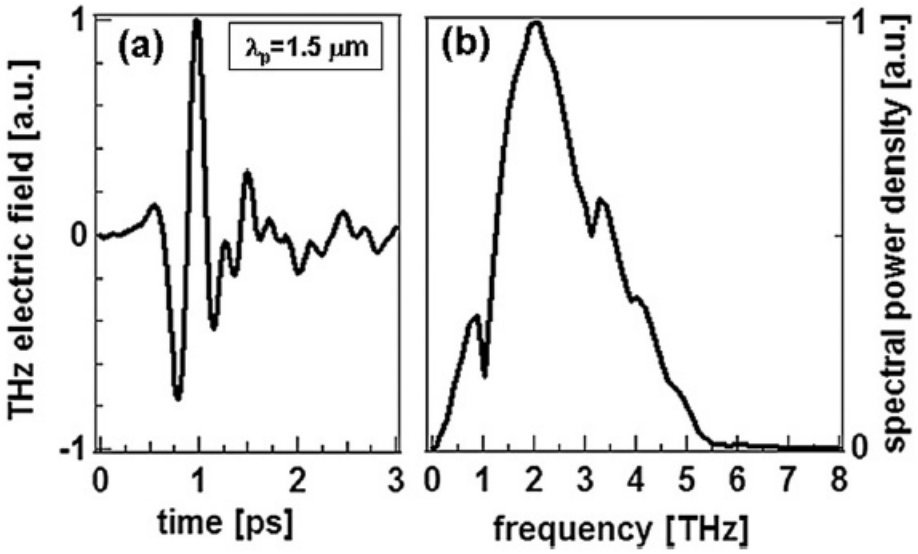

Figure 1.6: Electric field obtained using DAST crystal as the generation media. a) Time Trace obtain by Electro Optical Sampling. b) Associated Fourier Transform. Figure taken from [3]

nm light. This conversion might induces instability in the conversion. Moreover, the conversion must be good enough to generates pulses exceeding the mJ. Tentatives to use 800 nm light on such crystals have been realized by Vicario et al.[49]. The results were slightly better than ZnTe but under than $LiNbO_3$. Because of our laser parameters and OPA, the best decision was to use the tilted pulse front technique in $LiNbO_3$ which I will explain in the next section.

The tilted pulse front technique in the $LiNbO_3$

In the LN, the mismatch between group velocity of the pump and phase velocity is around 2. As the pump wave propagates in the crystal, THz wave is generated following a Cherenkov cone. The Cherenkov cone appears when a particle is traveling faster than the wave it emits see Fig 1.7a. The angle of the cone is defined as :

$$\theta_C = cos^{-1}(v_\phi^{THz}/v_g^{pump}) \tag{1.26}$$

However, if one could change the time where each components of the pulse front arrives as presented by the red arrows of Fig.1.7a), then using Huygens principle, one could constructively adds all THz waves.

The easiest way to do this experimentally is to use a grating. The grating will tilt the pulse front with an angle θ_T (see Fig.1.7b). The components which arrives first on the crystal will have a longer time in the crystal. As there is a mismatch in refractive index, THz generated by all the components will interfere constructively. A picture of my experimental set-up is shown in Fig 1.8. An imaging system (two cylindrical lens) is used to avoid too much wavelength dispersion and have a perfect image of the grating on the LN crystal.

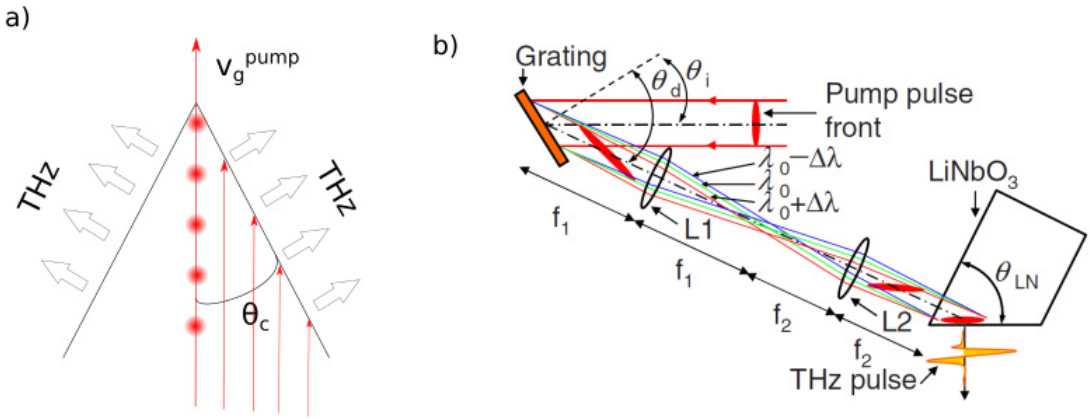

Figure 1.7: a) The particle (red sphere) with the speed v_g^{pump} is moving faster than the THz it emits causing the THz to be generated with an angle causing destructive interference. The angle θ_C is the ratio $cos^{-1}(v_\phi^{THz}/v_g^{pump})$. The red arrows are the delayed laser components that arrives later. b) Scheme of the implementation of the tilted pulse front technique. Figure adapted from [46]

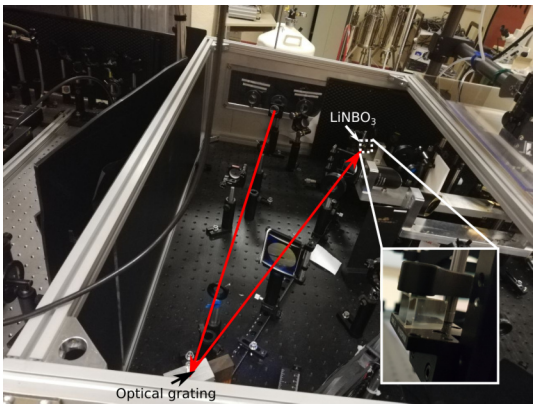

Figure 1.8: Experimental setup for the tilted pulse front. The 800nm femtosecond laser is send on a grating which tilts the pulse front (black line) with an angle θ_T. The tilted pulse front travels through an imaging system to avoid wavelength dispersion and finally to the crystal to generates THz.

As the pulse front is tilted, only the projection of the group velocity on the phase velocity of the THz is required :

$$v_g^{pump} cos\theta_T = v_\phi^{THz} \tag{1.27}$$

Which using equation 1.26 gives the equality between the Cherenkov and the tilted angles.

$$\theta_T = \theta_C \tag{1.28}$$

θ_T is a constant linked to the grating you choose, so one needs to choose the good grating for the right Cherenkov angle :

$$\theta_T = tan^{-1}(\frac{\lambda g}{n_{NIR}^{gr} m\, cos\theta_d}) \tag{1.29}$$

Where λ is the central wavelength of the pump, g is the groove density of the grating, m is the magnification factor of the lenses and θ_d is the diffraction angle of the grating.

1.3.3 THz generation in FEL

Light emitted in large Scale facilities such as Free Electron Laser or Synchrotron are relying on electrons to generate such light. When a electron is decelerating it emits light. This is the synchrotron radiation.

In Free Electron Laser, a bunch of electron is fired from a electron gun into a linear accelerator. While the electron bunches from the electron is kind of random after going through the linear accelerator, all of them are going into the same direction. Electrons are going through a set of magnets called the wiggler. It will make the electron beam oscillates in the transverse direction of the movement. At each times it needs to decelerate electrons will emits light that are interfering to each other coherently. This will create a very bright and coherent light source. The electron bunch is then recuperated through a beam dumper. The situation is represented in fig 1.9.

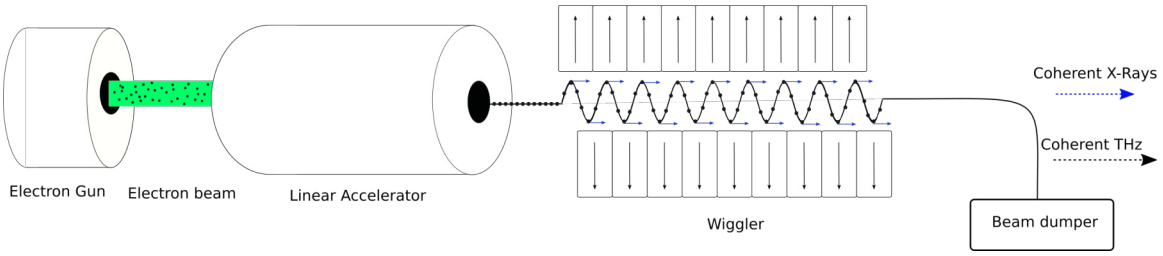

Figure 1.9: Light creation on FEL

By controlling the acceleration of the electrons one can control the duration of the pulse while controlling the spacing between the magnets will allows to control the wavelength of the pulses. The wavelength generated are available to very large spectra from infrared to hard x-rays with a very high brightness $10^{20} W/cm^2$. I will present in this section the method of generation at the TeraFermi Beamline.

As explained by Perucchi et al.[50] the electron bunch of a FEL is naturally emitting beam of 50fs to 1ps duration. Coherent light from 1 to 20 THz is therefore naturally emitted in such facilities. Quantitatively, the ratio between the power radiated by the bunch (P) over the power radiated from a single particle (P_s) can be written as :

$$\frac{P}{P_s} = N(1 - f(\omega)) + N^2(f(\omega)) \tag{1.30}$$

N is the number of electrons in the bunch and $f(\omega)$ is the form factor given as :

$$f(\omega) = \left| \int_{-\infty}^{\infty} e^{i\omega z/c} \rho(z) dz \right|^2 \tag{1.31}$$

With $\rho(z)$ being the normalized longitudinal charge density. Equation 1.30 possess posses two term, one is scaling linearly with the number of electrons while the other one is scaling quadratically. The linear term of equation 1.30 represents the incoherent emission of the bunch, the quadratic part represents the coherent emission. In FEL,

the number of electrons in the bunch is much higher than it is in Synchrotron ring. Doing so the coherent gain is of the order of 10^{10}.

At TeraFermi Beamline, they use the Coherent Transiant Radiation (CTR). In CTR, they place a metallic plate in the trajectory of the high energetic electrons. Electrons travel through the metallic plate target. This generates a current within the metallic plate, this current is then radiating back and forward of the metallic screen according to the Ginzburg-Frank formula [51] :

$$\frac{d^2U}{d\omega d\Omega} = \frac{e^2}{4\pi^3\epsilon_0 c} \cdot \frac{\beta^2 \sin^2\theta}{(1-\beta^2\cos^2\theta)^2} \tag{1.32}$$

Using this technique, single cycle THz pulses achieving up to 1 MV/cm with a spectra from 0-3 THz are generated at 50 Hz repetition rate. The pulse measured at sample position is presented in in Fig. 1.10:

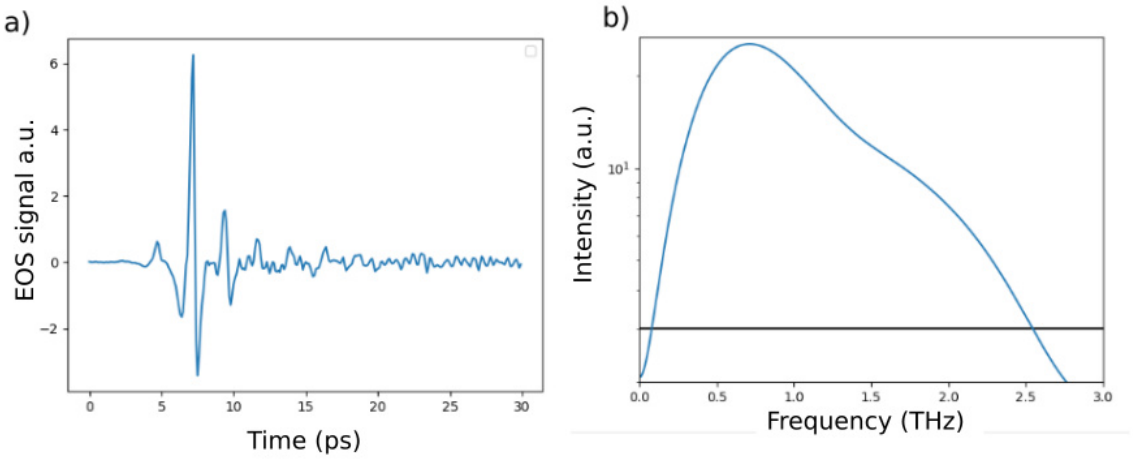

Figure 1.10: a) Time trace of the THz electric field taken at Fermi measured with EOS on a $100\mu m$. b) Associated Fourier Transform in log scale the black line is the noise floor.

Another example can be taken with the TELBE beamline at Dresden. In their Beamline they use the Coherent Diffraction Radiator source [52]. The electron bunch is directed onto an open resonator to generate the THz. The pulse directly generated with CDR is close to the one generated with CTR (as in the TeraFermi Beamline). One interesting aspect of the TELBE beamline is that they coupled their source to an undulator which allows to select precisely the THz wavelength. This allows for a choice of either a narrow band pulse for selective resonant THz or a broad single cycle. Fig. 1.11 presents the shape of the THz electric field from both sources at the TELBE Beamline.

As such, the choice of the FEL must be adequate to the experiment. For non resonant or non linear response of material in a low frequency region the TeraFermi beamline is more suited. However, for selective resonance and linear THz-TDS the TELBE beamline is a better choice. Other hutch specialized on THz in other FEL have their specifities but won't be detailed in this manuscript.

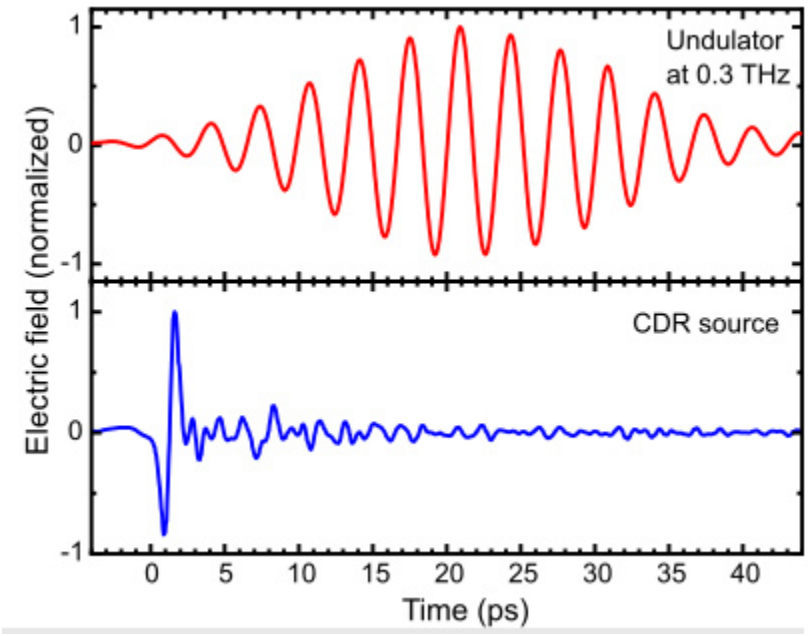

Figure 1.11: Up : THz electric field after the undulator. Down : Single cycle THz electric field right after the CDR source. Figure adapted from the TELBE web site.

1.4 THz detection techniques

The standard detectors used for optical wavelength cannot be used directly with THz wavelength. In the case of photodiodes, visible light is shinned on semi-conductors, electrons are promoted in the conduction band and generates a current. Because THz energy is smaller than the band gap of most semi conductor, this technology cannot be applied to create THz photodiode. Pyroelectric detector which are working in the Infrared frequency range are still working in the THz region. However, their sensitivity is low and required chopping at low frequency which will reduce considerably the signal to noise. Therefore detection techniques need to be developed. Most of those techniques are pump probe experiment and requires heavy set-up.

During my PhD I used Air Bias Coherent Detection (ABCD) and mainly Electro Optical sampling (EOS). I used pyroelectric detector and matrix of pyroelectric cells as a camera. In this section, I will present quickly ABCD detection. Then, I will then focus on EOS and explains data treatment of EOS traces as those are at the heart of most of my experimental results.

1.4.1 Air Bias Coherent Detection

ABCD detection is similar to Air Plasma generated technique as it allows to detect THz from a plasma generated in air [53, 54]. A plasma is generated in air, then the interaction between a laser field at frequency ω and the THz Electric field E_{THz} is described as follows by a third non linear effect, the four wave mixing :

$$E_{2\omega} \propto \chi^{(3)}_{air} E_\omega E_\omega E_{THZ} \tag{1.33}$$

$E_{2\omega}$,E_ω,E_{THz} are the electric field amplitude of the second harmonic 2ω, the funda-

mental ω and the THz wave. $\chi^{(3)}_{air}$ is the third order susceptibility of air. The Electric field of the second harmonic is proportional to the THz electric field, however it is hard to have access to the second harmonic and in practice we only have access to the intensity of the second harmonic $I_{2\omega}$ implying an incoherent detection i.e. the loss of the phase information. However, a smart method was designed by Dai and al. [53] by mixing a local oscillator at the second harmonic frequency. The intensity of second harmonic will be then described as follows :

$$I_{2\omega} \propto E^2_{2\omega} = (E_{THz} + E^{LO}_{2\omega})^2 = E^2_{THz} + 1E_{THz}E^{LO}_{2\omega} + E^{LO^2}_{2\omega} \tag{1.34}$$

$E^{LO}_{2\omega}$ is the electric field of the local oscillator, this term is provided by the second harmonic component of the white light generated by the laser induced air plasma. The first term of the equation is dominant when the Local oscillator is too weak, this lead to the incoherent measurement. The key toward coherent measurement is in the cross term. When the probe intensity is higher than the air ionization threshold, the local oscillator becomes dominant and then we have $I_{2\omega} \propto E_{THz}$ making possible coherent detection, this explains the first name of this technique Air breakdown coherent detection.

Karpowicz et al. [54] later proposed an even better method by applying an AC bias voltage at the focal point of both THz and optical beam. The AC bias voltage breaks the symmetry and adds a new source for the second harmonic and replace the local oscillator. Using such scheme they increased the signal to noise by one order of magnitude and reduced the power of the probe needed. This lead to the Air Bias Coherent Detection. The experimental set-up of Karpowicz et al. is presented in Fig. 1.12.

Only limitation of such measurement is the time duration of the probe. Indeed, the Fourier Transform is dependent of the number of points and by the time spacing. As there is only air as a detection media, there are no reflections coming from the detection so there is no limit to the number of points you can get. However spacing depends only on the time duration of your probe meaning that the only limitation is the pulse duration of your probe.

1.4.2 Electro Optical Sampling

The EOS technique is based on the birefringency of some crystals under an electric field, the principle is put on Fig 1.13.

Under the electric field, the material become birefringent, the polarization of the probe light will rotate. With the quarter wave plate, the polarization becomes elliptic going through the Wollaston prism will split the beam into two which intensities are modulated by the electric field. Using balanced detection, one can find the electric field.

For the interested reader, the derivation of EOS can be found in appendix of this manuscript. The main result obtained from this derivation is the following equation :

$$\frac{I_y - I_z}{I_y + I_z} = sin(\frac{2\pi l r_{41} n_0^3 E_{THz}}{\lambda}) \tag{1.35}$$

Where I_y, I_z are the polarization along the y and z directions, l is the crystal thickness, r_{41} is the non linear coefficient of the detection crystal, n_0 is the refractive index of the material and λ is the detection wavelength.

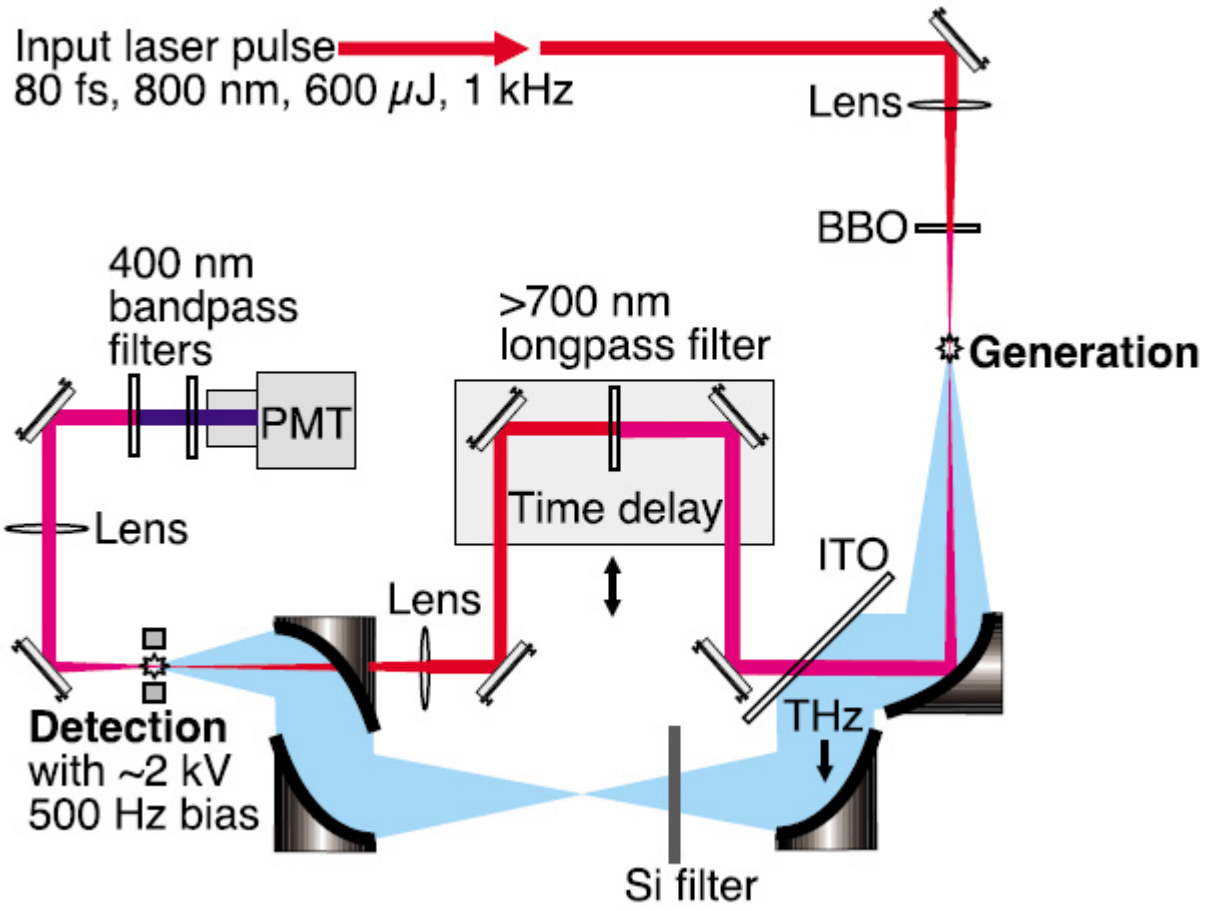

Figure 1.12: Example of an experimental set-up for ABCD Detection. In this example, they use THz generated through Air plasma. Electrodes are applied at the plasma edges to allow the coherent measurement. Figure taken from [54]

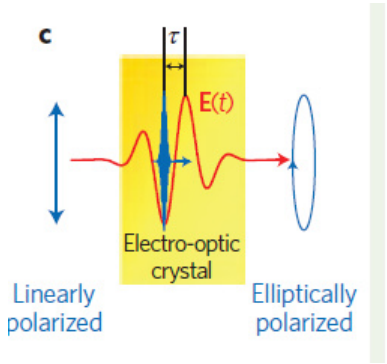

Figure 1.13: Linearly polarized becomes elliptical under the action of the THz electric field in the detection crystal. Figure adapted from [12]

High electric fields effects on Electro-optical sampling

Some sources are designed for very high value of electric field (a few hundreds of kV/cm). However, EOS presents some issue with too much Electric Field. From equation A.26, one can see that if the Electric field is beyond a value E_{max} then the signal is beginning

to decrease despite an higher real electric field. E_{max} is defined as follows :

$$E_{max} = \frac{\lambda}{4n_o^3 r_{41} l} \tag{1.36}$$

For a ZnTe of 500 μm the maximum electric field is roughly 90 kV/cm. When reaching higher electric field the pulse will appear distorted as represented in Fig. 1.14.

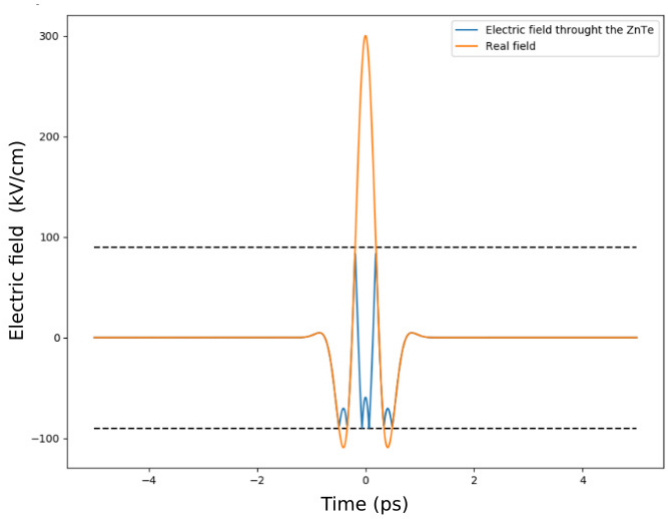

Figure 1.14: Simulation of the signal measured for a electric field higher than E_{max}

To increase E_{max}, one have to either choose a shorter crystal or to change the non linear coefficient (r_{41}). The value of the signal in function of the Electric field is represented in Fig. for two different crystals: the ZnTe and the GaP. The GaP has a non linear value of $0.88\,10^{-12} V/m$ whereas the ZnTe as one of $4.04\,10^{-12} V/m$.

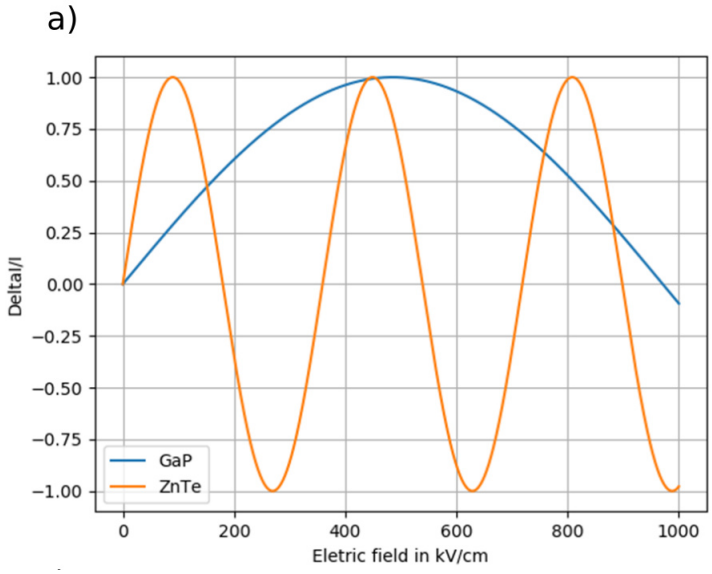

Figure 1.15: Signal value in function of the electric field for a ZnTe of 500 μm and a GaP of 300 mum

One can also use filters such as Si wafers to decrease the value of the Electric field. However, this will add echoes that are related to the Fabry Perot effect.

Fast Fourrier Transform and Reflection effect on EOS spectra

After recording the THz waveform in the time domain, the associated spectra has to be recovered from the the wave trace. To do so, the Fast Fourier Transform (FFT) algorithm is used. The algorithm is dependent of two parameter first the number of points in the scan which will give the number of points in the Fourier Transform. Then, the spacing between the points which will gives the frequency range of the obtained spectra. Therefore, to have a good frequency resolution, a large enough number of points is required. Roughly for a pump probe experiment, this implies that the time resolution of your probe will give you the frequency range of your Fourier Transform, the number of point of your scan will give you the spectral resolution.

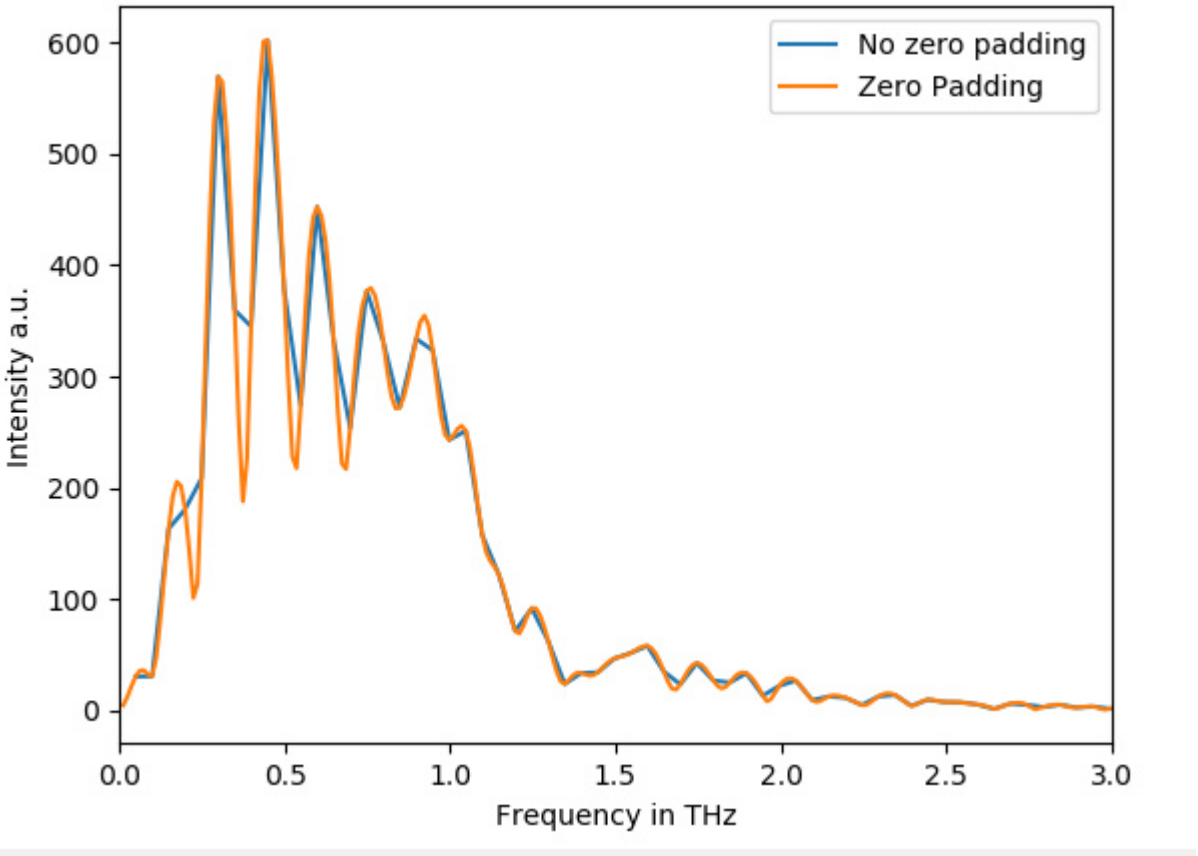

Figure 1.16: Fast Fourier Transform of a THz waveform with zero padding (orange) and no zero padding.

In Fig.1.16 is plotted in blue a direct Fourier Transform of a THz waveform. The spectra has very few points in it which explained the aspect of the curve. One way to smooth the curve is to pad the function. Padding means that zero are artificially added from both sides of the wave form to increase the number of points. Doing so, there is more points into the spectra as can be seen in the orange spectra of Fig.1.16. Zero padding is a good way to increase the number of points as it is not adding any information. Zero padding is closer to interpolation in some sense as all blue points coincide on an orange points.

While zero padding is enough to smooth the curve. The spectra obtained is comb-like and as such is not representative of the reality. To understand this comb behavior, we have to look at the THz waveform in the time domain. Such a waveform recorded using a 500 μm thick ZnTe is presented in Fig.1.17.

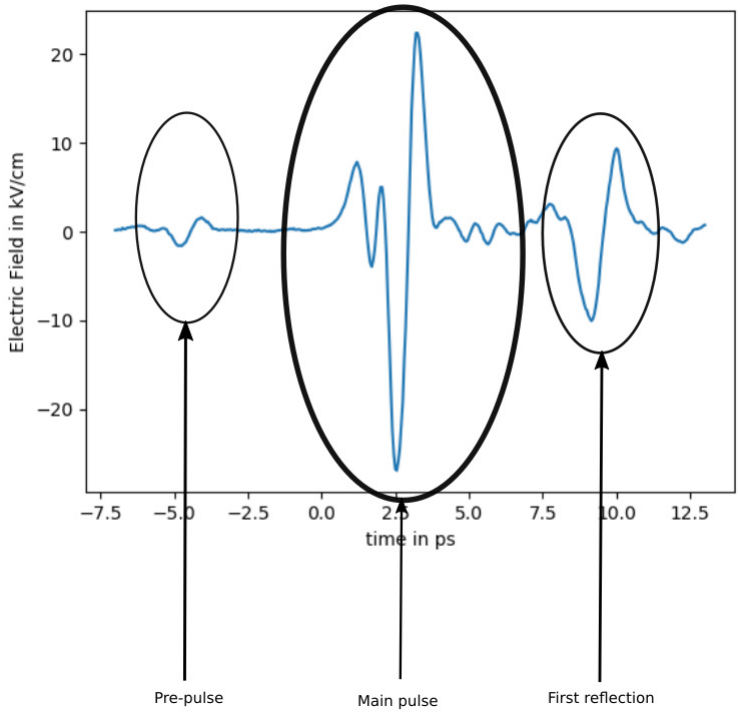

Figure 1.17: THz waveform in the time domain. Different part of the waveform are circled to be highlighted. The first one in time correspond to the pre-pulse, the second one to the main pulse and finally the third one to the first reflection.

On such waveform, we can observe three part of interest. The first part around -5ps, that we will call the pre-pulse. The second part around 2.5ps is the main pulse and the last one around 10 ps is the first Reflection. All pulses are separated by 8ps. The main pulse and first reflection can be explained using Fabry-Perot effect. Indeed, when THz travels through the detection crystal, when it reaches the end of the crystal a part is bounce back into the crystal. Then, the wave traveling back is again bouncing back in the original propagation direction. This implies that there is a smaller THz wave traveling later in the crystal that the original one. The separation in time of such waves is :

$$\Delta t = 2 * \frac{nl}{c} \tag{1.37}$$

Where n is the refractive index of the ZnTe, l is the thickness of the crystal and c is the speed of light. Knowing the refractive index of ZnTe to be around 3.2 (see Table 1.3.2) we can compute the separation to be around 10ps which is close to the experimental value. Moreover, the reflection amplitude can be computed relatively to the one of the main pulse using Fresnel Reflection :

$$E^{relative}_{reflection} = \frac{E_{reflection}}{E_{main}} = \frac{T_{air-ZnTe} r_{ZnTe-air} r_{ZnTe_air} T_{ZnTe-air}}{T_{air-ZnTe} T_{ZnTe-air}} = \frac{(n^{THz}_{ZnTe} - 1)^2}{(n^{THz}_{ZnTe} + 1)^2} \quad (1.38)$$

Using the numerical value of the refractive index of ZnTe in the THz domain, we obtain that the reflection should be 25% of the main pulse. This is in adequation with our experimental data. This explanation is resumed in Fig.1.18

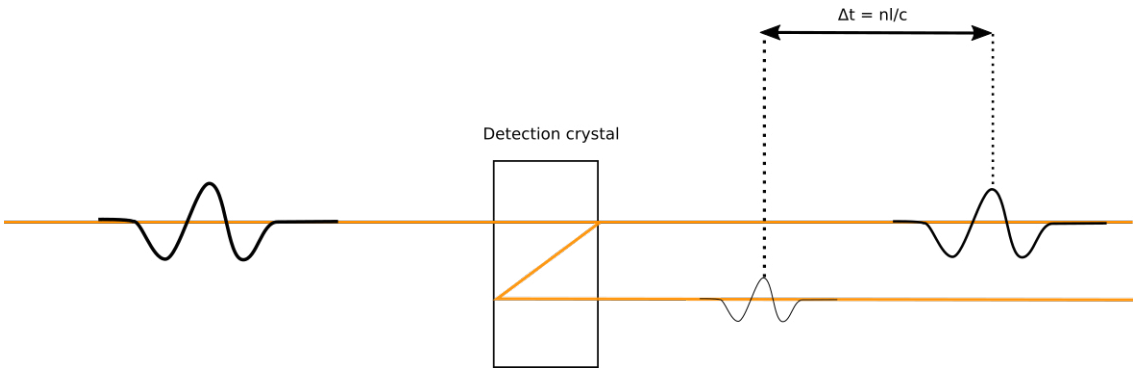

Figure 1.18: THz reflection in ZnTe leads to two distinct waves separated in time. The second wave is the fourth of the main pulse.

The pre-pulse is a bit more tricky to explain. As for THz, there are reflection of the probe within the detection crystal. For THz, all reflection can be separated thanks to the time resolution of the probe. However, reflection of the probe are all integrated by our fast photo-diodes which rising time cannot go below the ns. Therefore, the pre-pulse is the reflection of the probe which coincides with the THz pulse and is modulating the signal recovered by our diode. The separation in time is the same for pre pulse and first reflection as refractive index in THz regime and 800nm are very close to each other ($n^{ZnTe}_{THz} = 3.17$ and $n^{ZnTe}_{800nm} = 3.13$).

The Fabri Perot effect induces modulation at the frequency of the reflecion which explains why the spectra is comb like. This is the reason why a good windowing is needed. In our case, we choose the Hann window. The Hann window is a modulation of the signal using the following function :

$$w_0(x) \triangleq \left\{ \begin{array}{cc} \frac{1}{2}\left(1 + \cos\left(\frac{2\pi x}{L}\right)\right) = \cos^2\left(\frac{\pi x}{L}\right), & |x| \leq L/2 \\ 0, & |x| > L/2 \end{array} \right\} \quad (1.39)$$

This windowing smooth the function and is better than a square window because it reduces effect at the edges of the data set. A windowed wave form is presented in Fig. 1.19. The window smooth the data and vanished the reflections. The end points of the data set are 0 which allows an easy padding.

The window cancels the peaks in the spectra while keeping the general spectra as shown in Fig.1.20.

Because of the reflection of the detection crystal, the usable data in a wave form is restricted to a small part. While zero padding allows to a better data visualization, the amount of information is the same that with no padding. This means that the only way to increase the real frequency resolution is by delaying the reflections. To

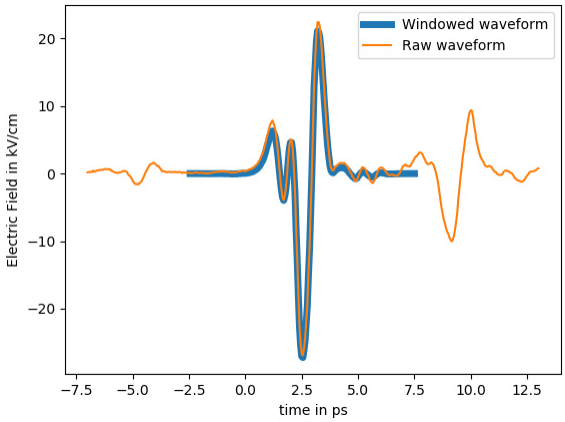

Figure 1.19: THz waveform in the time domain unwindowed (orange) and windowed (blue)

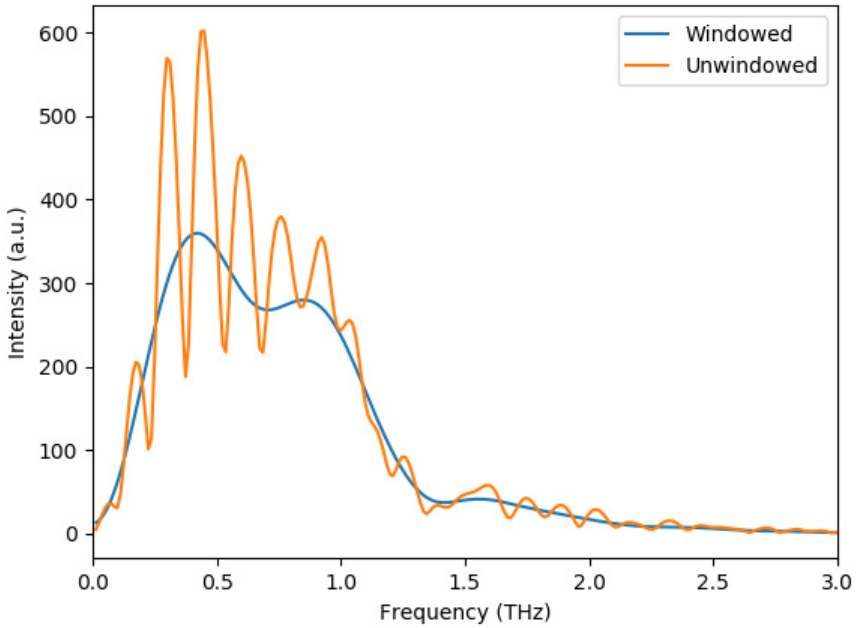

Figure 1.20: Fourier Transform of a windowed (blue) waveform and no window (orange) both spectra have the same padding.

do so larger crystal are necessary but by doing so the electric field region were Electro optical sampling is valid (polarization rotation is < 90 degrees) is reduced as well. This the main limitation of any Electro optical sampling measurements. While ABCD is better for any measurements of THz than EOS, the difficulty of creating such detection explains by itself the rarity of such detection.

1.5 Conclusion

To sum up this chapter, we first explained the fundamental principles of optics by understanding the microscopic aspect of the dielectric susceptibility using the Lorentz Model of the atom. While this model is semi-classic, it is enough to have a first understanding of non linear optic.

Then, we went through 3 different techniques of THz generation : Air Plasma, Optical Rectification and finally THz generation in Free Electron Laser with a focus on the THz generation used at the TeraFermi Beamline of the FERMI FEL in Trieste, Italy. The main characteristics of all the sources presented in the chapter are resumed in table ??.

THz source	Energy	Frequency Range	Peak Electric field (MV/cm)
Optical rectification (DAST)	$20\mu J$	0-4 THz	5MV/cm
Optical Recitfication (LiNbO3)	$3\mu J$	0-2 THz	1.2 MV/cm
TeraFermi Beamline	$2\mu J$	0-3 THz	1.1MV/cm
Two color Air Plasma	$\sim 2\mu J$	0 - 10 THz	$\sim$3MV/cm

Table 1.2: Recapitulative table of all the different THz generation sources

Optical rectification based on both organic crystal or $LiNbO_3$ are sources than can exceed MV/cm with a broadband but small frequency ranged mainly centered around 1 THz. Because of the low frequency regime preeminence, the electric field is often a very intense single cycle electric field. Thanks to those features, these sources are suited for both non linear spectroscopy in the sub 1 THz frequency region and for THz pump probe experiment.

Free Electron laser are sources very similar to Optical Rectification based sources. However, while electric field can achieve up to MV/cm for Optical rectification, most sources of such kind are using only around 500kV/cm pulses. On the other hand, most FEL sources are generated around MV/cm. Therefore, the FEL source is reliable tool to complete first experimentation done in the laboratory. Moreover, some beamline such as TELBE Beamline in Dresden added an undulator to their beam to select wavelength inside their pulses allowing for resonant pumping at chosen wavelength. The main drawback of FEL is that they are not easily accessible. Proposal have to be send to the team and accepted to realize the experiment. Even if accepted the experiment time is really short and experiment needs to be well prepared which implies that a laboratory source is required. A comparative table between TeraFermi and TELBE beamline is shown in table 1.3.

FEL	Energy	Bandwidth	Frequency-Range
TeraFermi	10	All	0-2.5 THz
TELBE Undulator	<= 10	0.2 THz	0-1.1 THz
TELBE CDR	0.25 mu J	All	0-1.5 THz

Table 1.3: Comparative table between FEL TeraFermi and the two modes of FEL TELBE.

Thanks to the frequency range being the widest for the Two color air plasma generation, this source is the most suited for spectroscopy over the whole frequency region.

While peak electric field is exceeding the other sources and a comparable energy in pulses this source is not as well suited for THz pump experiment. Indeed, because of the large number of high frequency component, the electric field shape in the time domain is oscillating too fast for electrons or dipole to align with the applied electric field.

The Optical Rectification based on $LiNbO_3$ was selected for our THz Set-up. This source is the most suited for the experiment we want to do as most of our samples presents strong absorption in the low frequency domain. Moreover, even if there is no absorption peak in the spectra generated using LN, the single cycle shape allows for non resonant effect on samples. Finally, the LN crystal was chosen over organic crystals because of the experimental set-up at disposition in our laboratory.

After selection of THz Generation an adequate THz Detection must be chosen and as such we explained two main techniques. Air Plasma Coherent Detection is a techniques that relies on four wave mixing using the third order non linear susceptibility of air. A bias electric field is used to be able to coherently detects THz spectra. Electro Optical sampling relies on the Pockels effect in media with no inversion symmetry. The crystal becomes birefringent under the applied Electric Field here the THz. Then, by measuring the phase retardance between the two polarization component, we can compute the exact electric field. Because of the reflection induced by the detection crystal, Electro Optical sampling frequency sampling is worse than ABCD detection. However, Electro sampling is far simpler to implement than the ABCD one and was selected for this reason.

As both the choice of THz source and detection are explained, the experimental set-up and the characterization of the source will be presented in the next chapter.

Chapter 2

Development of an intense THz source based on Optical Rectification in $LiNbO_3$

2.1 Introduction

In this chapter, I will describe the development of the intense THz source based on the Optical rectification in $LiNbO_3$ using the tilted pulse front technique. The development of such source requires to use different techniques to characterize the source. Indeed, as the generation and use of THz light is still in development there exist no commercial solution to measure precisely beamsize or energy. Moreover, the only experiment which gives large signal is Electro Optical sampling which is using a non standard set-up for detection.

As stated in the previous chapter, we choose the Electro Optical Sampling (EOS) for the detection of our THz signal. While allowing to make precise measure of the THz waveform as well as its electric field value, EOS is a pump probe experiment and can only be use as a characterization tool. Indeed, as the electric field value is dependent of the delay between the pump and probe changing a bit the path of pump or probe will change as well the delay between them. Ths implies that a EOS scan need to be realized after each modification of alignment. For this reason we used an infrared camera Pyrocam III from Spiricon. This camera was built to work in the infrared region but fortunately works in the THz region as well allowing for a more qualitative approach for THz optimization.

I will first describe the laboratory set-up I used to develop the source, a brief explanation of the Chirped Pulse Amplification will be given as well. Then, the alignment procedure will be explained to optimize the THz using the $LiNbO_3$, this section is of primary interest for newcomers in the THz field or future PhD and interns students in the Materiaux et Lumiere groupe in Rennes. The implementation in our laboratory of the EOS technique will be presented, more precisely how the data treatment was handled as well as the impact of broadband source on the experimental data. A technique using EOS for imagery will be presented. The final THz beam characteristics will be presented in this chapter as well. The study of THz generation efficiency in function of pulse duration will be presented. Finally, the THz source will be validated to reproduce

results from the literature with two experiment : Second harmonic modulation in the $\beta - Baryum\,Borate$ and Joule Heating in V_2O_3 thin film.

2.2 Laboratory overview

An overview of the lab is given in Fig 2.1:

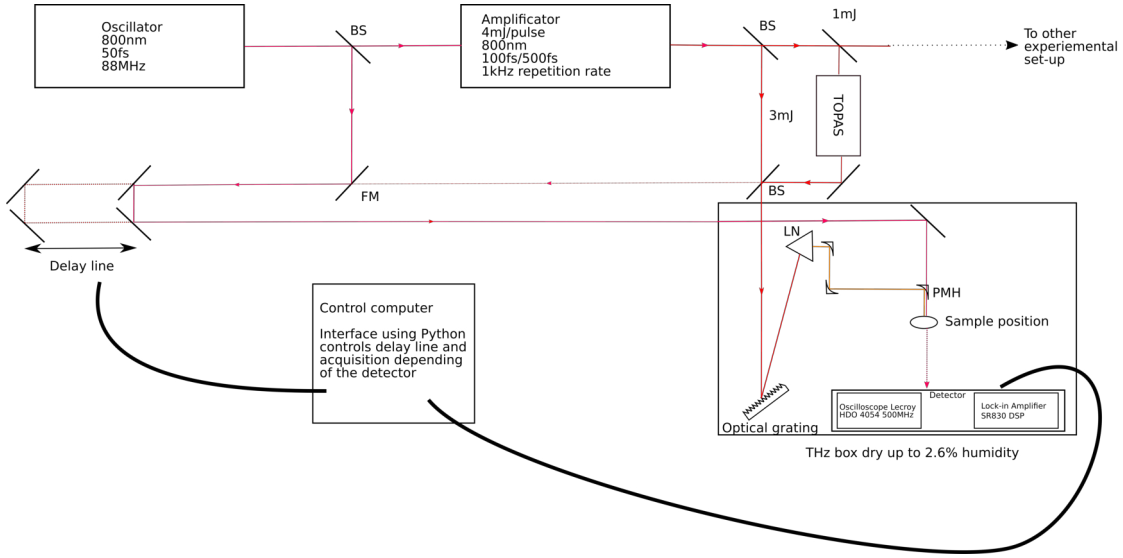

Figure 2.1: Schematic view of the lab. BS: Beam Splitter, FM : Flip Mirror, LN : Lithium Niobate, PMH : Parabolic Mirror with an Hole. To simplicity, probe light path is shown in pink, optical pump in red and THz light in orange.

All light in our laboratory is generated from an Optical oscillator : the MIRA. The MIRA generates a mode-locked pulse centered at 800nm with 40nm of full width at half maximum (FWHM) at 78MHz frequency, pulse duration is around 50 fs. This pulse is then split into two, one is generating the optical pump while the other is used as THz detection probe. The amplification is realized using Chirped Pulse Amplification(CPA) to amplify the pulse from the MIRA into a pulse centered at 800nm with 100fs pulse duration and an energy of 4mJ per pulse at 1kHz.

This pulse is split into one branch of 1mJ and one of 3mJ. The 3mJ branch is the optical pump of the system, while the 1mJ branch is either going to an Optical parametric amplification (OPA) to change the wavelength or to other experimental set-ups of interests for our team. If 800nm is the wavelength chosen, a Beam Splitter is used to put the beam on the path for the path of the probe.

The THz box is described more precisely on Fig 2.2 :

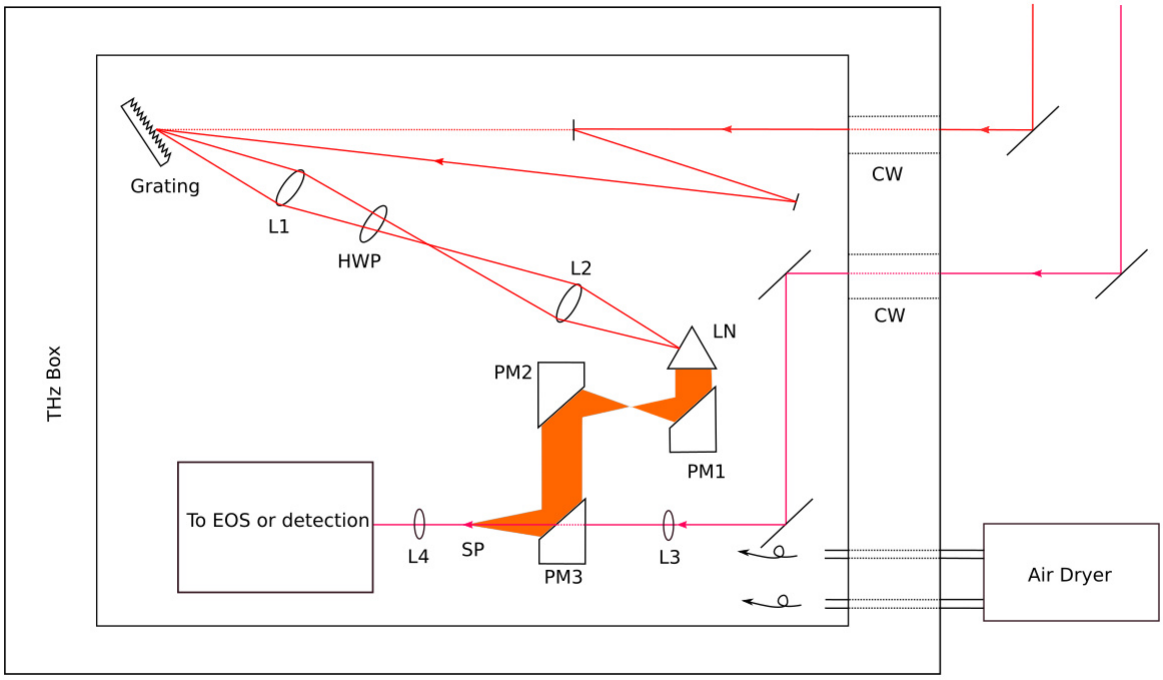

Figure 2.2: Same color scheme as Fig 2.1, CW : Coated window, L1 : Cylindrical lens 250mm, HWP : Half Wave Plate, L2 : Cylindrical Lens of 150mm(to check), LN : Lithium Niobate: PM1 : Parabolic Mirror 15,6 mm of focal, PM2 : Parabolic Mirror with 152mm of focal, PM3 : Parabolic Mirror with 50mm of focal length drilled to let the probe go through, L3 : Concave lens for the probe to focus the probe on the sample, L4 : Concave lens conjugated with L4 to colimate the probe, SP is the Sample Position

The pump is entering the box through a coated window that allows maximum transmission of the beam to conserve the energy, less than 1% is lost at this point. Then, two mirrors allows for a best aligning on the grating as the incidence angle on the grating is crucial. Then, the image of the grating is put on cylindrical lenses to do the perfect image of the grating on the Lithium Niobate (LN) Crystal. The THz generated are then focused with the help of three parabolas onto the Sample position. The probe is focused with a lens onto the sample position through the hole of the last parabolic mirror.

As THz is strongly absorbed by water, an Air Dryer is necessary in order to low the humidity percentage inside the box. Ideally, the setup should be used with the minimum path length of the THz to minimize the effective length of absorption of the water.

2.2.1 Laser generation using Chirped Pulse Amplification(CPA)

In the history of laser, there has been a huge limitation for mJ sub ps laser. The intensity of such laser is so high during the amplification process that damage threshold of the crystals used for the amplification are reached, this is also true for the mirror used within

the cavity. Strikland and Mourou [55] demonstrated the Chirped Pulse Amplification (CPA) technique that is still used nowadays for sub ps laser amplification. Their work has been rewarded with a Nobel Prize in 2018. The idea behind is simple, the pulse is lengthen before amplification and then compressed back to reach the mJ. An example is presented in Fig.2.4.

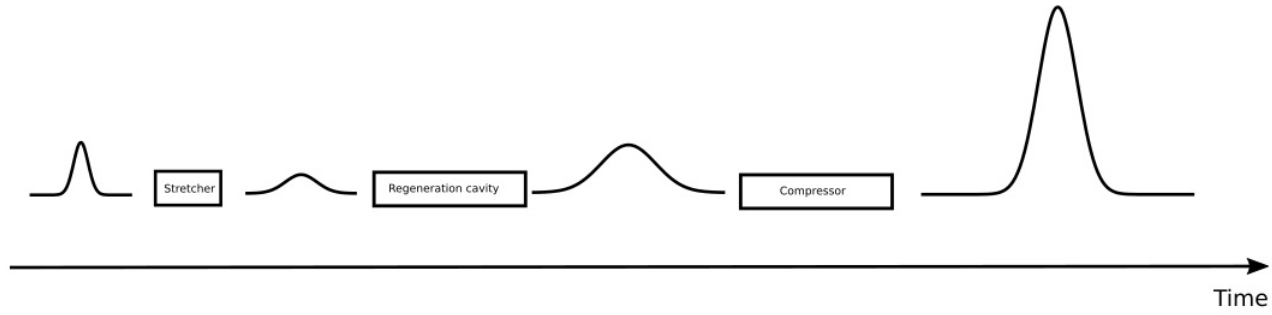

Figure 2.3: Scheme of the Chirped Pulse Amplification

The pulse to be amplified is going through the stretcher where it's pulse duration is increased. This is usually done by using a set of optical grating. Then, the long pulse is amplified into a regeneration cavity using a gain medium, in the case of 800nm light a Ti:Sapphire is generally used. Then, the long amplified pulse is compressed to sub ps duration. The pulse duration is closely linked to the spectra of a pulse. Indeed as light is an oscillatory electromagnetic field, a purely monochromatic light centered at frequency ω_0 is a Dirac:

$$E(\omega) = \delta(\omega) \tag{2.1}$$

Switching from frequency space to time space by Fourier Transform allows to write :

$$E(t) = e^{i\omega_0 t} \tag{2.2}$$

This is a continuous wave which frequency is centered at the frequency ω_0. In reality, spectra of laser pulses are not purely monochromatic, the spectra is then Gaussian in frequency. This linked the spectral fwhm to the temporal one. The sharper the peak, the longer the pulse. In our laser, the pulse duration is controlled by the use of a spatial mask. A mask is placed at the exit of the optical grating blocking a part of the pulse as presented in Fig.2.4.

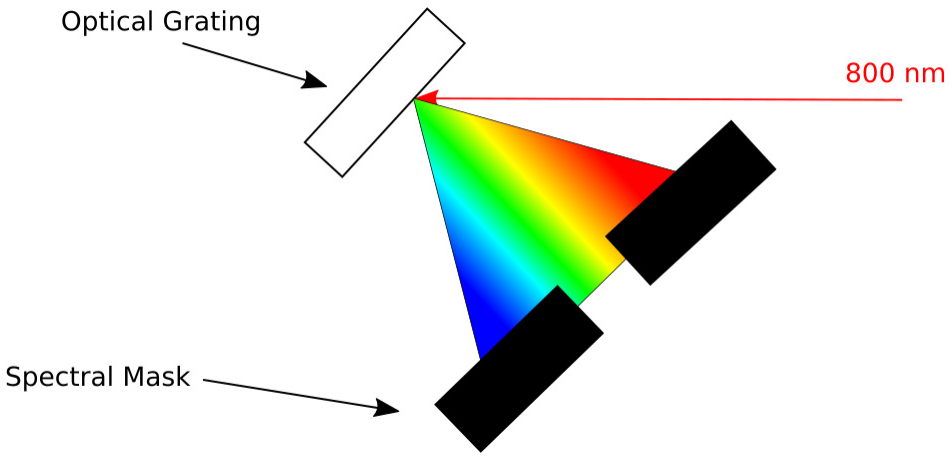

Figure 2.4: Spatial mask used to reduce the bandwidth of pulse in a CPA technique.

In our laboratory there are two amplified laser, the USP and the ELITE. The USP pulse duration is 52 fs as extracted from its spectra presented in Fig.2.5. The ELITE has two cavities with a different mask for each cavity, the first is called the Femto cavitiy with pulse duration being and the spectra of this cavity is presented in Fig. 2.6. The second cavity is called the cavity Pico and the pulse duration is around 500 fs. No spectra are available for this cavity as we don't have spectrometer with high enough resolution to extract the FWHM of the spectra.

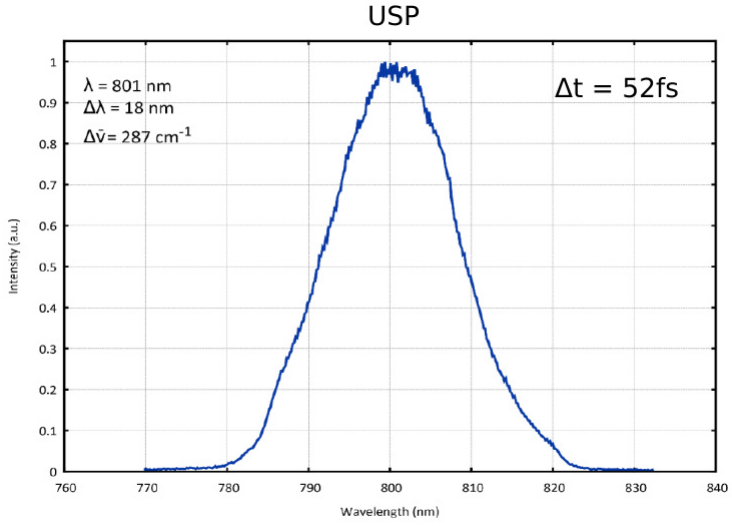

Figure 2.5: Spectra of the USP, the pulse duration associated is written at the right high corner.

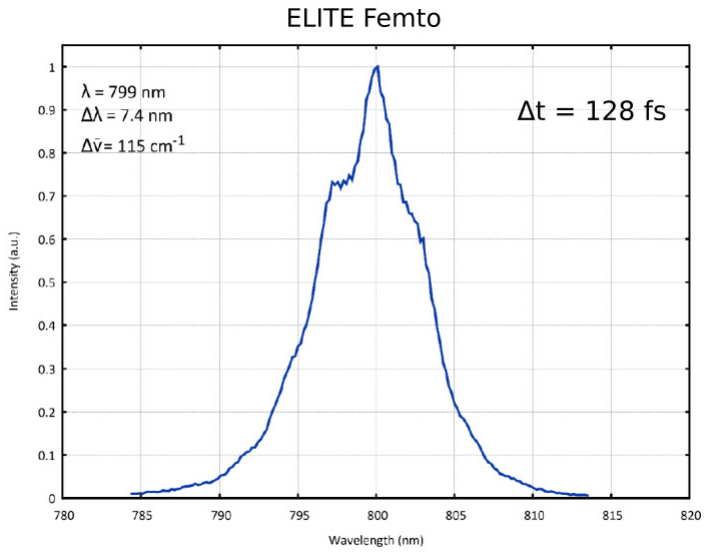

Figure 2.6: Spectra of the ELITE Femto cavity, the pulse duration associated is written at the right high corner.

2.3 Alignment procedure.

In order to obtain the maximum intensity for the THz electric field a fine alignment is required. This has to be done in two steps, the first step is the beam right at the exit, the second one is the alignment of the parabolic mirrors. Fig. 2.7 represents the crystal in the lab.

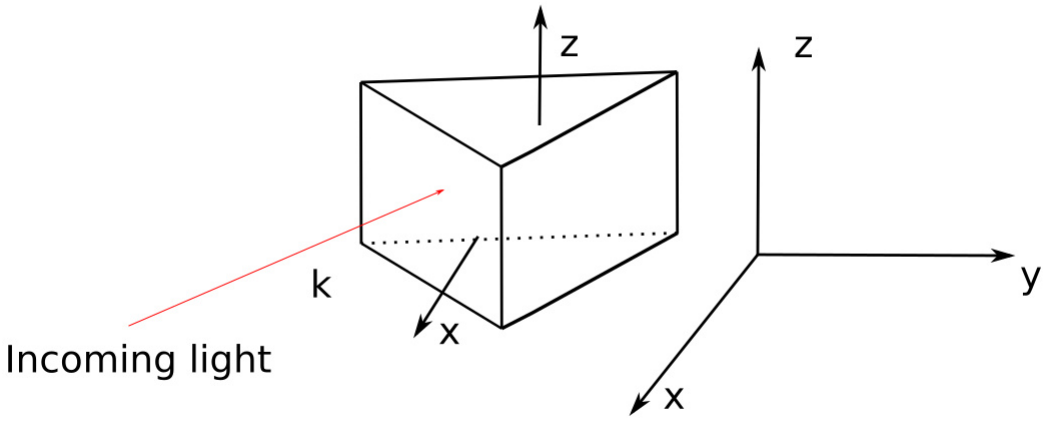

Figure 2.7: Representation of the LN in the lab, the axis are the lab axis.

In order to have the best generation possible for the THz, we used the following alignment scheme. First, after choosing the right angles for your crystal and grating, place the LN in the estimate right place. We choose to place the LN on to translation stages on in the X direction and one in the Y direction. In order, X and Y are chosen along one hole lines and in the end the THz should follow the X direction. Moreover,

the LN is place on rotation stages allowing the rotation along X and Z axis. Incoming light should arrive in the XZ plane.

First thing is to place the back reflection in place using the rotation mount, note that the back reflection should be perfect in the horizontal plane but it can go a bit down for the vertical back reflection. Then, use the translation stage to increase the signal on your pyroelectric detector. The optimization of the SHG is also a good way to increase the THz signal. Then, you should align the mirror incoming on the grating in order to optimize the signal. Finally, adjust the grating to again have the better signal. Do it again until you're satisfied. Best thing, is to keep the same order. Once the signal seems good to you, you should take care of the directions of the signal.

For this step, place the detectors on a motorized 3 axis stage is recommended. Indeed, you have to place the signal on a straight line, to do so, find the signal at a place close to the crystal, then following the x axis (this should be the direction the THz are following) go to the most far of the position you can. Then use the rotation stage of the crystal to maximize the signal. Go to the old position maximize the signal using the grating. Reiterate until satisfied. This operation should give you a straight and collimated beam. At this point you should check the divergence of your beam. It is important to have the less divergent possible beam for the alignment of the parabola.

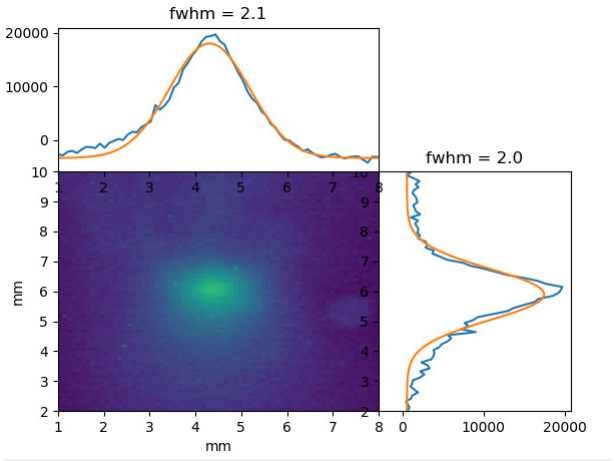

Figure 2.8: Picture untreated of the camera. Curves on top and on the sides are respectively vertical and horizontal projections of the beam. The FWHM presented is obtained from a Gaussian fit of the data.

To process the alignment of the parabola a custom plate was realized by our workshop. This plate limits the maximum number of degrees of freedom. First, the metallic plate must be aligned outside the THz box. An external diode is recommended to be used. A beam splitter must be used to generate two light beams, the points must travel parallel to each other onto the first parabola. The two beams must arrived on the edges of the first parabola. If each feet of the metallic plate is at the right height, the two beams should cross at the end of the last parabola at the same height they were before they enter the system of parabola.

Once the metallic plate is aligned, the plate can be place in the THz box. A pyroelectric camera that can detect THz must be used to visualize the beam. There are only 2 liberty degrees than can be used to obtain the smallest and most intense

THz focal spot. The first one is the angle between the first parabola and the THz beam direction, the second one is the position of the plate in the plane of the table. Adjust the angle, then the position to obtain the smallest and most intense THz beam on the camera. Note that you may need to use Si filters to attenuate the beam and avoid saturation on the pyroelectric camera.

2.4 Electro Optical sampling implementation

2.4.1 Data Treatment

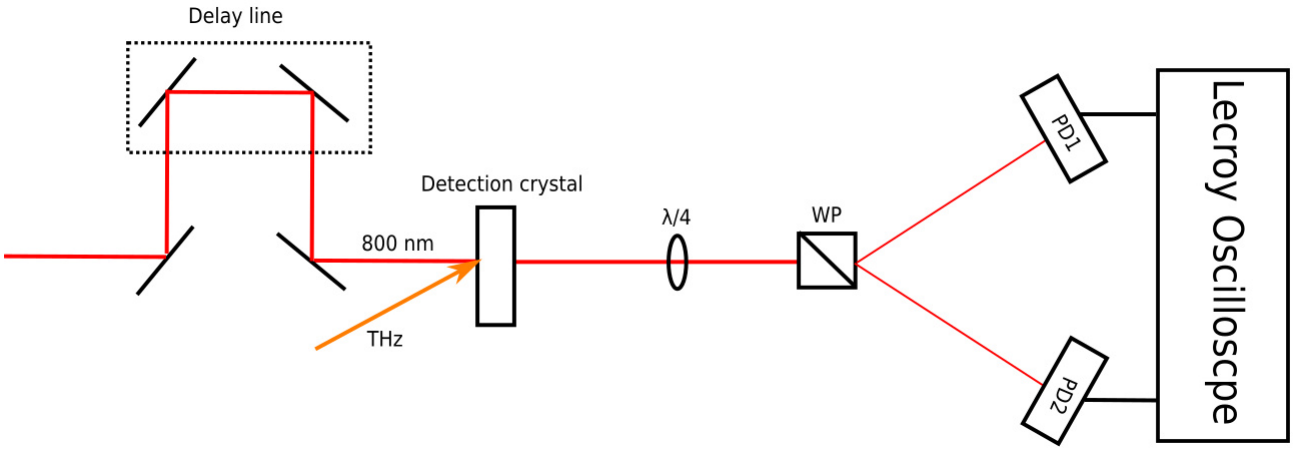

Figure 2.9: Experimental setup used for the Electro optical sampling. THz and the visible light are shown not colinear for clarity. PD1 and PD2 are photodiodes. WP is a Wollaston prism. $\lambda/4$ is a quarter wave blade.

I will present the case where the probe is taken from the MIRA with repetition rate of 78 MHz. Light was obtained using fast-photodiodes (rising time around 1-2 ns). The photodiodes were connected to two different channels of a Lecroy Oscilloscope which was used for data acquisition. The oscilloscope was triggered on a 1kHz basis with a signal coming from the laser timing tool. The experimental set-up is presented in Fig. 2.9 Raw data are presented in Fig.2.10:

As the THz repetition rate is 1kHz only one of the probe pulse will be modulated. The window of the scope is centered on the pulse which is in time overlap with the THz, this pulse is circled in Fig.2.10. This pulse can be found as there is still 800 nm that follows the THz path but have not been transformed. This leak is removed by placing a filter (a piece of paper, Si wafer, Teflon block). However, there is still a small part of it that is shined by reflection in the THz box onto the photodiodes. Such reflections are difficult to completely remove and explained why the circled pulse is a bit more intense than the other ones. When the THz pump and probe are at 0 delay the signal of one photo diode is decreased while the other one increased as predicted in equation . An example of what one should expect is presented in Fig. 2.11:

I will now explain how the data are refined from the raw data to the electric field. The time position of each peak is determined automatically. Anything above half the peak value is labeled as a pulse. Then, a fixed value is used to extend the pulses. The background for each pulse is automatically set-up as well by shifting and reducing the obtained window. The pulses and backgrounds automatically found are presented in Fig. 2.12:

From the pulse range detected automatically with the method explained above, the pulse is integrated to obtain its intensity. The central pulse which is the one modulated by the THz is normalized by the mean of the integrated value of peaks before and after. This is done to take into account shot to shot variation and increase signal to noise ratio.

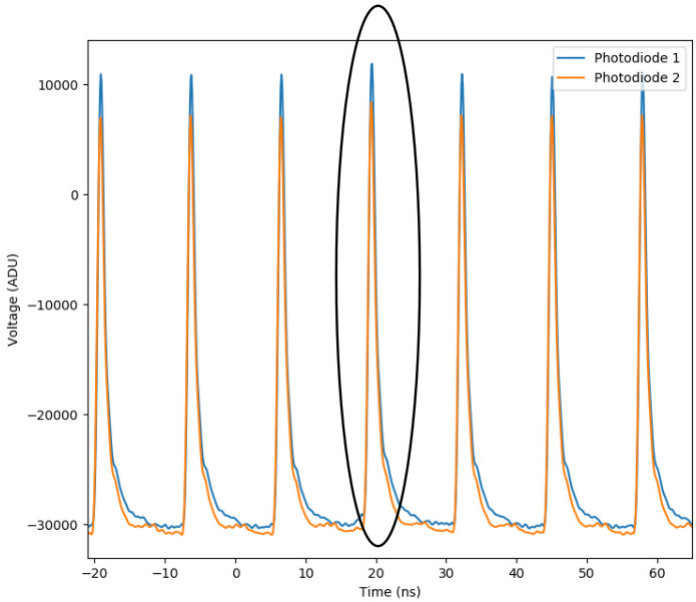

Figure 2.10: Raw data obtained from the oscilloscope showing the two channels. The peak circled is the peak which overlap in time with the THz pulse and will be modulated by the THz.

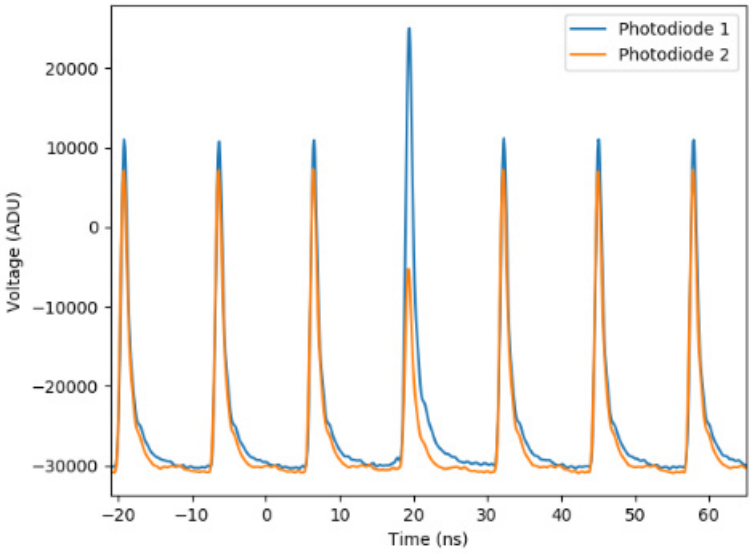

Figure 2.11: Raw data just as Fig.2.10 but THz and probe coincide in time.

This is done for both photodiodes independently. The EOS signal is then calculated from both diodes and the Electric field can be recovered taking into accounts the crystal non linear coefficient. An example of field treated using such method is presented in Fig. 2.13.

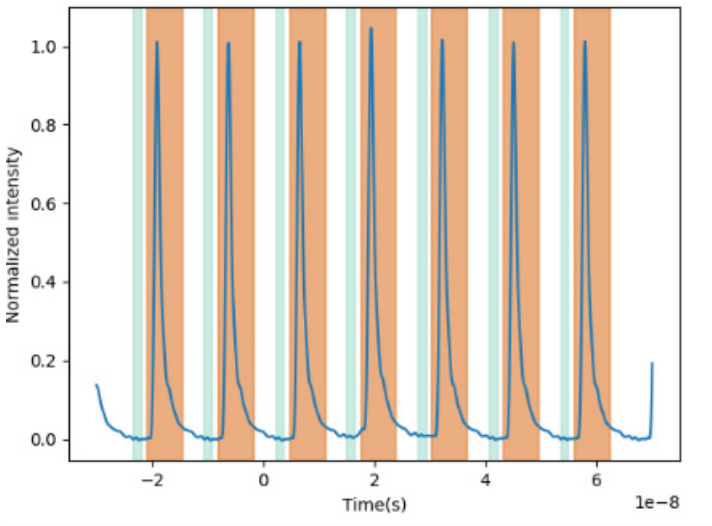

Figure 2.12: Raw data with the pulses automatically found. The orange background represents the pulse and the green one represents where the background is taken.

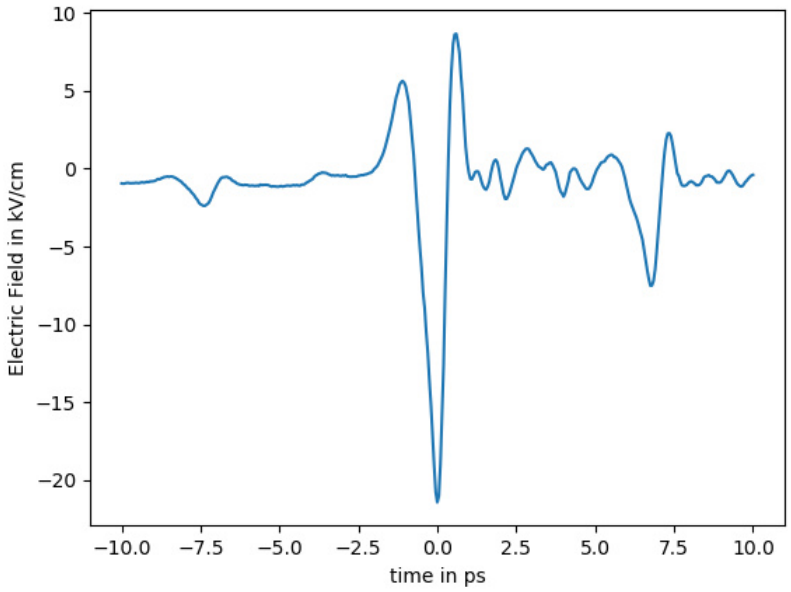

Figure 2.13: Example of a field measure using our EOS set-up and data treatment.

2.4.2 Impact of a broadband source on the EOS detection

No fs laser are perfectly monochromatic and show a broad band spectra. In our case, we are using a mode locked laser from an optical oscillator, it presents a spectra which is represented in Fig.2.14:

From Equation A.26 the wavelength of the probe pulse is important and therefore the broad band spectra of the probe might alters the signal.

In Fig. 2.15 is plotted the results of Eq.A.26 for different wavelength. As expected the E_{max} value i.e. the electric field value where $\frac{\Delta I}{I} = 1$ is shifting depending of the

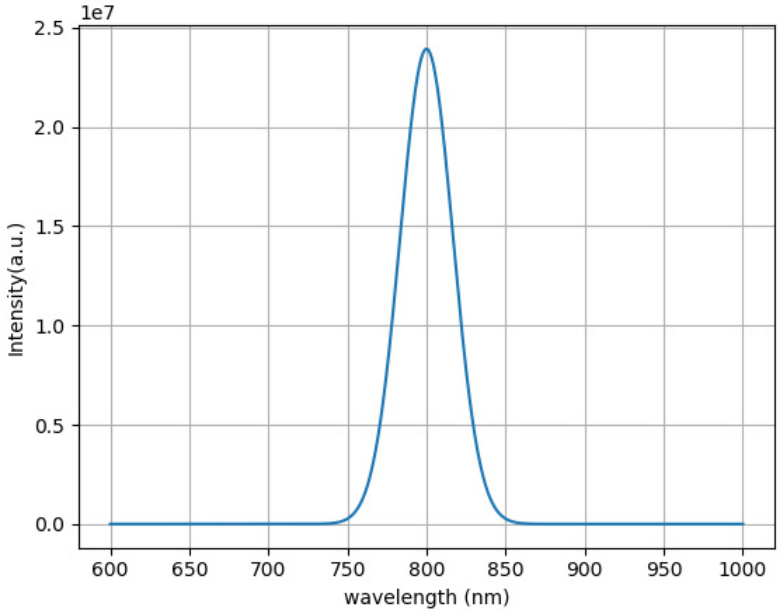

Figure 2.14: Spectra from our oscillator source which FWHM is 40 nm

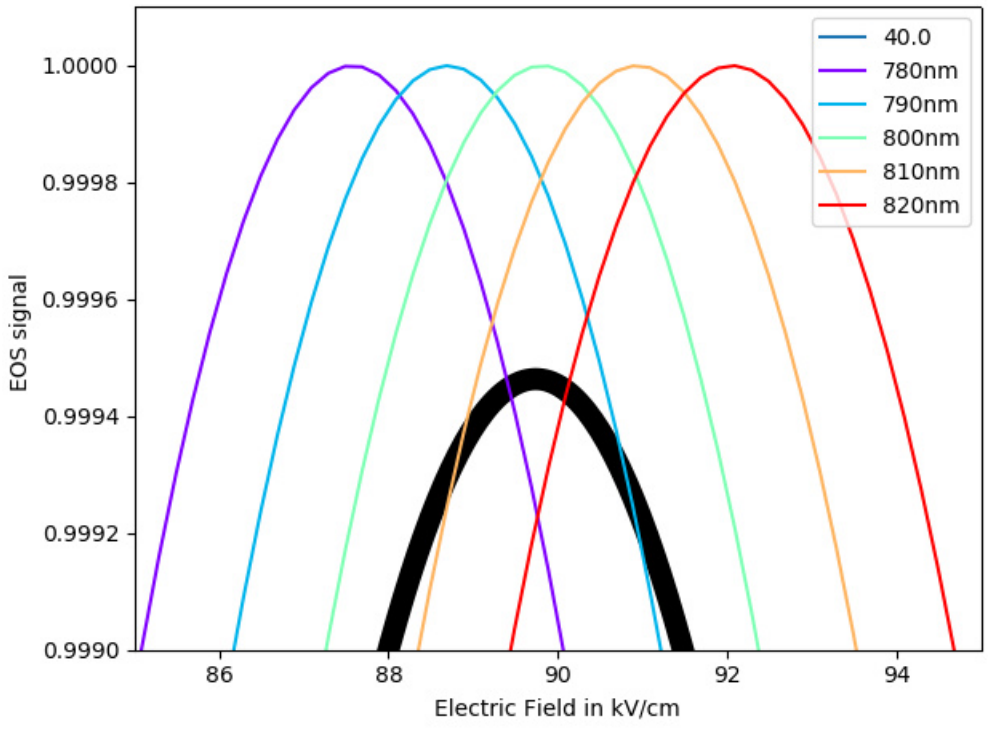

Figure 2.15: Full lines are representing different signal values in function of the electric field for different wavelength. Dashed lines is the integrated value obtain following the spectra show in Fig 2.14

wavelength is changing. In dashed line is plotted the mean value using a Gaussian probability law over the wavelength following the spectra show in Fig.2.14. The value

is almost not modified in this case.

In fact, the value begins to change for a spectra with FWHM of around 200nm (white light) which is represented in Fig. 2.16:

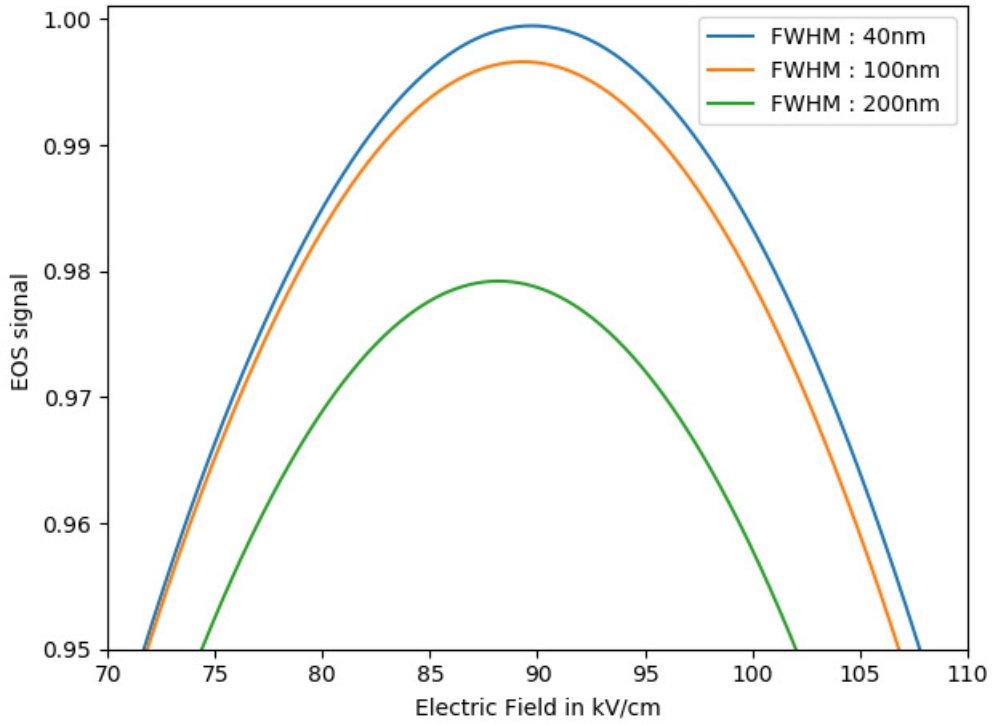

Figure 2.16: Integrated signal for the same central wavelength but with different dispersion.

To conclude, the impact of broadband spectra of 40 nm bandwidth is of the order of 0.001. Even when using white light with spectra going from 400 to 1200 nm the effects is a displacement of maximum electric field and a diminution of the maximum signal that you can observe. As such, any light can be used to do Electro Optical sampling measurements.

2.5 EOS Imagery

When dealing with intense THz radiation source, characterization of beam waist and energy are important. Standard EOS allows to characterize the intensity of the electric field and the spectral shape as well. However, you cannot measure the beam waist. EOS imagery is a simple trick that allows this measure. This technique has been used by Wu and al. [56] and we propose here an adaptation to our experimental set-up.

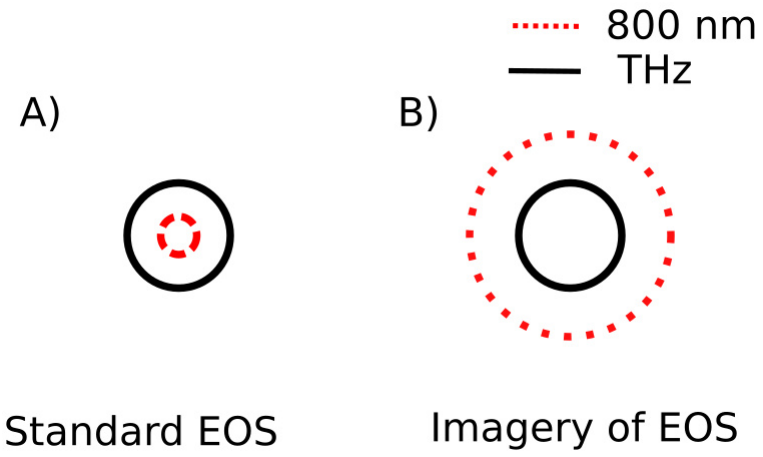

Figure 2.17: A) The probe beam is smaller than the THz beam ending with a full change in the polarization. B) The probe beam is bigger than the THz, only the part where they overlap see a change in the polarization.

In standard Electro optical sampling the beam is smaller than the size of the THz focus. Then, the THz will change the whole polarization of the beam which ends up in a change of intensity for the whole beam using EOS.

However, with EOS imagery, the probe is bigger than the THz beam. Therefore, only the part overlapping with the THz beam will see a modification of polarization and therefore a modification of intensity which will be spatially dependent. Analyzing this spatial dependence will allow us to characterize the size of the beam. Fig 2.17 is resuming the difference between the two EOS.

2.5.1 Electro optical sampling Imagery Set-up and repetition rate

The experimental set-up is presented in Fig. 2.19, note that we used a set of lenses to avoid diffraction of the probe through the hole of the parabola. This magnifying effect need to be taken into account when analyzing the images. In order, to quantify the magnifying, a calibration must be realized. A point was taken as a reference on the image of the camera (in our case the edge of the crystal) and then moved by a precise distance, we then compare it to the observed displacement to compute the magnifying effect.

Usually, we are using an high repetition rate probe to increase the signal to noise ration when dealing with standard EOS. In the case of imagery this is not a good option. Indeed as show in Fig. 2.18 only 0.1% of the shots of the probe are synchronized

with the pump. Using an oscilloscope as the detector will not have any impact of the measurement because the integration window is really small. However, using a camera which has a much bigger integration window will cause problem. As integration is basically a sum, the signal will be averaged in the noise. Therefore, there is a need to have the repetition rate matching for both pump and probe by either using an optical chopper or to change the probe and use a leak from the optical pump of the THz.

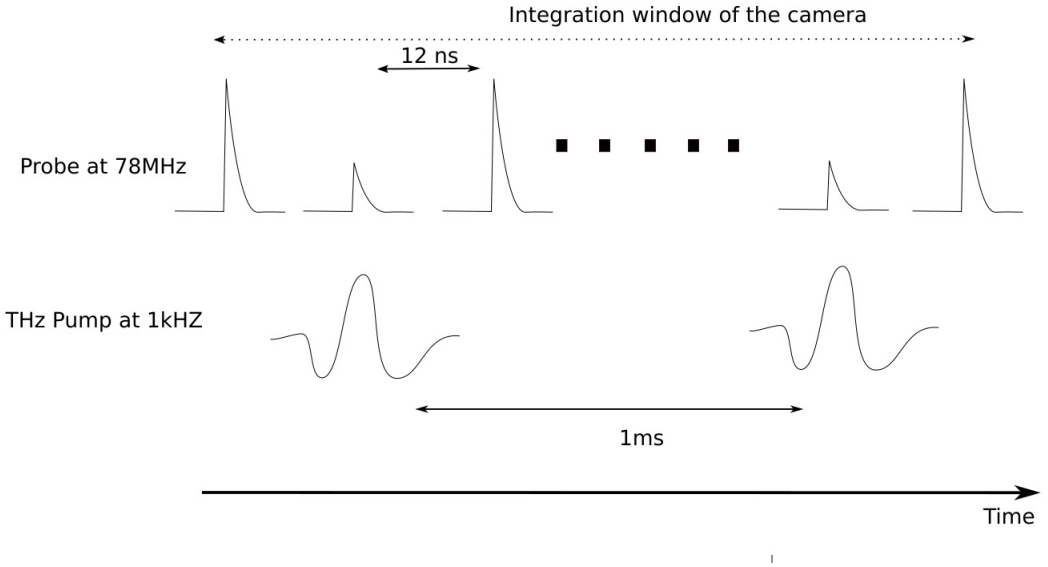

Figure 2.18: Figure showing the temporal overlap between the pump and the probe in a case where the repetition rate of the probe is greater than the one of the pump. The dot line represents the time integration of the camera.

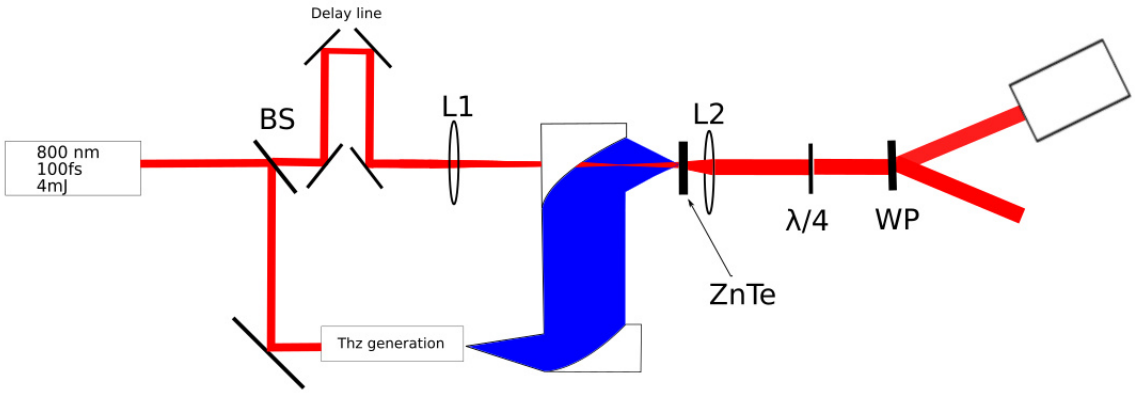

Figure 2.19: BS : Beam Splitter, L1 and L2 : convex lenses, WP: Wollaston Prism. The full beam is going through BS to have two branch, the first one is to generate THz : the pump, the other one serves as probe. THz beam is then collimated and refocused by Parabolic mirrors onto the ZnTe which is our EOS crystal. The probe beam goes through a delay line to see the THz beam at different timings. Here, we used a set of lenses to avoid diffraction of the hole of the parabola. Finally, once the beam is collimated, the probe is going through a quarter-wave blade then through a Wollaston prism. Only one part of the beam is detected by a Camera.

2.5.2 Data Analysis

To obtain the THz electric field spatial dependence, each pixel of the camera must be treated independantly as a single EOS trace. Indeed, the usual EOS measurement is taking the modulation of the central pixels. As such looking at the modulation of every pixel is a good trick to recover the THz electric field spatial dependence. Because of the repetition rate used, the reference must be taken at negative time delay as the pulse is not modified in that case. Taking the relative modulation over this image at each time delay allows to see the picture of the THz evolving in time. An example of the time and spatial evolution obtain through EOS imagery is presented in Fig.2.20

We can observe the spatial modulation of the THz beam. The ring that can be observed can be explained when the THz field is high enough to make the modulation higher than one in the Electro optic crystal.

2.5.3 Beamwaist determination

Once data has been treated, one can find the profile of the beam. Usually, the beam waist is depending of the intensity. With EOS, only the field is measured, therefore the computation of the square of the beam is needed. To compare with other instruments which integrates over time, the integration over the whole set of image is required. Results are presented in Fig.2.21 at best focus using the beam from the USP.

Beamwaist has been measured at different positions of the ZnTe to find the place were the THz beamwaist is the smallest. Fig. 2.22 presents the measured fwhm at different position of the ZnTe. Smallest beamwaist obtained is 0.6 mm in both directions (this THz beam was generated with the USP).

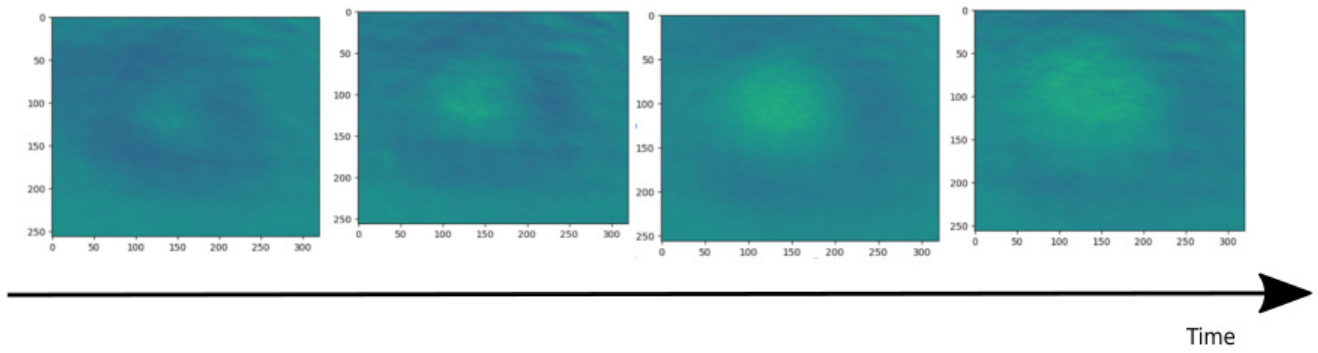

Figure 2.20: Images taken by the camera after different delay between the probe and the THz pulse.

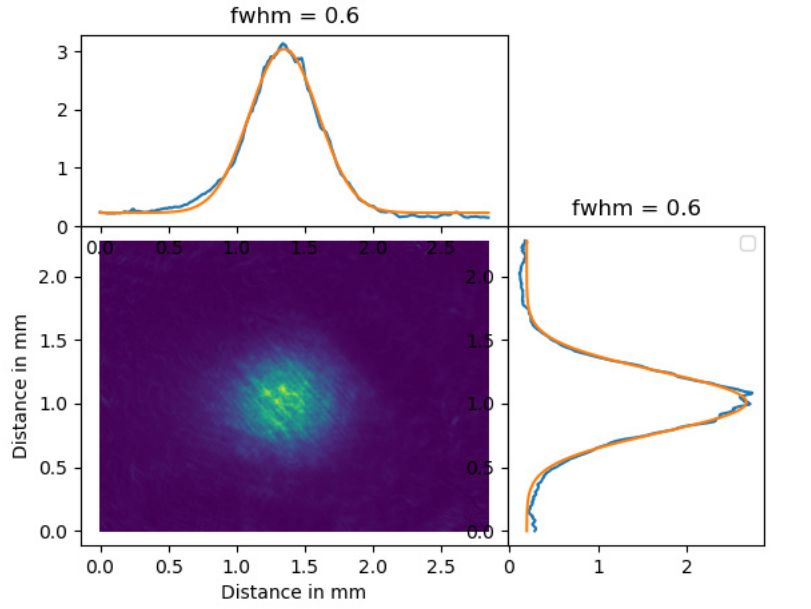

Figure 2.21: The central image is obtained by integrating over time the square of the field. The two 1D plots represents the fit using a gaussian profile along one axis. Full width at Half Maximum is given in mm.

2.6 THz Beam Characterization

.

To be able to use the source in experiment a good characterization of the pulse mandatory. In this section, I will present the characterization of the TeraHertz source I built. All the characterizations presented in this section were measured using the ELITE in this configuration: 4 mJ at 1 kHz repetition rate, pulse centered at 800 nm with 100 fs pulse duration. I will first present the size of the THz spot after the $LiNbO_3$ crystal and its divergence as well of how I measured it. Then, I will present the focal spot obtained after the 3 parabolic mirrors and finally I will present the electric field measured via Electro Optical Sampling.

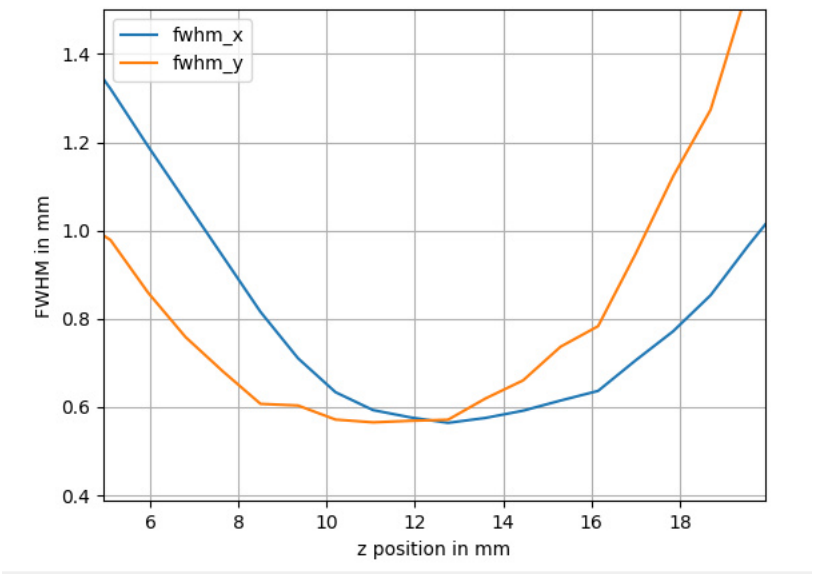

Figure 2.22: FWHM in both directions in function of the position of the ZnTe

I used a Pyrocam III from Spiricon to measure the spot size at the exit of the LN crystal. The camera was fixed on a three fold axis motorized stage. A scheme of the experiment is shown in figure 2.23. The camera is moved in the direction of propagation of the THz beam.

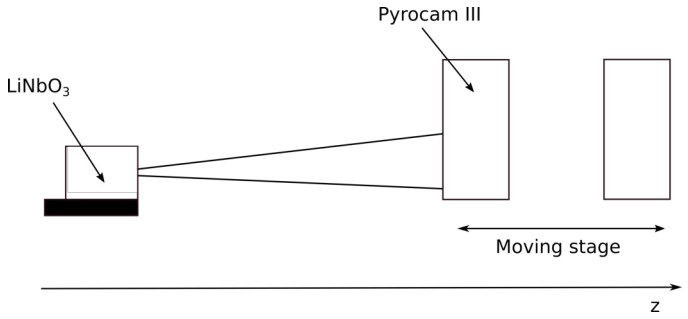

Figure 2.23: In order to monitor the changes in the horizontal and vertical direction, the camera is moving along the propagation z axis.

A first picture has been taken 5 mm after the generating crystal as presented in Fig2.24. The THz spot size is 2.1/2.0 mm at the exit of the crystal for our set-up.

By moving the camera along the propagation axis, the divergence of the beam can be extracted. First, I will define the divergence of a beam, this is the angle beam between the propagation direction and the direction chosen. Therefore there is two divergence one is horizontal and the other one is vertical. The Fig. 2.25 represents one of the divergence :

We can write the divergence as :

$$sin\theta = \frac{l}{2z} \tag{2.3}$$

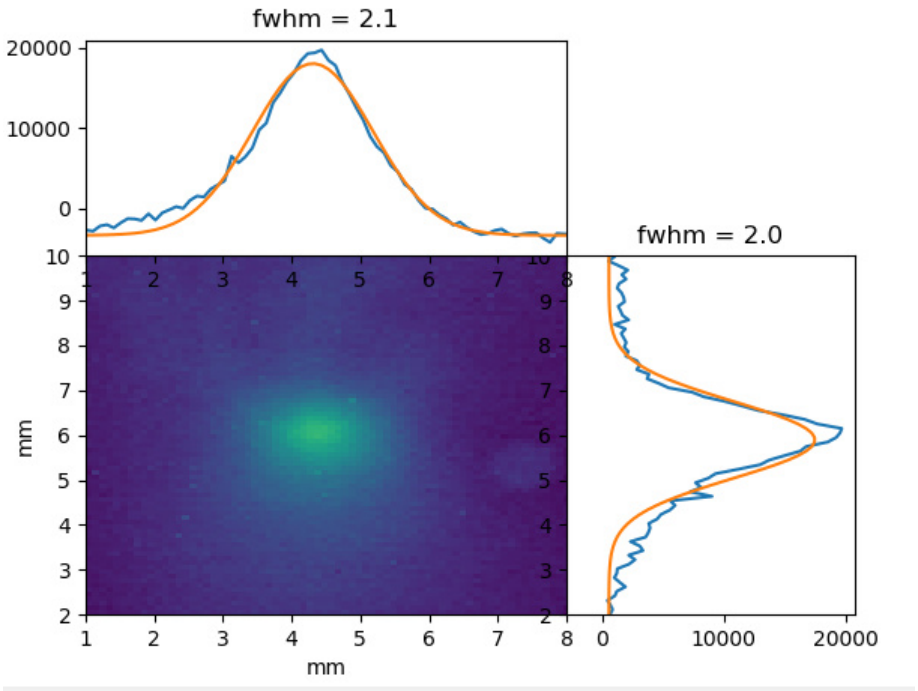

Figure 2.24: Picture untreated of the camera. Curves on top and on the sides are respectively vertical and horizontal projections of the beam. The FWHM presented is obtained from a Gaussian fit of the data.

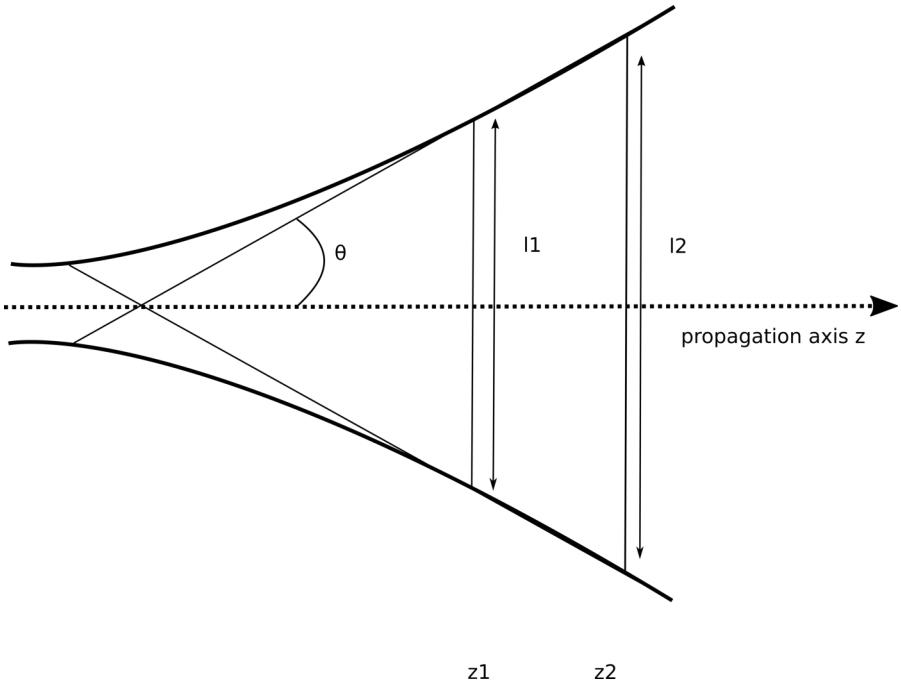

Figure 2.25: The divergence is the angle between the propagation axis and the real direction of propagation.

l is the FWHM of the beam. For laser the divergence is small enough to approximate $sin\theta$ in θ. Therefore, one can write :

$$l(z) = \frac{\theta}{2} z \tag{2.4}$$

Extracting the spot size for multiple positions as a function of z the distance between camera and crystal, I can measure the divergence of the beam from experimental data. The results of this experiment are plotted in Fig.2.26.

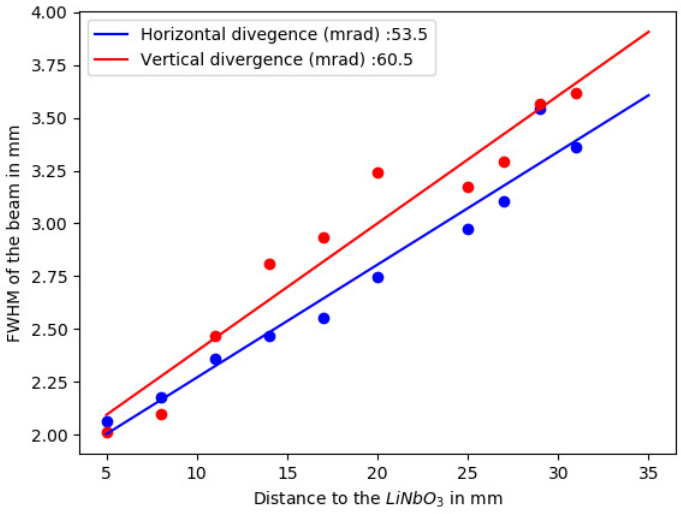

Figure 2.26: Extracted divergence from the different images for the two beams dimension.

The divergence of the spot is roughly 60 mrad in both direction. In comparison, the value obtained by Hirori et al.[39] was of 52 mrad. So the divergence of our spot is very close to their value.

Our experimental set-up was designed to obtained the most intense electric field. Therefore obtained the smaller THz spot is required. In order to do so, we use a set of 3 parabolic mirror. The low divergence of our beam is mandatory for such a set-up as it will induce optical aberration on the focal spot after the system of parabola. The first two parabola are used to increase the THz spot by a factor 10. Indeed, the spot size is inversely proportional to the beam diameter. This allows to go as close as possible to the diffraction limit. To help align the parabolic mirror, a metallic plate was designed with the help of our workshop. A picture of this plate is show in Fig.2.27. This plate freeze a large number of free parameter. Only position, angle and height are available for the alignment for an easier alignment.

The THz spot size was measured using the Pyrocam III from Spiricon after the system of 3 parabola. The spot size is 0.8 x 0.9 mm as presented in Fig. 2.28.

This experiment was also conducted using Electro Optical Sampling Imagery for very close results using both GaP and ZnTe crystal.

Classic EOS was used for measuring the time-domain electric field. A Peak field value of around 800kV/cm was obtained as presented in Fig.2.29a). The EOS was measured with a 300 μm GaP (3 Si wafer were put onto the beam path) and 500 μm ZnTe (7 Si onto the beampath). For clarity, only the GaP measure was shown but for it is exactly the same temporal trace in both cases. The spectra of the field is presented in Fig. 2.29b) in log scale. The frequency range accessible is 0 - 2.5 THz for this source.

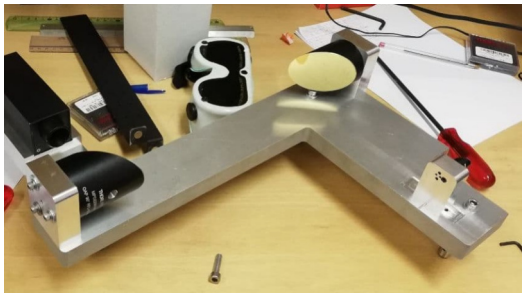

Figure 2.27: Picture of the parabolic plate used for THz alignment.

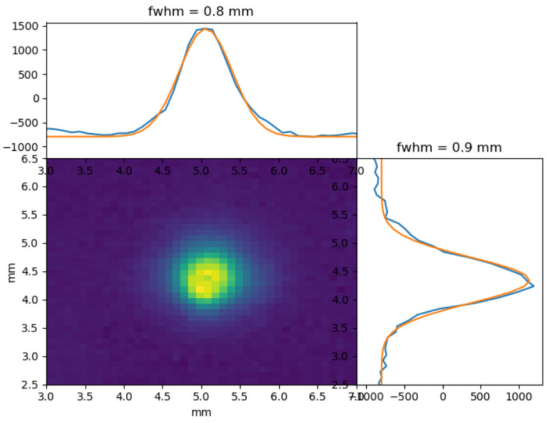

Figure 2.28: Image of the THz spot after the third parabola.

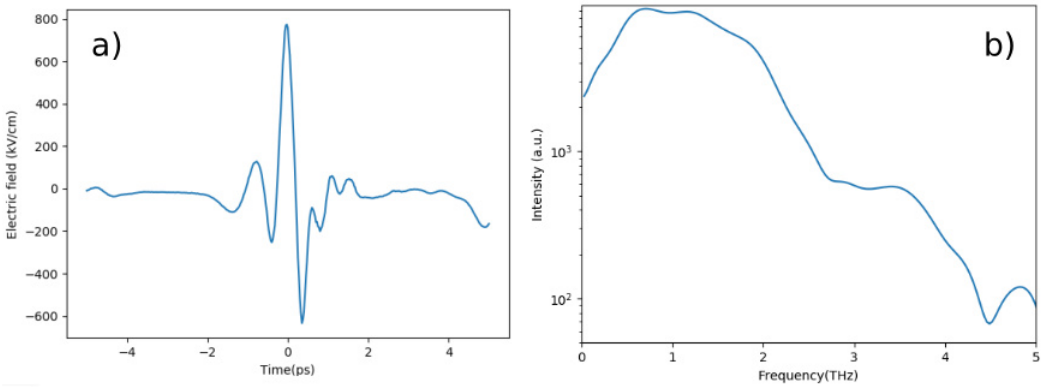

Figure 2.29: a) EOS trace obtained with a 300 μm GaP crystal, 3 Si wafer were placed on the path of the THz beam. b) Fourier Transform of the EOS trace.

The energy of the pulse can be extracted directly from the measure of the electric field.

$$U = \int \frac{1}{2}\epsilon_0 E^2(V) dV = \int\int\int \frac{1}{2}\epsilon_0 E^2(x,y,t)\, dx\, dy\, cdt \tag{2.5}$$

U is the energy, ϵ_0 is the dielectric permittivity and c the speed of light. The speed of light is here to take a volume with last direction being c times the time interval. We consider that the electric field has the same shape everywhere in the spot so we can split the integrals in two :

$$U = \frac{1}{2}\epsilon_0 \int E(t)cdt \int\int S(x,y)dx\,dy \tag{2.6}$$

With S being the Gaussian beam profile at the focal spot. Applying this equation on our experimental data, we obtained 4.5 μJ.

2.7 THz pulses generation efficiency with different pulse duration

In this section, I will present the characteristics of THz pulses generated from different pulses duration. It has been demonstrated by Blanchard et al. [57] that the pulse duration of the generation beam is of importance in the THz generation efficiency. In this work, they measure only the THz energy for a pulse duration varying from 100 to 300 fs, this is presented in Fig.2.30 .

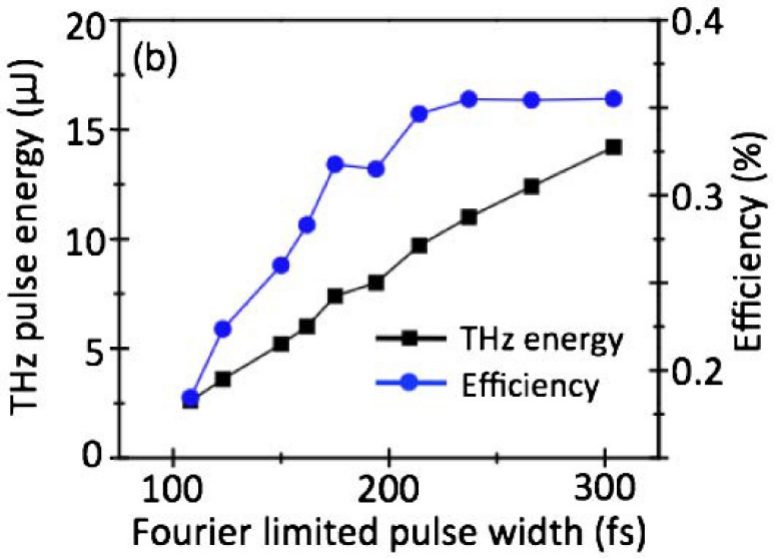

Figure 2.30: THz energy and efficiency in function of the Pulse duration adapted from [57]

We have access to 3 different pulse duration in our laboratory. We used those 3 different pulses duration to study the effects of the duration of the pump on the THz generation. As each cavity posses a different design the energy output of each cavity is different, the USP cavity has an energy of 2mJ/pulse, the Femto Cavity has an energy of 3.5mJ/pulse and the Pico cavity has an energy of 2.8mJ/pulse. The waveform were obtained using EOS detection. The results obtained are presented in Fig. 2.31

The THz waveform are very different for each pulse duration. The pulse generated with the USP cavity has an electric field value of 150 kV/cm, the pulse generated with the Femto cavity is 410 kV/cm and the pulse generated with the Pico Cavity is 310kV/cm. While the difference between the Femto and Pico cavity is mainly in the symmetry of the pulse, oscillations can be observed in the pulse generated by the USP(see Fig. 2.31a and b). The pulse energy and efficiency are respectively for the USP, Femto cavity, Pico cavity : 90 nJ and 0.004% efficiency, 0.96 μJ and 0.03% efficiency, 1.1 μJ and 0.04% efficiency (see Fig. 2.31c). The energy were obtained from the THz waveform using the method explained in the previous section. The beamsize was measured using the PyrocamIII for each pulse giving similar shape of 800 μm for each pulse.

The electric field value is the smallest with 150 kV/cm for the USP (shortest pulse duration) as expected from the results of Blanchard et al. For optimal THz generation,

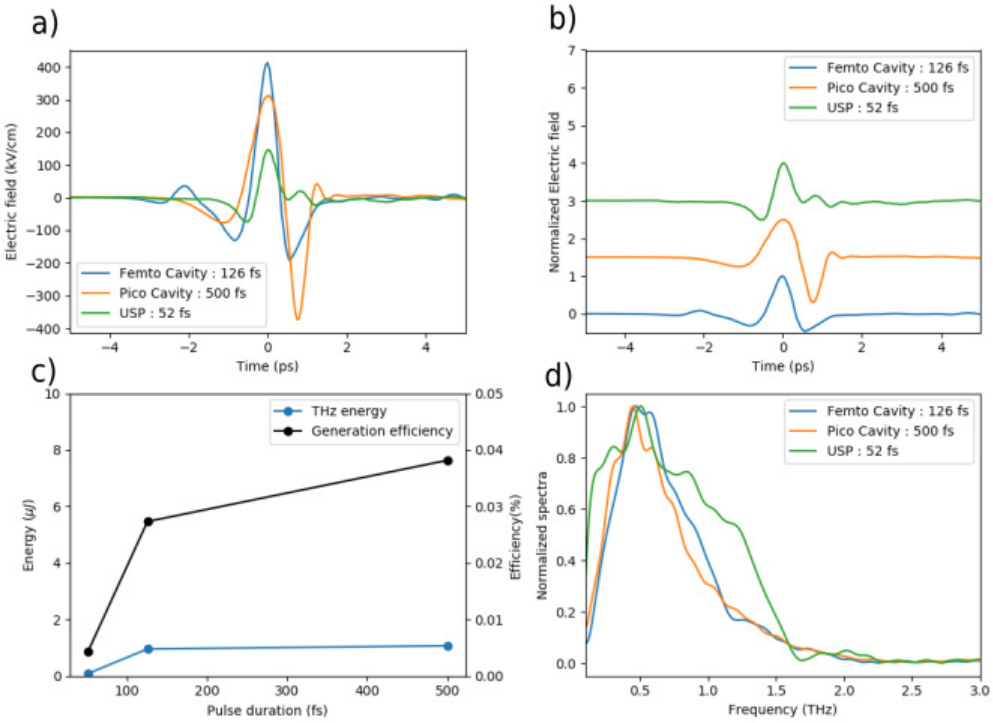

Figure 2.31: a) 3 THz waveform in the time domain for 3 pulse duration : 52fs, 126 fs and 500fs b) Same THz pulses in the time domain. c) THz energy and conversion efficiency as function of pulse duration. d) Fourier Transform of the THz waveform.

the THz beam has to be focused on the $LiNbO_3$, the instantaneous power is much more important with the USP than with the other cavity because of the pulse duration. Using USP damages were observed on the $LiNbO_3$ which is explained by this instantaneous power being higher Therefore, this electric field value seems to be a maximum accessible with this pulse duration of the USP.

While the electric field value is more important in the case of the Femto Cavity than for the Pico Cavity, the energy of the pulse obtained from the Femto Cavity is smaller than for the one generated with the Pico cavity. The efficiency is also better for the pulse duration of 500 fs. This is in agreement with the results of Blanchard et al. as the conversion energy is better with a 500 fs generation pulse than for the one generated with a 100 fs pulse. Our results show that the electric field and the shape is better suited for single cycle THz electric field with pulse of 100 fs duration.

The efficiency and energy of our pulses are lower than the ones from Blanchard et al. One of the difference between their work and ours is the way of obtaining the energy. Blanchard et al. measured the energy from a pyroelectric detector while we computed directly the energy from the Electro Optical sampling trace. The computation was derived as follows :

Hirori et al.[46] computed the energy of their pulse to be 2 μJ using the equation of Reid et al.[58] which is :

$$W_{\mathrm{THz}} = \frac{\tau A \epsilon_0 \left| E_{\mathrm{THz}}^{\mathrm{pk}} \right|^2}{2} \tag{2.7}$$

τ is the 1/e (electric field) THz pulse width, A is the area of the THz beam, $E_{\mathrm{THz}}^{\mathrm{pk}}$ is the peak radiated THz field. This equation is mostly valid for single cycle electric field. We used this equation on our experimental data of the femto cavity and obtain 1.3 μJ instead of 0.9 μJ which is an overestimation of 44%. Moreover, Hirori et al. found that the energy measured using their pyroelectric was around 3 μJ which is again an overestimation. This explained the overall lower energies and efficiency observed in comparison to the one from Blanchard et al. However, the shape of our data is close to the one obtained by Blanchard et al.

The associated spectra are presented in Fig. 2.31 c). The spectra is broader in the case of the short pulse generated with the USP. There is a significant increase of the spectra in the 0.7-1.5 THz region in comparison the two other pulses. The spectra obtained from the Pico cavity is narrower and red-shifted than the one of the Femto cavity. As such, for a THz-TDS purpose short pulses are the one to used.

To conclude this study, the choice of the pulse duration is very important to determine the characteristics of the THz generated. A short pulse can be used for broader spectra. A long pulse will increase the energy in each THz pulse for a lower electric field. The pulse from the Femto cavity is intermediate and shows the better single cycle as well as the strongest electric field value. We choosed the pulse generated from the Femto cavity over the one from the Pico Cavity for two reason. First, the strong electric field obtained with the Femto cavity allows to induce non-resonant non linear effect. Second, the pulse from the Femto cavity can be used as a probe for THz pump probe experiment with a better time resolution than if the Pico cavity was used.

2.8 Characterization of a metallic grid based set of THz polarizer

To control the THz electric field in experiments optics have to be used similarly to experiments using visible wavelength. However, visible light optics cannot be used directly at TeraHertz wavelength and specific optics have to be designed. We used a set of metallic grid TeraHertz polarizer from Tydex. I will first explained how the metallic grid can be used as a polarize for THz wavelength. Then, I will present the characterization realized at Rennes using our THz source.

There has been a lot of work invested into the search of good THz polarizer. One of the best technologies is based on metallic grid wires.[59]. The metallic wires are grown, usually Al, on a substrate which isn't absorbing the THz. Each wires is grown parallel to each other along a chosen direction. The transmitted part of the incident TeraHertz electric field corresponds to the one perpendicular to the wires direction. Fig.2.32 adapted from [59] presents a view of the optic at the wire scale :

As our THz source is linearly polarized, we want to use a couple of THz polarizer to control the THz intensity on our sample. The first polarize is mounted on a precise rotating mount to control the polarization. The second one is placed afterward in a fixed direction which is parallel to the table plane. By tweaking the direction of the first THz polarizer, the THz will follow a Malus Law, this implies the following dependence:

$$I_0(\theta) = cos^2(\theta) \tag{2.8}$$

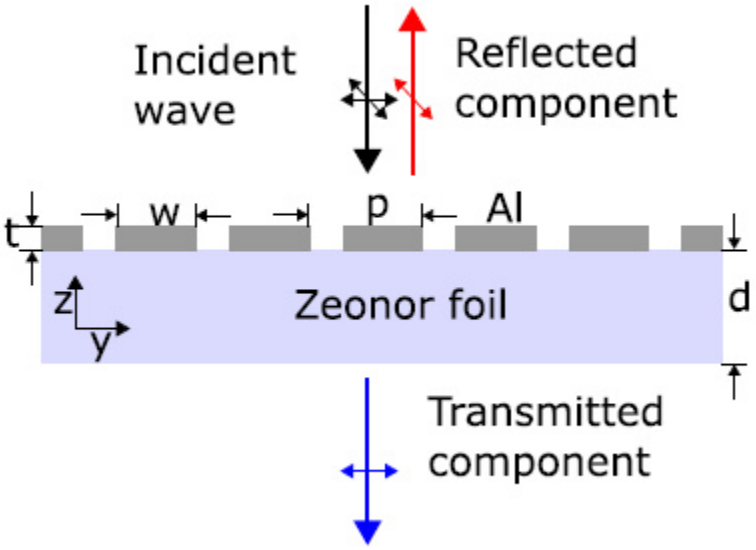

Figure 2.32: Metallic grid THz polarizer set-up, figure adapted from[59]

We used Electro Optical Sampling to measure the THz electric field at different angle between the two polarizers. The results are presented in Fig.2.33

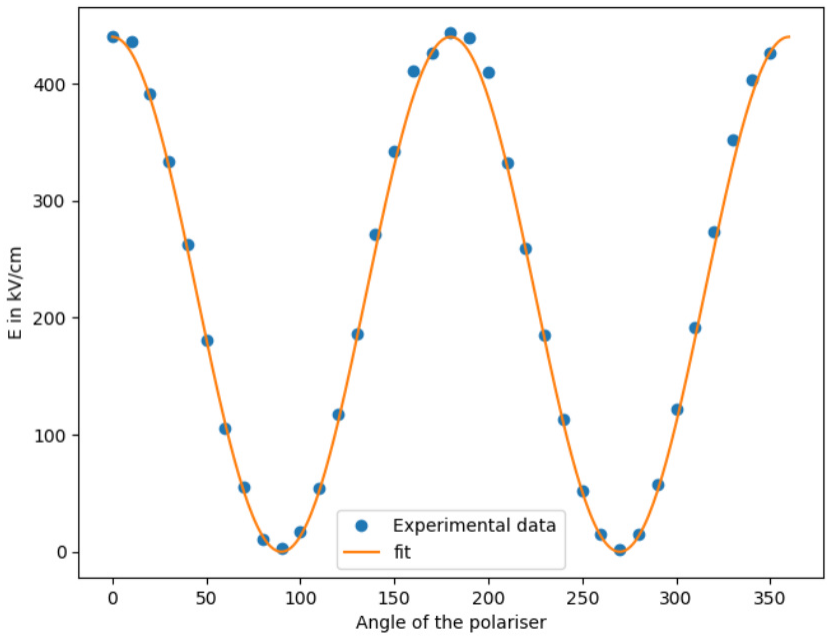

Figure 2.33: THz electric field at different angles between the two metallic grid wires polarize. The points are the experimental data while the full line is a cos^2 fit.

The THz electric field is following the Malus Law as expected with the use of 2 polarizer. While those polarizers are fully functional, the use of those polarizers implies a loss of around 10% on the THz electric field.

2.9 Validation of the THz source with two examples

In order to validate the THz source built, two experiment were conducted to reproduce results from the literature. First, the modulation of Second Harmonic Generation by the THz pulse and then an THz pump optical probe experiment at room temperature in V_2O_3 thin film. As those results are only here to validate the source, I will not get into much details of the physic beneath each results and will give more of an hand waving approach.

2.9.1 Second Harmonic generation modulated by the THz electric field in $\beta - Baryum\,Borate$ or BBO

Context and sample information

BBO is a crystal which crystallizes in the R3c space group. Those crystals are now widely used in non linear optic application. Most of Second Harmonic generation is generated using BBO crystal. Moreover, as Terahertz generation through two color plasma in air is using a BBO, a lot of research were conducted on the crystal by the community [5, 60, 61, 62, 63, 64]. The paper that was the most interesting for us was the one from Chen et al.[5]. In this paper, they used a Terahertz electric field to modulate the generation of Second Harmonic of the crystal, with a maximum electric field of 160 kV/cm generated through Optical Rectification in $LiNbO_3$ see Fig.2.34. This modulation was explained through four wave mixing in the sample a third order non linear effect.

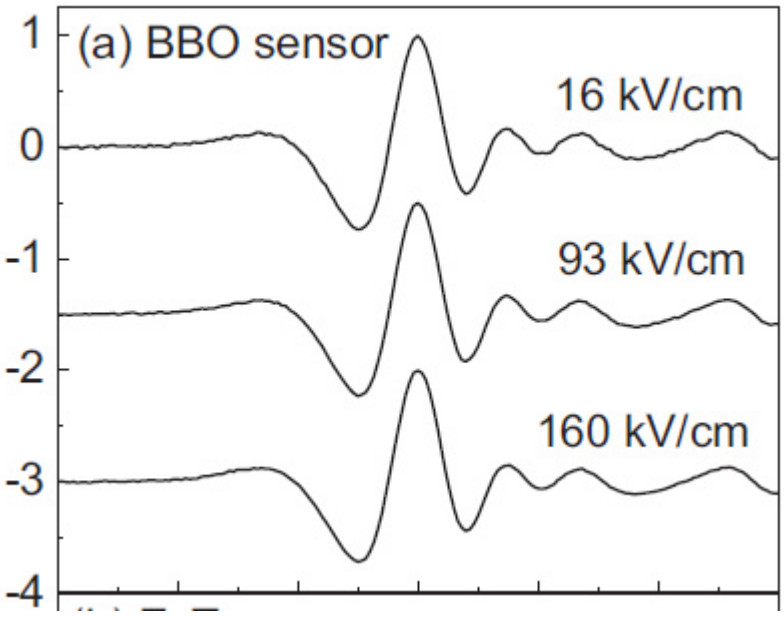

Figure 2.34: Modulation of the Second Harmonic by a THz electric field in function to excitation adapted from [5]

In the paper, they propose BBO as a new detector for intense Terahertz electric field in comparison with EOS crystal. Indeed, as explained in the previous chapter, when

reaching an high enough electric field, the polarization became to rotate and appears a smaller signal inducing a false spectra. However, this limitation is not present for detection through Second Harmonic Generation in BBO.

The aim of this experiment was to reproduce the data from Chen et al. and to extrapolate them using higher value of the Terahertz electric field, to check if there was any non-linearities. Moreover, this was a good starting point to understand the so called Terahertz Field Induced Second Harmonic or TFISH. The crystal I used was 2.5 mm thick BBO. This BBO was furnished by Light conversion to be used in a TOPAS for generating Second Harmonic. The face we used was (5 -8, -16) and was determined using an X-Ray diffractometer.

Experimental Set-Up

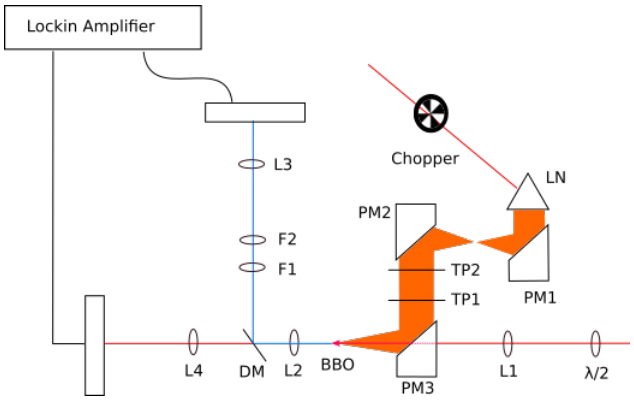

Figure 2.35: Experimental Set-Up we used: PM are for parabolic Mirror. L are concave lens : L1 is 150mm, L2 100m L3 and L4 are 50mm focal length. DM is for Dichroic Mirror, F1 and F2 are filters. $\lambda/2$ is an halfwave blade. PD1 and PD2 are photodiodes. TP1 and TP2 are two TeraHertz polarizer

A schematic of the experimental set-up is presented in Fig.2.35. The sample was put onto the sample position SP at the focal spot of the parabolic mirror PM3. I focused 800 nm light taken from the Elite (1kHz rep rate at 800nm with 80 fs of FWHM) onto the sample through the parabolic mirror in order to have focal length of both pump and probe to coincide spatially.

An half wave blade was put onto the probe path in order to maximize the generation of Second Harmonic through the sample.

The SH was reflected with a Dichroic Mirror (DMLP490 from Thorlabs) onto two filters a FESH0450 and FGB37 also from Thorlabs in order to filter remaining 800 nm. The signal was collected on a photo diode connected to a lockin amplifier. An optical chopper was used on the pump path at 500 Hz.

The crystal was placed onto an homemade rotating Sample Holder (see Fig. 2.36)

We checked before starting the experiment that the collected light on the photodiode was Second Harmonic generated by the BBO crystal. Data are presented in Fig.2.37.

Second Harmonic intensity is proportional to the square of the input energy :

$$I_{SHG} \propto E_{800}^2 \tag{2.9}$$

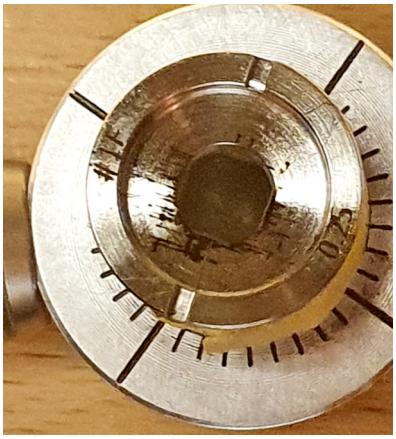

Figure 2.36: Photo of the sample holder

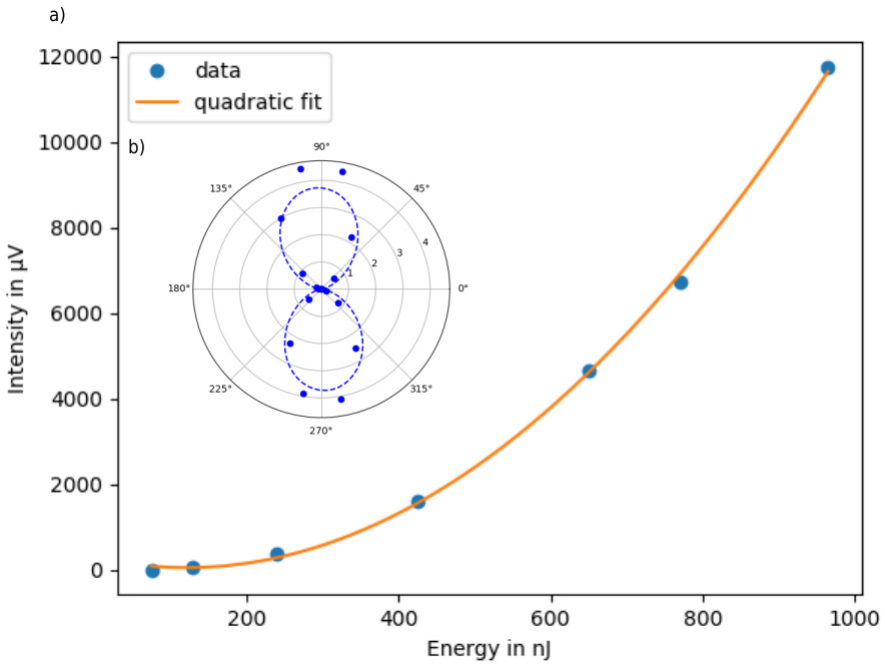

Figure 2.37: a) Power dependence of the SHG. b) Polarization dependence of the SHG.

Where E_{800} is the energy of 800 nm shine into the sample. The signal obtained in Fig.2.37a) has been fitted with a square function and is therefore perfectly quadratic. Moreover, phase matching conditions are imposed by the angle θ of the polarization of incident light with the crystal axis [26]. The phase matching condition equation is presented here :

$$\sin^2\theta = \frac{\frac{1}{n_0(\omega)^2} - \frac{1}{n_0(2\omega)^2}}{\frac{1}{n_e(2\omega)^2} - \frac{1}{n_0(2\omega)^2}} \tag{2.10}$$

Therefore, the signal is modulated by a $\sin^2$ function, this has been demonstrated on Fig.2.37b). We can therefore assume that the probe light measured was rightfully Second Harmonic generated from the BBO.

Experimental results

I first did an experiment using the electric field as an external parameter. I used a set of crossed metallic wire polarizer. The transmitted light going through the two polarizers follow the Malus Law [65] :

$$I = I_0 cos^2(\theta) \tag{2.11}$$

Where θ is the angle between the two polarizers. Controlling θ allows to control the value of the electric field. This set of polarizers have been tested before using Electro Optical sampling, the results are shown in Fig. 2.38 presenting a good adequation with Malus law. This allowed me to use them to control the electric field amplitude by setting the last polarizer along the electric field and changing the first one.

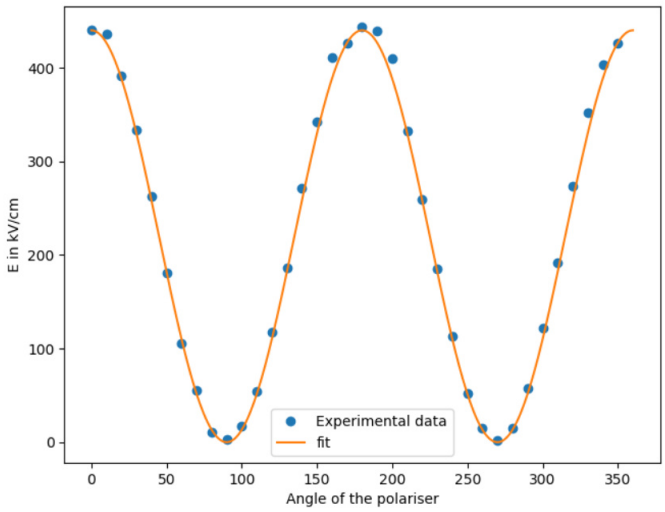

Figure 2.38: Maximum electric field measure with Electro optical sampling at different angle between the polarizers. The fit equation is Eq.2.11

In figure 2.39 is plotted the TFISH signal for different electric field. The signal diminished with the electric field until there is no more signal. In figure 2.40is represented the signal at different electric field values. There is a good adequacy between my data and the data from Chen et al.[5]. The waveform is the same at higher electric field indicating that the signal stays linear at higher electric fields that the values obtained by Chen et al.

The maximum of the absolute value of the signal depending of the angle between the polarizer is plotted in Fig.2.41a) . This signaled is following a cosine squared function. Therefore, we expect that the signal is linear with the electric field, indeed:

$$S(\theta)\,\alpha\,cos(\theta)^2)\,\alpha\,E(\theta) \tag{2.12}$$

Mapping the value in angle into the value in electric field, we can plot the Fig. 2.41b). This figure shows evidence of the linearity of the signal. Moreover, this linearity is the same that the one found in the literature which validates the THz Pump set-up. The remaining of this section will continue this study beyond the work of Chen et al.

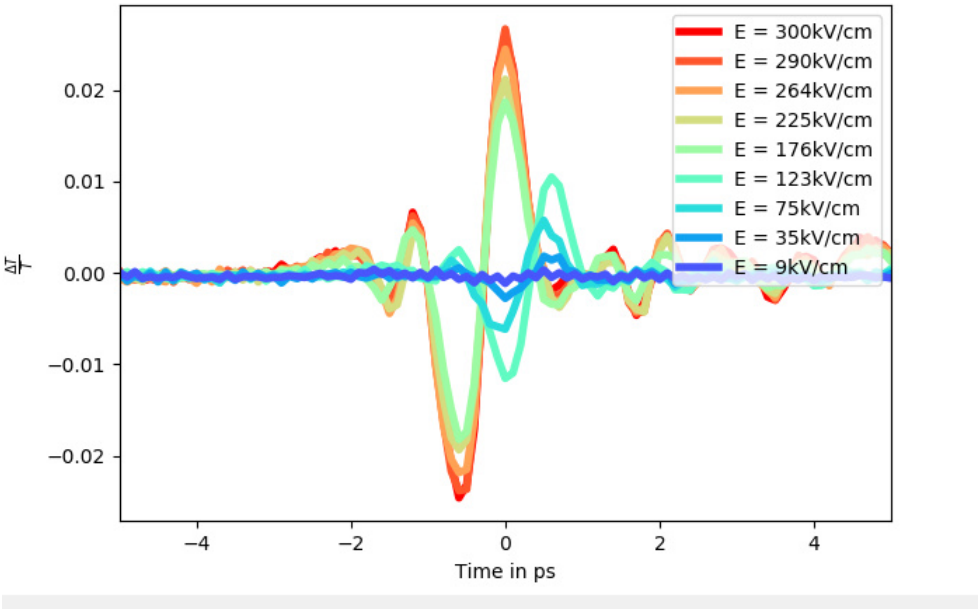

Figure 2.39: TFISH signal at different values of the electric field.

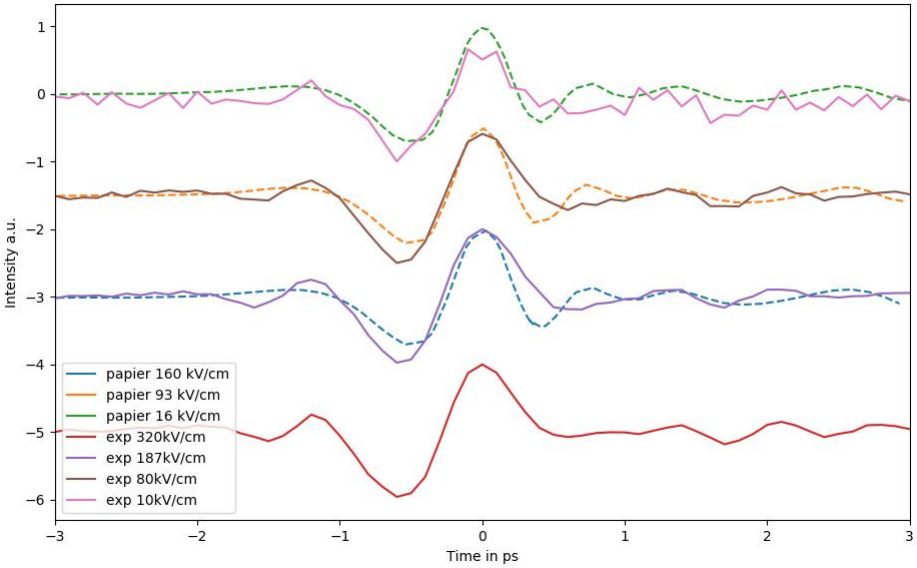

Figure 2.40: Normalized waveform of the signal for different value of the electric field. Dashed line are references from Chen et al. Solid lines are my work.

Polarization study

At longer time scale showed the appearance of another peak after the main one as shown in Fig.2.42.

In order to understand these two peaks, a polarization study has been done in addition of the electric fields measurement. Because, no TeraHertz halfwave blade were available in our lab, we turned the crystal using the rotating sample holder. To only measure the effects of the TeraHertz polarization with respect to the crystalline axis (the angle ϕ, an optical halfwave blade was used on the probe side to always generate

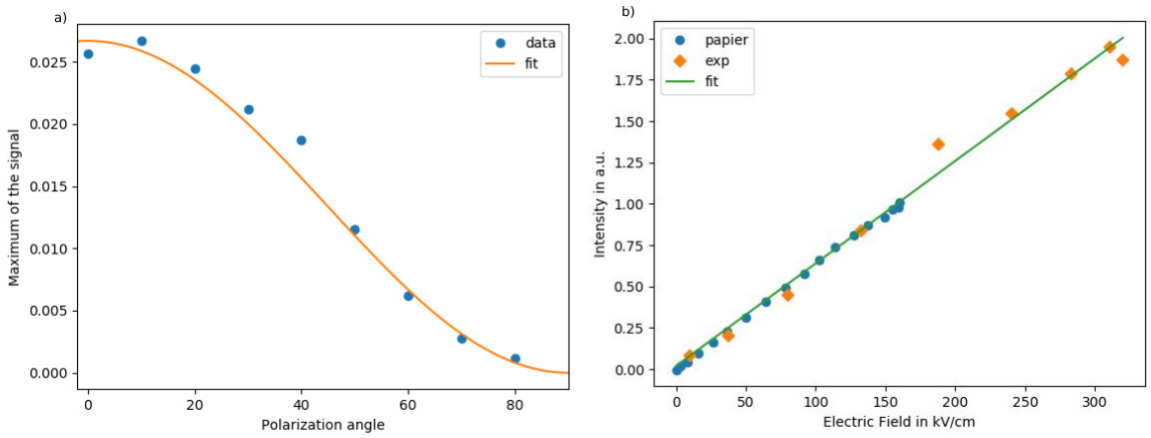

Figure 2.41: a) Maximum intensity of the signal plotted versus the angle of the crystal. The fit is a : $Acos^2(x)$. b) Maximum of the signal in function of the electric field. Blue dots are taken from Chen et al. Orange diamonds are the experimental values I obtained. I normalized my value so that the value at 160kV/cm is equivalent to the one of Chen et al.

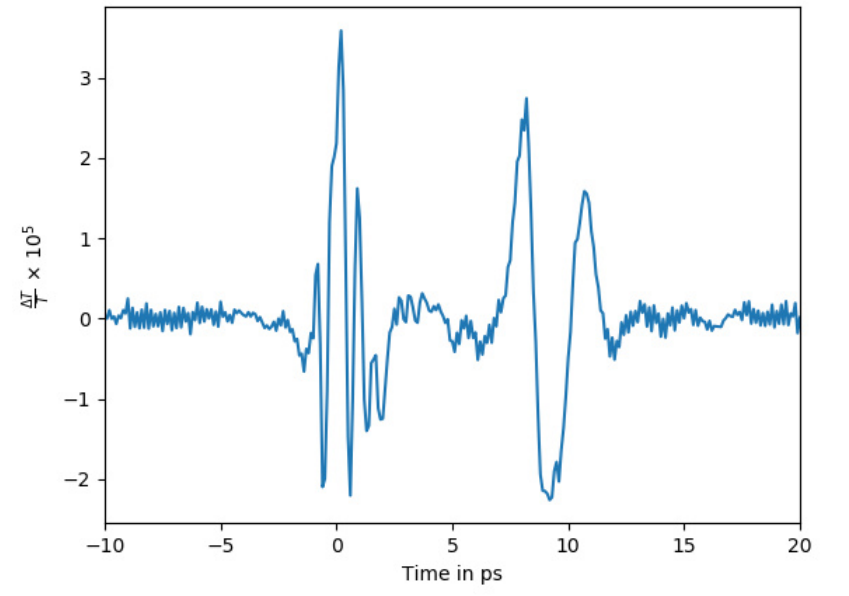

Figure 2.42: Longer time scale signal.

the maximum of Second Harmonic Generation. The results are summarize in Fig. 2.43 a).

A a function of ϕ, the signal is lost from one peak to the other one. This is represented by the arrow on Fig.2.43. The signal at t = 0 (namely the maxima of the first peak) is represented in Fig.2.44. This signal is fitted by a cosine function.

In order to understand this change in the signal, we performed Time domain Spectroscopy on our sample using our THz-TDS set-up that will be presented in the next chapter. That way we were able to measure the refractive index of our sample. This is

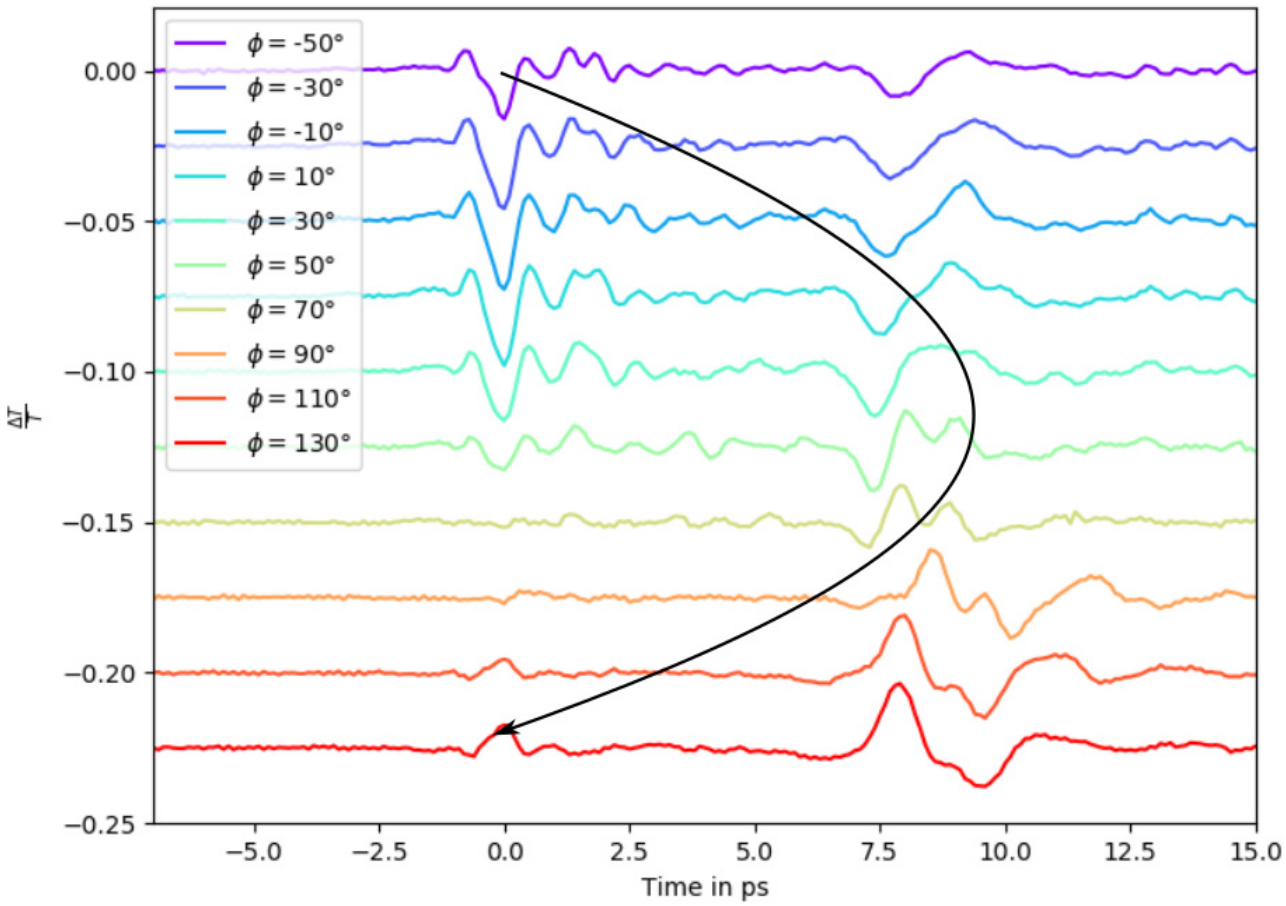

Figure 2.43: Signal at different angle between the crystal axis and the polarization. Plots are just shifted one from the other for better clarity. Plots are not normalized. The dashed line represents time zero. A selected number of traces (one over two) were plotted for clarity. The arrows is showing the shift between the two peaks

.

shown in Fig. 2.45.

The refractive indexes we obtained are adequate with the literature [63] and they exhibit a strong birefringence with a maximum of $\Delta n \approx 0.4$. For our sample, this induces a shift of around 7 ps between our components which is close to the 10 ps observed in our signal. Allowing us to assess that we observed the split of the pulse within the two components of the optical ellipsoid.

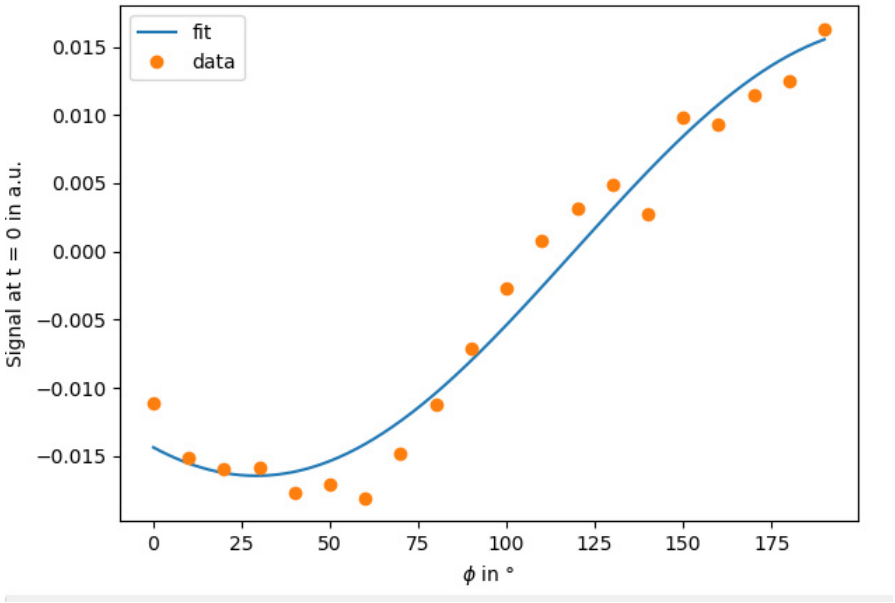

Figure 2.44: Signal at t = 0 for different angles between TeraHertz electric field and crystalline axis. The data have been fitted by a simple Acos(x + ϕ)

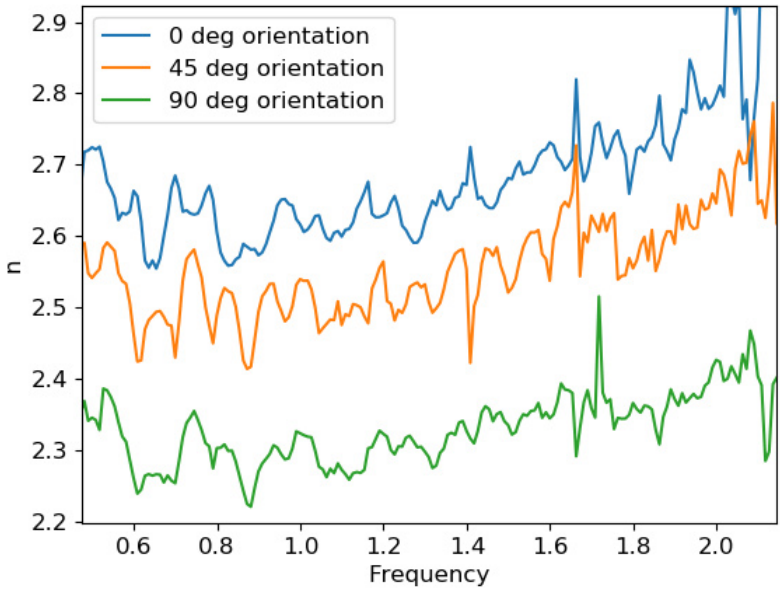

Figure 2.45: Refractive index of BBO for different angle between crystal axis and TeraHertz electric field.

Finally, as the two components are different, their Fourier analysis have to be done separately. This is shown in Fig.2.46. We observed high frequency component in the Fourier Spectra of the first peak in comparison to the first one. This is an hint for Second or higher harmonic Generation of TeraHertz within the BBO. However, this is not conclusive enough data and further investigations needs to be done.

To conclude this section, we have demonstrated that our THz experimental set-up is valid by reproducing the results of the literature. Moreover, by increasing the intensity

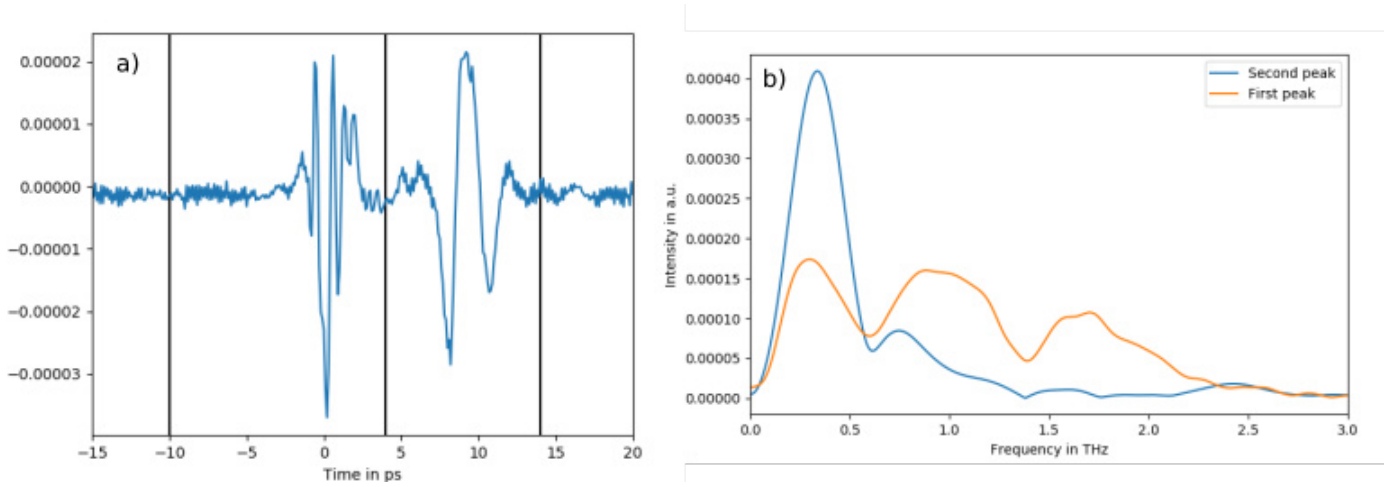

Figure 2.46: a) Temporal modulation of Second Harmonic, the horizontal lines shows the domain used for doing the Fourier Transform. b) Associated Spectra used with the two domains.

of the electric field, we observed more non linear effects that seems to be linked to High Harmonic Generation in the THz frequency domain using BBO.

2.9.2 THz pump optical probe in V2O3 thin film at room temperature

Sample Introduction

The V_2O_3 is a compound which crystallizes in the $R\bar{3}c$ space group[66]. This crystal is a typical Mott insulator. Unlike usual band insulator, Mott insulator are related to the correlation of electrons. Electrons can hope from one site to another with a certain probability, if the correlation is too strong (the Coulomb repulsion) then there is no hopping possible and so no conduction. The phase diagram of V_2O_3 is presented in Fig.2.47 adapted from [67]. At low temperature, the system is in an antiferromagnetic insulator phase. At high temperature high pressure, the system is in a paramagnetic metal phase. At low temperature low pressure the system is in a paramagnetic insulating phase. The pressure in this sample can be tuned by substituting Cr atom to V atom in the structure. In this compound, the Mott insulator transition is caused by the pressure, when the pressure is high enough the hopping is easier and allows the metallic transition.

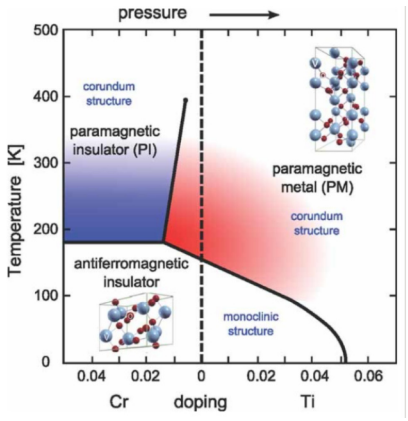

Figure 2.47: Phase Diagram of V_2O_3 adapted from [67].

When an electric field is applied on V_2O_3, an insulating to metal transition can be generated [**?**]. As such, this compound has attracted interest to create memory devices. The study of this compound under light irradiation is very diverse from optical measurement to infrared and even THz meausrements [68, 69, 70, 71, 72]. One interesting idea with this compound is to use the single cycle and intense electric field of the THz pulse to induce the Insulator to Metal Phase transition. To understand, the property of the THz light on this compound a first study was realised in the Paramagnetic metal Phase (PM). This study will be presented in this section.

Experimental Set-Up

The experiment was done on a 200 nm thick thin film deposited on a Sapphire plate 1cm x 1cm. The sample we used was undoped and studied at room temperature so deep in the Parmagnetic Metal insulating (see Fig.2.47. This sample was provided to us by the Institut des Matériaux Jean Rouxel in Nantes. We realized an THz Pump Optical Probe in a transmission set-up at room temperature. The wavelength used for the probe

was 740nm. The absorption of the sample was OD1 for the visible range. The pump and probe are collinear, the spatial overlap is realized using a PyrocamIII. Finally, the temporal overlap is realized beforehand using an EOS set-up. The probe light is collected onto a photodiode connected to a lockin-amplifier. An optical chopper is placed on the pump path at the frequency 500Hz. A part of the probe light was recorded outside the box to use as a reference for a proper balance detection. 750nm Shortpass filters were put in front of the detection photodiode to discard any 800nm remaining from the pump within the box. This set-up is very similar to the one presented in the previous section (see Fig.2.35).

Experimental results and interpretation

The experimental results we obtained are presented in Fig.2.48:

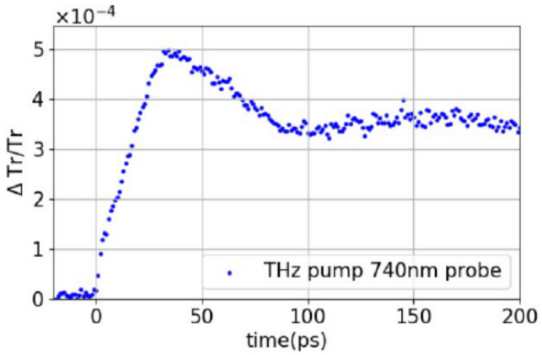

Figure 2.48: Variation of 740 nm light transmitted through V_2O_3 thin film over time. Those are unpublished data. Vertical black lines delimits the time scales of the sample.

The variation of the 740 nm follows 3 time scales. First period is from 0 to 25ps, the signal is increasing linearly with time. Then, from 25 to 90 ps, the signal is relaxing, finally it reaches a plateau. As THz excitation is not longer than 1ps, this cannot be only electrical aspect. Sound velocity in V_2O_3 is 8000m/s, for a 200nm thick film, an acoustic wave will take 25ps to travel in the sample, therefore acoustic time scale is the good time scale to look at for this first period.

Levchut et al. [73] measured an ultrafast Joule Effects generated by THz electric Field in Bi_2Te_3. The THz pump heats the electron generating a strain wave into the sample. This strain wave travels at the speed of sound and changes the refractive index in the film via thermoelastic coupling. As the wavelength of THz is bigger than the thickness of the film, a strain wave is generated from both sides of the film. When the two strains have finished their travels, the strain needs to homogenized and relax in the film reaching a plateau. Those studies have been more deeply conducted by Guenole Huitric. The full explanation including fit of the data and theoretical explanation might be found in his PhD Manuscript.

However, we can conclude at this stage that it is possible to induce thermoelastic effects in V_2O_3 thin films. This is close to results from the literature and so validates the use of the THz to pump effects on metals. This shows that our THz set-up can also be used in cases where the signal is not linear with the electric field and to trigger phenomena on much longer timescales that the THz electric field itself.

2.10 Conclusion

This chapter was dedicated to explain the development en characteristics of the THz Source I built during my PhD Thesis. This source represents most of my time during this PhD taking around 2 years of work. The characteristics of this source are one of the most performing in the world nowadays using the $LiNbO_3$ crystal. The performance of this source are resumed in in Table 2.1:

Peak Electric field	Energy	Beamsize
800 kV/cm	4.5 μJ	800 μm

Table 2.1: Recapitulative table of the characteristics of the source.

The development of this source but also the detection techniques use laser sources which pulse duration is required to be in the femtosecond timescale. Those lasers are generated using Chireped Pulse Amplification (CPA) which have been presented in this chapter. Most of the light sources used in those experiment are generated from the same pulse and non linear optic is used to choose the wavelength.

The alignment procedure for optical rectification in $LiNbO_3$ has been detailed. This procedure should be helpful for future user or person who would want to start a new THz source based on this technique.

The development of the source raised the development of Electro Optical sampling. The data treatment of Electro Optical Sampling has been detailed as well as the effects of broadband sources on the experimental data. Indeed, to do a proper Electro Optical Sampling, the pulse duration of the probe needs to be less than 100 fs. Therefore, the probe pulse is naturally broadband. Moreover, we use Electro optical sampling in a non-standard way to measure the beam waist of our THz pulse. We were able to compare this measure with images taken with the Pyrocam III for similar results.

This source has been validated with two experiments : Second Harmonic Modulation with THz in BBO crystal and THz pump Optical Probe in V_2O_3 thin film. The first experiment reproduces the results of the literature and even improve the results by observing new phenomena thanks to the more intense THz source and thicker crystal. The second experiment presents results very similar to what have been observed in other compounds using THz pump Probe experiment. Those two results validate the use of the source which can then be used for new physics.

The main objective of this PhD thesis was to develop and characterize an intense THz source. This objective is now fulfilled. This source can now be used for more challenging experiments. Spin Crossover materials have been widely studied but not much using THz light. Moreover, the study of Spin Crossover materials using THz light was done mostly using THz as probe [74, 75]. We want to apply our source to those materials to do Pump Probe experiment which has not been done using THz as a pump. We developed a THz-TDS set-up that will be presented in chapter 3 and chapter 4 will summarize all our studies on Spin Crossover materials.

Chapter 3

Theory and development of a THz Time Domain Spectroscopy Set-up

3.1 Theory of Time Domain Spectroscopy

3.1.1 Introduction

One important quantity in light matter interaction is the complex refractive index. When light travels through a media there are three possibilities : reflection, transmission and absorption. The amplitude of the initial wave is divided between the reflected, transmitted and absorbed :

$$A + R + T = 1 \tag{3.1}$$

The understanding of this sorting is the field of linear optic as already presented in the second chapter of this manuscript. These quantities are related to the complex refractive of the material :

$$\tilde{n}(\omega) = n(\omega) - i\kappa(\omega) \tag{3.2}$$

$\tilde{n}$ is wavelength dependent and as such different experimental techniques are required to determine it. For visible light, ellipsometry is a technique of choice. This technique relies on the reflected light at the surface of the sample and a precise control of the angle of reflection at the surface. However, when dealing with THz wavelength ellipsometry cannot be used and new method are required.

The most widely used technique to measure the complex refractive index in the THz range is the Time Domain Spectroscopy. This technique relies on coherent measurements of the THz electric field using either EOS or ABCD detection scheme.

Theory to extract the complex refractive index have been theoretically derived by Duvilaret et al. [76] and [77]. I will present now the theory of TDS based on their work.

3.1.2 Time Domain Spectroscopy hypothesis

The aim of Time domain spectroscopy is to extract the complex refractive index of a material. EOS or ABCD detection measures the THz field at different position in time. Through Fourier transform of the time domain waveform, the spectra of the THz pulse is obtainable. The spectra is changed through a medium and therefore we can extract the frequency dependent complex refractive index. The transfer function which measures the differences between the two spectra is hence mandatory to have access to the information sought.

$$H(\omega) = \frac{E_{sample}(\omega)}{E_{ref}(\omega)} \tag{3.3}$$

$E_{sample}(\omega)$ and $E_{ref}(\omega)$ are the spectra observed respectively under through the materials and and air.

The derivation of the transfer function can be done under the following hypothesis :

- For the sample :
  - Homogeneous, plan with parallel faces;
  - Isotropic and with no surface charges in order to avoid unexpected reflections;
  - Possessing an electromagnetic linear response;
- For THz beam :
  - Plane wave front on the sample;
  - Normal incidence;

3.1.3 The theoretical transfer function

Definitions of equations used

For the following, this convention will be adopted :

$$\tilde{n}(\omega) = n(\omega) - i\kappa(\omega) \tag{3.4}$$

n is the refractive index of the medium and κ it's extinction coefficient. Those are the parameters we seek to find through the algorithm.

The Fresnel index represents the reflection and transmission between two mediums. If the light is traveling from a medium 1 to a medium 2, they are written :

$$r_{12} = \frac{\tilde{n}_2 - \tilde{n}_1}{\tilde{n}_2 + \tilde{n}_1} \tag{3.5}$$

$$t_{12} = \frac{2\tilde{n}_2}{\tilde{n}_2 + \tilde{n}_1} \tag{3.6}$$

When dealing with mono crystal, the medium 1 is often air as crystals are usually mounted on goniometer head without any substrate.

Finally, let's write down the dissipation of light through a medium.

$$P(\omega, z) = e^{\frac{-i\tilde{n}\omega z}{c}} \tag{3.7}$$

When the refractive index is real this is just a plane wave. The imaginary part translates into a extinction coefficient.

Derivation of the transfer function

Let medium 0 be vacuum, medium 1 the sample, E_{init} the initial amplitude of the field and finally x the distance between the source of the wave and the detector. Hence, the reference field is :

$$E_{ref} = E_{init} P_0(x) \tag{3.8}$$

For a sample of length l, the sample field is :

$$E_{samp} = E_{init} P_0(x-l) T_{01} P_1(l) T_{10} \tag{3.9}$$

Therefore the transfer function is :

$$H^{th} = \frac{E_{samp}}{E_{ref}} = P_0(-l) T_{01} P_1(l) T_{10} \tag{3.10}$$

Which translates to :

$$H^{th} = \frac{4\tilde{n}}{(\tilde{n}+1)^2} e^{-i\frac{(\tilde{n}-1)l\omega}{c}} \tag{3.11}$$

The figure 3.1 is resuming the derivation in the case of air.

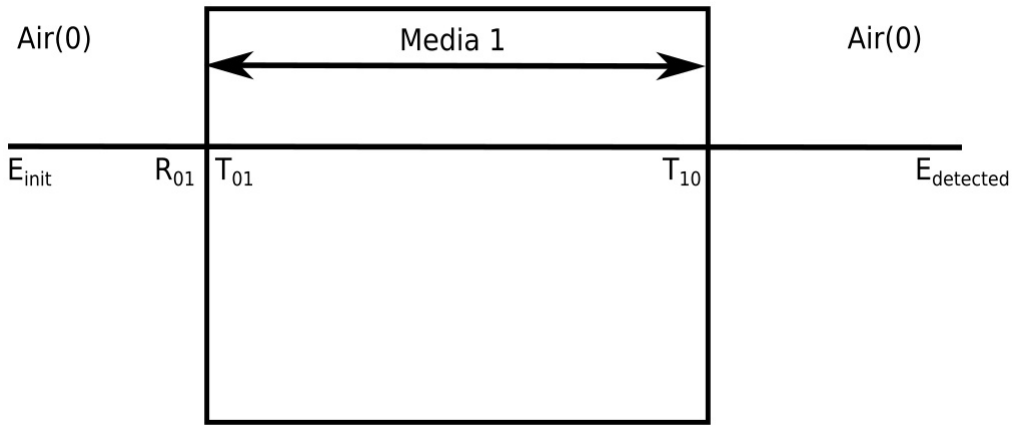

Figure 3.1: Summary of the calculation

3.1.4 Simulation of a THz waveform traveling through a media

To allow analytic derivations, we will assume that the refractive index is frequency independent. Moreover our wave packet is centered on zero in time.

Real refractive index

First, the real case which is easier to derive. The transfer function is analytic in frequency space. The transmission is independent of frequency and is therefore a loss in the amplitude of the field due to the part which is reflected. Going back to time

$$\psi(t) = T \int e^{-\omega^2/2} e^{-i\frac{(n-1)l\omega}{c}} e^{+i\omega t} d\omega \tag{3.12}$$

This is only a temporal translation and a loss of amplitude.

Complex refractive index

Replacing n by n - ik in the precedent equation gives :

$$\psi(\omega) = \frac{4(n-i\kappa)}{(n+1-i\kappa)^2} e^{-\kappa\omega l/c} e^{-in\omega l/c} \tag{3.13}$$

The real refractive index will just have a translation effect as discussed above. The transmission is not changing the form. Therefore, the extinction coefficient impact the form and the amplitude.

We have considered that Fabry-Perot effect is reduced to one which should be take into consideration if the sample is not thick enough.

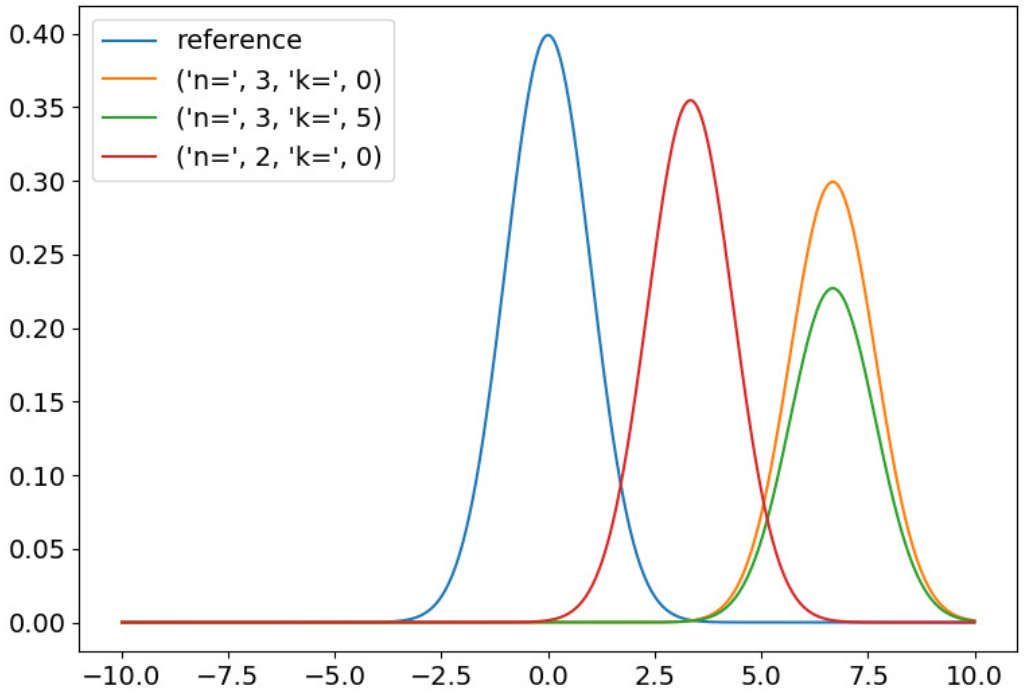

Figure 3.2: Wave packet before and after going through a medium with no extinction coefficient and with. The real part impact both the amplitude and a time translation. The imaginary part only the amplitude and the shape.

From experimental data, one can extract the experimental transfer function namely :

$$H^{exp} = \frac{E_{samp}}{E_{ref}} \tag{3.14}$$

Using the transfer function derived earlier we can write :

$$\phi(H^{exp}) = \frac{(n-1)l\omega}{c} \tag{3.15}$$

One crucial point at this stage is the unwrapping of the phase. The phase is going almost linearly with the phase and therefore the phase will jump from π to $-\pi$. We therefore need to reconstruct the phase to discard those jumps see Fig 3.3.

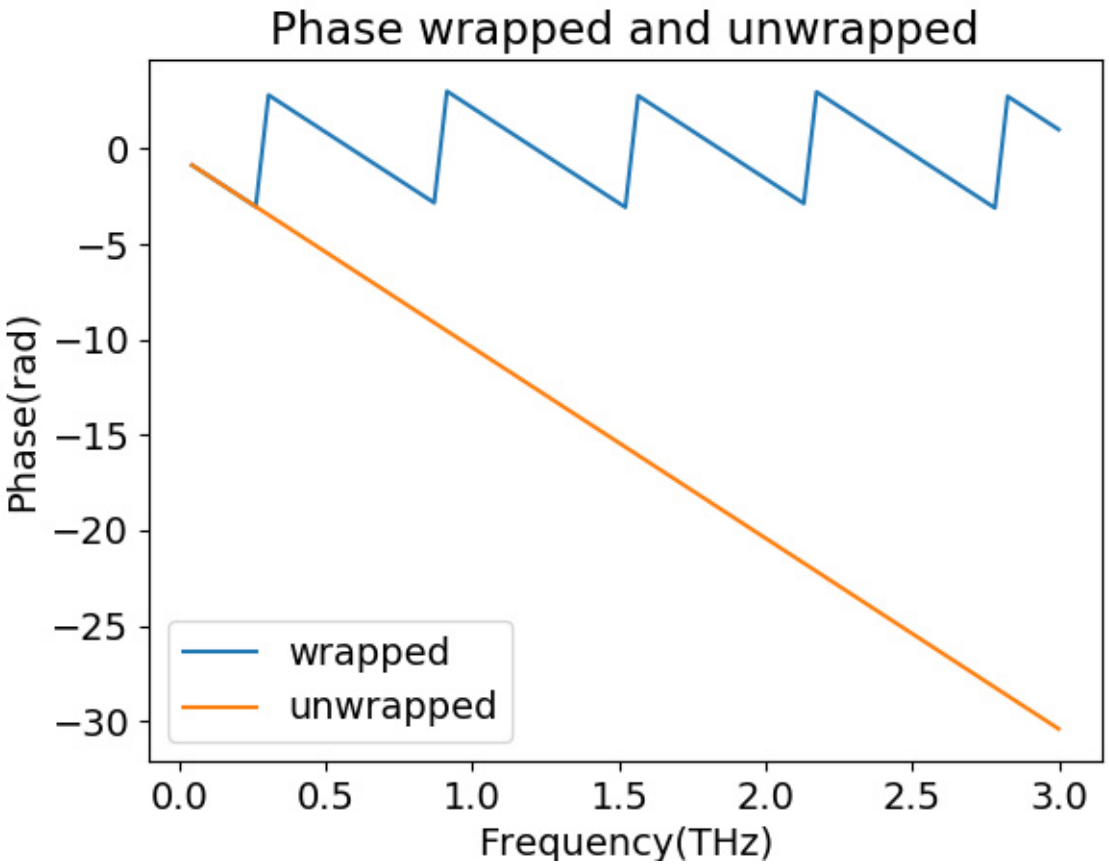

Figure 3.3: Effects of the unwrapping of the phase.

The analytic phase has a term that can go beyond π and hence the necessity of the unwrapping process. This allows the extraction of the real refractive index n from the phase of the experimental data.

The complex refractive index κ can be obtained from the magnitude :

$$|H^{exp}| = |\frac{4(n-i\kappa)}{(n+1-i\kappa)^2}|e^{-\kappa\omega l/c} \tag{3.16}$$

To obtain the real value of the complex refractive index κ, the value of the real refractive index is required. However, often we are only interested in the shape of the complex refractive index which will indicates the absorption peaks. Therefore we can approximate as follows :

$$\kappa \propto \frac{c}{\omega l} log|H^{exp}| \tag{3.17}$$

Therefore, it is often sufficient to take the log of the modulus of the transfer function to obtain the absorption spectra.

3.2 Time Domain Spectroscopy Set-Up characterization using Bi-Chlorophenylsulphone (BCPS)

3.2.1 Scientific Context

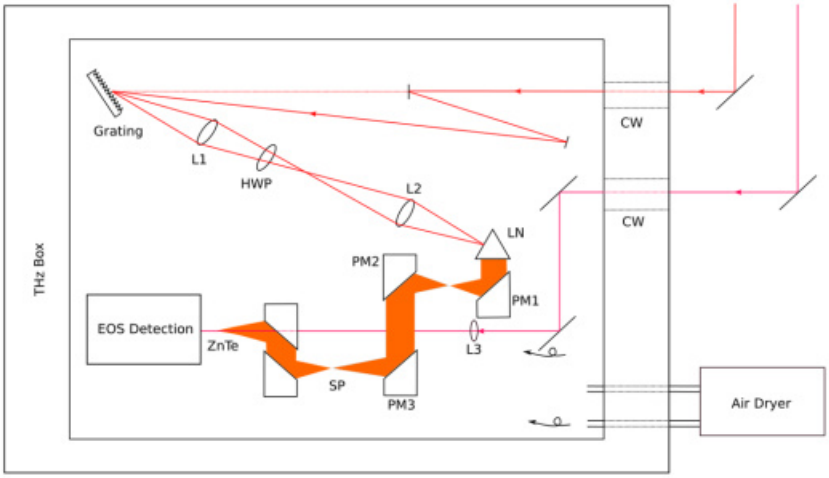

Figure 3.4: Set-Up used for Time Domain Spectroscopy.

A THz Time Domain Spectroscopy set-up was built in Rennes to perform low frequency spectroscopy see Fig.3.4. Two parabolic mirrors were placed after the third parabola PM3 (after the sample position). The first parabola is used to recollimate the beam. The first parabola focal length is the same as the third parabola in order to keep the same beam waist. The second one is used to focus the beam on the detection crystal. The second parabola focal length is chosen to be longer than the parabola used to focus at the sample position to avoid any non linearity in the detection crystal.

The characterization of the THz-TDS set-up is required before usage. We choosed the bis (4-chlorophenyl) sulphone or BCPS. The crystal space group is I2/a (number 15). This is a monoclinic crystal at room temperature with cell parameters : a = 20.204 A; b=5.008; c = 12.259. [78] Below 150K the crystal transits to an incommensurate phase. This crystal has been widely studied by our group in the past for its soft mode properties. A soft mode is a mode which frequency is going to zero when the temperature is close the transition temperature. This has been studied using neutron diffraction and Brillouin scattering. As the frequency of such mode is very low, a

far infrared measurement was performed at the time. Such set-up was homemade at Rennes in the past and dismantle since, it consists of a bolometer and interferometry of an infrared source. The results are presented in Fig.3.5 adapted from [79].

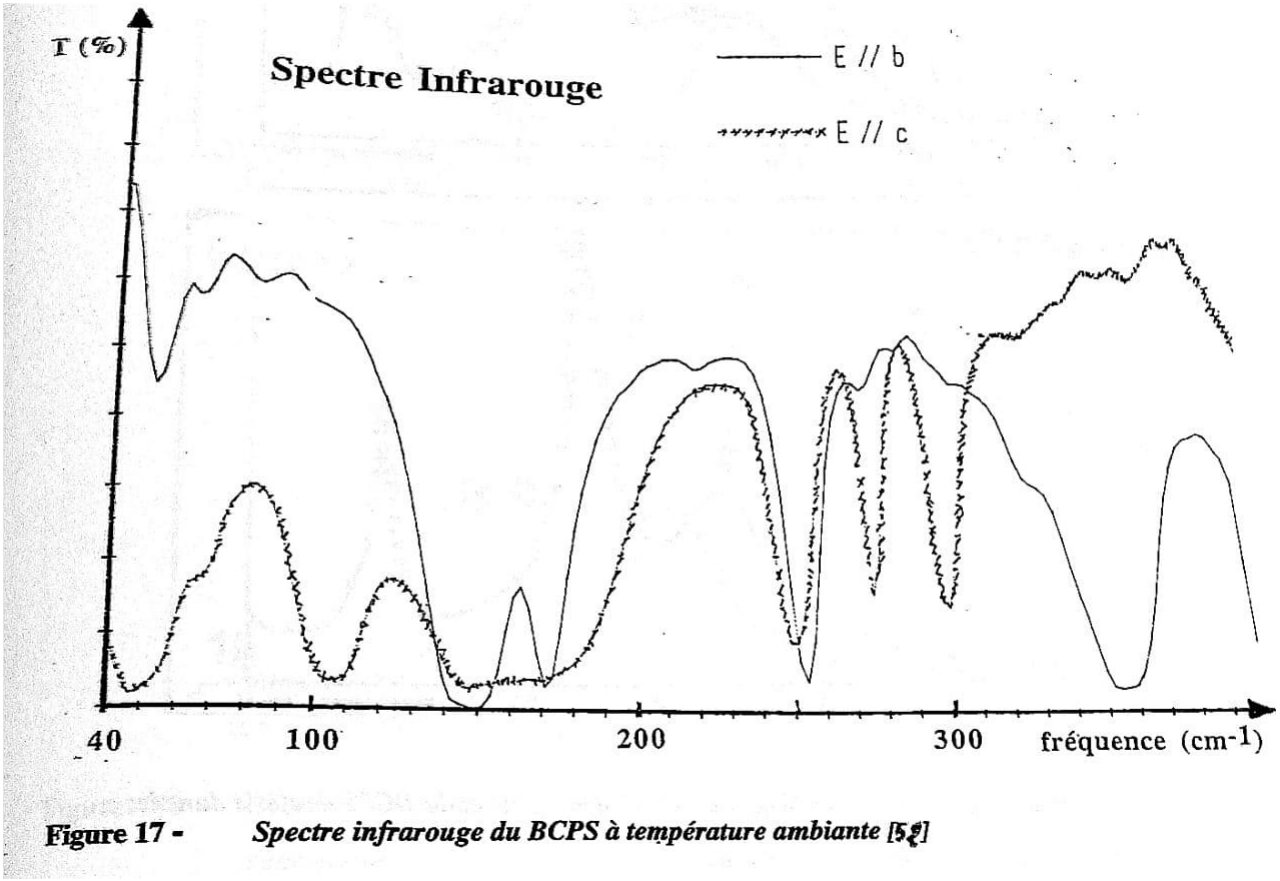

Figure 3.5: Far infrared spectroscopy of the BCPS adapted from [79]

We are interested in the very low frequency (40-60 cm^{-1}) of the spectra of Fig.3.5. This frequency range correspond to the 1-2 THz. Depending of the polarization direction with respect to the crystal axis, the spectra are different. The spectra shown are along b direction and c direction. The a direction is not presented here as the results would be the same as the c direction because of the crystal symmetry. In both directions, the crystal presents two absorption modes around between 50 cm^{-1} (1.5 THz) and 60 cm^{-1} (1.8THz). Those modes will be used as a benchmark for our TDS Set-Up. As the crystal structure is bi-axial, there is 3 distinct refractive index in all the crystal direction, they were recorded to be respectively in the a,c,b direction : $n_x = 1.603$, $n_y = 1.653$, $n_z = 1.785$ [79] at 578 nm. The refractive index in the visible range will be compared to the data obtained from the TDS in the THz range.

The THz TDS set-up was coupled to a cryogenic system. This system is a a nitrogen liquid gun. The nitrogen flow is deposited on the crystal to cool it without contact. A close cryostat would need specific windows to be used in a TDS set-up. Indeed, the windows will add reflection in the THz electric field recorded and might induce artifacts in the measure. Therefore, a cryogun is the preferential choice when not too low temperature are required for the measure.

3.2.2 Experimental results

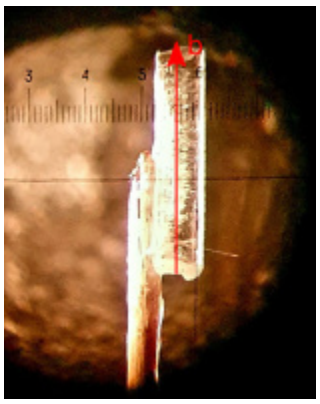

Figure 3.6: BCPS crystal used for the measure, the b axis of the crystal is presented with a red arrow.

The crystal used is presented in Fig.3.6. The crystal was glued on top of a cactus needle. The crystal was oriented using a X-ray diffractometer beforehand. The BCPS absorbs more in the a-c plane than in the b direction, to avoid absorption saturation the b direction was chosen. The crystal thickness was 800 μm and was measured with a microscope.

Spectra were recorded in a range 90K to room temperature increasing the temperature. Each spectra was recorded at static temperature. The reference scan was recorded at room temperature. In Fig.3.7, 3 time domain electric field are plotted. The black scan is the reference, the red scan is room temperature and the purple one 90K.

The spectra at 90K and room temperature are delayed in time with respect to the reference by 1.7 ps. Using the following formula, a first approximation of the real part of the refractive index can be estimated :

$$\Delta t = \frac{(n-1)l}{c} \tag{3.18}$$

Where l is the thickness of the sample and c is the speed of light in the void. For a delay of 1.7,ps and thickness 800 μm a refractive index of 1.7 is expected. The shape of the main peak is altered from the reference. Oscillations are generated after the main peak as well and differs at room temperature and 90 K. As there is no electric field at time zero of the reference, all light is going through the crystal and there is no mix between wave from a reference and crystal.

I will briefly recall to the reader the transfer function derived in the last section with air as the second media :

$$H = \frac{E_{samp}}{E_{ref}} = e^{k\omega l/c} e^{i(n-1)\omega l/c} \tag{3.19}$$

As such the real refractive index is the phase of the transfer function while the modulus is the imaginary part. The data treatment of the phase is performed on the reference and on the sample. Then, the real refractive index can be extracted using the following formula:

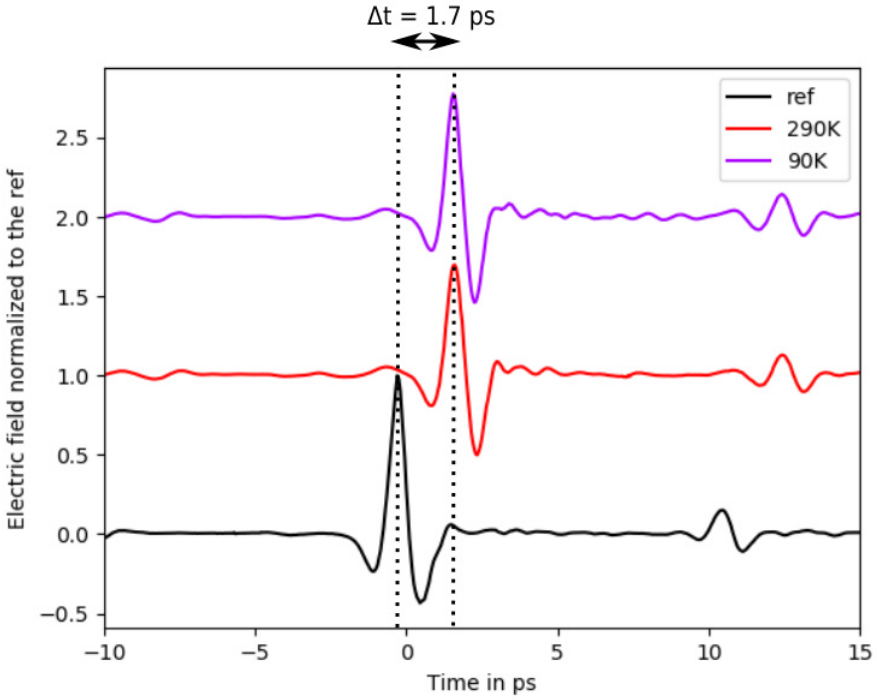

Figure 3.7: Electric field measured outside of the sample for the reference (black), at Room Temperature (290K red) and at 90K (violet).

$$n(\omega) = \frac{c}{2\pi l\omega}(\phi_{sample} - \phi_{ref}) + 1 \tag{3.20}$$

With l the thickness, c the speed of light and ω the frequency (the 2π factor is here to switch to angular frequency), ϕ_{sample} and ϕ_{ref} are respectively the phase of the sample and the reference. The absorption or Optical Density can be extracted using :

$$OD = -log\frac{|E_{sample}|}{|E_{ref}|} \tag{3.21}$$

With $|E_{sample}|$ and $|E_{ref}|$ being the modulus of the electric field spectra. In Figure 3.8, the OD of the BCPS as a function of the frequency are plotted in Fig.3.8.

In Fig.3.8, the presence of 2 modes is also measured for each temperature. The first one, in the range 1.2 - 1.4 THz and the second one in the range 1.7 - 1.9 THz. The two measured peaks are consistent with the peak measure by Sougoti [79] presented in Fig.3.5.

The central value of the first mode for all temperature is plot in Fig.3.2.2. The data set is fitted by a linear function. This linear shift of the mode can be explained by the hardening of modes with the temperature. Phonons are explained in first approximation by a classical harmonic oscillator and should be temperature independent. In reality, non linearity have to be taken into account. As the lattice is compressed at lower temperature, the frequency of phonon will increase, this increase in the vibrational frequency is called hardening. This indicates the cooling has been successful and is clear indication of the phononic nature of the absorption peak.

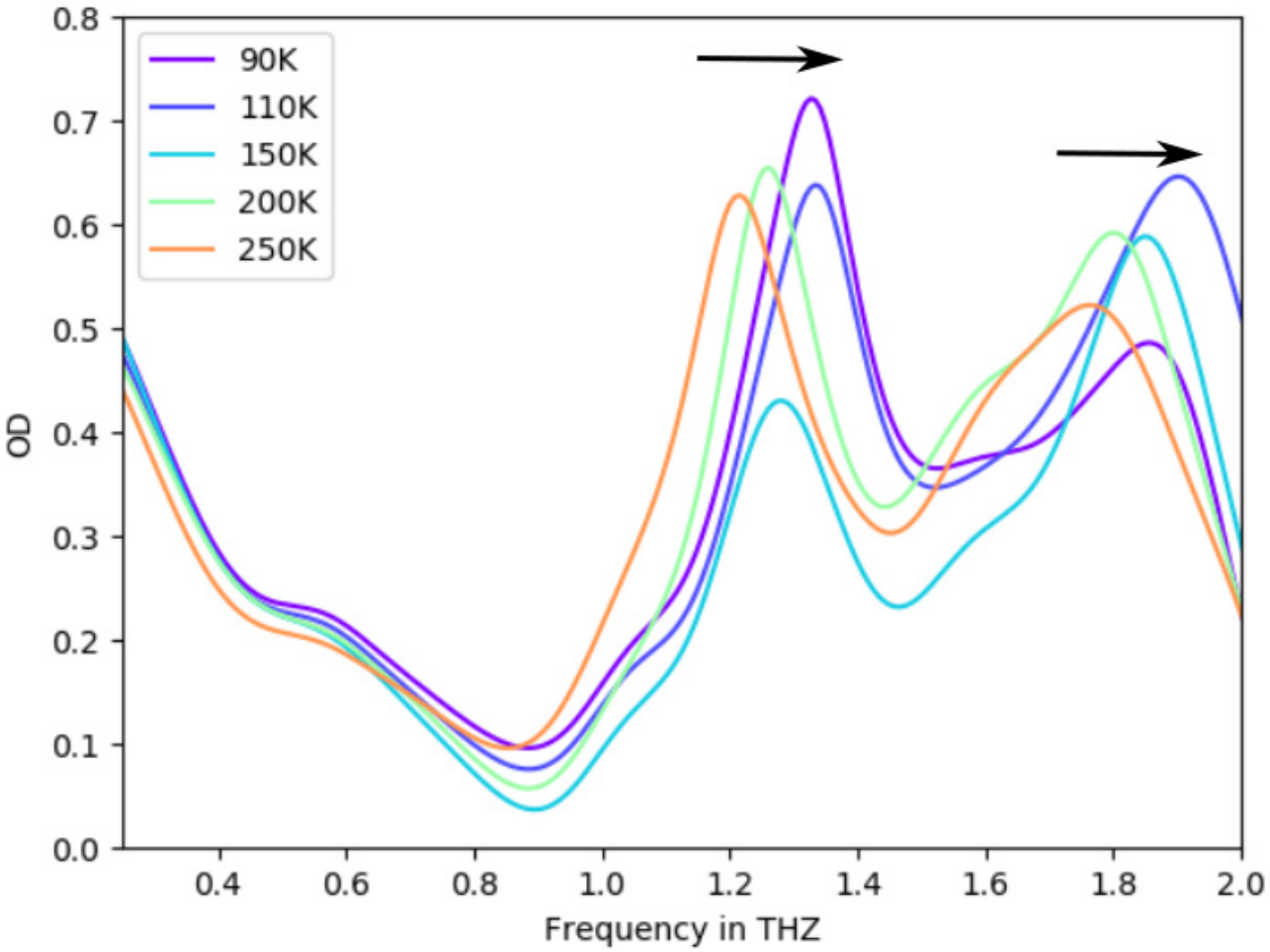

Figure 3.8: Optical Density (OD) measured at 90K, 110K, 150K, 200K and 250K. The arrows shows the hardening of the mode with the temperature.

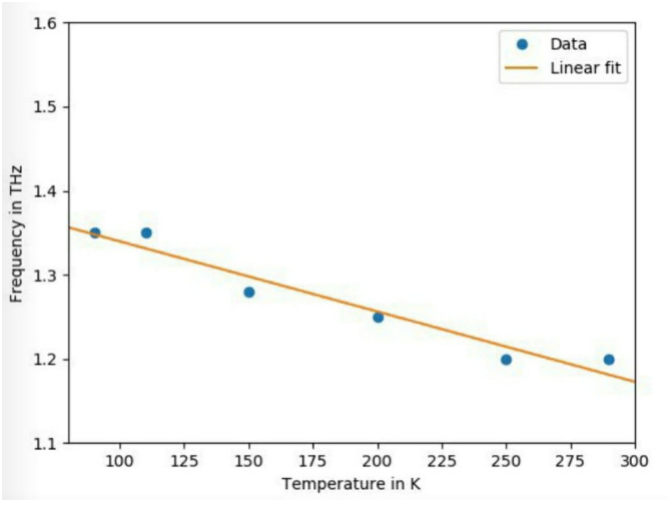

The real refractive index of BCPS is plotted in Fig.3.9. The real refractive index of BCPS in the b direction is measured at 1.56 (Fig.3.8a, which is close to the approximate

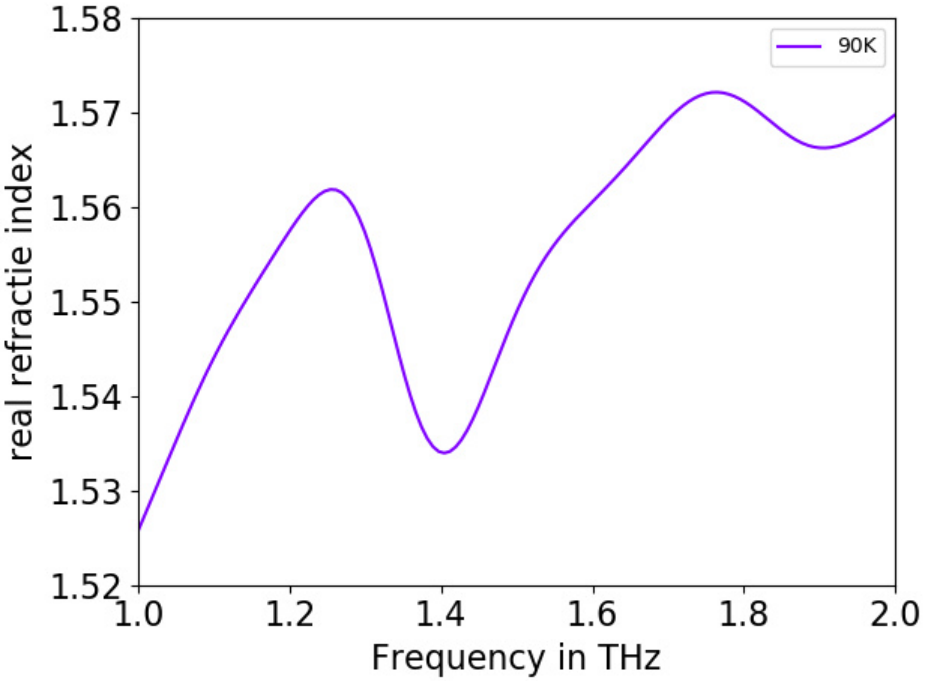

Figure 3.9: Real refractive index of the BCPS measured at 90K.

value of 1.7 obtained from the time domain. This insures the self consistence of data analysis. This value is lower than the value obtained in the visible range. This is in adequation with the theory as the real refractive index is extrapolated to $1/\lambda^2$.At 90K, the jumps are higher in frequency : 1.4 and 1.9 THz. Only 1 temperature is presented for clarity. Both the components of the refractive index are related to each other through Kramers Kronig relationship. This explains that where there is an absorption peak, the phase is affected. Treating both phase and amplitude of the measure spectra is a self consistent way to insure the existence of an absorption peak.

In conclusion, the mode measured using Time Domain Spectroscopy is consistent with the far infrared measurements which validates our experimental method and set-up. Moreover, the TDS set-up allows to have access to more information than the far infrared by measuring the phase and so the real refractive index. Finally, the cryogenic set-up implementation was a success and allows to observe the hardening of the modes with the temperature. While those modes are characterized experimentally, calculations have to be derived to understand the real nature of such modes.

3.3 Conclusion

To conclude, we explained the theory of Time Domain Spectroscopy. This technique relies on the extraction of the complex refractive index. This extraction is possible as most THz measures are done with coherent detection. The coherent measures allows to measure both the phase and magnitude of the THz electric field. Those two components allows to recover both real and imaginary parts of the refractive index.

We implement the THz-TDS set-up by adding two parabolic mirrors after the set-up presented in the previous chapter. In order to validate our data treatment as well as the experimental procedure, we realized THz-TDS of the BCPS compound. This compound was previously study by our group in the far infrared region. As such we were able to compare the absorption peak and so validate our technique. Moreover, we were able to follow the influence of temperature on the absorption mode and so validate as well our cryogenic experimental set-up.

This THz-TDS branch will be used to either perform non linear THz-TDS or linear TDS to study different effects. Thanks to this THz-TDS branch, the THz set-up built in this PhD project is very versatile and can be used either as a pump as shown in the previous chapter or as a probe. As such, this will prove to be a reliant tool for the future of the laboratory. Finally, the cryogenic set-up will be used either for THz pump or THz-TDS experiment.

Chapter 4

Spectroscopy of Spin Crossover compounds : Raman and Time Domain Spectroscopy

4.1 Introduction

4.1.1 Introduction to Spin Crossover compound

Spin crossover compounds are prototypes of bi-stable molecular systems. The molecules contain a transition metal ions such as Fe, Ni or Co with organic ligand. Those compounds are switching from an High Spin (HS) electronic state, stable at high temperature, to a Lows Spin (LS) electronic state, stable at low temperature. This process is entropy driven as the entropy of the HS state is higher than the one of the LS state due to the different of spin multiplicity and to the change in vibration frequencies. [80, 8, 81, 6, 82, 83, 84, 85, 86, 87] The change of spin (or electronic state) is often accompanied by strong molecular geometry rearrangement. The molecular geometry rearrangement will induce changes in the volume of the molecule.

The change of spin state in Spin crossover compound can be explained with ligand field theory. In the case of materials based on Fe2+ the 3 electrons are on the 3d orbitals of the Fe. For a perfectly octahedral configuration, the ligand field will split the orbitals in e_g and t_{2g}. The d_{z^2} and $d_{x^2-y^2}$ orbitals overlapped with the ligand which destabilize those orbitals, they are the e_g. The d_{xy},d_{xz} and d_{yz} are in plane and not disturbed by the ligand, they are the t_{2g}. The splitting induced by the ligand field will pair up the electrons in the t_{2g} orbitals. This will reduce the spin multiplicity to 0 in this case as presented in Fig.4.1. The distance between the Fe and its ligand (by example Nitrogen N) will change the energy band gap between the t_{2g} and e_g orbitals. When the distance is large enough (band gap will decrease) the electrons can jump back in the e_g orbitals. When the distance is shorter, the vibrational frequency will increase, therefore, the potential landscape of the molecule will also be stiffer in the LS state than in the HS state.

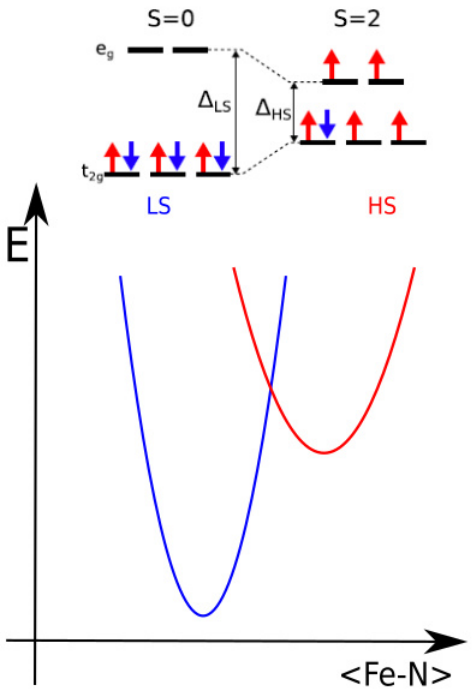

Figure 4.1: Electronic configuration in LS and HS state adapted from [87]. For each configuration the electrons are either on the stabilized t_{2g} or unstabilized e_g orbitals. The spin crossover potential energy as a function of the distance Fe-N is plotted to presents the different energy barrier associated.

An important aspect of the SCO compound is that the transition LS to HS is not only triggered by temperature or pressure. Under visible light irradiation, the compound can switch from the LS to the HS state. The 3d electrons of the transition metal are promoted to the ligand (in the Metal to Ligand Charge Transfer MLCT band). Then, the system relax into the High Spin state by passing through intermediate state. This process involves vibrational cooling which triggers coherent phonon.

The exemple of $[Fe(bpy)_3]^{2+}$ is presented in Fig. 4.2. Fig. 4.2 a) presents a schematic path for the molecule. The pump photon transfers the electron from the t_{2g} 3d orbital of the Fe to an anti bounding orbital of the ligand L(π^*). The system decays then to the HS state of the molecule were 2 electrons populate the e_g orbital and spin multiplicity is 2. The time scale involved in this process are presented in Fig. 4.2 b). The electron is promoted almost instantaneously in the MLCT band. The photo-excited relax to the HS state through an intermediary ^3T state($t_{2g}^5 e_g^1 L^0$) within 120 fs. This drives coherent phonon which oscillations are 265 fs period. Phonon are dispersed after 330 fs because of dephasing. Lemke et al. suggests that the ^3T intermediate state is at the origin of this dephasing. The system relaxes via an incoherent vibrational cooling phase during 1.6 ps. More generally, this photo-excited HS state is metastable and very long lived at low temperature as presented in Fig.4.3 taken from [88].

This phenomenon is called Light Induced Excited Spin State Trapping LIESST. The photo excited HS state is metastable up to a certain temperature where the relaxation becomes too fast, this temperature is called T(LIESST). The T(LIESST) is measured

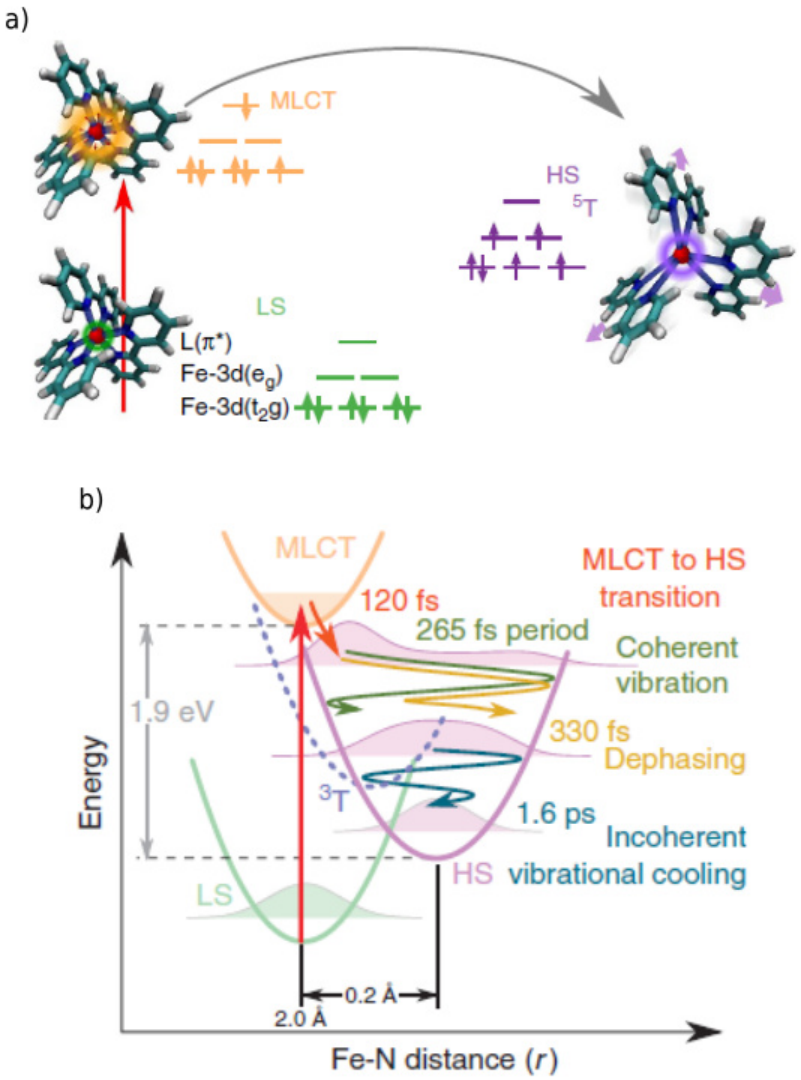

Figure 4.2: a) Schematic light-induced excited spin-state trapping for $[Fe(bpy)_3]^{2+}$, where the Fe (red) is bonded to six N (blue) of the bpy ligands b)Schematic representation of the structural trapping during the light-induced spin-state conversion in $[Fe(bpy)_3]2^+$ from LS to HS state along the Fe-N distance reaction coordinate r. The photoexcited MLCT (manifold) decays, through the ^3T state ($t_{2g}^5 e_g^1 L^0$), towards the HS state within (120(10) fs) and a large fraction of energy is dissipated. It expands and coherently oscillates (breathing mode, 265 fs period) around the HS equilibrium structure while losing energy. The wave packet disperses at 330 fs time constant and vibrationally cools inside the HS state potential within 1.6 ps. Both figures are adapted from [80]

dynamically generally using SQUID technique, the magnetic susceptibility of the compound is measured while heating up the sample from 0K at the rate of 0.3K/min.[81]. There exists a reverse phenomenon which is the reverse(LIESST). In this case, light is shined onto the photo-excited HS state and the molecule relaxes into the LS state. Marino et al.[89] studied the reverse LIESST effect on $[Fe(ptz)_6](BF_4)_2$ compound.

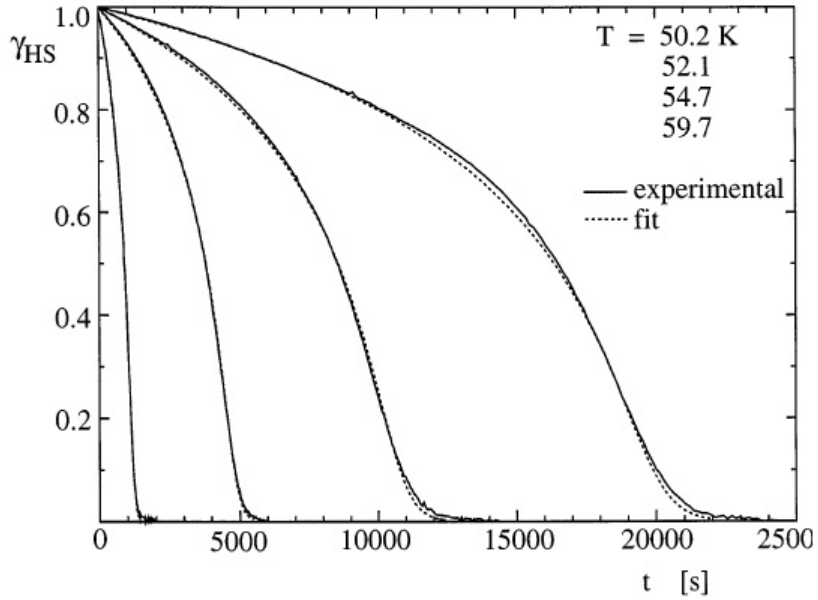

Figure 4.3: High spin fraction in the $[Fe(ptz)_6](BF_4)_2$ as a function of time. Figure adapted from [88]

Both optical pathways are presented in Fig. 4.4. For the LIESST, the LS state is pumped into the MLCT with a 305 nm light. It relaxes into the HS state through the $^3T_1$ intermediate state. For the reverse LIESST effect, the HS state is pumped into the ^5E state with 830 nm light. The system relaxes then in the LS state through the same $^3T_1$ intermediate state.

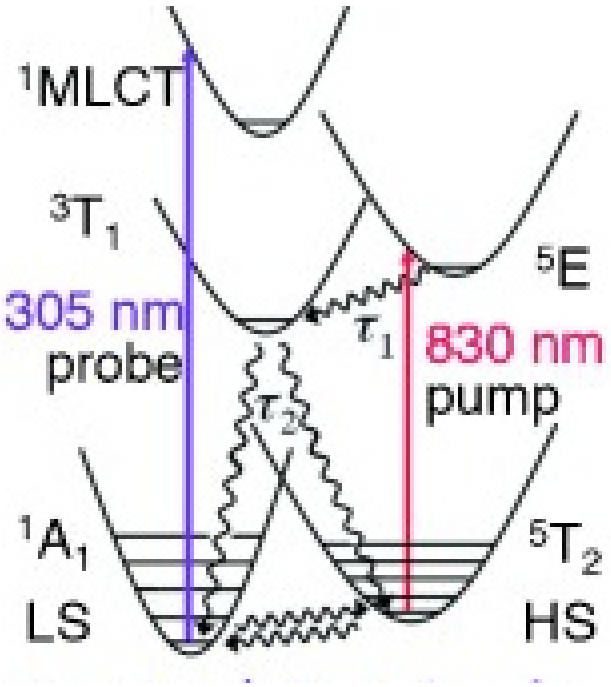

Figure 4.4: Optical pathway of LIESST and reverse LIESST effect for the $[Fe(ptz)_6](BF_4)_2$. For the LIESST, the LS state is pumped into the MLCT with a 305 nm light. It relax into the HS state through the $^3T_1$ intermediate state. For the reverse LIESST effect, the HS state is pumped into the ^5E state with 830 nm light. The system relax then in the LS state through the same $^3T_1$ intermediate state. Figure adapted from [89]

4.1.2 Phonon modes and symmetry

Phonon are collective vibrational modes in the solid state and they have the symmetries of the different irreducible representations of the symmetry group. The change in frequency accompanying the SCO contributes to an important vibrational entropy [90]. As such, those particles are very sensitive to symmetry of the compound. To understand the properties of matter in the solid state, a good knowledge of the vibration modes is mandatory. In particular, the presence or lack of inversion symmetry in the compound allows to divide the modes in two categories. If the movement induced by the vibration keeps the inversion symmetry, those modes are called *gerade*. The vibration modes which violates the inversion symmetry are called *ungerade*. u modes are IR or THz active while g are Raman active. If the crystal doesn't possess an inversion symmetry then there is no such distinctions between the modes.

The symmetry of a crystal is resumed by the space group which contains all the symmetry operation of the crystal. Raman, IR or THz techniques can only probe modes at the center of the Brillouin zone and therefore it is sufficient to consider the point group of the space group. The different irreducible representations of the point group are listed in a character table. All zone-center phonons in a crystal belong to one and unique representation. Each representation preserves different symmetries. The character table of $Fe(phen)_2(NCS)_2$ crystal is presented in Fig.4.5 adapted from [91]. The point group of the $Fe(phen)_2(NCS)_2$ crystal is mmm.

D_{2h} (mmm)	E	$C_2(z)$	$C_2(y)$	$C_2(x)$	i	$\sigma(xy)$	$\sigma(xz)$	$\sigma(yz)$		
A_g	1	1	1	1	1	1	1	1		x^2, y^2, z^2
B_{1g}	1	1	−1	−1	1	1	−1	−1	R_z	xy
B_{2g}	1	−1	1	−1	1	−1	1	−1	R_y	xz
B_{3g}	1	−1	−1	1	1	−1	−1	1	R_x	yz
A_u	1	1	1	1	−1	−1	−1	−1		
B_{1u}	1	1	−1	−1	−1	−1	1	1	z	
B_{2u}	1	−1	1	−1	−1	1	−1	1	y	
B_{3u}	1	−1	−1	1	−1	1	1	−1	x	

Figure 4.5: Character Table of the $Fe(phen)_2(NCS)_2$ spin crossover compound adapted from [91]

Density function theory (DFT) allows predicting the vibrational modes of matter. At the exception of the A_u representation, all modes can be probed using Raman, IR and THz spectroscopy. The character table indicates also how the representation transforms itself. In this example, B_{1u}, B_{2u} and B_{3u} are IR or THz actives and are probed by light which polarization in the z,y and x direction respectively. The A_g, B_{1g},B_{2g} and B_{3g} transforms like X^2,Y^2,Z^2 (for the A_g representation), XY for the B_{1g}, XZ for the B_{2g} and YZ for B_{3g}. Using Raman Spectroscopy with linearly polarized light at the entrance coupled to an analyzer at the output allows to select the vibrational modes.

For the rest of the chapter, we will focus on spectroscopic study of the $Fe(phen)_2(NCS)_2$ spin crossover compound. We first will focus on the study of LIESST effect using Raman Spectroscopy. Then, we will look at the Time Domain spectroscopy TDS which allows to measure the phonons in the THz frequency domain. The Time Domain Spectroscopy (TDS) set-up in Rennes will be presented and characterized. Finally, results of TDS on $Fe(phen)_2(NCS)_2$ obtained in Rennes will be presented.

4.2 Raman spectroscopy of $Fe(phen)_2(NCS)_2$

4.2.1 Compound characteristics

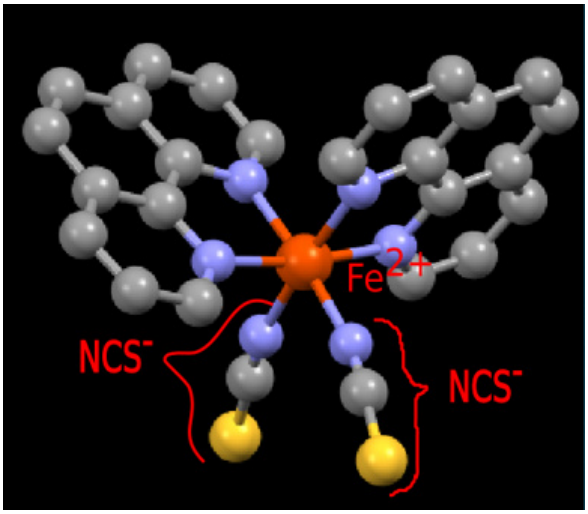

Figure 4.6: Molecule of $Fe(phen)_2(NCS)_2$

First, we will present the characteristics of $Fe(phen)_2(NCS)_2$(phen =1,10 phenantroline) compound. This compound has been and is widely studied as a prototype for the spin transition and therefore the literature associated to this compound is extensive [92, 93, 94, 6, 8, 94, 95, 96]. This molecule is composed of an Fe^{2+} core which is bound to 6 N. Two of them are part of a (NCS^-) while the four others are part of two phenantroline group(Fig.4.6. The crystalline space group is Pbcn (orthorombic). Molecules are placed on the 2 fold axis, head to tail. The crystal has a shape of a diamond which long axis is the b axis and short axis the a, see Fig.4.7.

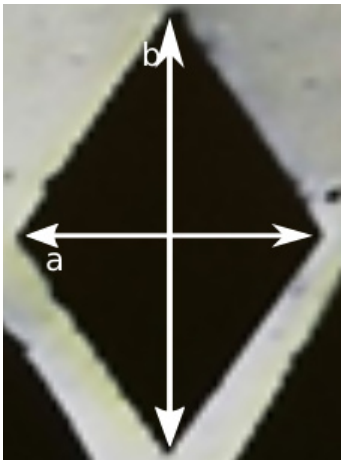

Figure 4.7: Crystal of $Fe(phen)_2(NCS)_2$, crystal axis a and b are shown.

The $Fe(phen)_2(NCS)_2$ undergoes a spin transition from a LS (S=0) state to and HS (S=2) state. This transition happens around 170K as presented in Fig.4.8 adapted from [97]a. On the same figure T(LIESST) is also measured to be 62K. Above 62K the

relaxation rate of the photo excited HS state becomes very fast. A change of volume of around 10% accompanies the transition and is localized on the distance between the Fe and the N [98] (see also Fig.4.8b adapted from Supplementary Material of [8].

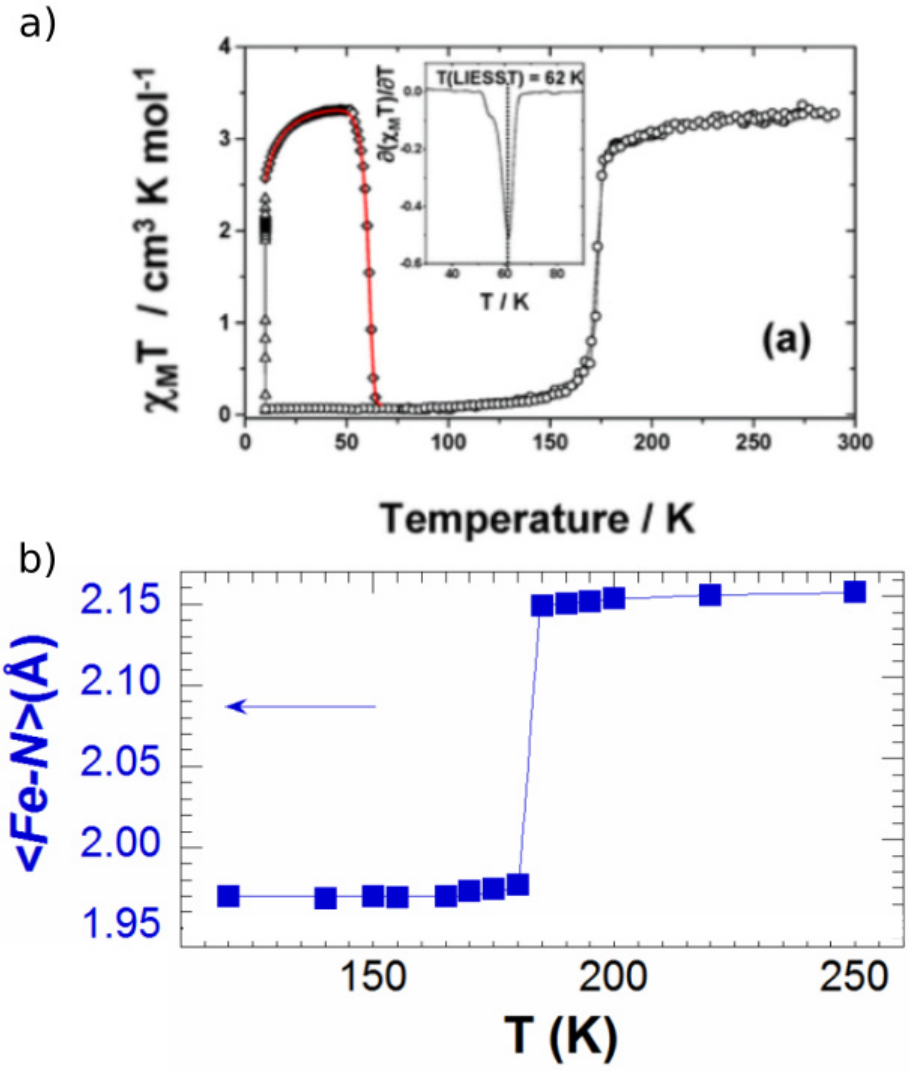

Figure 4.8: a)Magnetic susceptibility of $Fe(phen)_2(NCS)_2$ as a function of temperature. Both thermal transition and LIESST are shown on this figure. Figure adapted from [97]. Distance <Fe-N> in the $Fe(phen)_2(NCS)_2$ as a function of temperature. Figure adapted from Supplementary Materials of [8]

4.2.2 Probing Spin transition with Raman Spectroscopy

We performed Raman Spectroscopy with an Invia Spectrometer from Renishaw (Fig.4.9. We used two different laser wavelengths: 633 nm obtained from a HeNe laser and 785 nm with a laser diode. The temperature was controlled by a HFS600E-PB4 platine from Linkam. Light was linearly polarized along the b axis of the crystal and only parallel polarization was recovered using a linear polarizer. Since the unit cell in the

Figure 4.9: Micro Raman used for the measurements.

crystal contains 4 molecules, there are 8 N-CS stretching modes of symmetry A_g, A_u, B_{1g}, B_{2g}, B_{3g}, B_{1u}, B_{2u} or B_{3u}, see Fig.4.5. Only the g modes are Raman-active and the laser polarization used allows for probing the Ag mode only, which allows avoiding the superposition of signals from other modes of different symmetries. For both measurements performed at 633 nm and 785 nm we used a microscope objective to focus the laser on an around 4 μm spot on a single crystal.

The thermal dependence of the vibrational modes of $[Fe(phen)_2(NCS)_2]$ has already been presented in the literature, [99, 84, 91] and there are many modes exhibiting frequency shifts between LS and HS states. Here we focus our attention on the high frequency range (1900-2200 cm^{-1}) in order to probe modes involving essentially the $C \equiv N$ bonding. Moreover, we take advantage of light polarization for probing the single N-CS stretching mode of Ag symmetry. Fig.4.10 displays Raman spectra recorded for A_g symmetry (bb polarization) at different temperatures above and below the spin transition temperature. At 293 K, the system is fully in the HS state, as characterized by the A_g N-CS stretching mode around 2070 cm^{-1}. At 133 K, the system is fully in the LS state, as characterized by the Ag N-CS stretching mode around 2114 cm^{-1}. Just above the phase transition, at 193 K and 173 K, a small fraction of the molecules converts to the LS state, while at 163 K a weak signal of HS molecules is also observed. All these features are in good agreement with magnetic susceptibility data providing a phase transition temperature $T_{1/2}$ 173 K with partial conversion on each side. This confirms the sensitivity of Raman spectroscopy to probe the spin state reported in various systems, even though the measurement may be affected by a weak heating from the laser, lower than 5 K.

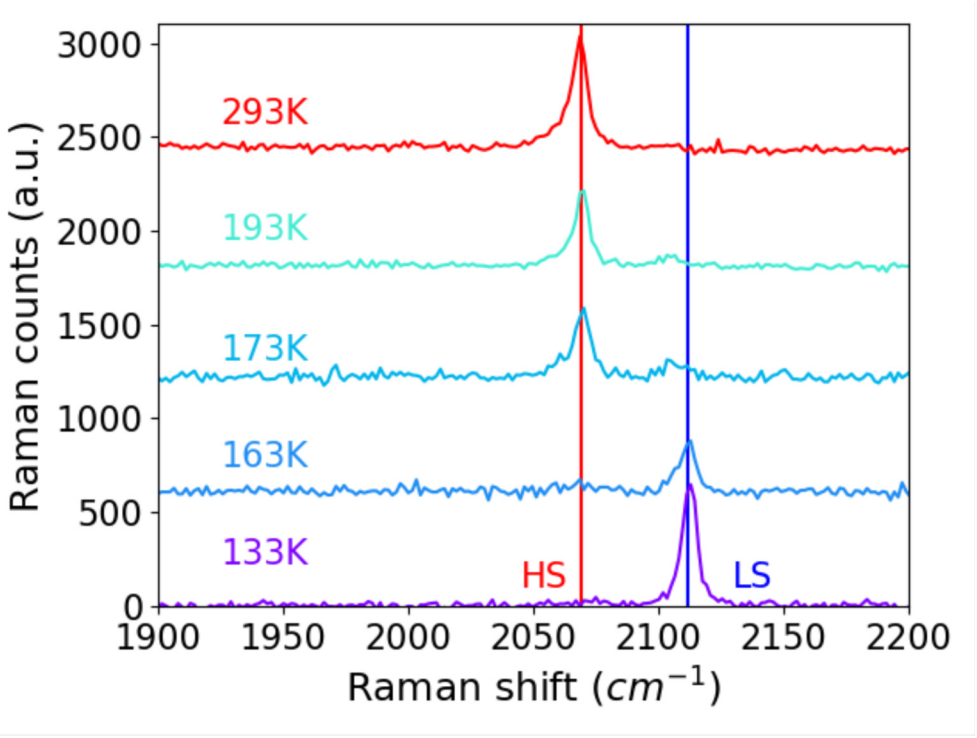

Figure 4.10: Temperature dependence of the frequency of the A_g Raman N-CS stretching modes between the HS and LS phase.

4.2.3 LIESST above T(LIESST) using Raman Spectroscopy

Figure 4.11 shows spectra obtained for 633 nm excitation at $100W/cm^2$ and $200W/cm^2$ in the lower temperature range. For both fluences, a single Raman peak is observed around 2114 cm^{-1} at 123 K, which corresponds to the LS mode. At 113 K, while the main peak is still centered at 2114 cm^{-1}, a weak peak appears at 2070 cm^{-1}, which corresponds to the HS state. As temperature is lowered to 103 K and 93 K, there is a spectral weight transfer from the LS peak to the HS peak. At 88 K, the low spin peak has almost disappeared for a fluence of $200W/cm^2$, while it is still present at $100W/cm^2$. At 83 K for both laser fluences the system is mainly in the HS state under the 633 nm excitation of the Raman set-up.

The bottom curves in Fig 4.11 shows similar measurements performed with 785 nm excitation for the same similar laser fluences as 633 nm excitation. The intensity of the peaks was rescaled to match the scale of 633 nm because the signal amount differs in function of the probe wavelength. However, for 785 nm excitation only the LS peak is present at 83 K, and there is no conversion towards the HS state. This indicates that the HS state observed for 633 nm excitation is photoinduced. Indeed, the d-d and MLCT bands driving LIESST for $[Fe(phen)_2(NCS)_2]$ are around 650 nm. However, 785 nm excitation can't induce electronic transition as the photon energy is lower than the gap of the LS state, as characterized by the lack of absorption above 750 nm. We underline that the photoinduced HS state upon 633 nm excitation is not due to laser heating because the effect decreases as temperature increases. At last, since the observed effect decreases as temperature increases (Fig. 4.11) we can underline that the photoinduced HS state observed here upon 633 nm excitation is not due to laser heating. Kato et al

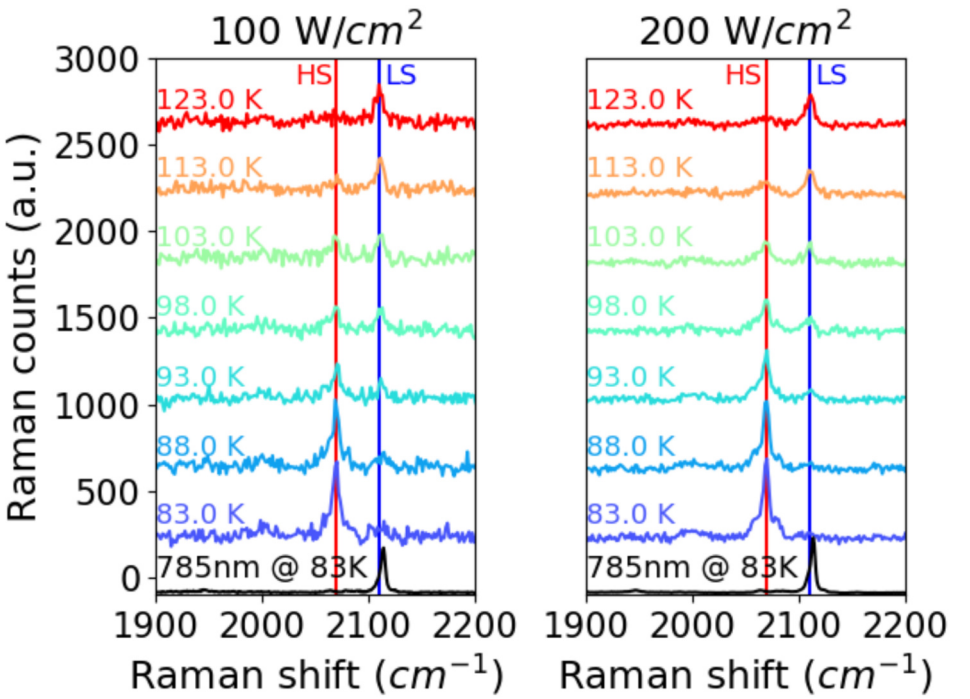

Figure 4.11: Temperature dependence of the frequency of the A_g Raman N-CS stretching on approaching T(LIESST) measured at 633 nm (colored) and 785 nm (black).

reported similar phenomena by using x-ray diffraction for monitoring the effect of light excitation. They demonstrated the on-off optical control of spin-state switching and excluded laser heating effect.[100]

As the impact of light fluence on the Raman spectra was important, we conducted SQUID measurements under light for different fluences.The photomagnetic measurements were carried out on a thin layer of polycrystals of $[Fe(phen)_2(NCS)_2]$, using a laser diode coupled to an optical fiber through the cavity of a MPMS-5 Quantum Design SQUID magnetometer. The standardized procedure for registering the T(LIESST) properties was as previously published. After slow cooling to 20 K (in the LS state), the sample was irradiated at 650 nm, at various fluences (from 10 to 80 mW/cm^2). The magnetization change was followed until the photo-saturation point was reached. The temperature was then increased at a temperature scan rate of 0.5 K/min, keeping the light irradiation on, until the compound fully relaxes to the LS state. In the absence of irradiation, the magnetization was also measured from 10 to 300 K to follow the thermal spin transition and obtain a reference curve.

Fig. 4.12 shows the evolution with temperature and under continuous light excitation of the fraction γ of molecules in HS state, extracted from magnetic susceptibility. Even though the laser fluence is much lower than for micro-Raman, it is clear that the photostationary HS fraction is stabilized towards higher temperature as laser fluence increases. The photostationary half conversion temperature $T_{1/2}^{h\nu}$, where γ=1/2 under light irradiation, shifts from 59 K (0.01 W/cm^2) to 62 K (0.08 W/cm^2).

The observed photostationary population of the HS state is due to the well-known competition between the photoinduced $LS \rightarrow HS$ conversion and thermally-activated

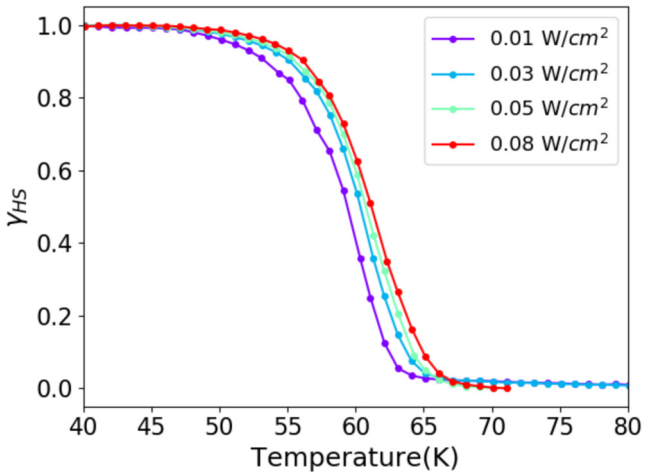

Figure 4.12: Temperature dependence of the photostationary HS fraction measured with SQUID.

$HS \rightarrow LS$ relaxation. In order to discuss this phenomena, we use a simplified version of the model introduced by Desaix et al [101] which describes the competition between photoexcitation driven by permanent light irradiation and relaxation towards the non-excited state. These authors considered a relaxation rate depending on the HS fraction γ, due to cooperative interactions, which modulate the energy barrier. The following master equation from Desaix et al, describes the evolution of γ under competing photoinduced $LS \rightarrow HS$ conversion and thermally-activated $HS \rightarrow LS$ relaxation:

$$\frac{d\gamma}{dt} = \phi_{LS\rightarrow HS} - \phi_{HS\rightarrow LS} = I_0\omega(1-\gamma) - \gamma k_\infty e^{-\frac{E_a(0)}{kT}} e^{-\alpha\gamma} \tag{4.1}$$

Where $I_0\omega$ is the probability per time unit for a LS molecule to switch to the HS state, with I_0 the beam fluence (in $photons/s/cm^2$) and ω a proportionality factor which includes the absorption cross-section of the optical transition driving LIESST. α is the self-acceleration factor, which is important for describing non-exponential relaxations. In the case of the $[Fe(phen)_2(NCS)_2]$ system investigated here, the cooperative interactions are not so strong: the thermal conversion exhibits pretransitional conversion and at high temperature the relaxation curves from the photoinduced HS state are close to exponential.[97] In this case, we can simplify Desaix's model and neglect the self-acceleration factor in a first approximation and for a non-cooperative system, the equation can be reduced to :

$$\frac{d\gamma}{dt} = I_0\omega(1-\gamma) - \gamma k_\infty e^{-\frac{E_a}{kT}} \tag{4.2}$$

The photostationary state is found for :

$$\frac{d\gamma}{dt} = 0 \tag{4.3}$$

$$I_0\omega(1-\gamma) = \gamma k_\infty e^{-\frac{E_a}{kT}} = \gamma k(T) \tag{4.4}$$

Where k(T) is the temperature dependence of the $HS \rightarrow LS$ relaxation rate for an exponential decay. This is reasonable since Balde et al have reported an almost

linear evolution of ln(k(T)) with temperature.[97] In this way, the photostationary HS fraction depends on the thermal relaxation rate and on the laser fluence, which rescales k(T) to r(T)

$$\gamma(T) = \frac{1}{1 + \frac{k(T)}{I_0\omega}} = \frac{1}{1 + r(T)} \tag{4.5}$$

The half-conversion photo-stationary equilibrium, $\gamma = \frac{1}{2}$, occurs when k(T) = $I_0\omega$, i.e. when the $LS \rightarrow HS$ conversion and $HS \rightarrow LS$ relaxation rates are equal. We define $T^{h\nu}_{\frac{1}{2}}(I_0\omega)$ as the temperature for which half-conversion is reached under laser fluence I_0 for a non-cooperative system, with known k(T) and ω. In this way, the light fluence I_0 is the control parameter for reaching photostationary equilibrium. Fig. 4.14a shows the calculated dependence of the photo-stationary HS fraction with temperature, using the k(T) values reported by Balde et al[97] and presented in Fig.4.13 to help the reader.

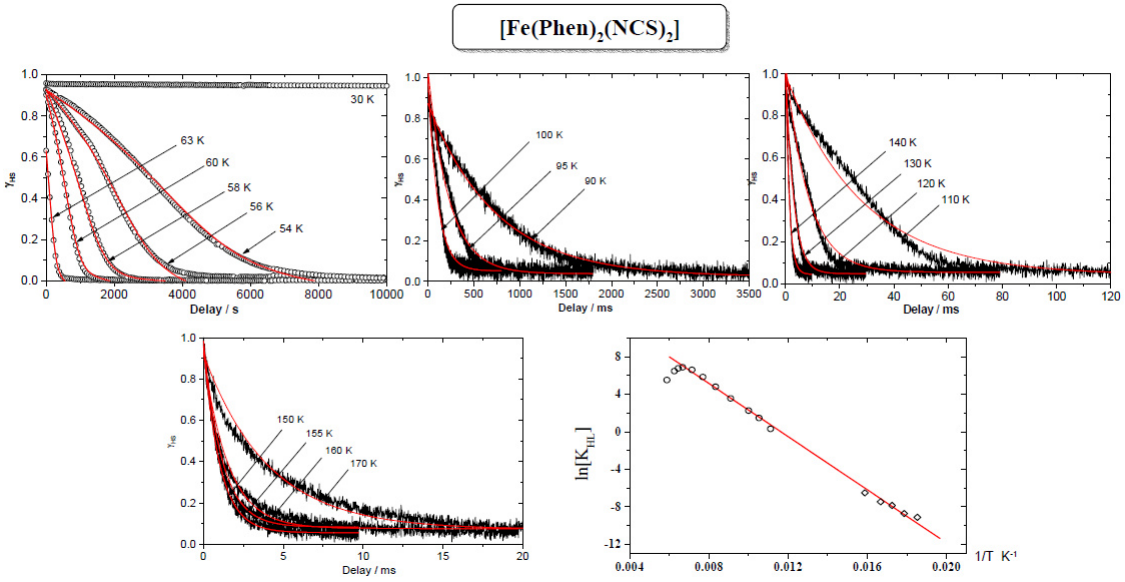

Figure 4.13: High fraction in function of time for different temperature. The relaxation rate as a function of the temperature is plotted down right of the figure. This figure is adapted from [97]

Since the relaxation rate in SCO materials is known to change by 12 orders of magnitude with temperature, the laser fluence also has to change by orders of magnitudes to shift $T^{h\nu}_{\frac{1}{2}}$. For example, Balde et al measured k(85 K) = 1. Photo-stationary half conversion at $T^{h\nu}_{\frac{1}{2}} = 85$ K is then possible when $I_0\omega = 1$, which corresponds to 1 photon absorbed per molecule and per second, as the quantum efficiency of LS $\rightarrow$ HS photo-conversion is close to 1. For reaching photo-stationary half conversion at $T^{h\nu}_{\frac{1}{2}}$ =60 K, where k(60K) = 0.0002, the laser fluence should therefore be reduced by almost 4 orders of magnitude compared to 85 K. This agrees with light fluence used for Raman experiments (100 W/cm^2) where $\gamma = \frac{1}{2}$ at $T^{h\nu}_{\frac{1}{2}}$ =90 K and SQUID experiment(0.01 W/cm^2) where $\gamma = \frac{1}{2}$ at $T^{h\nu}_{\frac{1}{2}} = 60$ K. The model, considering the k(T) data reported

for [Fe(phen)2(NCS)2], predicts a shift of $T_{\frac{1}{2}}^{h\nu}$ from ≈ 55 to ≈ 90 K if the light fluence increases by 4 orders of magnitude (Fig. 4.14b). During the SQUID experiment, the limited increase in light fluence from 0.01 to 0.08 W/cm2 allows for a small shift of $T_{\frac{1}{2}}^{h\nu}$ of about 3 K.

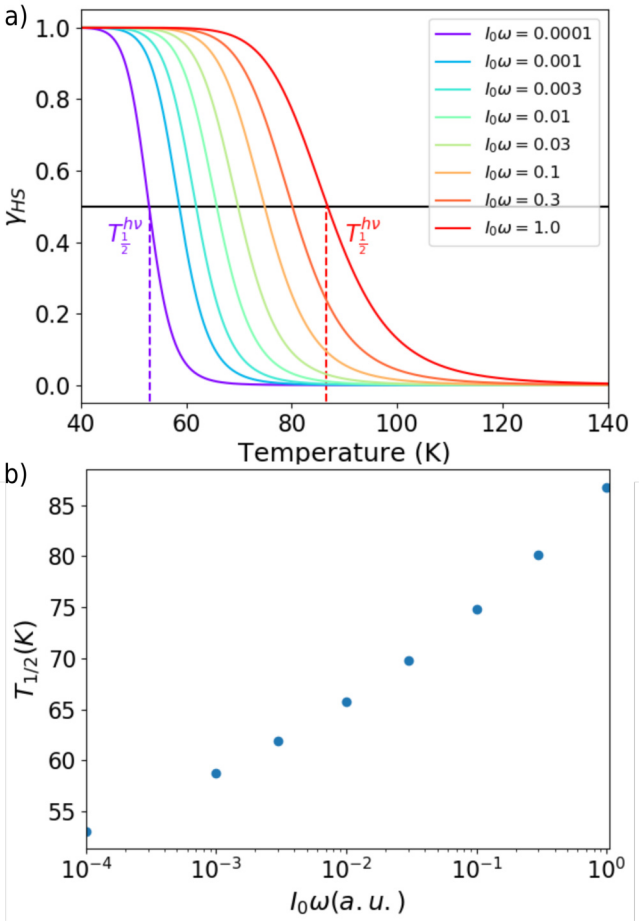

Figure 4.14: a) Calculated temperature dependence of the photostationary HS fraction. b) Evolution of $T_{1/2}^{h\nu}$ with $I_0\omega$.

Fig.4.15 summarizes the experimental and theoretical results. In addition to Raman and SQUID data, we include reflectivity measurements published by Bertoni et al. [6] with an intermediate fluence, more difficult to estimate since reflectivity mainly probes changes induced by a white light excitation close to surface, where optical excitation is higher than in the bulk. The fit of the experimental data with the model, provides some $I_0\omega$ values ($I_0\omega = 1$ for Raman $I_0\omega = 0.001$ for SQUID data) which confirms that for [Fe(phen)2(NCS)2] it is necessary to increase the laser fluence by 4 orders of magnitude to shift $T_{\frac{1}{2}}^{h\nu}$ 30 K above T(LIESST). The different shapes of the experimental data compared to the fit may come from the approximation that [Fe(phen)2(NCS)2] is a non-cooperative system. However, the order of magnitude of the shift of $T_{\frac{1}{2}}^{h\nu}$ with $I_0\omega$ is in good agreement with experimental data.

Another study by Kato et al[100] evidenced that the photoresponse of this materials is more important under excitation at 532 nm, which allows a 88% conversion at 92

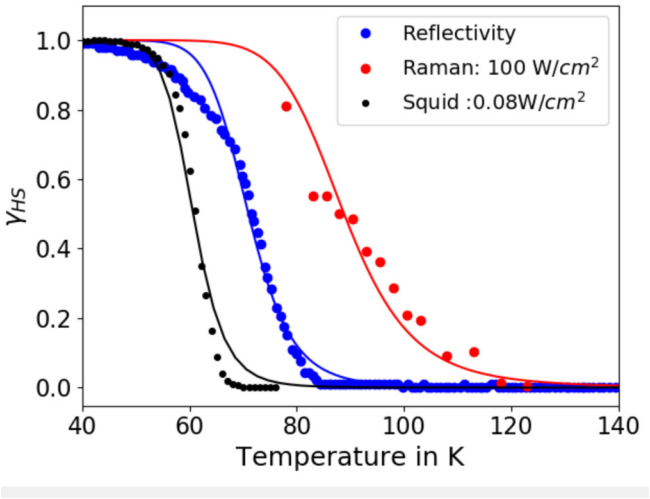

Figure 4.15: Temperature dependence of the photostationary HS fraction from SQUID (black), reflectivity (blue) and micro-Raman (red) measurements. The continuous lines are a fit of the data with $I_0\omega$ as free parameter.

K with $I_0 = 2\ W/cm^2$. The highest absorption at 532 nm translates in higher ω, compared to 633 nm in our experiment, and finally the products $I_0\omega$ are comparable in both experiments.

We discussed the possibility to investigate the LIESST processes in SCO materials well above T(LIESST) under high light fluence. A simple model explains that, for no or weakly cooperative systems, a photo-stationary half photo-conversion is observed when the when the number of absorbed photons per second equals the relaxation rate. With this respect, μ-Raman technique allows observing LIESST at lower cost by using liquid-nitrogen operating cryostat instead of He-operating ones, without using sophisticated time-resolved technique and with the possibility to investigate micro-crystals. Tracking how photo-stationary half-conversion evolves with temperature and light fluence is then another approach for measuring $HS \leftarrow LS$ thermal relaxation rates. This work lead to a publication that can be found in appendix of this document.

4.3 Time Domain Spectroscopy of $Fe(phen)_2(NCS)_2$

4.3.1 Time Domain Spectroscopy of $Fe(phen)_2(NCS)_2$ using a THz air-plasma source.

We used a THz air-plasma broadband source from Tanaka Lab in Kyoto. A picture of their set-up is presented in Fig. 4.16

In their set-up the light is focused on the BBO via a parabolic mirror. Light is going through a polarizer to ensure the THz chosen polarization. This source has mainly been used to do THz-Time Domain Spectroscopy. A Si wafer was put on the THz electric field to removed the traces of 400nm and 800nm that were used for THz generation. Time Domain Spectroscopy was performed on $Fe(phen)_2(NCS)_2$ using this set-up [91]. The detection was performed with the ABCD detection technique. Fig. 4.17 presents a reference electric field used for our measurements.

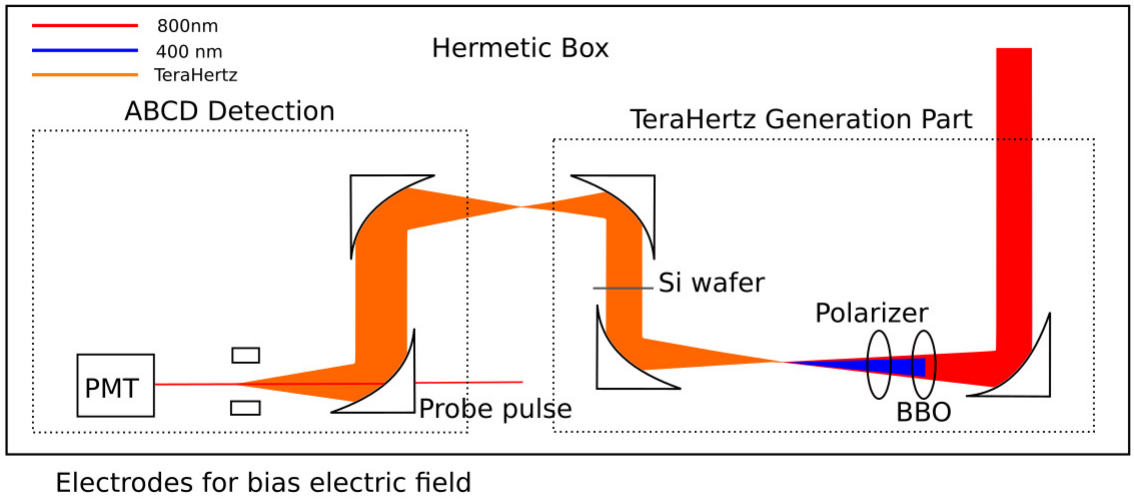

Figure 4.16: Picture of the two color air plasma set-up at Tanaka Lab.

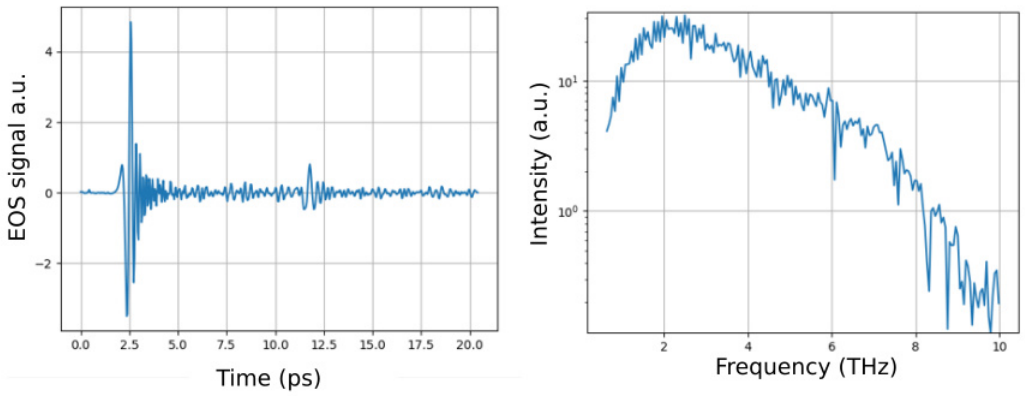

Figure 4.17: THz electric field obtained from a plasma source and its associated Fourrier Transform

The spectra is broadband from 0-10THz. The time domain electric field is presenting fast oscillations in the first ps (around 100fs). A reflection attributed to the Si wafer can be observed after 10 ps. The results I present here were published by Collet et al.[91]. The THz-TDS was conducted on the two crystals glued with two different orientations a (short axis) and b (long axis). The polarization choice allows to select the modes symmetry, along b the modes belong to the B_{2u} representation while along a to the B_{3u}. The result of this experiment was 2 distinct spectra and are presented in Fig.4.18.

In this figure, we observe a large number of peaks. The most absorbing modes are at 2.8 THz for the B_{2u} representation and 3 THz for the B_{3u} representation. The B_{2u} mode is an antisymmetric breathing mode of the molecule. The B_{3u} mode corresponds to an asymmetric stretching of the $Fe - N_{phen}$ bonding and torsion of the Fe-NCS bonding. While I used those results in this result I didn't participate in this experiment.

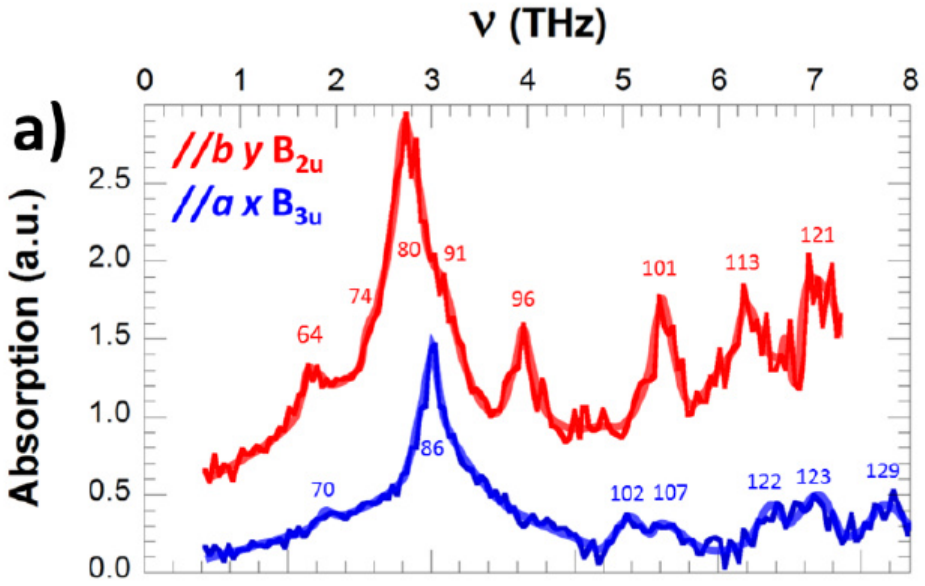

Figure 4.18: Absorption spectra of $Fe(phen)_2(NCS)_2$, the electric field parallel to b corresponds to the B_{2u} representation while the electric field parallel to a corresponds to the B_{3u}. Figure adapted from [91]. The numbers are the modes number which description can be found in Table 2 of reference [91]

4.3.2 Time Domain Spectroscopy of $Fe(phen)_2(NCS)_2$ using Optical Rectification

In Rennes, we performed another TDS measurements focused on the low frequency region that was not observable in the previous data. We performed only measurements for the electric field parallel to the crystal b direction. The time domain electric fields are shown in Fig.4.19.

The crystal thickness was evaluated to around 10 μm, this explains why the electric field through the $Fe(phen)_2(NCS)_2$ is delayed far less than for the BCPS. However, the main peak is strongly altered as well as the oscillations.

In Fig. 4.20 is presented the Fourier Transform of the waveform presented in Fig. 4.19. An Hanning window has been used to cancel the effects of the reflection. For both curves, the solid line represents the Fourier Transform of padded waveform, the dots points are the Fourier transform of the data within the window. The red curves are the reference. The blue curves are the field observed through the $Fe(phen)_2(NCS)_2$ with the polarization parallel to the b axis of the crystal. As the pulse duration of our probe is 35 fs, we choosed a 50 fs step size for the temporal waveform. This translates to a frequency range of 10 THz for our Fourier Transform. The spectral resolution can be obtained from the unpadded data. We obtain a 0.1 THz frequency resolution. The main limitation for the spectral resolution is the reflection of the ZnTe. We can observe a strong absorption peak around 1 THz in this curves. Moreover, the coincidence between padded and unpadded data confirms the existence of this mode and that it is not an artifact from Data Treatment.

In Fig.4.21, the Optical density is presented. This Optical Density was taken using the following equation :

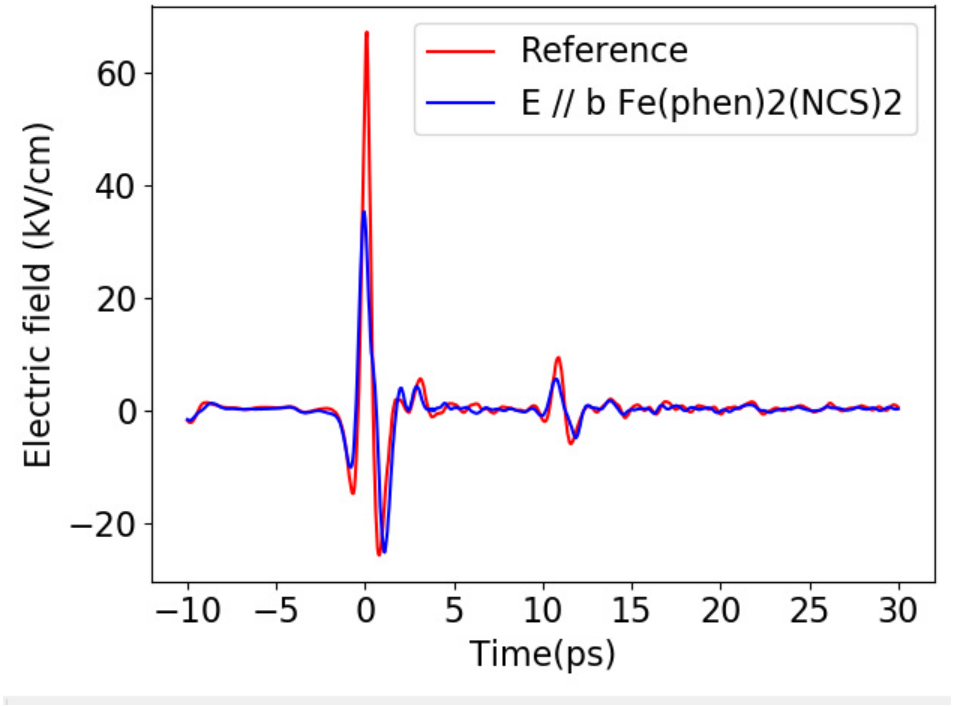

Figure 4.19: Reference scan (blue) and scan on $Fe(phen)_2(NCS)_2$ (red).

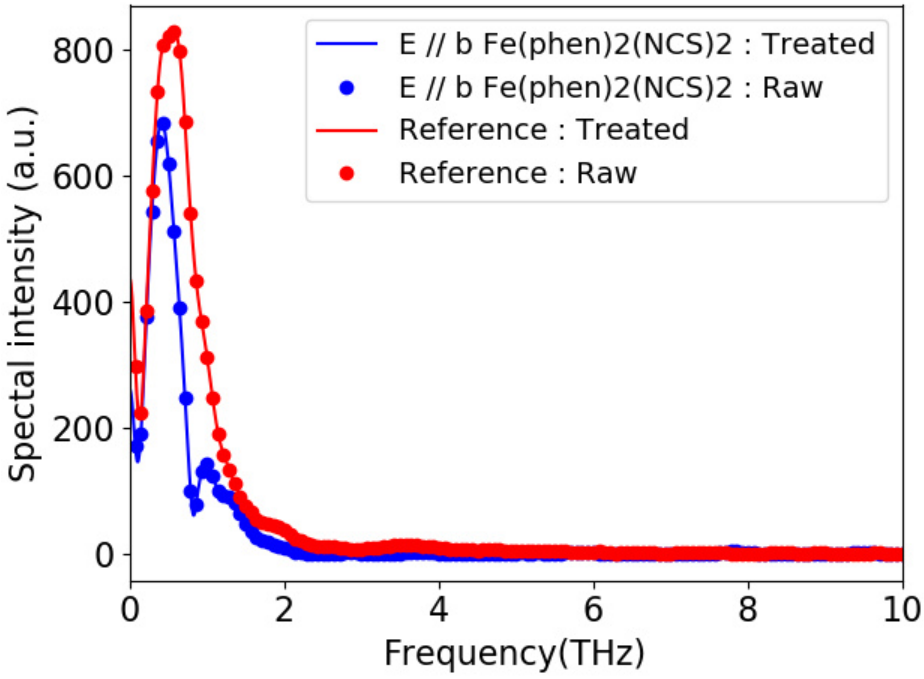

Figure 4.20: Fourier Transform of the time traces presented in Fig.4.19.

$$OD = -log_{10}\frac{E_sample}{E_{ref}} \tag{4.6}$$

In addition to the mode around 1.7 THz reported by Collet et al, our THz source

with intense signal around 1 THz allows observing two additional modes at 0.8 THz and 1.2 THz. This work has been done in preparation of the TeraFermi Experiment that will be explained in the next section.

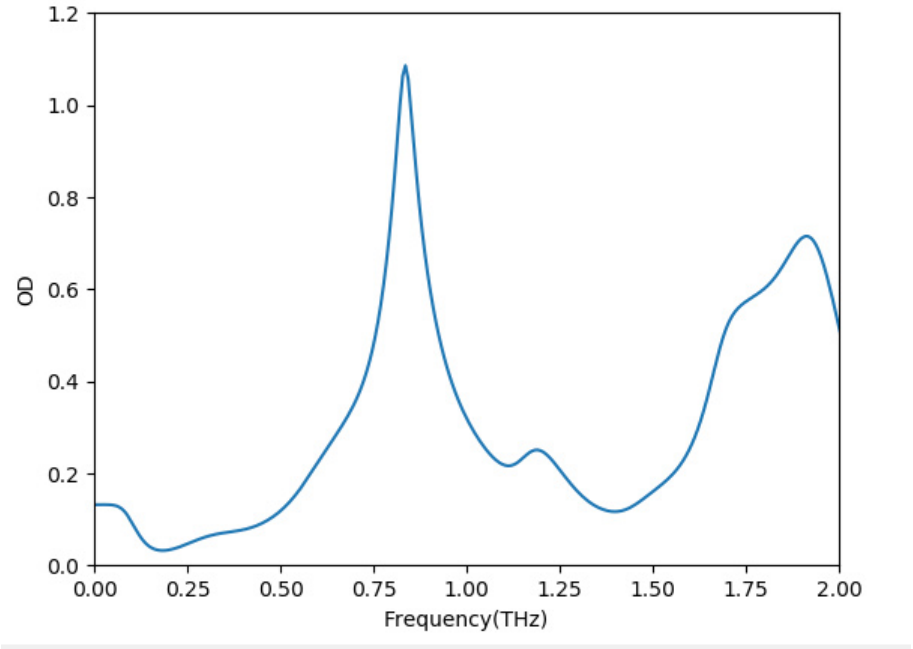

Figure 4.21: Optical density of the $Fe(phen)_2(NCS)_2$ for the B_{2u} representation in the low THz frequency range.

4.4 THz pump optical probe on $Fe(phen)_2(NCS)_2$

4.4.1 Photo induced phase transition in $Fe(phen)_2(NCS)_2$

The $Fe(phen)_2(NCS)_2$ is a compound which photoinduced phase transition have been widely studied in the past [8, 7, 6]. Most of these experiments were realized using visible light as a pump. The compound is initially in the Low Spin state then using ultra-fast techniques, the movie of the transition can be recorded. It has been demonstrated that for this compound the electron from the metal is promoted to the ligand orbitals, this is the Metal to Ligand Charge Transfer (MLCT). For the $Fe(phen)_2(NCS)_2$, this energy is around 500nm. Then, the system relax to multiple intermediates before reaching the High Spin state. The path that follows the system is presented in Fig.4.22.

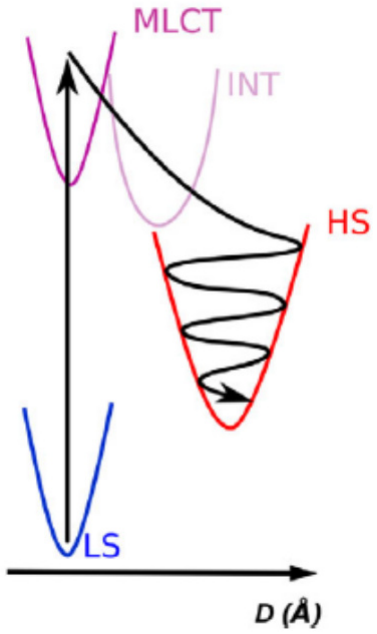

Figure 4.22: Path of the $Fe(phen)_2(NCS)_2$ compound after light irradiation adapted from [8]

When the system reaches the High Spin state, this is an highly excited state which increases the phonon modes populations. Once the phonon modes are populated, the vibrational cooling takes place. The phonons are generated coherently, this will raise oscillations which frequency is the one of the populated mode[8]. This can be seen in Fig.4.23. The oscillations observed are around 390 fs, the corresponding frequency is around 2.5 THz. This mode has been assigned to the symmetric torsion mode.

The $Fe(phen)_2(NCS)_2$ molecule possess a dipolar momentum which originates from the $(NCS)^-$ group and the Fe^2+. This creates a dipole along the b direction of the cell, which is also the C_2 axis of the molecule. The application of an external electric field on the molecule will acts on its dipole. As the dipolar momentum is directly linked to the distance between the Fe and the N this will be as acting directly on the reaction coordinate of this transition. Two possibilities can be used for the external electric field,

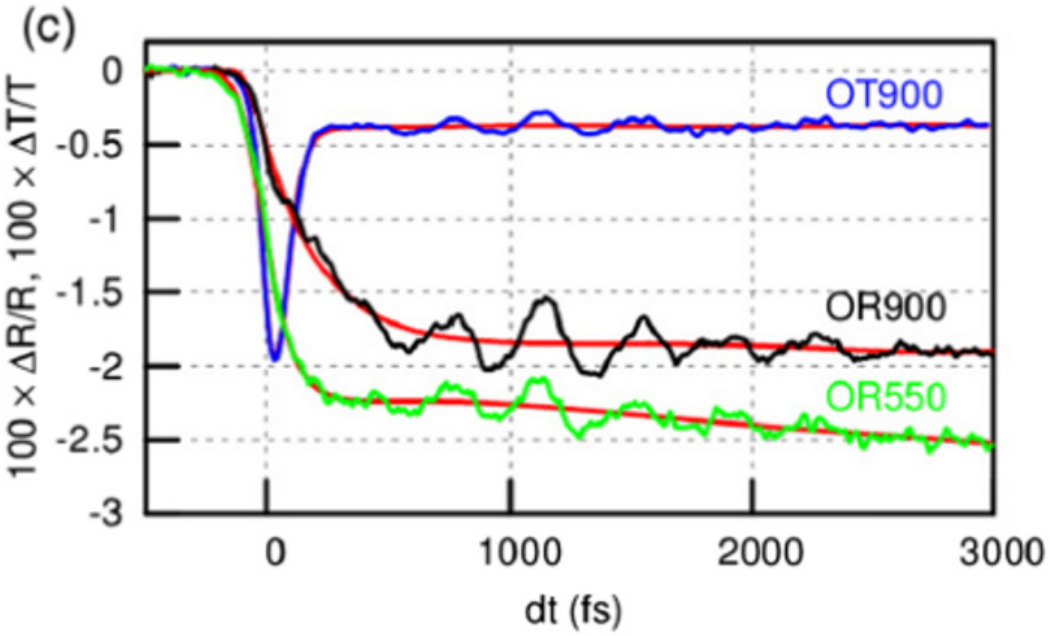

Figure 4.23: Change in Optical Transmission or Optical reflectivity at different wavelength adapted from [8].

an oscillatory electric field which frequency is in resonance with the potential well and an intense electric field out of resonance. In both cases the THz are the right tool to apply this electric field by using either narrow band THz or intense single cycle electric field.

In this section, I will present first preliminary numerical work used as a proof of concept for the THz pump experiment. Then, I will present the results obtained on a non centro symmetric spin crossover compound, the $[Fe(TPA)(TCC)]PF_6$. To conclude this section, results obtained at the TeraFermi Beamline on the $Fe(phen)_2(NCS)_2$ and results using a THz Pump Probe experiment will be presented and discussed.

4.4.2 Preliminary work : Numerical Simulation

In order to test the effect of an intense THz electric field on the $Fe(phen)_2(NCS)_2$, numerical simulations have been performed. The crystal symmetry includes an inversion symmetry. The inversion symmetry forces two opposite directions for the dipolar momentum. This is presented in Fig. 4.24.

By applying an electric field along the b axis, there will two opposites movements for the molecules as there are two opposite dipolar momentum.

$$m\ddot{x} = -\nabla V \pm E(t)x \tag{4.7}$$

x represents the distance between the metal and its ligand. V is the potential landscape of the molecule and E is the THz electric field. The $\pm$ sign is here to take into account the two opposite response of the dipole to the electric field. In this section, two potential landscape will be studied : first the simple case of an harmonic potential, second the case of a double well potential which is the case of the $Fe(phen)_2(NCS)_2$.

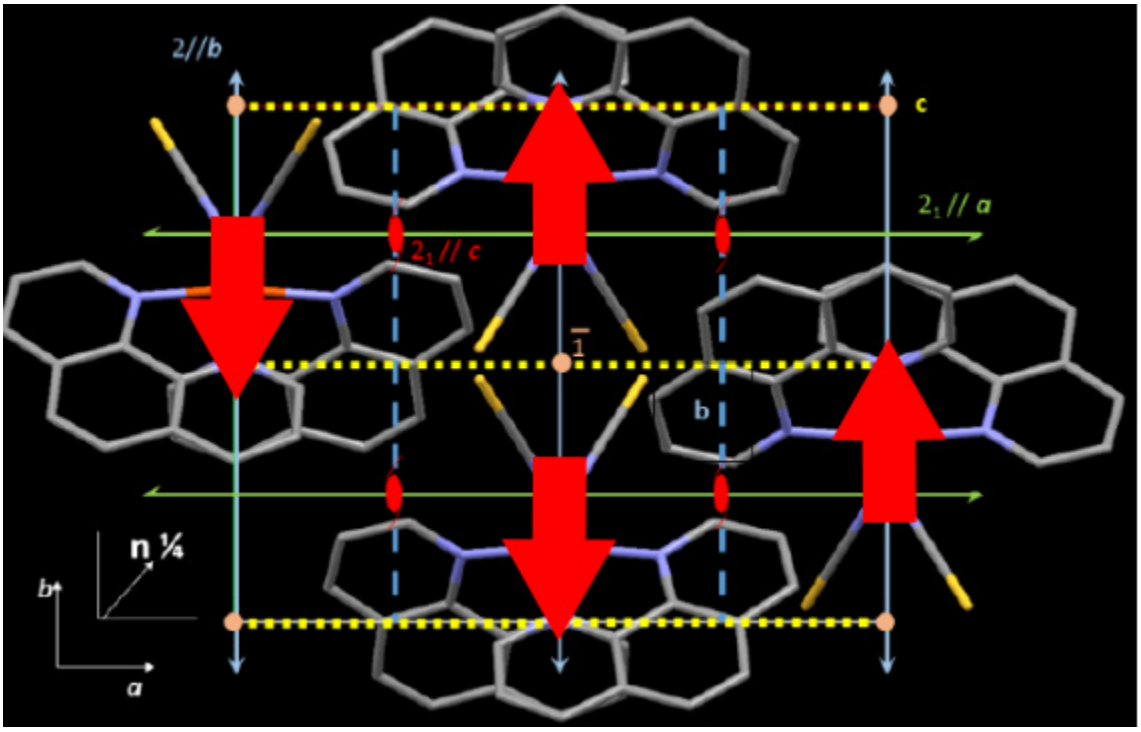

Figure 4.24: Picture of the unit cell of the $Fe(phen)_2 - NCS)_2$ crystal. The picture is shown in the ab plane. Symmetry elements are represented. The red arrows represents the dipolar momentum of the molecule. This figure is based on the figure from Collet et al.[91]

Single potential well

The case of the single potential well corresponds to the molecule deeply in one of the states. The potential energy used in this case is a simple harmonic well :

$$V = \frac{1}{2}kx^2 \tag{4.8}$$

First, let's take into consideration a constant electric field starting at time 0 applied on the sample. This can be seen as the effect of the electric field at each time t. The effect on both types of molecules up and down is presented in Fig. 4.25

In this case, the molecules are either compressed or expanded by the electric field depending if the molecule dipolar momentum is along or opposite to the electric field. Therefore, the electric field effect on the molecule results in a compression or dilatation of the molecule.

The potential well curvature is given by the resonance frequency of this well. This frequency is taken as the frequency of the breathing mode of the molecule. This is true in the case of the High Spin potential. We repeat the simulation for two electric field. The first one is in resonance with the potential well, the second one is far from the resonance of the well. The effects of such electric fields are presented in Fig. 4.26.

For both cases, the average distance is following the electric field. However, the amplitude of the displacement is more important in the case of resonant pulse (Fig.4.26a) than for the above resonance pulse (Fig.4.26b). This is the natural answer of any har-

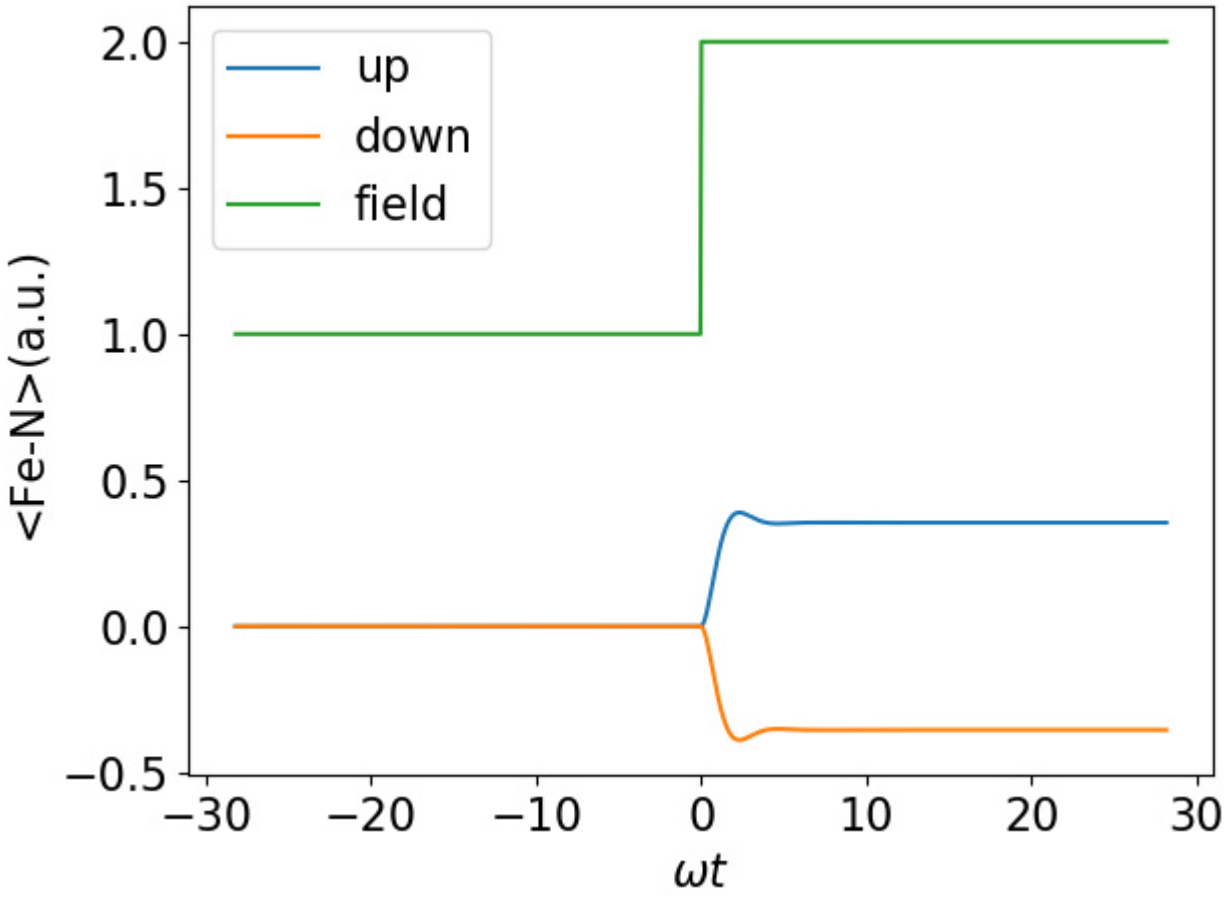

Figure 4.25: Effect of a constant electric field (green) on the average distance Fe-N for the case of molecules Up (blue) or Down (orange)

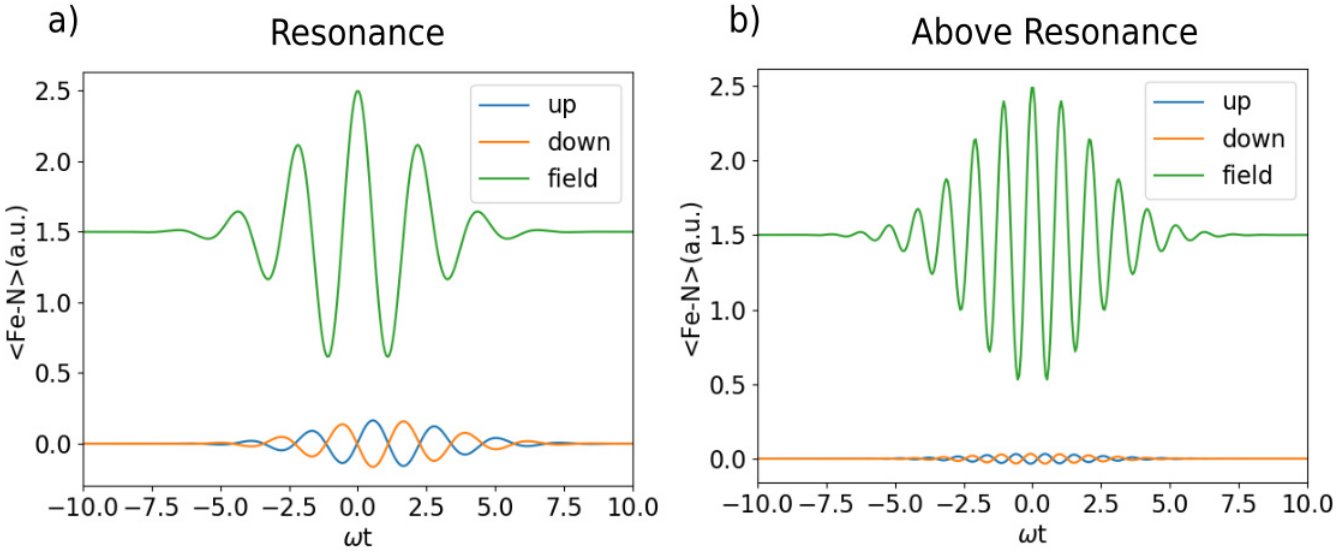

Figure 4.26: a) Case of the pulse in Resonance with the potential well. b) Case of the pulse out of resonance with the potential well.

monic oscillator to any external field. Now that the basis of the simulation are placed, a more realistic potential well can be used.

Double potential well

We consider the potential of the $Fe(phen)_2(NCS)_2$ compound as a double well potential along the <Fe-N> distance. We present the potential used in Fig.4.27. The first well is centered at 2.0 Å and corresponds to the Low Spin State, the second well is centered at 2.2 Å and corresponds to the High Spin State. the curvature of the High Spin well is chosen to corresponds to frequency of 2.8 THz which is the anti-symmetric breathing mode which can be excited by the THz pulse. The curvature of the Low Spin state is chosen to be stiffer (hardening of the mode) because of the compression of the molecule. This is backed-up by Ronayne et al that have demonstrated that at low temperature there is a increase of the frequency for most of the modes.[99] In this subsection, we will call the molecules which dipolar momentum is parallel with the THz electric field up and the molecules which dipolar momentum is anti parallel to the THz electric field down.

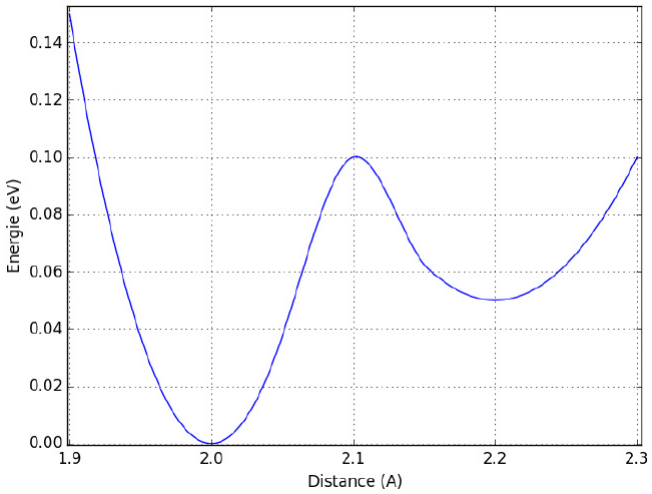

Figure 4.27: Double Well potential used in the simulation.

The initial condition we choose for this simulation is that molecules are initially at rest in the HS well, meaning that the average distance <Fe-N> is at 2.2 Å. We consider two different kinds of THz pulses: narrow band THz pulses which can be obtained in FEL using undulator, single cycle broadband pulses as the one obtained using Optical Rectification in $LiNbO_3$. We will first treat the case of the narrow band pulse. We consider two pulses, one pulse centered at the resonance of the High Spin well 2.8 THz. The other pulse frequency is chosen at 5.6 THz far from the resonance frequency. Results are presented in Fig.4.28.

In the case of resonant THz pulse, <Fe-N> is oscillating following the electric field with large amplitude. The amplitude of the movement is large enough to bring the molecule from the HS well and trapped them into the LS well. Around t=0 the difference in distance between the molecules Up and down is maximum. This means that around time zero, the inversion symmetry is broken and can be observed by the polar modes.

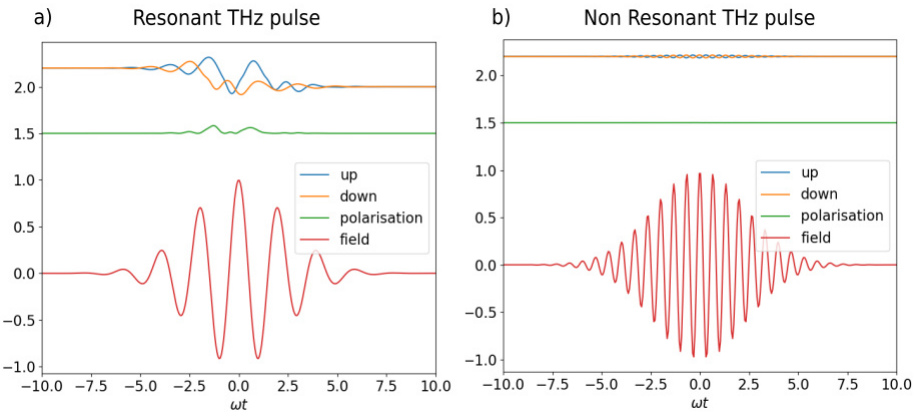

Figure 4.28: a) Case of Resonant THz electric field. b) Case of non resonant THz electric field. For both figures, the used electric field is presented in red above the modulation for both molecules up and down. The squared difference of distance between the molecules is plotted below.

For an above resonance THz pulse, the effect is very similar to the case of a single well potential and the molecules stay trapped in the High Spin well. The molecules motion can't follow the field. The polarization (the squared difference of distance between the molecules) is non zero during the pulse. The effects of narrowband THz pulse can be probed in two ways. First, Second Harmonic Generation can be used to probed the temporary break of the inversion of symmetry caused by the pulse. Because molecules are trapped in the LS state, X-rays can be used to probe a change of volume in the whole crystal.

The case of broadband THz pulse is presented in Fig.4.29. Here again, the molecules are following the electric fields in opposite ways. The Up molecules are trapped inside the Low Spin well while the Down molecules are trapped inside the High Spin well. In this case the difference in distance is way more important inducing an important polarization in the crystal. Moreover, this out of equilibrium polarization is induced for a time which is longer than the duration of the external THz electric field. This phenomenon can be probed optically with Second Harmonic Generation in the same way than for narrowband. Unlike the narrowband case, the break of symmetry should be longer than the electric field duration. This implies that the Second Harmonic Generation should be probed for a longer time than the narrowband case Because of the loss of inversion symmetry, the crystal symmetry group change from Pbcn to Pb2n. This will allows the emergence of Bragg peaks, (h0l) l = 2n+1 and (h00) h=2n+1.

The only way to use X-rays to probe such changes is the use of fs X-Ray. Indeed, in those simulations we haven't take into considerations the time required to relax to the real ground state. Also, as the most changes induced by the THz pulse are centered in a few ps, using sub ps pulses as probe is mandatory. X-FEL are the only place in the world where such X-Rays can be fount. On the other hand, Second Harmonic Generation is a technique of choice to observe the effect of a THz pulse on the $Fe(phen)_2(NCS)_2$ compound and can be performed in the laboratory as ultra-fast optical laser are more common nowadays. The choice of Second Harmonic Generation probing was made to obtain first results before going to Large Scale Facilities. First, we study the Second

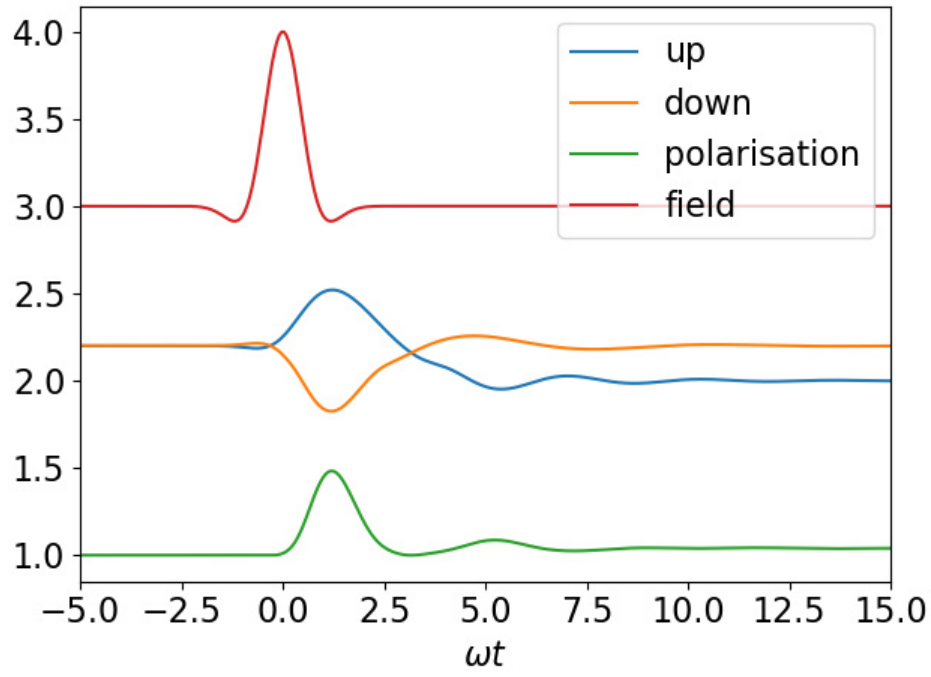

Figure 4.29: Case of Broadband THz pulse.

Harmonic Generation in a spin Crossover compound which no inversion symmetry, the $Fe(TPA)(TCC)PF_6$. Then, we realized THz - Pump Optical Probe experiment on the $Fe(phen)_2(NCS)_2$ compound.

4.4.3 Second Harmonic Generation in $[Fe(TPA)(TCC)]PF_6$

Crystal structure

The $[Fe(TPA)(TCC)]PF_6$ is a Fe^{3+} spin crossover compound. The thermal spin transition of this sample is from a LS state S = 1/2 to an HS state S = 5/2. This system can form two different polymorph : a monoclinic ($P2_1/a$) and a orthorombic ($Pna2_1$). The spin crossover temperatures of the two polymorphism differ, T = 203K for the orthorombic sample and T = 214K for the monoclinic.[102] The crystal consists of cation layers which alternates with an anion PF_6 layer. The orthorombic which point group is $Pna2_1$ presents a lack of inversion symmetry which allows a dipolar momentum along the c axis in the crystal. A picture of the crystal in the bc plane of the unit cell is presented in Fig.4.30.

Thanks to the structural feature of the $[Fe(TPA)(TCC)]PF_6$ compound, this compound was chosen to generate Second Harmonic as a test experiment. The $[Fe(TPA)(TCC)]PF_6$ orthorombic polymorph looks like a small plate which long axis is a and short axis is b. A picture of the crystal is shown in Fig. 4.31.

Second Harmonic Measurements

We used 800 nm light to measure the Second Harmonic in this compound, this implies that we want to measure 400 nm light. Similarly to $Fe(phen)_2(NCS)_2$, the

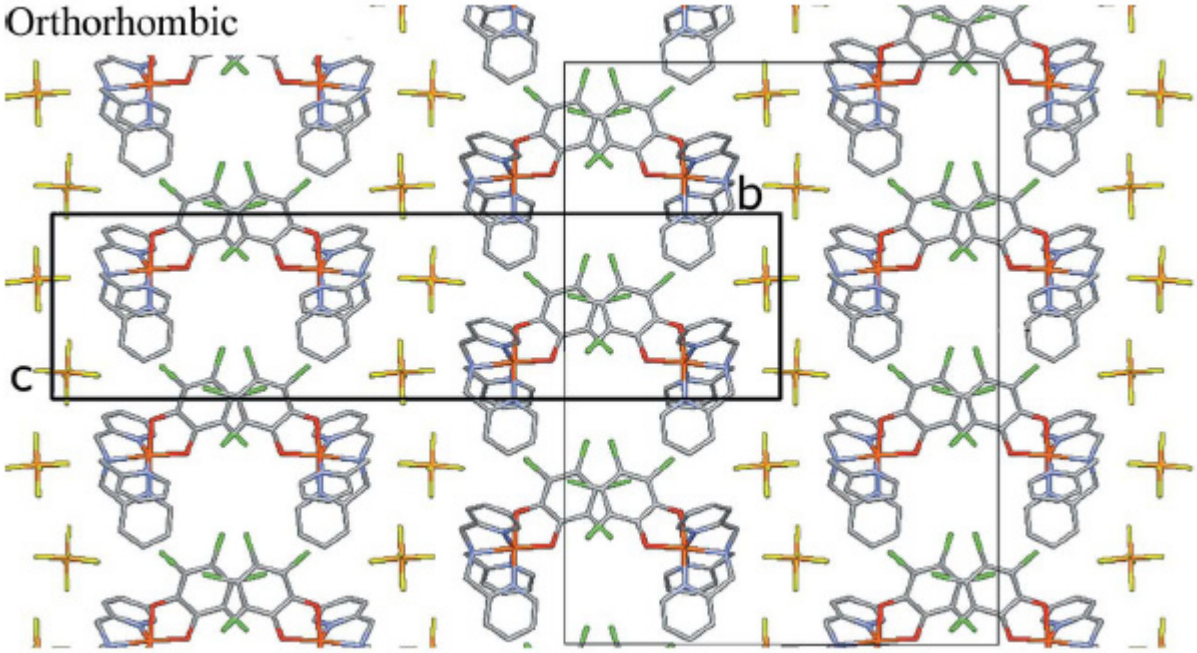

Figure 4.30: $[Fe(TPA)(TCC)]PF_6$ unit cell in the bc plane. The PF_6 anions are the yellow crosses while the cation is the [Fe(TPA)(TCC)] part.Figure adapted from [102]

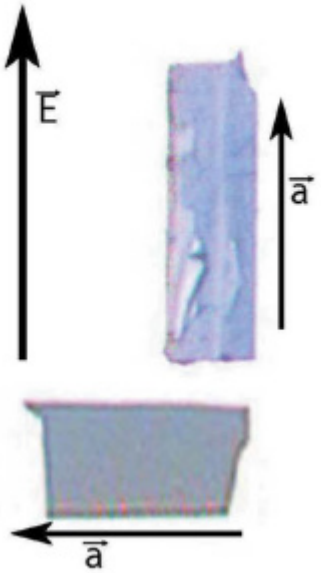

Figure 4.31: Picture of a $[Fe(TPA)(TCC)]PF_6$ orthorombic polymorph crystal. The crystal aspect depends on the light polarization. The a axis is the long axis and the c axis is the short one. Figure adapted from [102]

$[Fe(TPA)(TCC)]PF_6$ compound absorbs light around 400 nm that includes photon generated from Second Harmonic. Therefore, Second Harmonic Generation cannot be

detected in transmission as most of the photons will be absorbed as soon as they are generated. As such, reflection is the only possibility to observe in this compound Second Harmonic from 800 nm. However, as we expect the number of photons generated by Second Harmonic to be quite low even in reflectivity, a Photo-Multiplier Tube (PMT) was used to increase the signal even if a few photons only reach the detector. The experimental set-up is presented in Fig.4.32

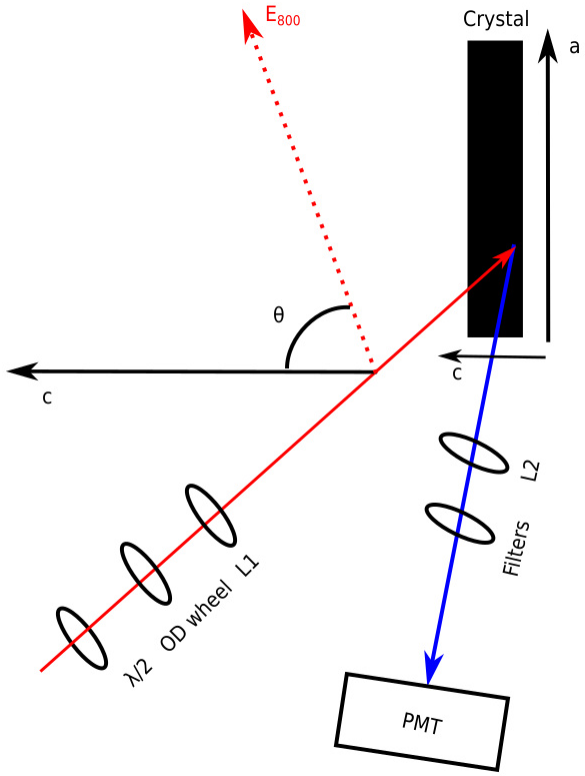

Figure 4.32: Scheme of the experimental set-up used for testing SHG in $[Fe(TPA)(TCC)]PF_6$. L1 and L2 are two convex lens of 5 cm focal length. PMT is the photo-multiplier tube. The red dashed line is the polarization direction of the light, the θ is the angle between the polarization of light and the c axis of the $[Fe(TPA)(TCC)]PF_6$

We used an halfwave blade to control the polarization and an OD wheel to control the power of the 800 nm light. A set of filters was placed in front of the PMT in order to only let through 400 nm light. The PMT was also shield to avoid the detection of parasitic light. Finally, all the experiment was performed with as little light as possible for the same reason. The crystal was glued on a glass plate. A camera was used to ensure the alignment between the crystal and the laser. The glass plate was used to find and align the reflection on the PMT. The measurement procedure is then the same than for the one exposed in the BBO section. The experimental results are presented in Fig.4.33.

We observe in Fig.4.33 the same behavior as for BBO. The intensity of the signal is quadratic with the energy while the intensity of the signal depending of the polarization is proportional to a sin^2. Moreover, the signal is maximum when the polarization is along the c axis of the crystal as expected. This is backed up by the fit of the data. This demonstrates than Second Harmonic Generation is possible in Spin Crossover

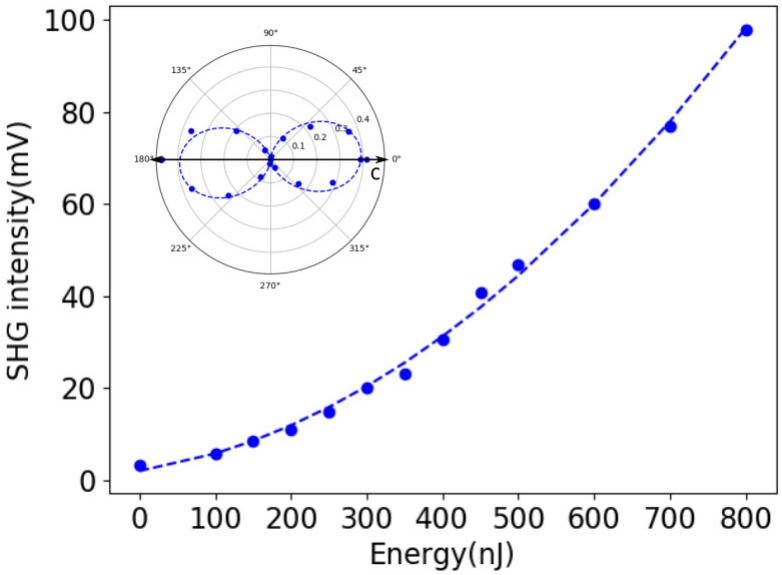

Figure 4.33: Linear plot : Intensity dependence of the SH signal on the PMT. The dashed line is a fit of the data. Polar plot : Intensity of SH signal as a function of the angle between polarization and crystal axis. The dashed line is a fit of the data. The c axis of the crystal is shown in black

compound even if difficult to measure.

This experiment has been reproduced at Tanaka Lab in Kyoto on another experimental set-up. The results were the same on those data which supports the earlier argument. We used the THz Air plasma source (see Fig.4.17) to try a THz Pump Second Harmonic probe experiment. The idea was to modulate the second harmonic generation of $[Fe(TPA)(TCC)]PF_6$ using THz light. Unfortunately, the experiment was unsuccessful. We think that the cause might be to the shape of the THz air plasma. Indeed, the fast oscillations(less than 100 fs) linked to the High frequency of the spectra are too short for the atomic motions to have the time to respond. This integrates their movements to be close to zero which might explains why we didn't get any signal.

The preliminary works being successful, I did two experiment on the $Fe(phen)_2(NCS)_2$, the first was conducted at the TeraFermi Beamline and the second in Rennes.

4.4.4 THz pump optical probe experiment and perspectives

The Second Harmonic Generation in the $Fe(phen)_2(NCS)_2$ compound is an experiment that requires an heavy set-up. Because of the Optical rectification THz generation technique that we have in Rennes, a lot of Second Harmonic of the Optical pump for the THz is shined in the box. Therefore, a lot of 400 nm light could be detected by the Photo-Multiplier Tube. As such wavelength within a range of 400 to 1600 nm as to be used to generate photon in the 400 - 800 wavelength. As the stability of our TOPAS is lower in this wavelength range and the alignment of reflection crystal in the infrared is delicate, a first THz Pump Optical Transmission was first decided to be conducted. The crystal symmetry induces two dipole orientations, therefore the THz electric field will induce two opposite movements of molecules. The molecules will have opposite

directions in the potential. One set of molecules will absorb more, while the other set will absorbs less. Because of the non linearity of the potential, they will be not displaced with an equivalent amount and as such the energy split will differs which will allows a change in the optical absorption in this compound. This argument is resumed in Fig.4.34.

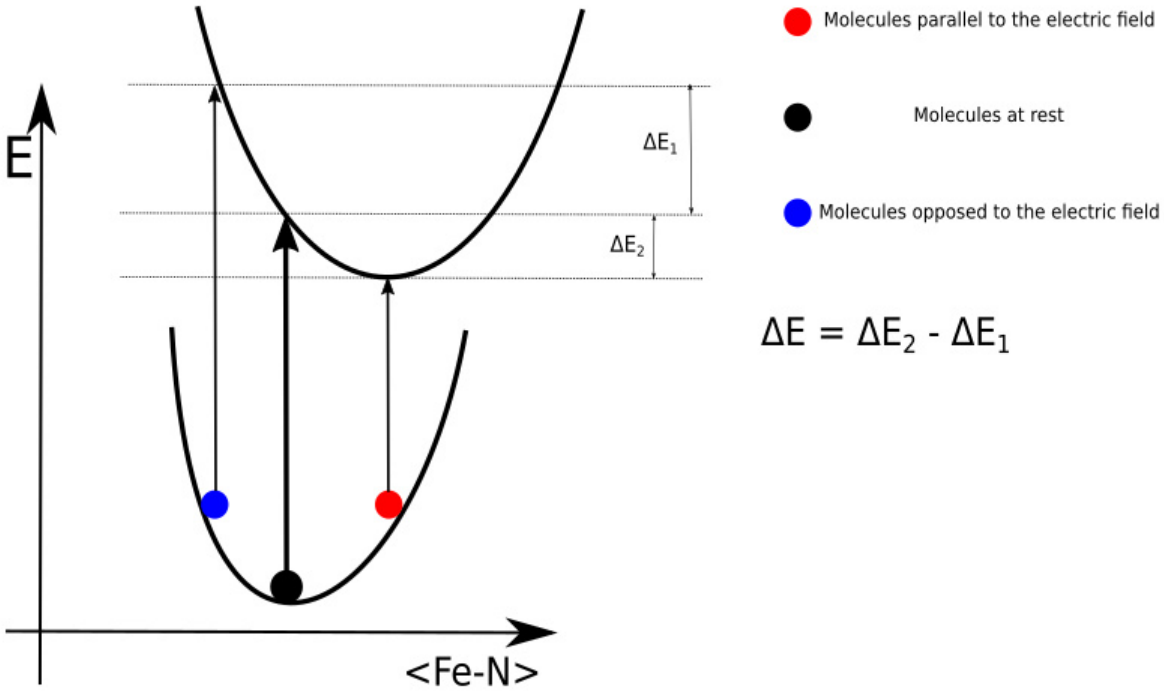

Figure 4.34: Energy profile of the $Fe(phen)_2(NCS)_2$, 3 types of molecules are presented. The black molecule is the molecule at rest without electric field applied, the red molecule is the molecule which dipolar momentum is parallel to the electric field, the blue molecule is the molecule which dipolar momentum is anti-parallel to the electric field.

Because of the inversion symmetry of the molecule, only the absolute value of the field will matter in the signal.Set E_{THz} to be an arbitrary value of the electric field. Let's assume E_{THz} to be positive, then the first half S_1 of the molecule will absorb more while the other half S_2 will absorb less. If E_{THz} is negative, S_1 set of molecules will absorb less while S_2 will absorb more. Those situations are one and the same as S_1 and S_2 contains the same number of molecules by symmetry. Therefore, the signal expected from this experiment is expected to be the absolute value of the THz electric field or the square of the Electric field.

We realized this experiment with a probe light wavelength of 740 nm. The THz electric field value was of 300 kV/cm for this experiment. The Experimental Set-Up is the same that for the experiment with the V_2O_3 compound. The Pump and Probe polarization were aligned parallel to each other along the b axis of the crystal. The results obtained is presented in Fig.??. The THz pump electric field is plotted as reference on the figure. The measured signal is completely following the THz electric field and as such the measured signal is linear with the THz electric field.

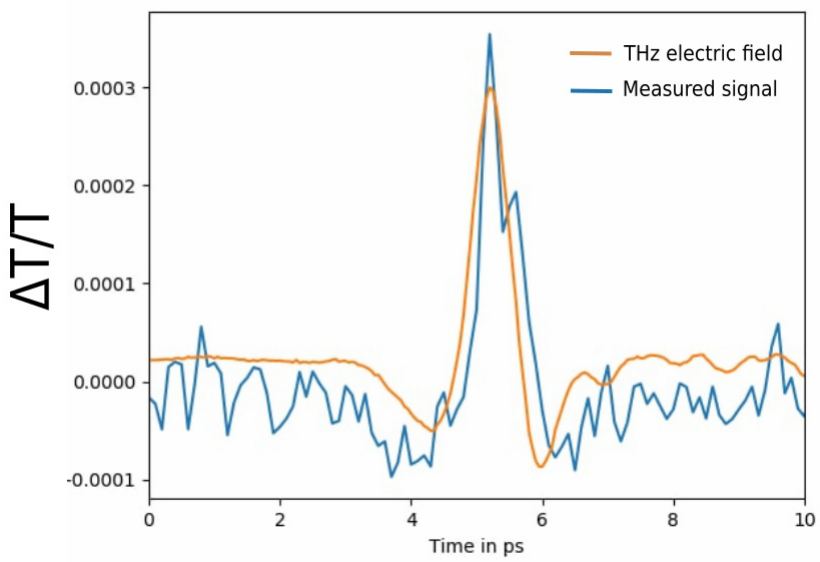

Figure 4.35: Measured signal at 740 nm in blue, THz pump of this experiment measured with EOS in orange plotted as a reference.

This is in complete contradiction with the original idea of this experiment. This experiment represents though the first result obtained on a Spin Crossover compound using THz pump optical probe experiment/

No SHG experiment have been done on this compound because of the lack of remaining time of this PhD thesis.

4.5 Conclusion

To conclude this chapter, the symmetry and vibrational modes of a Spin crossover compound, the $Fe(phen)_2(NCS)_2$ were discussed. First, we studied this compound using Raman Spectroscopy, this allowed us to study in a new way the Light Induced Exited Spin State Trapping (LIESST) effect. Possibility to investigate the LIESST processes in SCO materials well above T(LIESST) under high light fluence. A simple model explains that, for no or weakly cooperative systems, a photo-stationary half photo-conversion is observed when the when the number of absorbed photons per second equals the relaxation rate. With this respect, μ-Raman technique allows observing LIESST at lower cost by using liquid-nitrogen operating cryostats instead of He-operating ones, without using sophisticated time-resolved technique and with the possibility to investigate micro-crystals. Tracking how photo-stationary half-conversion evolves with temperature and light fluence is then another approach for measuring HS $\rightarrow$ LS thermal relaxation rates.

The Time Domain Spectroscopy in the THz region was explained as well as the data treatment we used and showed that the use of two different THz light sources allows to cover a larger part of the THz spectra.

A first THz pump optical probe experiment was realized on the $Fe(phen)_2(NCS)_2$ compound. We first realized some numerical simulations to determine the effect of a

THz electric field on the compound. We were able to determine that the electric field should break the inversion symmetry and change transiently the distance between the Fe and the ligand. To prepare this experiment, we realized a measure of Second Harmonic Generation on the $Fe(TPA)(TCC)PF_6$ compound which has no inversion symmetry. We were able to measure Second Harmonic Generation in this compound by using a Photo Multiplier Tube as the number of SHG photon is small. We went to the TeraFermi Beamline to try measure a change in the THz Spectra of the $Fe(phen)_2(NCS)_2$ compound under intense THz electric field but were not able to because of jitter issues. Finally, we observed the first THz pump optical probe signal on the $Fe(phen)_2(NCS)_2$ compound. This result is promising but the interpretation is hard. Indeed, the signal is linear with the THz electric field which is in contradiction with the inversion symmetry of the crystal.

General conclusion and Perspectives

This PhD project was first focused on the building of an intense THz source. The choice of Optical rectification in $LiNbO_3$ using the tilted pulse front technique. This technique presents the advantage of having an intense single cycle electric field that can reach up to 1.2MV/cm and an associated broadand spectra that is suitable for THz-TDS in the range 0-2 THz. This choice was made over organic crystal such as DSTMS or DAST because of the laser characteristics available in our laboratory. We choosed the Electro-Optical sampling detection technique for an easier implementation of the experimental set-up.

The development of the THz source was a success. An electric field value of 800kV/cm was obtained using this source. The beam was focused on a 800 μm spot which was close to the smallest possible spot that can be obtained with our experimental condition. A THz-TDS set-up was built and caracterized using the bi chlorophenylesulphone (BCPS) crystal. The THz set-up was also coupled to a cryogenic system which helped the characterization of the THz-TDS branch. As such the primary objective of this PhD project was fulfilled.

The analysis of the modes of the $Fe(phen)_2(NCS)_2$ spin crossover compound led us to the study of the LIESST effect in the same compound. We understood that LIESST can be studied above the standard T(LIESST) temperature with sufficient laser fluence for the measure. This result will prove to be useful to study LIESST as study using He are expansive and ultra fast techniques are not available in most laboratories.

The study of the $\beta-BaryumBorate$ was performed with a very intense electric field. The results were comparable with the one obtained in the literature. By allying the study of the crystal using THz-TDS and THz pump probe experiment we were able to explained the splitting of the THz pulse in two. Moreover, a lead towards high harmonic generation of the THz frequency using BBO was observed. This study allowed us to ally both THz-TDS technique and THz pump probe technique to understand PIPT in this system. Those results proves the complementary of the two techniques and demonstrate the need to have both techniques available in the laboratory.

The photo-induced signal observed in V_2O_3 is observed on a different time scale than BBO. BBO is a non resonant response that is only following the THz electric field in a few ps. In V_2O_3 the time scale is two decades up with signal lasting for 200 ps. This result was explained by strain waves generated through Joule heating generated by the THz pulse. Further studies on this compound has been conducted by Guenole Huitric and will be discussed in its PhD Thesis. Those studies include THz intensity measurement, change of sample and substrate and theoretical models.

Those two experiments allowed to validate the use of the THz source built in this work to perform experiments on compounds that were not studied yet using THz either

as a pump or as a probe. To finish this project, the focus was made on a spin crossover compound : the $Fe(phen)_2(NCS)_2$.

THz-TDS was performed on the $Fe(phen)_2(NCS)_2$ spin crossover compound using both an Air-plasma source and the THz-TDS set-up I built in Rennes. The Air-plasma source which is very broadband allows to measure a lot of vibration mode. However, it is not suited for the low frequency THz region namely sub 1.5 THz. Two vibrational modes were observed using the Set-UP in Rennes which were not observed using the THz-Air Plasma. This shows the complementary between generation techniques that have to be used for a full study of the THz modes.

Finally, numerical study and experiment were performed on the $Fe(phen)_2(NCS)_2$ compound to predict the experimental results that we would obtained. However, the results that we obtained were not in concordance with our predictions. This implies that the study of this compound is only at its beginning. To complete the study of this compound, THz pump Second Harmonic Probe should be realized. Such results could be compare with the second Harmonic Generation measured in the $Fe[TPA-TCC]PF_6$. In an other hand, the modulation of Second Harmonic Generation of the same compound with the THz could be measured to have a better understanding of the phenomenon in Spin Crossover system. The ultimate goal of the study in those compound would be the use of X-Ray obtained at LCLS or SwissFel coupled to a THz pump. Using X-ray might be a better tool to observe the wanting phenomenon.

A way to continue this PhD work would be to change completely the family of compound studied. As stated in the introduction, ferromagnet and anti-ferromagnet have properties that can be probed with THz. The multi-ferroic compounds are quite interesting for the coupling between their properties. The $BiFeO_3$ compound presents both ferroelectricity and magnetic ordering. An idea is to trigger magnetic events using only the polarization of this compound. We performed non linear THz-TDS as a first experiment to observe the effects of the THz electric field on the spectra. The results are presented in Fig.4.36.

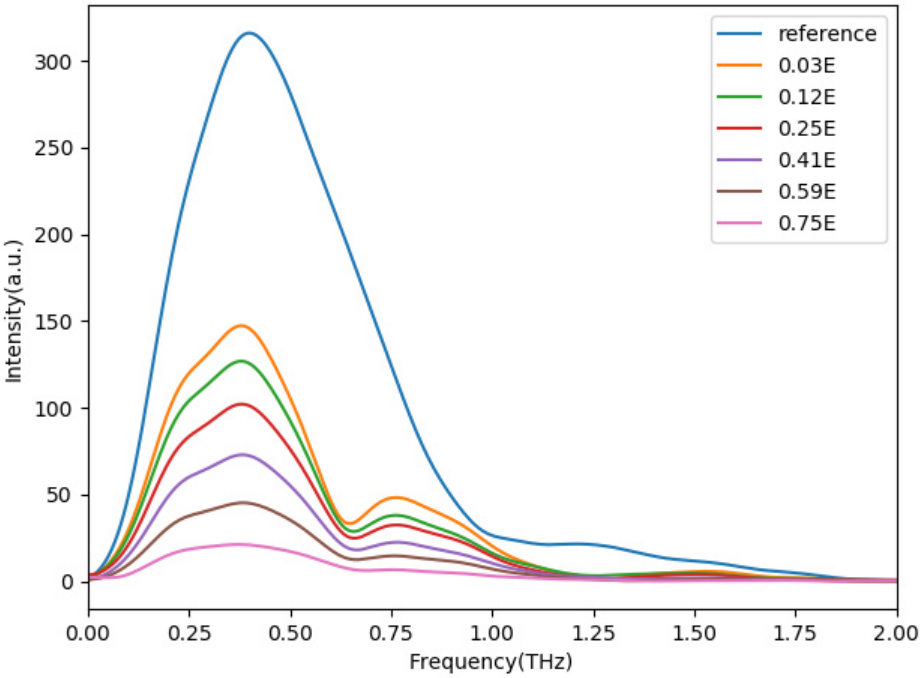

Figure 4.36: Spectra of the $BiFeO_3$ compound taken for different values of the THz electric field.

We observe three modes, the first at 0.3 THz, the second at 0.65 THz and the last at 1.25 THz. We observed a strong non linearity on the mode at 0.65 which is narrower and shifted towards lower frequency. Those results have not been fully studied yet. However, they are the first step for a further study on such compound using the THz source built during this PhD source.

The results obtained in this PhD work are very diverse and prove that the THz can be used in a large scope of materials or physics. The use of THz in all the field of physics will continue to grow over the years until THz becomes an as common technique in photo induced phenomena as any others.

Appendix A

EOS derivation

A.1 The linear electro optic effect

So far, equations were written as scalar quantities. But, when going through vectors one need to rewrite the equations.

$$P_i = \sum_j \chi_j^{(1)} E_j + \sum_{j,k} \chi_{ijk}^{(2)} E_j E_k + ... \tag{A.1}$$

The k-th optical susceptibility becomes a tensor of rank k.
Let's rewrite the relation between D the displacement vector and E.

$$\overrightarrow{D} = \hat{\epsilon}\overrightarrow{E} \tag{A.2}$$

Here $\hat{\epsilon}$ represents a matrix. In a lossless non-optically active material, this matrix is real and symmetric, this implies that there exists a set of coordinates which diagonalize the matrix. Let the new set of coordinates be (X,Y,Z). We can write :

$$\begin{pmatrix} D_x \\ D_y \\ D_z \end{pmatrix} = \begin{pmatrix} \epsilon_{XX} & 0 & 0 \\ 0 & \epsilon_{YY} & 0 \\ 0 & 0 & \epsilon_{ZZ} \end{pmatrix} \begin{pmatrix} E_x \\ E_y \\ E_z \end{pmatrix} \tag{A.3}$$

The energy density write itself as :

$$U = \frac{1}{8\pi}\overrightarrow{D}.\overrightarrow{E} = \frac{1}{8\pi}(\frac{D_X^2}{\epsilon_{XX}} + \frac{D_Y^2}{\epsilon_{YY}} + \frac{D_Z^2}{\epsilon_{ZZ}}) \tag{A.4}$$

Here, we use the principal axis which are easier to use because the matrix is diagonal. Writing the coordinates (X,Y,Z) as :

$$X = \left(\frac{1}{8\pi U}\right)^{1/2} D_X, \quad Y = \left(\frac{1}{8\pi U}\right)^{1/2} D_Y, \quad Z = \left(\frac{1}{8\pi U}\right)^{1/2} D_Z \tag{A.5}$$

Then equation (A.3) becomes :

$$\frac{X^2}{\epsilon_{XX}} + \frac{Y^2}{\epsilon_{YY}} + \frac{Z^2}{\epsilon_{ZZ}} = 1 \tag{A.6}$$

The ellipsoid describes by this equation is known as the optical indicatrix. When not in the principal axis, the most general form of this equation become :

$$\left(\frac{1}{n^2}\right)_1 x^2 + \left(\frac{1}{n^2}\right)_2 y^2 + \left(\frac{1}{n^2}\right)_3 z^2 + 2\left(\frac{1}{n^2}\right)_4 yz + 2\left(\frac{1}{n^2}\right)_5 xz + 2\left(\frac{1}{n^2}\right)_6 xy \quad \text{(A.7)}$$

The $(1/n^2)_i$ are related to the ϵ_i through a change of coordinates. The derivation presents no real interest and will therefore be discarded.

The plane perpendicular to the propagation direction will cut the ellipsoid, the curve created is an ellipse which axis gives the values of the refractive indexes and the polarization of the D vector.

Studying the change in the optical indicatrix will help understand how the polarization is modified. First let's define the *impermeability tensor* :

$$\overrightarrow{E} = \hat{\eta}\overrightarrow{D} \quad \text{(A.8)}$$

This tensor is just the inverse of $\hat{\epsilon}$, he is also real and symmetric within the principal axis. We can rewrite the equation A.7 as :

$$\eta_{11}x^2 + \eta_{22}y^2 + \eta_{33}z^2 + 2\eta_{23}yz + 2\eta_{13}xz + 2\eta_{12}xy \quad \text{(A.9)}$$

Combining equations A.7 and A.9, we have equality between those elements. Let's assume that the impermeability tensor can be expanded into power series of the applied field. It follows :

$$\eta_{ij} = \eta_{ij}^{(0)} + \sum_k r_{ijk}E_k + \sum_{kl} s_{ijkl}E_{kl} \quad \text{(A.10)}$$

r_{ijk} is the tensor describing the linear electro-optic effect also known as Pockels and s_{ijkl} describes quadratic effects : the Kerr Effects, as the Kerr effects is low in the case we study we will discard those terms and set $s_{ijkl} = 0$. As the impermeability tensor is real and symmetric therefore $r_{ijk} = r_{jik}$. To simplify the writing, the third-rank tensor is then write as a two dimension matrix r_{hk} with notate :

$$h = \{ \begin{array}{rl} 1 & for \quad ij = 11, \\ 2 & for \quad ij = 22, \\ 3 & for \quad ij = 33, \\ 4 & for \quad ij = 23\, or\, 32, \\ 5 & for \quad ij = 13\, or\, 31, \\ 6 & for \quad ij = 12\, or\, 21, \end{array} \quad \text{(A.11)}$$

Those contracted notations follows the 1/n tensor and is completely related to it. Doing a simple substraction in A.10 one can write :

$$\Delta(\frac{1}{n^2}_i) = \sum_j r_{ij}E_j \quad \text{(A.12)}$$

Here Δ is representing the difference. This can be written explicitly as :

$$\begin{pmatrix} \Delta(\frac{1}{n_1^2}) \\ \Delta(\frac{1}{n_2^2}) \\ \Delta(\frac{1}{n_3^2}) \\ \Delta(\frac{1}{n_4^2}) \\ \Delta(\frac{1}{n_5^2}) \\ \Delta(\frac{1}{n_6^2}) \end{pmatrix} = \begin{pmatrix} r_{11} & r_{12} & r_{13} \\ r_{21} & r_{22} & r_{23} \\ r_{31} & r_{32} & r_{33} \\ r_{41} & r_{42} & r_{43} \\ r_{51} & r_{52} & r_{53} \\ r_{61} & r_{62} & r_{63} \end{pmatrix} \begin{pmatrix} E_x \\ E_y \\ E_z \end{pmatrix} \tag{A.13}$$

This is a set of 6 coupled equations to resolve which is practically very hard to solve. Fortunately, the symmetry of crystals allows some parts of the tensor to vanish and simplify this equation. Also notes that the Pockels effect can only occur in non-centrosymmetric crystal. Indeed, as everything is related to the dielectric tensor which is zero in centro symmetric crystal.

A.2 Application to Electro optical sampling in ZnTe

In our experiment, we are using ZnTe which crystalline order allows to write the electro optic tensor as :

$$\begin{pmatrix} 0 & 0 & 0 \\ 0 & 0 & 0 \\ 0 & 0 & 0 \\ r_{41} & 0 & 0 \\ 0 & r_{41} & 0 \\ 0 & 0 & r_{41} \end{pmatrix} \tag{A.14}$$

Using this tensor, one can rewrite the equation A.9 :

$$\frac{x^2}{n_x^2} + \frac{y^2}{n_y^2} + \frac{z^2}{n_z^2} + 2yzr_{41}E_x + 2xzr_{41}E_y + 2xyr_{41}E_z = 1 \tag{A.15}$$

As ZnTe is a cubic crystal, the n_i are equal between each others. Simplifying again the equation. All the equations are written in the ZnTe crystalline coordinates. To solve this equations, one needs to cancel the cross terms using change of coordinates.

$$x = \frac{x' + y'}{\sqrt{2}}, y = \frac{x' + y'}{\sqrt{2}}, z' = z, \tag{A.16}$$

(x,y,z) becomes (x',y',z') in this set of coordinates. Moreover, one can write $\overrightarrow{E_{THz}}$ as (see fig) :

$$\overrightarrow{E_{THz}} = E_{THz} \begin{pmatrix} \frac{sin\phi}{\sqrt{2}} \\ -\frac{sin\phi}{\sqrt{2}} \\ cos\phi \end{pmatrix} \tag{A.17}$$

The equation becomes :

$$\frac{x'^2 + y'^2 + z'^2}{n_0^2} + 2r_{41}E_{THz}sin\phi z'y' - r_{41}E_{THz}cos\phi(x'^2 - y'^2) \tag{A.18}$$

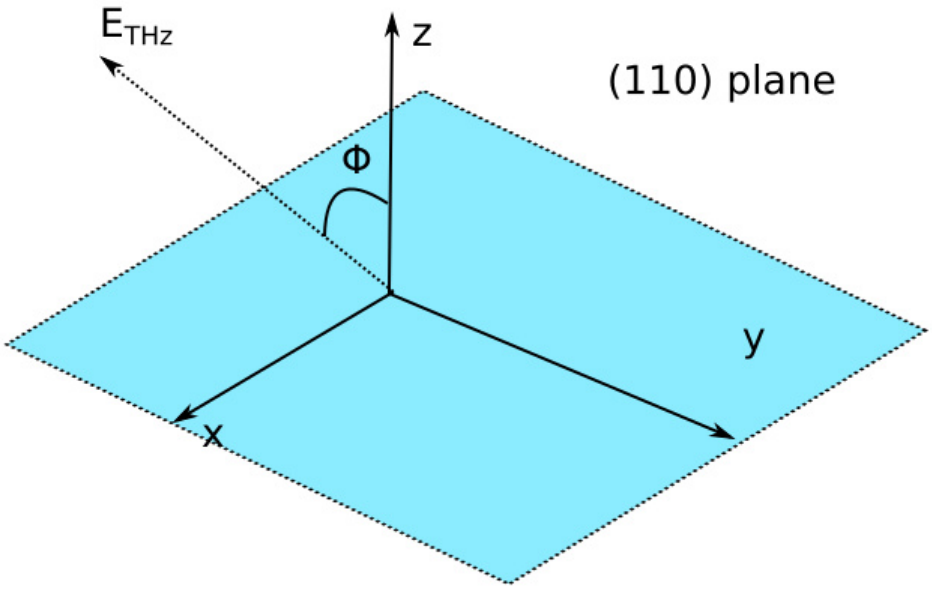

Figure A.1: Sketch of the situation, the electric field posses an angle between the z axis. The plane of paper is the (110).

$$x'^2(\frac{1}{n_0^2} + r_{41}E_{THz}cos\phi) + y'^2(\frac{1}{n_0^2} - r_{41}E_{THz}cos\phi) + \frac{z'^2}{n_0^2} + 2r_{41}E_{THz}sin\phi z'x' \quad \text{(A.19)}$$

One more rotation along x' is required to vanish the last cross terms. Let set this rotation angle to be θ. The new set of coordinates is therefore :

$$x' = x'', y' = y''cos\theta - z''sin\theta, z' = y''sin\theta + z''cos\theta \quad \text{(A.20)}$$

Expanding in the new set of coordinates one found the following expression in front of the cross-terms :

$$E_{THz}r_{41}(-cos\alpha\, sin2\theta + 2sin\alpha\, cos2\theta)y''z'' \quad \text{(A.21)}$$

For this equation to be zero, θ must obey the following relation :

$$2\theta = arctan(2tan\alpha) \quad \text{(A.22)}$$

We can finally write the equation without the cross terms :

$$
\begin{aligned}
& x''^2\left(\frac{1}{n_0^2}+E_{THz}r_{41}cos\alpha\right) \\
+\, & y''^2\left(\frac{1}{n_0^2}-E_{THz}r_{41}[cos\,\alpha\, sin^2\theta+cos(\alpha\,+\,2\theta)]\right) \\
+\, & z''^2\left(\frac{1}{n_0^2}-E_{THz}r_{41}[cos\,\alpha\, cos^2\theta-cos(\alpha\,+\,2\theta)]\right)
\end{aligned}
\tag{A.23}
$$

We can then rewrite the two refractive index :

$$
\begin{aligned}
n_{y''}(\alpha) &\approx n\,+\,\frac{n^3}{2}E_{THz}[cos\,\alpha\, sin^2\theta+cos(\alpha\,+\,2\theta)] \\
n_{y''}(\alpha) &\approx n\,+\,\frac{n^3}{2}E_{THz}[cos\,\alpha\, cos^2\theta-cos(\alpha\,+\,2\theta)]
\end{aligned}
\tag{A.24}
$$

From equation A.24 it is clear that the ZnTe becomes birefingeant under the THz electric field. Therefore, an optical probe will accumulates a phase difference under its two components ending with an ellipsoidal polarization. Using a quarter wave plate and a Wollaston Prism one can separate the two components.

The signal will end up being proportional to the phase difference of the two:

$$
\begin{aligned}
I_y &= \frac{I_0}{2}\left[1\,+\,sin(\frac{2\pi\Delta nl}{\lambda})\right] \\
I_z &= \frac{I_0}{2}\left[1\,-\,sin(\frac{2\pi\Delta nl}{\lambda})\right]
\end{aligned}
\tag{A.25}
$$

Where l is the crystal thickness. From equation A.24 it is clear that Δn is proportional to the THz electric field. We can therefore quantitatively measure the THz electric field from the difference of intensity from the photo diodes as :

$$
\frac{I_y-I_z}{I_y+I_z}=sin(\frac{2\pi l r_{41}n_0^3E_{THz}}{\lambda})
\tag{A.26}
$$

Note that we took the maximum of the signal here with the good orientation for both probe and pump.

Appendix B

Publication of the LIESST effect

Chemical Physics Letters 791 (2022) 139395

Contents lists available at ScienceDirect

Chemical Physics Letters

journal homepage: www.elsevier.com/locate/cplett

Shifting photo-stationary light-induced excited spin state trapping equilibrium towards higher temperature by increasing light fluence

Lucas Gournay [a], Ievgeniia Chaban [a], Jean-Yves Mevellec [b,*], Bernard Humbert [b], Etienne Janod [b], Laurent Guerin [a], Marco Cammarata [a], Nathalie Daro [c], Guillaume Chastanet [c,*], Eric Collet [a,*]

[a] Univ Rennes, CNRS, IPR (Institut de Physique de Rennes), UMR 6251, F-35000 Rennes, France
[b] Université de Nantes, CNRS, Institut des Matériaux Jean Rouxel, IMN, UMR 6502, F-44000 Nantes, France
[c] Univ. Bordeaux, CNRS, Bordeaux-INP, ICMCB, UMR 5026, F-33600 Pessac, France

ARTICLE INFO

Keywords:
LIESST
Spin Crossover
Photoinduced phenomena
Raman
Out-of-equilibrium

ABSTRACT

The Light-Induced Excited Spin-State Trapping (LIESST) process allows tuning the electronic state of spin-crossover materials from low (LS) to high spin (HS) states. The photoinduced HS state is long-lived, up to a characteristic temperature, T(LIESST), above which the system relaxes rapidly to the LS state. We study the effect of light irradiance on competing LS → HS up-conversion and HS → LS thermal relaxation on the [Fe(phen)$_2$(NCS)$_2$] system. Raman spectroscopy and magnetic measurements are used to investigate this phenomenon. An empiric model describes the competition between up conversion and thermal relaxation mechanisms and the stabilization of photo-stationary state towards higher temperature.

1. Introduction

Light is a tool to access states of matter, sometimes hidden at thermal equilibrium, which provides opportunities for photonic technologies. Spin Crossover materials (SCO) are textbook examples of bistable systems, which undergo spin-state conversion from low-spin (LS) to high-spin (HS) state [1–3]. The relative stability of HS and LS states is balanced under the effect of various external parameters, including temperature and pressure. For example, the LS to HS conversion at thermal equilibrium comes from the entropy change between LS and HS phases [4–13]. This includes both the spin multiplicity contribution and the vibrational entropy contribution due to the shift of vibrational frequencies [3]. In addition, optical excitation involving electronic transition around metal center can lead to LS → HS spin-state switching as a result of the Light-Induced Excited Spin-State Trapping (LIESST) process [14]. A crucial point for observing transient LIESST, or reverse-LIESST, is the lifetime of the photoinduced state. In the first study of the LIESST effect, performed in solution, McGarvey et al. used nanosecond laser excitation and flash photolysis to induce and probe the dynamics of the spin equilibrium on the hundreds of ns timescale [15]. Decurtins et al. investigated the LS → HS solid-state photoswitching in crystals at low temperatures (below 50 K) [14] where the long-lived photoinduced HS state can be probed by more conventional techniques such as optical spectroscopy. During the last decade, ultrafast spectroscopic techniques have been intensively used to study the LIESST effect on few Fe(II) compounds. LIESST occurs typically within 150 fs for metal-to-ligand charge-transfer excitation and within 70 fs for d-d excitation [16–25], and is driven by the activation and damping of the molecular breathing mode that elongates the Fe-ligand bonds [16–17,19–21,26]. The reverse LIESST process is much slower and occurs within 40 ps [27]. Ultrafast techniques allow probing relaxation from photoinduced HS to ground LS states, but more interestingly also allow probing the multi-step conversion process in solid states where, in addition to sub-ps molecular photo-switching, delayed cooperative elastic conversion and thermal conversion also occur [28–34].

The lifetime of the photo-induced state and the temperature at which photoswitching occurs are crucial aspects for various applications [35,36]. In this way, for spin-crossover materials, the T(LIESST) temperature corresponds to a characteristic relaxation temperature, where the lifetime of the metastable photoinduced state, which is photoinduced at low temperature, becomes short in the dark. For comparing the lifetime of the photoinduced HS state in various systems, the T(LIESST) temperature was defined as the inflexion point of the relaxation from the HS state, photoinduced at 10 K, upon slow warming in the dark with a

* Corresponding authors.
E-mail addresses: Jean-Yves.Mevellec@cnrs-imn.fr (J.-Y. Mevellec), guillaume.chastanet@icmcb.cnrs.fr (G. Chastanet), eric.collet@univ-rennes1.fr (E. Collet).

https://doi.org/10.1016/j.cplett.2022.139395
Received 3 December 2021; Received in revised form 24 December 2021; Accepted 18 January 2022
Available online 22 January 2022

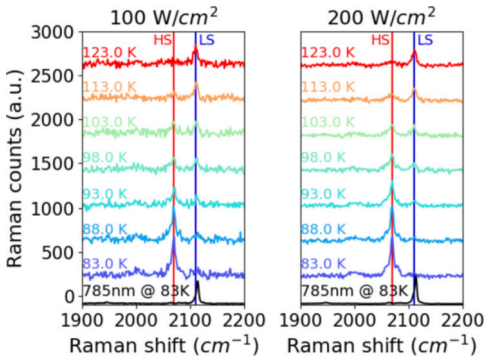

Fig. 2. Temperature dependence of the frequency of the A_g Raman N ↔ CS stretching mode in low temperature region and measured at 633 nm (colored) and 785 nm (black).

absorption above 750 nm [40,51]. At last, since the observed effect decreases as temperature increases (Fig. 2) we can underline that the photoinduced HS state observed here upon 633 nm excitation is not due to laser heating. Kato *et al* reported similar phenomena by using x-ray diffraction for monitoring the effect of light excitation. They demonstrated the on–off optical control of spin-state switching and excluded laser heating effect [52].

As the impact of light fluence on the Raman spectra was important, we conducted SQUID measurements under light for different light fluences. Fig. 3 shows the evolution with temperature and under continuous light excitation of the fraction γ of molecules in HS state, extracted from magnetic susceptibility. Even though the laser fluence is much lower than for micro-Raman, it is clear that the photo-stationary HS fraction is stabilized towards higher temperature as laser fluence increases. The photo-stationary half conversion temperature $T_{\frac{1}{2}}^{hv}$, where $\gamma = \frac{1}{2}$ under light irradiation, shifts from 59 K (0.01 W/cm^2) to 62 K (0.08 W/cm^2).

The observed photo-stationary population of the HS state is due to the well-known competition between the photoinduced LS → HS photoconversion and thermally-activated HS → LS relaxation. In order to discuss this phenomenon, we use a simplified version of the model introduced by Desaix et al. [53], which describes the competition between photoexcitation driven by permanent light irradiation and

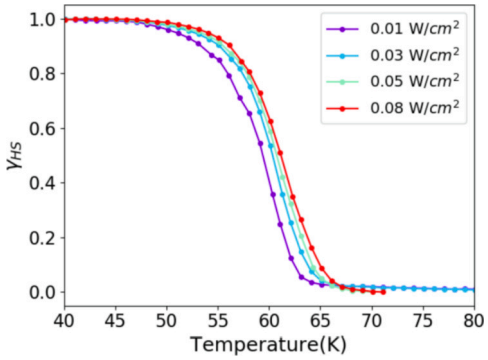

Fig. 3. Temperature dependence of the photo-stationary HS fraction γ extracted from SQUID measurements.

relaxation towards the non-excited state. These authors considered a relaxation rate depending on the HS fraction γ, due to cooperative interactions, which modulate the energy barrier. The following master equation from Desaix et al, describes the evolution of γ under competing photoinduced LS → HS conversion and thermally-activated HS → LS relaxation:

$$\frac{d\gamma}{dt} = \varnothing_{LS\to HS} - \varnothing_{HS\to LS} = I_0\omega(1-\gamma) - \gamma k_\infty \exp(-\frac{E_a(0)}{kT})\exp(-\alpha\gamma)$$

Where $I_0\omega$ is the probability per time unit for a LS molecule to absorb a photon and switch to the HS state, with I_0 the beam fluence (in photons/s/cm^2) and ω a proportionality factor, which includes the absorption cross-section of the optical transition driving LIESST.α is the self-acceleration factor, which is important for describing non-exponential relaxations. In the case of the [Fe(phen)$_2$(NCS)$_2$] system investigated here, the cooperative interactions are not so strong: the thermal conversion exhibits pretransitional conversion and at high temperature the relaxation curves from the photoinduced HS state are close to exponential [54]. In this case, we can simplify Desaix's model and neglect the self-acceleration factor in a first approximation and for a non-cooperative system, the equation can be reduced to

$$\frac{d\gamma}{dt} = I_0\omega(1-\gamma) - \gamma k_\infty \exp(-\frac{E_a}{kT})$$

The photo-stationary state is then found for

$$\frac{d\gamma}{dt} = 0$$

$$I_0\omega(1-\gamma) = \gamma k_\infty \exp\left(-\frac{E_a}{kT}\right) = \gamma k(T)$$

$k(T)$ is the temperature dependence of the HS → LS relaxation rate for an exponential decay. This is reasonable since Badle *et al* have reported an almost linear evolution of $\ln(k(T))$ with $\frac{1}{T}$ for [Fe(phen)$_2$(NCS)$_2$] [40,54]. In this way, the photo-stationary HS fraction depends on the thermal relaxation rate and on the laser fluence, which rescales $k(T)$ to $r(T)$

$$\gamma(T) = \frac{1}{1+\frac{k(T)}{I_0\omega}} = \frac{1}{1+r(T)}$$

The half-conversion photo-stationary equilibrium, $\gamma = \frac{1}{2}$, occurs when $k(T) = I_0\omega$, *i.e.* when the LS → HS conversion and HS → LS relaxation rates are equal. We define $T_{\frac{1}{2}}^{hv}(I_0\omega)$ as the temperature for which half-conversion is reached under laser fluence I_0 for a non-cooperative system, with known $k(T)$ and ω. In this way, the light fluence I_0 is the control parameter for reaching photostationary equilibrium.

Fig. 4a shows the calculated dependence of the photo-stationary HS fraction with temperature, using the $k(T)$ values reported by Baldé et al. [54] Since the relaxation rate in SCO materials is known to change by 12 orders of magnitude with temperature [55], the laser fluence also has to change by orders of magnitudes to shift significantly $T_{\frac{1}{2}}^{hv}$. For example, Baldé et al measured $k(85K) = 1$ [54]. Photo-stationary half-conversion at $T_{\frac{1}{2}}^{hv} = 85$ K is then possible when $I_0\omega = 1$, which corresponds to 1 photon absorbed per molecule and per second, as the quantum efficiency of LS → HS photoconversion is close to 1. For reaching photo-stationary half conversion at $T_{\frac{1}{2}}^{hv} = 60$ K, where $k(60K) = 0.0002$ [54], the laser fluence should therefore be reduced by almost 4 orders of magnitude compared to 85 K. This agrees with light fluence used for Raman experiments (100 W/cm^2) where $\gamma = \frac{1}{2}$ at $T_{\frac{1}{2}}^{hv} = 90$ K and SQUID experiment (0.01 W/cm^2) where $\gamma = \frac{1}{2}$ at $T_{\frac{1}{2}}^{hv} = 60$ K. The model, considering the $k(T)$ data reported for [Fe(phen)$_2$(NCS)$_2$] [54], predicts a shift of $T_{\frac{1}{2}}^{hv}$ from ≃55 to ≃90 K if the light fluence increases by 4 orders of

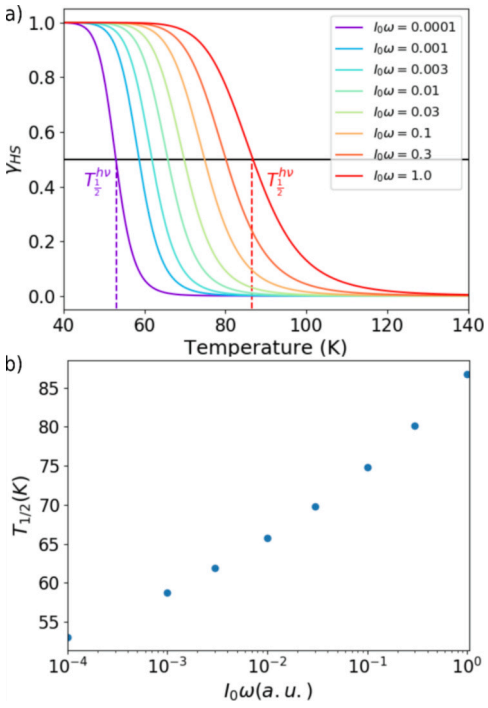

Fig. 4. a) Calculated temperature dependence of the photo-stationary HS fraction γ. b) Evolution of the photo-stationary half-conversion temperature $T_{\frac{1}{2}}^{h\nu}$ with light excitation $I_0\omega$.

magnitude (Fig. 4b). During the SQUID experiment, the limited increase in light fluence from 0.01 to 0.08 W/cm^2 allows for a small shift of $T_{\frac{1}{2}}^{h\nu}$ of about 3 K.

Fig. 5 summarizes the experimental and theoretical results. In addition to Raman and SQUID data, we include reflectivity measurements published in ref. [16] with an intermediate fluence, more difficult to estimate since reflectivity mainly probes changes induced by a white light excitation close to surface, where optical excitation is higher than in the bulk. The fit of the experimental data with the model, provides some $I_0\omega$ values ($I_0\omega = 1$ for Raman$I_0\omega = 0.001$ for SQUID data) which confirms that for $[Fe(phen)_2(NCS)_2]$ it is necessary to increase the laser fluence by 4 orders of magnitude to shift $T_{\frac{1}{2}}^{h\nu}$ 30 K above T(LIESST). The different shapes of the experimental data compared to the fit may come from the approximation that $[Fe(phen)_2(NCS)_2]$ is a non-cooperative system. However, the order of magnitude of the shift of $T_{\frac{1}{2}}^{h\nu}$ with $I_0\omega$ is in good agreement with experimental data.

Another study by Kato et al. [52] evidenced that the photoresponse of this materials is more important under excitation at 532 nm, which allows a 88% conversion at 92 K with$I_0 = 2$ W/cm^2. The highest absorption at 532 nm translates in higher ω, compared to 633 nm in our experiment, and finally the products $I_0\omega$ are comparable in both experiments.

4. Conclusions

This paper discusses the possibility to investigate the LIESST processes in SCO materials well above T(LIESST) under high light fluence. A simple model explains that, for no or weakly cooperative systems, a photo-stationary half photo-conversion is observed when the when the number of absorbed photons per second equals the relaxation rate. With this respect, μ-Raman technique allows observing LIESST at lower cost by using liquid-nitrogen operating cryostats instead of He-operating ones, without using sophisticated time-resolved technique and with the possibility to investigate micro-crystals. Tracking how photo-stationary half-conversion evolves with temperature and light fluence is then another approach for measuring HS → LS thermal relaxation rates.

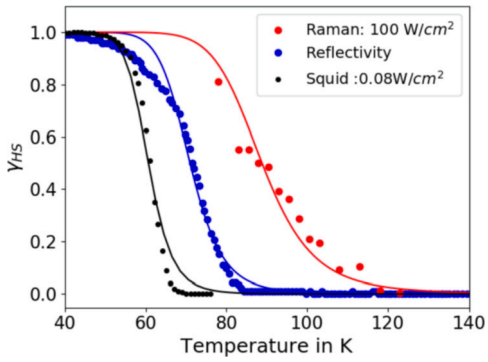

Fig. 5. Temperature dependence of the photo-stationary HS fraction γ from SQUID (black), reflectivity (blue) and micro-Raman (red) measurements. The continuous lines are a fit of the data with $I_0\omega$ as free parameter. (For interpretation of the references to colour in this figure legend, the reader is referred to the web version of this article.)

Declaration of Competing Interest

The authors declare that they have no known competing financial interests or personal relationships that could have appeared to influence the work reported in this paper.

Acknowledgements

The authors gratefully acknowledge Agence Nationale de la Recherche for financial support undergrant, ANR-19-CE30-0004 ELECTROPHONE, ANR-19-CE29-0018 MULTICROSS. L.G. and E.C. thanks the University Rennes 1 and the Fondation Rennes1 for funding.

***Author** contributions*

E.C., J.-Y.M., E.J., L.Gu, M.C. and B.H conceived and coordinated the project in the frame of the ANR ELECTROPHONE and MULTICROSS projects. L.Go., I.C., J.-Y.M. and B.H. performed the Raman experiment and analyzed the data. N.D. synthesized the samples. G.C. performed the SQUID measurements and analyzed the data. L. Go. and E.C. developed the photo-stationary model. E.C. and L. Go wrote the manuscript with significant contributions from B.H., J.-Y.M., E.J. and G.C.. All authors contributed to discussions and gave comments on the manuscript.

References

[1] Halcrow, M. A., *Spin-crossover materials : properties and applications.* Wiley: 2013; p xviii, 546 p.
[2] P. Gütlich, A. Hauser, H. Spiering, Thermal and Optical Switching of Iron(II) Complexes, Angew. Chemie-Int. English 33 (20) (1994) 2024–2054.

[3] W. Nicolazzi, A. Bousseksou, Thermodynamical aspects of the spin crossover phenomenon, Cr Chim 21 (12) (2018) 1060–1074.

[4] K.L. Ronayne, H. Paulsen, A. Höfer, A.C. Dennis, J.A. Wolny, A.I. Chumakov, V. Schünemann, H. Winkler, H. Spiering, A. Bousseksou, P. Gütlich, A. X. Trautwein, J.J. McGarvey, Vibrational spectrum of the spin crossover complex [Fe(phen)(2)(NCS)(2)] studied by IR and Raman spectroscopy, nuclear inelastic scattering and DFT calculations, PCCP 8 (40) (2006) 4685–4693.

[5] M. Buron-Le Cointe, J. Hébert, C. Baldé, N. Moisan, L. Toupet, P. Guionneau, J. F. Létard, E. Freysz, H. Cailleau, E. Collet, Intermolecular control of thermoswitching and photoswitching phenomena in two spin-crossover polymorphs, Phys. Rev. B 85 (6) (2012), https://doi.org/10.1103/PhysRevB.85.064114.

[6] J.P. Tuchagues, A. Bousseksou, G. Molnar, J.J. McGarvey, F. Varret, The role of molecular vibrations in the spin crossover phenomenon, Top Curr Chem 235 (2004) 85–103.

[7] G. Brehm, M. Reiher, S. Schneider, Estimation of the vibrational contribution to the entropy change associated with the low- to high-spin transition in Fe(phen)(2)(NCS)(2) complexes: Results obtained by IR and Raman spectroscopy and DFT calculations, J. Phys. Chem. A 106 (50) (2002) 12024–12034.

[8] A. Metatla, H. Latelli, W. Nicolazzi, A. Bousseksou, Vibration-driven thermal transition in binuclear spin crossover complexes, European Phys. J. B 85 (6) (2012), https://doi.org/10.1140/epjb/e2012-30132-1.

[9] M. Sorai, S. Seki, Phonon coupled cooperative low-spin 1A1high-spin 5T2 transition in [Fe(phen)2(NCS)2] and [Fe(phen)2(NCSe)2] crystals, J. Phys. Chem. Solids 35 (4) (1974) 555–570.

[10] J.H. Takemoto, B. Streusand, B. Hutchinson, Far-Infrared Spectra of Some Fe(1,10-Phenanthroline)2x2 Complexes, Spectrochim. Acta A 30 (3) (1974) 827–834.

[11] H. Watanabe, K. Tanaka, N. Bréfuel, H. Cailleau, J.-F. Létard, S. Ravy, P. Fertey, M. Nishino, S. Miyashita, E. Collet, Ordering phenomena of high-spin/low-spin states in stepwise spin-crossover materials described by the ANNNI model, Phys. Rev. B 93 (1) (2016), https://doi.org/10.1103/PhysRevB.93.014419.

[12] E. Collet, G. Azzolina, Coupling and decoupling of spin crossover and ferroelastic distortion: Unsymmetric hysteresis loop, phase diagram, and sequence of phases, Phys. Rev. Mater. 5 (4) (2021), 044401.

[13] G. Azzolina, R. Bertoni, E. Collet, General Landau theory of non-symmetry-breaking and symmetry-breaking spin transition materials, J. Appl. Phys. 129 (8) (2021) 085106, https://doi.org/10.1063/5.0041453.

[14] S. Decurtins, P. Gütlich, C.P. Köhler, H. Spiering, A. Hauser, Light-induced excited spin state trapping in a transition-metal complex: The hexa-1-propyltetrazole-iron (II) tetrafluoroborate spin-crossover system, Chem. Phys. Lett. 105 (1) (1984) 1–4.

[15] l. Lawthers, J.J. Mcgarvey, Spin-State Relaxation Dynamics in Iron(Iii) Complexes - Photochemical Perturbation of the 2t Reversible 6a Spin Equilibrium by Pulsed-Laser Irradiation in the Ligand-to-Metal Charge-Transfer Absorption-Band, J. Am. Chem. Soc. 106 (15) (1984) 4280–4282.

[16] R. Bertoni, M. Cammarata, M. Lorenc, S.F. Matar, J.-F. Létard, H.T. Lemke, E. Collet, Ultrafast light-induced spin-state trapping photophysics investigated in Fe(phen)2(NCS)2 spin-crossover crystal, Acc Chem. Res. 48 (3) (2015) 774–781.

[17] M. Cammarata, R. Bertoni, M. Lorenc, H. Cailleau, S. Di Matteo, C. Mauriac, S. F. Matar, H. Lemke, M. Chollet, S. Ravy, C. Laulhe, J.F. Létard, E. Collet, Sequential Activation of Molecular Breathing and Bending during Spin-Crossover Photoswitching Revealed by Femtosecond Optical and X-Ray Absorption Spectroscopy, Phys. Rev. Lett. 113 (22) (2014), 227402.

[18] S. Zerdane, M. Cammarata, O. Iasco, M.-L. Boillot, E. Collet, Photoselective MLCT to d-d pathways for light-induced excited spin state trapping, J. Chem. Phys. 151 (17) (2019) 171101, https://doi.org/10.1063/1.5127507.

[19] H.T. Lemke, K.S. Kjær, R. Hartsock, T. Brandt van Driel, M. Chollet, J.M. Glownia, S. Song, D. Zhu, E. Pace, S.F. Matar, M.N. Nielsen, M. Benfatto, K.J. Gaffney, E. Collet, M. Cammarata, Coherent structural trapping through wave packet dispersion during photoinduced spin state switching, Nat. Commun. 8 (2017) 15342.

[20] S. Zerdane, L. Wilbraham, M. Cammarata, O. Iasco, E. Rivière, M.L. Boillot, I. Ciofini, E. Collet, Comparison of structural dynamics and coherence of d–d and MLCT light-induced spin state trapping, Chem. Sci. 8 (2017) 4978–4986.

[21] A. Marino, M. Cammarata, S.F. Matar, J.-F. Létard, G. Chastanet, M. Chollet, J. M. Glownia, H.T. Lemke, E. Collet, Activation of coherent lattice phonon following ultrafast molecular spin-state photo-switching: A molecule-to-lattice energy transfer, Struct. Dyn. 3 (2) (2016) 023605, https://doi.org/10.1063/1.4936290.

[22] G. Auböck, M. Chergui, Sub-50-fs photoinduced spin crossover in [Fe(bpy)(3)](2+), Nat. Chem. 7 (8) (2015) 629–633.

[23] N. Huse, H. Cho, K. Hong, L. Jamula, F.M.F. de Groot, T.K. Kim, J.K. McCusker, R. W. Schoenlein, Femtosecond Soft X-ray Spectroscopy of Solvated Transition-Metal Complexes: Deciphering the Interplay of Electronic and Structural Dynamics, J. Phys. Chem. Lett. 2 (8) (2011) 880–884.

[24] K.S. Kjær, T.B. Van Driel, T.C.B. Harlang, K. Kunnus, E. Biasin, K. Ledbetter, R. W. Hartsock, M.E. Reinhard, S. Koroidov, L. Li, M.G. Laursen, F.B. Hansen, P. Vester, M. Christensen, K. Haldrup, M.M. Nielsen, A.O. Dohn, M.I. Pápai, K. B. Møller, P. Chabera, Y. Liu, H. Tatsuno, C. Timm, M. Jarenmark, J. Uhlig, V. Sundström, K. Wärnmark, P. Persson, Z. Németh, D.S. Szemes, É. Bajnóczi, G. Vankó, R. Alonso-Mori, J.M. Glownia, S. Nelson, M. Sikorski, D. Sokaras, S. E. Canton, H.T. Lemke, K.J. Gaffney, Finding intersections between electronic excited state potential energy surfaces with simultaneous ultrafast X-ray scattering and spectroscopy, Chem. Sci. 10 (22) (2019) 5749–5760.

[25] W.K. Zhang, R. Alonso-Mori, U. Bergmann, C. Bressler, M. Chollet, A. Galler, W. Gawelda, R.G. Hadt, R.W. Hartsock, T. Kroll, K.S. Kjaer, K. Kubicek, H. T. Lemke, H.Y.W. Liang, D.A. Meyer, M.M. Nielsen, C. Purser, J.S. Robinson, E. I. Solomon, Z. Sun, D. Sokaras, T.B. van Driel, G. Vanko, T.C. Weng, D.L. Zhu, K. J. Gaffney, Tracking excited-state charge and spin dynamics in iron coordination complexes, Nature 509 (7500) (2014) 345–348.

[26] M. Chergui, E. Collet, Photoinduced structural dynamics of molecular systems mapped by time-resolved x-ray methods, Chem. Rev. 117 (16) (2017) 11025–11065.

[27] A. Marino, P. Chakraborty, M. Servol, M. Lorenc, E. Collet, A. Hauser, The Role of Ligand- Field States in the Ultrafast Photophysical Cycle of the Prototypical Iron(II) Spin- Crossover Compound $[Fe(ptz)_6](BF_4)_2$, Angew. Chem.-Int. Ed. 53 (15) (2014) 3863–3867.

[28] R. Bertoni, E. Collet, H. Cailleau, M.-L. Boillot, A. Tissot, J. Laisney, C. Enachescu, M. Lorenc, Temperature dependence of the cooperative out-of-equilibrium elastic switching in a spin-crossover material, Phys. Chem. Chem. Phys. 21 (12) (2019) 6606–6612.

[29] K. Ridier, A.-C. Bas, V. Shalabaeva, W. Nicolazzi, L. Salmon, G. Molnár, A. Bousseksou, M. Lorenc, R. Bertoni, E. Collet, H. Cailleau, Finite Size Effects on the Switching Dynamics of Spin-Crossover Thin Films Photoexcited by a Femtosecond Laser Pulse, Adv. Mater. 31 (25) (2019) 1901361, https://doi.org/10.1002/adma.v31.2510.1002/adma.201901361.

[30] R. Bertoni, M. Lorenc, H. Cailleau, A. Tissot, J. Laisney, M.-L. Boillot, L. Stoleriu, A. Stancu, C. Enachescu, E. Collet, Elastically driven cooperative response of a molecular material impacted by a laser pulse, Nat. Mater. 15 (6) (2016) 606–610.

[31] R. Bertoni, M. Lorenc, T. Graber, R. Henning, K. Moffat, J.-F. Létard, E. Collet, Cooperative elastic switching vs. laser heating in [Fe(phen)2(NCS)2] spin-crossover crystals excited by a laser pulse, CrystEngComm 18 (38) (2016) 7269–7275.

[32] E. Collet, M. Lorenc, M. Cammarata, L. Guerin, M. Servol, A. Tissot, M.L. Boillot, H. Cailleau, M. Buron-Le Cointe, 100 Picosecond Diffraction Catches Structural Transients of Laser-Pulse Triggered Switching in a Spin-Crossover Crystal, Chem.-European J. 18 (7) (2012) 2051–2055.

[33] E. Collet, N. Moisan, C. Balde, R. Bertoni, E. Trzop, C. Laulhe, M. Lorenc, M. Servol, H. Cailleau, A. Tissot, M.L. Boillot, T. Graber, R. Henning, P. Coppens, M. Buron-Le Cointe, Ultrafast spin-state photoswitching in a crystal and slower consecutive processes investigated by femtosecond optical spectroscopy and picosecond X-ray diffraction, PCCP 14 (18) (2012) 6192–6199.

[34] M. Lorenc, J. Hebert, N. Moisan, E. Trzop, M. Servol, M. Buron-Le Cointe, H. Cailleau, M.L. Boillot, E. Pontecorvo, M. Wulff, S. Koshihara, E. Collet, Successive Dynamical Steps of Photoinduced Switching of a Molecular Fe(III) Spin-Crossover Material by Time-Resolved X-Ray Diffraction, Phys. Rev. Lett. 103 (2) (2009), 028301.

[35] G. Chastanet, C. Desplanches, C. Baldé, P. Rosa, M. Marchivie, P. Guionneau, A critical review of the T(LIESST) temperature in spin crossover materials – What it is and what it is not, Chem. Squared 2 (2018) 2, https://doi.org/10.28954/csq10.28954/2018.csq.07.001.

[36] G. Chastanet, M. Lorenc, R. Bertoni, C. Desplanches, Light-induced spin crossover—Solution and solid-state processes, Cr Chim 21 (12) (2018) 1075–1094.

[37] J.-F. Létard, L. Capes, G. Chastanet, N. Moliner, S. Létard, J.-A. Real, O. Kahn, Critical temperature of the LIESST effect in iron(II) spin crossover compounds, Chem. Phys. Lett. 313 (1-2) (1999) 115–120.

[38] E. Collet, G. Azzolina, T. Ichii, L. Guerin, R. Bertoni, A. Moréac, M. Cammarata, N. Daro, G. Chastanet, J. Kubicki, K. Tanaka, S.F. Matar, Lattice phonon modes of the spin crossover crystal [Fe(phen)2(NCS)2] studied by THz, IR, Raman spectroscopies and DFT calculations, European Phys. J. B 92 (1) (2019), https://doi.org/10.1140/epjb/e2018-90553-2.

[39] M. Marchivie, P. Guionneau, J.A.K. Howard, G. Chastanet, J.-F. Létard, A.E. Goeta, D. Chasseau, Structural characterization of a photoinduced molecular switch, J. Am. Chem. Soc. 124 (2) (2002) 194–195.

[40] C. Balde, C. Desplanches, A. Wattiaux, P. Guionneau, P. Gutlich, J.F. Letard, Effect of metal dilution on the light-induced spin transition in [Fe(x)Zn(1–x)(phen)2(NCS)2] (phen = 1,10-phenanthroline), Dalton Trans. 20 (2008) 2702–2707.

[41] J.-J. Lee, H.-S. Sheu, C.-R. Lee, J.-M. Chen, J.-F. Lee, C.-C. Wang, C.-H. Huang, Y. u. Wang, X-ray absorption spectroscopic studies on light-induced excited spin state trapping of an Fe(II) complex, J. Am. Chem. Soc. 122 (24) (2000) 5742–5747.

[42] J.-F. Létard, P. Guionneau, L. Rabardel, J.A.K. Howard, A.E. Goeta, D. Chasseau, O. Kahn, Structural, magnetic, and photomagnetic studies of a mononuclear iron (II) derivative exhibiting an exceptionally abrupt spin transition. Light-induced thermal hysteresis phenomenon, Inorg. Chem. 37 (17) (1998) 4432–4441.

[43] J.A. Real, B. Gallois, T. Granier, F. Suez-Panama, J. Zarembowitch, Comparative investigation of the spin-crossover compounds Fe(btz)2(NCS)2 and Fe(phen)2(NCS)2 (where btz = 2,2'-bi-4,5-dihydrothiazine and phen = 1,10-phenanthroline). Magnetic properties and thermal dilatation behavior and crystal structure of Fe(btz)2(NCS)2 at 293 and 130 K, Inorg. Chem. 31 (24) (1992) 4972–4979.

[44] R.H. Herber, VTFTIR and light-induced excited spin state trapping in bis(2,2'-bipyridine)bis(thiocyanato)iron and related spin-crossover compounds, Inorg. Chem. 26 (1) (1987) 173–178.

[45] V. Briois, C.C.D. Moulin, P. Sainctavit, C. Brouder, A.M. Flank, Full Multiple-Scattering and Crystal-Field Multiplet Calculations Performed on the Spin Transition Fe-Ii(Phen)(2)(Ncs)(2) Complex at the Iron K(2,3) and L(2,3) X-Ray-Absorption Edges, J. Am. Chem. Soc. 117 (3) (1995) 1019–1026.

[46] E. Collet, P. Guionneau, Structural analysis of spin-crossover materials: From molecules to materials, Cr Chim. 21 (12) (2018) 1133–1151.

[47] G. Baranović, D. Babić, Vibrational study of the Fe(phen)(2)(NCS)(2) spin-crossover complex by density-functional calculations, Spectrochim Acta A 60 (5) (2004) 1013–1025.

[48] M. Reiher, Theoretical Study of the Fe(phen)2(NCS)2 Spin-Crossover Complex with Reparametrized Density Functionals, Inorg. Chem. 41 (25) (2002) 6928–6935.

Bibliography

[1] Osamu Sato. Dynamic molecular crystals with switchable physical properties. *Nature Chemistry*, 8(7):644–656, Jul 2016.

[2] Keiichiro Nasu, Huai Ping, and Hideo Mizouchi. Photoinduced structural phase transitions and their dynamics. *Journal of Physics: Condensed Matter*, 13(35):R693–R721, aug 2001.

[3] Christoph P. Hauri, Clemens Ruchert, Carlo Vicario, and Fernando Ardana. Strong-field single-cycle thz pulses generated in an organic crystal. *Applied Physics Letters*, 99(16):161116, 2011.

[4] T. Morimoto, T. Miyamoto, H. Yamakawa, T. Terashige, T. Ono, N. Kida, and H. Okamoto. Terahertz-field-induced large macroscopic polarization and domain-wall dynamics in an organic molecular dielectric. *Phys. Rev. Lett.*, 118:107602, Mar 2017.

[5] Jian Chen, Pengyu Han, and X.-C. Zhang. Terahertz-field-induced second-harmonic generation in a beta barium borate crystal and its application in terahertz detection. *Applied Physics Letters*, 95(1):011118, 2009.

[6] Roman Bertoni, Marco Cammarata, Maciej Lorenc, Samir F. Matar, Jean-François Létard, Henrik T. Lemke, and Eric Collet. Ultrafast light-induced spin-state trapping photophysics investigated in fe(phen)2(ncs)2 spin-crossover crystal. *Accounts of Chemical Research*, 48(3):774–781, 2015. PMID: 25705921.

[7] R. Bertoni, M. Lorenc, T. Graber, R. Henning, K. Moffat, J.-F. Létard, and E. Collet. Cooperative elastic switching vs. laser heating in [fe(phen)2(ncs)2] spin-crossover crystals excited by a laser pulse. *CrystEngComm*, 18:7269–7275, 2016.

[8] Marco Cammarata, Roman Bertoni, Maciej Lorenc, Hervé Cailleau, Sergio Di Matteo, Cindy Mauriac, Samir F. Matar, Henrik Lemke, Matthieu Chollet, Sylvain Ravy, Claire Laulhé, Jean-Fran çois Létard, and Eric Collet. Sequential activation of molecular breathing and bending during spin-crossover photoswitching revealed by femtosecond optical and x-ray absorption spectroscopy. *Phys. Rev. Lett.*, 113:227402, Nov 2014.

[9] Marco Cammarata, Serhane Zerdane, Lodovico Balducci, Giovanni Azzolina, Sandra Mazerat, Cecile Exertier, Matilde Trabuco, Matteo Levantino, Roberto Alonso-Mori, James M. Glownia, Sanghoon Song, Laure Catala, Talal Mallah,

Samir F. Matar, and Eric Collet. Charge transfer driven by ultrafast spin transition in a cofe prussian blue analogue. *Nature Chemistry*, 13(1):10–14, Jan 2021.

[10] Matthew C. Asplund, Preston T. Snee, Jake S. Yeston, Matthew J. Wilkens, Christine K. Payne, Haw Yang, Kenneth T. Kotz, Heinz Frei, Robert G. Bergman, and Charles B. Harris. Ultrafast uv pump ir probe studies of c h activation in linear, cyclic, and aryl hydrocarbons. *Journal of the American Chemical Society*, 124(35):10605–10612, Sep 2002.

[11] A. Tokmakoff, B. Sauter, and M. D. Fayer. Temperature-dependent vibrational relaxation in polyatomic liquids: Picosecond infrared pump–probe experiments. *The Journal of Chemical Physics*, 100(12):9035–9043, 1994.

[12] Tobias Kampfrath, Koichiro Tanaka, and Keith A. Nelson. Resonant and nonresonant control over matter and light by intense terahertz transients. *Nature Photonics*, 7(9):680–690, Sep 2013.

[13] Hervé Cailleau, Maciej Lorenc, Laurent Guérin, Marina Servol, Eric Collet, and Marylise Buron-Le Cointe. Structural dynamics of photoinduced molecular switching in the solid state. *Acta Crystallographica Section A*, 66(2):189–197, Mar 2010.

[14] D. M. Fritz, D. A. Reis, B. Adams, R. A. Akre, J. Arthur, C. Blome, P. H. Bucksbaum, A. L. Cavalieri, S. Engemann, S. Fahy, R. W. Falcone, P. H. Fuoss, K. J. Gaffney, M. J. George, J. Hajdu, M. P. Hertlein, P. B. Hillyard, M. Horn von Hoegen, M. Kammler, J. Kaspar, R. Kienberger, P. Krejcik, S. H. Lee, A. M. Lindenberg, B. McFarland, D. Meyer, T. Montagne, E. D. Murray, A. J. Nelson, M. Nicoul, R. Pahl, J. Rudati, H. Schlarb, D. P. Siddons, K. Sokolowski-Tinten, Th. Tschentscher, D. von der Linde, and J. B. Hastings. Ultrafast bond softening in bismuth: Mapping a solid's interatomic potential with x-rays. *Science*, 315(5812):633–636, 2007.

[15] M. Harmand, R. Coffee, M. R. Bionta, M. Chollet, D. French, D. Zhu, D. M. Fritz, H. T. Lemke, N. Medvedev, B. Ziaja, S. Toleikis, and M. Cammarata. Achieving few-femtosecond time-sorting at hard x-ray free-electron lasers. *Nature Photonics*, 7(3):215–218, Mar 2013.

[16] Klaus Sokolowski-Tinten, Christian Blome, Juris Blums, Andrea Cavalleri, Clemens Dietrich, Alexander Tarasevitch, Ingo Uschmann, Eckhard Förster, Martin Kammler, Michael Horn-von Hoegen, and Dietrich von der Linde. Femtosecond x-ray measurement of coherent lattice vibrations near the lindemann stability limit. *Nature*, 422(6929):287–289, Mar 2003.

[17] E. Collet, M. Harmand, M-E. Couprie, and M. Cammarata. La revolution x-fel : des lasers à rayons x pour sonder la matière. *Reflets de la physique*, 2015.

[18] D. Boschetto, E. G. Gamaly, A. V. Rode, B. Luther-Davies, D. Glijer, T. Garl, O. Albert, A. Rousse, and J. Etchepare. Small atomic displacements recorded in bismuth by the optical reflectivity of femtosecond laser-pulse excitations. *Phys. Rev. Lett.*, 100:027404, Jan 2008.

[19] Verdad C. Agulto, Kazuhiro Toya, Thanh Nhat Khoa Phan, Valynn Katrine Mag-usara, Jiajun Li, Melvin John F. Empizo, Toshiyuki Iwamoto, Ken Goto, Hisashi Murakami, Yoshinao Kumagai, Nobuhiko Sarukura, Masashi Yoshimura, and Makoto Nakajima. Anisotropic complex refractive index of beta-ga2o3 bulk and epilayer evaluated by terahertz time-domain spectroscopy. *Applied Physics Letters*, 118(4):042101, 2021.

[20] I. Katayama, H. Aoki, J. Takeda, H. Shimosato, M. Ashida, R. Kinjo, I. Kawayama, M. Tonouchi, M. Nagai, and K. Tanaka. Ferroelectric soft mode in a $srtio_3$ thin film impulsively driven to the anharmonic regime using intense picosecond terahertz pulses. *Phys. Rev. Lett.*, 108:097401, Feb 2012.

[21] Mukesh Jewariya, Masaya Nagai, and Koichiro Tanaka. Ladder climbing on the anharmonic intermolecular potential in an amino acid microcrystal via an intense monocycle terahertz pulse. *Phys. Rev. Lett.*, 105:203003, Nov 2010.

[22] S. Houver, L. Huber, M. Savoini, E. Abreu, and S. L. Johnson. 2d thz spectroscopic investigation of ballistic conduction-band electron dynamics in insb. *Opt. Express*, 27(8):10854–10865, Apr 2019.

[23] Tatsuya Miyamoto, Hiroyuki Yada, Hiromichi Yamakawa, and Hiroshi Okamoto. Ultrafast modulation of polarization amplitude by terahertz fields in electronic-type organic ferroelectrics. *Nature Communications*, 4(1):2586, Oct 2013.

[24] Tobias Kampfrath, Alexander Sell, Gregor Klatt, Alexej Pashkin, Sebastian Mährlein, Thomas Dekorsy, Martin Wolf, Manfred Fiebig, Alfred Leitenstorfer, and Rupert Huber. Coherent terahertz control of antiferromagnetic spin waves. *Nature Photonics*, 5(1):31–34, Jan 2011.

[25] Kirill Grishunin, Thomas Huisman, Guanqiao Li, Elena Mishina, Theo Rasing, Alexey V. Kimel, Kailing Zhang, Zuanming Jin, Shixun Cao, Wei Ren, Guo-Hong Ma, and Rostislav V. Mikhaylovskiy. Terahertz magnon-polaritons in tmfeo3. *ACS Photonics*, 5(4):1375–1380, Apr 2018.

[26] R. Boyd. *Non linear optics*. Acamedic Press, 1992.

[27] D. H. Auston, K. P. Cheung, and P. R. Smith. Picosecond photoconducting hertzian dipoles. *Applied Physics Letters*, 45(3):284–286, 1984.

[28] K. Y. Kim, A. J. Taylor, J. H. Glownia, and G. Rodriguez. Coherent control of terahertz supercontinuum generation in ultrafast laser–gas interactions. *Nature Photonics*, 2(10):605–609, Oct 2008.

[29] Shu-Wei Huang, Eduardo Granados, Wenqian Ronny Huang, Kyung-Han Hong, Luis E. Zapata, and Franz X. Kärtner. High conversion efficiency, high energy terahertz pulses by optical rectification in cryogenically cooled lithium niobate. *Opt. Lett.*, 38(5):796–798, Mar 2013.

[30] C. Vicario, A. V. Ovchinnikov, S. I. Ashitkov, M. B. Agranat, V. E. Fortov, and C. P. Hauri. Generation of 0.9-mj thz pulses in dstms pumped by a cr:mg2sio4 laser. *Opt. Lett.*, 39(23):6632–6635, Dec 2014.

[31] H. Hamster, A. Sullivan, S. Gordon, W. White, and R. W. Falcone. Subpicosecond, electromagnetic pulses from intense laser-plasma interaction. *Phys. Rev. Lett.*, 71:2725–2728, Oct 1993.

[32] T. Löffler, F. Jacob, and H. G. Roskos. Generation of terahertz pulses by photoionization of electrically biased air. *Applied Physics Letters*, 77(3):453–455, 2000.

[33] H A Hafez, X Chai, A Ibrahim, S Mondal, D Férachou, X Ropagnol, and T Ozaki. Intense terahertz radiation and their applications. *Journal of Optics*, 18(9):093004, aug 2016.

[34] K. Kim, A. Taylor, J. Glownia, and et al. Coherent control of terahertz supercontinuum generation in ultrafast laser–gas interactions. *Nature Photonics*, jul 2008.

[35] K. Y. Kim, J. H. Glownia, A. J. Taylor, and G. Rodriguez. Terahertz emission from ultrafast ionizing air in symmetry-broken laser fields. *Opt. Express*, 15(8):4577–4584, Apr 2007.

[36] Ki-Yong Kim, James H. Glownia, A. J. Taylor, and George Rodriguez. High-power broadband terahertz generation via two-color photoionization in gases. *IEEE Journal of Quantum Electronics*, 48:797–805, 2012.

[37] Ki-Yong Kim. Generation of coherent terahertz radiation in ultrafast laser-gas interactions. *Physics of Plasmas*, 16(5):056706, 2009.

[38] Matteo Clerici, Marco Peccianti, Bruno E. Schmidt, Lucia Caspani, Mostafa Shalaby, Mathieu Giguère, Antonio Lotti, Arnaud Couairon, Fran çois Légaré, Tsuneyuki Ozaki, Daniele Faccio, and Roberto Morandotti. Wavelength scaling of terahertz generation by gas ionization. *Phys. Rev. Lett.*, 110:253901, Jun 2013.

[39] H. Hirori, A. Doi, F. Blanchard, and K. Tanaka. Single-cycle terahertz pulses with amplitudes exceeding 1 mv/cm generated by optical rectification in linbo3. *Applied Physics Letters*, 98(9):091106, 2011.

[40] Z. Liu, C. Vaswani, L. Luo, D. Cheng, X. Yang, X. Zhao, Y. Yao, Z. Song, R. Brenes, R. J. H. Kim, J. Jean, V. Bulović, Y. Yan, K.-M. Ho, and J. Wang. Coherent band-edge oscillations and dynamic longitudinal-optical phonon mode splitting as evidence for polarons in perovskites. *Phys. Rev. B*, 101:115125, Mar 2020.

[41] János Hebling, Ka-Lo Yeh, Matthias C. Hoffmann, Balázs Bartal, and Keith A. Nelson. Generation of high-power terahertz pulses by tilted-pulse-front excitation and their application possibilities. *J. Opt. Soc. Am. B*, 25(7):B6–B19, Jul 2008.

[42] X.Ropagnol. *Développement d'une source de radiation térahertz (THz) intense et mise en forme d'impulsions THz à partir d'une antenne de grande ouverture de ZnSe*. PhD thesis, Université du Québec, 2014.

[43] Ajay Nahata, Aniruddha S. Weling, and Tony F. Heinz. A wideband coherent terahertz spectroscopy system using optical rectification and electro-optic sampling. *Applied Physics Letters*, 69(16):2321–2323, 1996.

[44] Torsten Löffler, Markus Kreß, Mark Thomson, Tobias Hahn, Noboru Hasegawa, and Hartmut G Roskos. Comparative performance of terahertz emitters in amplifier-laser-based systems. *Semiconductor Science and Technology*, 20(7):S134–S141, jun 2005.

[45] F.G. Sun, W. Ji, and X.-C. Zhang. Two-photon absorption induced saturation of thz radiation in znte. In *Conference on Lasers and Electro-Optics (CLEO 2000). Technical Digest. Postconference Edition. TOPS Vol.39 (IEEE Cat. No.00CH37088)*, pages 479–480, 2000.

[46] H.Hirori, d F.Blanchard A.Doi a, and K.Tanaka. Single-cycle terahertz pulses with amplitudes exceeding 1 mv/cm generated by optical rectification in linbo3. 2011.

[47] Markus Walther, Kasper Jensby, Søren Rud Keiding, Hidenori Takahashi, and Hiromasa Ito. Far-infrared properties of dast. *Opt. Lett.*, 25(12):911–913, Jun 2000.

[48] Elsa Abreu, Danylo Babich, Etienne Janod, Sarah Houver, Benoît Corraze, Laurent Cario, and Steven Johnson. Thz driven dynamics in mott insulator gata4 se8. In *2019 44th International Conference on Infrared, Millimeter, and Terahertz Waves (IRMMW-THz)*, pages 1–2, 2019.

[49] B. Monoszlai, C. Vicario, M. Jazbinsek, and C. P. Hauri. High-energy terahertz pulses from organic crystals: Dast and dstms pumped at ti:sapphire wavelength. *Opt. Lett.*, 38(23):5106–5109, Dec 2013.

[50] A.Perruchi, S.D.Mitri, G.Penco, E.Allaria, and S.Lupi. The terafermi terahertz source at the seeded fermi free-electron-laser facility. *Review of scientific Instruments*, 2013.

[51] S. Casalbuoni, B. Schmidt, and P. Schmüser. Far-infrared transition and diffraction radiation. *Tesla Report*, 2005.

[52] L. G. Sukhikh, A. P. Potylitsyn, and D. A. Verigin. Simulation of Coherent Diffraction Radiation Generation by Pico-Second Electron Bunches in an Open Resonator. In *Journal of Physics Conference Series*, volume 732 of *Journal of Physics Conference Series*, page 012019, July 2016.

[53] Jianming Dai, Xu Xie, and X.-C. Zhang. Detection of broadband terahertz waves with a laser-induced plasma in gases. *Phys. Rev. Lett.*, 97:103903, Sep 2006.

[54] Nicholas Karpowicz, Jianming Dai, Xiaofei Lu, Yunqing Chen, Masashi Yamaguchi, Hongwei Zhao, X.-C. Zhang, Liangliang Zhang, Cunlin Zhang, Matthew Price-Gallagher, Clark Fletcher, Orval Mamer, Alain Lesimple, and Keith Johnson. Coherent heterodyne time-domain spectrometry covering the entire "terahertz gap". *Applied Physics Letters*, 92(1):011131, 2008.

[55] Donna Strickland and Gerard Mourou. Compression of amplified chirped optical pulses. *Optics Communications*, 55(6):447–449, 1985.

[56] Q. Wu, D. Hewitt, and X.-C. Zhang. Two-dimensional electro-optic imaging of thz beams. *Applied Physics Letter*, jun 1996.

[57] F. Blanchard, X. Ropagnol, H. Hafez, H. Razavipour, M. Bolduc, R. Morandotti, T. Ozaki, and D. G. Cooke. Effect of extreme pump pulse reshaping on intense terahertz emission in lithium niobate at multimillijoule pump energies. *Opt. Lett.*, 39(15):4333–4336, Aug 2014.

[58] Matthew Reid and Robert Fedosejevs. Quantitative comparison of terahertz emission from (100) inas surfaces and a gaas large-aperture photoconductive switch at high fluences. *Appl. Opt.*, 44(1):149–153, Jan 2005.

[59] A. Ferraro, D. C. Zografopoulos, M. Missori, M. Peccianti, R. Caputo, and R. Beccherelli. Flexible terahertz wire grid polarizer with high extinction ratio and low loss. *Opt. Lett.*, 41(9):2009–2012, May 2016.

[60] Elmer Estacio, Shigeki Saito, Tomoharu Nakazato, Yusuke Furukawa, Toshihiro Tatsumi, Minh Pham, Marilou Cadatal-Raduban, Carlito Ponseca, Hiroshi Mizuseki, Yoshiyuki Kawazoe, and Nobuhiko Sarukura. Terahertz birefringence of beta-bab2o4 (bbo) crystal. *2008 Conference on Quantum Electronics and Laser Science Conference on Lasers and Electro-Optics, CLEO/QELS*, pages 1 – 2, 06 2008.

[61] J. Hah, W. Jiang, Z-H. He, J. A. Nees, B. Hou, A. G. R. Thomas, and K. Krushelnick. Enhancement of thz generation by feedback-optimized wavefront manipulation. *Opt. Express*, 25(15):17271–17279, Jul 2017.

[62] Markus Kress, Torsten Löffler, Susanne Eden, Mark Thomson, and Hartmut G. Roskos. Terahertz-pulse generation by photoionization of air with laser pulses composed of both fundamental and second-harmonic waves. *Opt. Lett.*, 29(10):1120–1122, May 2004.

[63] Jingle Liu, Xiaoyu Guo, Jianming Dai, and X.-C. Zhang. Optical property of beta barium borate in terahertz region. *Applied Physics Letters*, 93(17):171102, 2008.

[64] Qiang Su, Weiwei Liu, Dan Lu, Pengfei Qi, Olga Kosareva, and Nan Zhang. Influence of the tilting angle of a bbo crystal on the terahertz radiation produced by a dual-color femtosecond laser. *IEEE Transactions on Terahertz Science and Technology*, 9(6):669–674, 2019.

[65] *Field Guide to Polarization*. SPIE, 2005.

[66] P.D. Dernier. The crystal structure of v2o3 and (v0.962cr0.0382)2o3 near the metal-insulator transition. *Journal of Physics and Chemistry of Solids*, 31(11):2569–2575, 1970.

[67] P. Hansmann, A. Toschi, G. Sangiovanni, T. Saha-Dasgupta, S. Lupi, M. Marsi, and K. Held. Mott–hubbard transition in v2o3 revisited. *physica status solidi (b)*, 250(7):1251–1264, 2013.

[68] Elsa Abreu, Siming Wang, Juan Gabriel Ramírez, Mengkun Liu, Jingdi Zhang, Kun Geng, Ivan K. Schuller, and Richard D. Averitt. Dynamic conductivity scaling in photoexcited v_2o_3 thin films. *Phys. Rev. B*, 92:085130, Aug 2015.

[69] Elsa Abreu, Stephanie N. Gilbert Corder, Sun Jin Yun, Siming Wang, Juan Gabriel Ramírez, Kevin West, Jingdi Zhang, Salinporn Kittiwatanakul, Ivan K. Schuller, Jiwei Lu, Stuart A. Wolf, Hyun-Tak Kim, Mengkun Liu, and Richard D. Averitt. Ultrafast electron-lattice coupling dynamics in vo_2 and v_2o_3 thin films. *Phys. Rev. B*, 96:094309, Sep 2017.

[70] M. K. Liu, B. Pardo, J. Zhang, M. M. Qazilbash, Sun Jin Yun, Z. Fei, Jun-Hwan Shin, Hyun-Tak Kim, D. N. Basov, and R. D. Averitt. Photoinduced phase transitions by time-resolved far-infrared spectroscopy in v_2o_3. *Phys. Rev. Lett.*, 107:066403, Aug 2011.

[71] Flavio Giorgianni, Joe Sakai, and Stefano Lupi. Overcoming the thermal regime for the electric-field driven mott transition in vanadium sesquioxide. *Nature Communications*, 10(1):1159, Mar 2019.

[72] A. X. Gray, M. C. Hoffmann, J. Jeong, N. P. Aetukuri, D. Zhu, H. Y. Hwang, N. C. Brandt, H. Wen, A. J. Sternbach, S. Bonetti, A. H. Reid, R. Kukreja, C. Graves, T. Wang, P. Granitzka, Z. Chen, D. J. Higley, T. Chase, E. Jal, E. Abreu, M. K. Liu, T.-C. Weng, D. Sokaras, D. Nordlund, M. Chollet, R. Alonso-Mori, H. Lemke, J. M. Glownia, M. Trigo, Y. Zhu, H. Ohldag, J. W. Freeland, M. G. Samant, J. Berakdar, R. D. Averitt, K. A. Nelson, S. S. P. Parkin, and H. A. Dürr. Ultrafast terahertz field control of electronic and structural interactions in vanadium dioxide. *Phys. Rev. B*, 98:045104, Jul 2018.

[73] A. Levchuk, B. Wilk, G. Vaudel, F. Labbé, B. Arnaud, K. Balin, J. Szade, P. Ruello, and V. Juvé. Coherent acoustic phonons generated by ultrashort terahertz pulses in nanofilms of metals and topological insulators. *Phys. Rev. B*, 101:180102, May 2020.

[74] P. Mounaix, N. Lascoux, J. Degert, E. Freysz, A. Kobayashi, N. Daro, and J.-F. Letard. Dielectric characterization of [fe(nh2 trz)3]br2 h2o thermal spin crossover compound by terahertz time domain spectroscopy. *Applied Physics Letters*, 87(24):244103, 2005.

[75] B. Viquerat, J. Degert, M. Tondusson, E. Freysz, C. Mauriac, and J. F. Létard. Time-domain terahertz spectroscopy of spin state transition in [fe(nh2 trz)3]2+ spin crossover compounds. *Applied Physics Letters*, 99(6):061908, 2011.

[76] J.-L. Coutaz L.Dulivaret, F. Garet. A reliable method for extraction of material parameters in terahertz time-domain spectroscopy. *IEEE*, 1996.

[77] Christian Ketchazo nsenguet Ketchazo Nsenguet. *Imaging in the terahertz domain*. Theses, Université de Grenoble, June 2012.

[78] J. Ollivier, J. Etrillard, M. Sougoti, B. Toudic, C. Ecolivet, and P. Bourges. Structural and dynamical aspects of the incommensurate molecular system bis(4-chlorophenyl) sulfone. *Ferroelectrics*, 183(1):283–289, 1996.

[79] Moussa Sougoti. *Etudes de transitions structurales par techniques optiques (biréfringence, Raman, Billouin) et diffusion de neutrons : application au Bis -4-Chlorophényle) sulphone (BCPS)*. PhD thesis, Université de Rennes 1, 1994.

[80] Henrik T. Lemke, Kasper S. Kjær, Robert Hartsock, Tim B. van Driel, Matthieu Chollet, James M. Glownia, Sanghoon Song, Diling Zhu, Elisabetta Pace, Samir F. Matar, Martin M. Nielsen, Maurizio Benfatto, Kelly J. Gaffney, Eric Collet, and Marco Cammarata. Coherent structural trapping through wave packet dispersion during photoinduced spin state switching. *Nature Communications*, 8(1):15342, May 2017.

[81] Chastanet et al. *Chem. Sq.*, 2(2), 2018.

[82] M. Buron-Le Cointe, J. Hébert, C. Baldé, N. Moisan, L. Toupet, P. Guionneau, J. F. Létard, E. Freysz, H. Cailleau, and E. Collet. Intermolecular control of thermoswitching and photoswitching phenomena in two spin-crossover polymorphs. *Phys. Rev. B*, 85:064114, Feb 2012.

[83] Jean-Pierre Tuchagues, Azzedine Bousseksou, Gábor Molnár, John J. McGarvey, and François Varret. *The Role of Molecular Vibrations in the Spin Crossover Phenomenon*, pages 84–103. Springer Berlin Heidelberg, Berlin, Heidelberg, 2004.

[84] G. Brehm, M. Reiher, and S. Schneider. Estimation of the vibrational contribution to the entropy change associated with the low- to high-spin transition in fe(phen)2(ncs)2 complexes: Results obtained by ir and raman spectroscopy and dft calculations. *The Journal of Physical Chemistry A*, 106(50):12024–12034, 2002.

[85] Metatla, A., Latelli, H., Nicolazzi, W., and Bousseksou, A. Vibration-driven thermal transition in binuclear spin crossover complexes. *Eur. Phys. J. B*, 85(6):205, 2012.

[86] A. Marino, M. Cammarata, S. F. Matar, J.-F. Létard, G. Chastanet, M. Chollet, J. M. Glownia, H. T. Lemke, and E. Collet. Activation of coherent lattice phonon following ultrafast molecular spin-state photo-switching: A molecule-to-lattice energy transfer. *Structural Dynamics*, 3(2):023605, 2016.

[87] Manuel Gruber, Toshio Miyamachi, Vincent Davesne, Martin Bowen, Samy Boukari, Wulf Wulfhekel, Mebarek Alouani, and Eric Beaurepaire. Spin crossover in fe(phen)2(ncs)2 complexes on metallic surfaces. *The Journal of Chemical Physics*, 146(9):092312, 2017.

[88] Andreas Hauser, Jelena Jeftić, Harald Romstedt, Roland Hinek, and Hartmut Spiering. Cooperative phenomena and light-induced bistability in iron(ii) spin-crossover compounds. *Coordination Chemistry Reviews*, 190-192:471–491, 1999.

[89] Andrea Marino, Pradip Chakraborty, Marina Servol, Maciej Lorenc, Eric Collet, and Andreas Hauser. The role of ligand-field states in the ultrafast photophysical cycle of the prototypical iron(ii) spin-crossover compound [fe(ptz)6](bf4)2. *Angewandte Chemie International Edition*, 53(15):3863–3867, 2014.

[90] William Nicolazzi and Azzedine Bousseksou. Thermodynamical aspects of the spin crossover phenomenon. *Comptes Rendus Chimie*, 21(12):1060–1074, 2018. Spin crossover phenomenon / Phénomène de transition de spin.

[91] E. Collet, G. Azzolina, T. Ichii, and et al. Lattice phonon modes of the spin crossover crystal [fe(phen)2(ncs)2] studied by thz, ir, raman spectroscopies and dft calculations. *The European Physic Journal B*, jan 2019.

[92] Markus Reiher. Theoretical study of the fe(phen)2(ncs)2 spin-crossover complex with reparametrized density functionals. *Inorganic Chemistry*, 41(25):6928–6935, 2002. PMID: 12470092.

[93] E.W. Müller, H. Spiering, and P. Gütlich. Spin transition in [fe(phen)2(ncs)2] and [fe(bipy)2(ncs)2]: Hysteresis and effect of crystal quality. *Chemical Physics Letters*, 93(6):567–571, 1982.

[94] M. Sorai and S. Seki. Phonon coupled cooperative low-spin 1a1high-spin 5t2 transition in [fe(phen)2(ncs)2] and [fe(phen)2(ncse)2] crystals. *Journal of Physics and Chemistry of Solids*, 35(4):555–570, 1974.

[95] S. Shi, G. Schmerber, J. Arabski, J.-B. Beaufrand, D. J. Kim, S. Boukari, M. Bowen, N. T. Kemp, N. Viart, G. Rogez, E. Beaurepaire, H. Aubriet, J. Petersen, C. Becker, and D. Ruch. Study of molecular spin-crossover complex fe(phen)2(ncs)2 thin films. *Applied Physics Letters*, 95(4):043303, 2009.

[96] V. Ksenofontov, A. B. Gaspar, G. Levchenko, B. Fitzsimmons, and P. Gütlich. Pressure effect on spin crossover in [fe(phen)2(ncs)2] and [cri2(depe)2]. *The Journal of Physical Chemistry B*, 108(23):7723–7727, Jun 2004.

[97] Cherif Balde, Cedric Desplanches, Alain Wattiaux, Philippe Guionneau, Philippe Gütlich, and Jean-Francois Letard. Effect of metal dilution on the light-induced spin transition in [fexzn 1 x(phen)2(ncs)2] (phen = 1,10 phenanthroline). *Royal Society of Chemistry*.

[98] Mathieu Marchivie, Philippe Guionneau, Judith A. K. Howard, Guillaume Chastanet, Jean-François Létard, Andres E. Goeta, and Daniel Chasseau. Structural characterization of a photoinduced molecular switch. *Journal of the American Chemical Society*, 124(2):194–195, Jan 2002.

[99] Kate L. Ronayne, Hauke Paulsen, Andreas Höfer, Andrew C. Dennis, Juliusz A. Wolny, Aleksandr I. Chumakov, Volker Schünemann, Heiner Winkler, Hartmut Spiering, Azzedine Bousseksou, Philipp Gütlich, Alfred X. Trautwein, and John J. McGarvey. Vibrational spectrum of the spin crossover complex [fe(phen)2(ncs)2] studied by ir and raman spectroscopy, nuclear inelastic scattering and dft calculations. *Phys. Chem. Chem. Phys.*, 8:4685–4693, 2006.

[100] K. Kato, M. Takata, Y. Moritomo, A. Nakamoto, and N. Kojima. On-off optical switching of the magnetic and structural properties in a spin-crossover complex. *Applied Physics Letters*, 90(20):201902, 2007.

[101] A. Desaix, O. Roubeau, J. Jeftic, J. G. Haasnoot, K. Boukheddaden, E. Codjovi, J. Linarès, M. Noguès, and F. Varret. Light-induced bistability in spin transition solids leading to thermal and optical hysteresis. *The European Physical Journal B - Condensed Matter and Complex Systems*, 6(2):183–193, Nov 1998.

[102] Eric Collet, Marie-Laure Boillot, Johan Hebert, Nicolas Moisan, Marina Servol, Maciej Lorenc, Loïc Toupet, Marylise Buron-Le Cointe, Antoine Tissot, and Joelle Sainton. Polymorphism in the spin-crossover ferric complexes [(TPA)FeIII(TCC)]PF6. *Acta Crystallographica Section B Structural Science*, 65(4):474–480, July 2009.

[103] Paul C. M. Planken, Han-Kwang Nienhuys, Huib J. Bakker, and Tom Wenckebach. Measurement and calculation of the orientation dependence of terahertz pulse detection in znte. *J. Opt. Soc. Am. B*, 18(3):313–317, Mar 2001.

[104] Tingting Qi, Young-Han Shin, Ka-Lo Yeh, Keith A. Nelson, and Andrew M. Rappe. Collective coherent control: Synchronization of polarization in ferroelectric pbtio$_3$ by shaped thz fields. *Phys. Rev. Lett.*, 102:247603, Jun 2009.

[105] R. Mankowsky, A. von Hoegen, M. Först, and A. Cavalleri. Ultrafast reversal of the ferroelectric polarization. *Phys. Rev. Lett.*, 118:197601, May 2017.

[106] C. Mariette, M. Lorenc, H. Cailleau, E. Collet, L. Guérin, A. Volte, E. Trzop, R. Bertoni, X. Dong, B. Lépine, O. Hernandez, E. Janod, L. Cario, V. Ta Phuoc, S. Ohkoshi, H. Tokoro, L. Patthey, A. Babic, I. Usov, D. Ozerov, L. Sala, S. Ebner, P. Böhler, A. Keller, A. Oggenfuss, T. Zmofing, S. Redford, S. Vetter, R. Follath, P. Juranic, A. Schreiber, P. Beaud, V. Esposito, Y. Deng, G. Ingold, M. Chergui, G. F. Mancini, R. Mankowsky, C. Svetina, S. Zerdane, A. Mozzanica, A. Bosak, M. Wulff, M. Levantino, H. Lemke, and M. Cammarata. Strain wave pathway to semiconductor-to-metal transition revealed by time-resolved x-ray powder diffraction. *Nature Communications*, 12(1):1239, Feb 2021.

[107] G. Azzolina, R. Bertoni, C. Mariette, M. Cammarata, E. Trzop, C. Ecolivet, M. Sander, M. Levantino, H. Tokoro, K. Imoto, M. Yoshikiyo, S. Ohkoshi, and E. Collet. Out-of-equilibrium lattice response to photo-induced charge-transfer in a mnfe prussian blue analogue. *J. Mater. Chem. C*, 9:6773–6780, 2021.

[108] Wojciech Gawelda, Andrea Cannizzo, Van-Thai Pham, Frank van Mourik, Christian Bressler, and Majed Chergui. Ultrafast nonadiabatic dynamics of [feii(bpy)3]2+ in solution. *Journal of the American Chemical Society*, 129(26):8199–8206, 2007. PMID: 17559211.

[109] T.Q. Qiu and C.L. Tien. Short-pulse laser heating on metals. *International Journal of Heat and Mass Transfer*, 35(3):719–726, 1992.

[110] M.Koch I.Pupeza, R.Wilk. Highly accurate optical material parameter determination with thz time-domain spectroscopy. *Optical Society Agency*, 2007.

[111] Julien Tranchant, Madec Querre, Etienne Janod, Marie-Paule Besland, Benoet Corraze, and Laurent Cario. Mott memory devices based on the mott insulator (v1-xcrx)2o3. pages 1–4, 2018.

[112] D. H. Auston, K. P. Cheung, J. A. Valdmanis, and P. R. Smith. Ultrafast optical electronics: From femtoseconds to terahertz. In Gerard Albert Mourou, David M. Bloom, and Chi-H. Lee, editors, *Picosecond Electronics and Optoelectronics*, pages 2–8, Berlin, Heidelberg, 1985. Springer Berlin Heidelberg.

[113] A. Tomasino, A. Parisi, S. Stivala, P. Livreri, A. C. Cino, A. C. Busacca, M. Peccianti, and R. Morandotti. Wideband thz time domain spectroscopy based on optical rectification and electro-optic sampling. *Scientific Reports*, 3(1):3116, Oct 2013.

UNIVERSITÉ DE RENNES 1

Titre : Développement d'une source THz intense dans le but de déclencher des réponses électroniques et structurelles des matériaux.

Mots clés : Ultrarapide, THz, Photo-induit

Résumé : Le rayonnement THz permet un large spectre d'application dans le domaine de l'optique ultra rapide et notamment dans les expériences dîtes pompe-sonde. Cependant, l'accessibilité de source de rayonnement THz intense en laboratoire est encore restreinte. Il est donc nécessaire de développer de nouvelles sources au laboratoire. Dans cette thèse, une source THz basée sur le redressement optique dans le cristal de $LiNbO_3$ utilisant la technique du front d'onde inclinée a été développé et caractérisé. Le rayonnement THz associé à cette source est un simple cycle dont la durée est proche de la ps. Ce rayonnement peut donc être utilisé afin d'appliquer des champs électriques excédent les 500KV/cm sur une durée suffisamment importante pour permettre les mouvements des molécules ou des atomes. Cet aspect permet d'utiliser le rayonnement THz comme une pompe dans les expériences pompe-sonde. De plus, le spectre associé au rayonnement THz permet de réaliser la spectroscopie basse fréquence qui n'est pas accessible autrement. Un dispositif expérimental de spectroscopie du domaine temporelle a été également développé afin d'obtenir le spectre THz des matériaux. Ces deux aspects du rayonnement THz ont été utilisé sur un système à transition de spin le $Fe(phen)_2(NCS)_2$. L'intrication des degrés de liberté électronique et structurel de ce composé rend particulièrement intéressante l'utilisation du rayonnement THz. En effet, le champ électrique THz permet d'agir sur la structure du composé et ainsi d'induire des changements dans l'absorption optique. De plus, les basses fréquences du rayonnement THz permettent de compléter les études des mouvements collectifs des molécules dans le cristal ou phonon. Nous avons ainsi pu observer les premières modulations de transmission optique dans ce composé utilisant une pompe THz. De plus, la source THz développée dans cette thèse a permis d'observer des pics d'absorptions qui n'avait pas été mesuré auparavant. Ce travail de thèse a ainsi pu démontrer l'importance du rayonnement THz dans la physique ultra rapide moderne.

Title : Development of an intense pulsed THz source to trigger structural and electronic response of materials.

Keywords : de 3 à 6 mots clefs

Abstract : THz radiation allows a wide spectrum of applications in the field of ultra-fast optics and in particular in so-called pump-probe experiments. However, the accessibility of intense THz radiation sources in the laboratory is still restricted. It is therefore necessary to develop new sources in the laboratory. In this thesis, a THz source based on optical rectification in the LiNbO3 crystal using the tilted pulsefront technique was developed and characterized. The THz radiation associated with this source is a single cycle whose duration is close to the ps. This radiation can therefore be used to apply electric fields in excess of 500KV/cm over a sufficiently long period to allow the movements of molecules or atoms. This aspect allows THz radiation to be used as a pump in pump-probe experiments. In addition, the spectrum associated with THz radiation makes it possible to perform low-frequency spectroscopy which is not otherwise accessible. An experimental device for time domain spectroscopy has also been developed in order to obtain the THz spectrum of materials. These two aspects of THz radiation have been used on a spin transition system Fe(phen)2(NCS)2. The entanglement of the electronic and structural degrees of freedom of this compound makes the use of THz radiation particularly interesting. Indeed, the THz electric field makes it possible to act on the structure of the compound and thus to induce changes in the optical absorption. In addition, the low frequencies of THz radiation make it possible to complete studies of the collective motions of molecules in the crystal or phonon. We were thus able to observe the first modulations of optical transmission in this compound using a THz pump. In addition, the THz source developed in this thesis made it possible to observe absorption peaks that had not been measured before. This thesis work was thus able to demonstrate the importance of THz radiation in modern ultra-fast physics.